KERNFORSCHUNGSANLAGE JÜLICH GmbH
Institut für Reaktorwerkstoffe
Association EURATOM – KFA

COMPARISON OF HIGH PURITY FINE GRAIN GRAPHITES FROM DIFFERENT SUPPLIERS WITH REGARD TO PHYSICAL, MECHANICAL AND THERMAL PROPERTIES

by

Wolfgang Delle
Jochen Linke
Hubertus Nickel
Erich Wallura

Jül-Spez-401
May 1987
ISSN 0343-7639

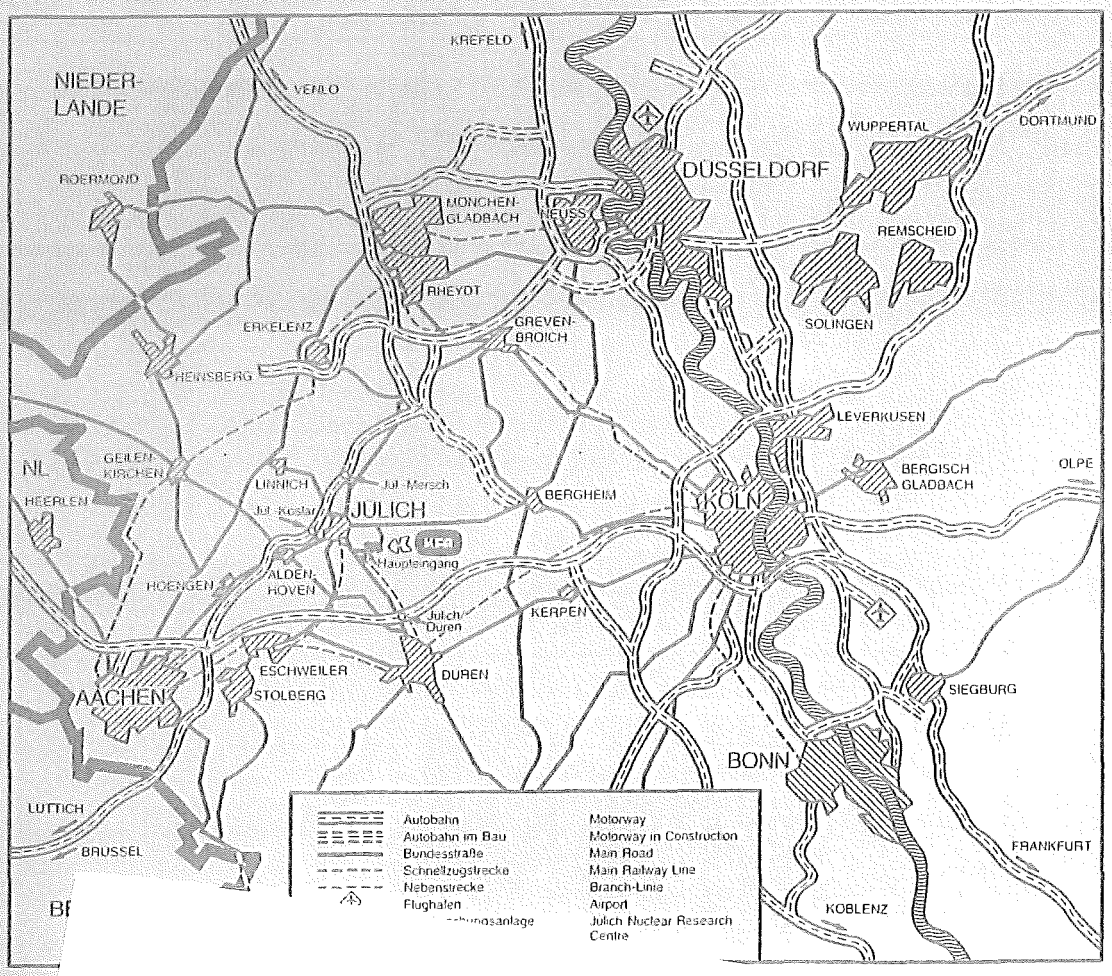

Als Manuskript gedruckt

Spezielle Berichte der Kernforschungsanlage Jülich – Nr. 401
Institut für Reaktorwerkstoffe Jül-Spez-401

Zu beziehen durch: ZENTRALBIBLIOTHEK der Kernforschungsanlage Jülich GmbH
Postfach 1913 · D-5170 Jülich (Bundesrepublik Deutschland)
Telefon: 02461/610 · Telex: 833556-0 kf d

– Final Report –

COMPARISON OF HIGH PURITY FINE GRAIN GRAPHITES FROM DIFFERENT SUPPLIERS WITH REGARD TO PHYSICAL, MECHANICAL AND THERMAL PROPERTIES

The work has been conducted
under

THE ARTICLE 14 CONTRACT JD4/9009

between

THE JET JOINT UNDERTAKING,
THE EUROPEAN ATOMIC ENERGY COMMUNITY

and

EURATOM/KFA ASSOCIATION

Abstract

By order of The Jet Joint Undertaking, The European Atomic Energy Community, eight high purity fine grain graphites and one carbon fibre composite were investigated with regard to a number of properties as far as to their thermal shock behaviour.

The following properties were determined:

- Apparent density
- Total and open porosity
- Electrical resistivity between room temperature and 1000°C
- Thermal conductivity between 100°C and 1000°C
- Linear thermal expansion between room temperature and 1000°C
- Dynamic Young's modulus
- Bending strength and fracture deflexion.

A number of impurities - including sulfur - were determined. Multi-element analytical methods, such as spark source mass spectrometry and optical atom emission spectrometry with excitation in an inductively coupled plasma, were used rendering the simultanious detection of about 45 elements. Sulfur was detected by the classical method of burning to SO_2 and application of infrared.

Four series of thermal shock and erosion experiments were carried out on all graphites and the carbon fibre composite.

For this purpose, graphite samples were exposed to a defocussed electron beam of different power densities and pulse durations. The erosion behaviour of the particular materials differred significantly.

Kurzfassung

Im Auftrag des Jet Joint Undertaking, Europäische Atomenergie-Gemeinschaft, wurden im Institut für Reaktorwerkstoffe der Kernforschungsanlage Jülich GmbH acht Feinkorngraphite hoher Reinheit und ein faserverstärktes Kohlenstoffmaterial im Hinblick auf eine Anzahl von Eigenschaften wie auch auf ihre thermische Schockbeständigkeit untersucht.
Folgende Eigenschaften wurden gemessen:

- Rohdichte
- Gesamt- und offene Porosität
- Spezifischer elektrischer Widerstand zwischen Raumtemperatur und 1000°C
- Wärmeleitfähigkeit zwischen 100°C und 1000°C
- Lineare thermische Ausdehnung zwischen Raumtemperatur und 1000°C
- Dynamischer Elastzitätsmodul
- Biegefestigkeit und Bruchbiegung

Eine Anzahl von Verunreinigungen - einschließlich Schwefel - wurde bestimmt. Multielement-Analysenverfahren wie Funken-Massenspektrometrie und optische Atomemissionsspektrometrie mit Anregung in einem induktiv gekoppelten Plasma wurden benutzt, um den gleichzeitigen Nachweis von 45 Elementen zu ermöglichen. Schwefel wurde durch die klassisch-chemische Methode des Verbrennens zu SO_2 und Nachweis durch Infrarot nachgewiesen.

Vier Reihen von Thermoschock- und Erosionsexperimenten wurden an allen Graphiten und dem faserverstärkten Kohlenstoff durchgeführt. Zu diesem Zweck wurden Graphitproben einem defokussierten Elektronenstrahl unterschiedlicher Leistungsdichte und Pulsdauer ausgesetzt. Das Erosionsverhalten der einzelnen Materialien unterschied sich beträchtlich.

- F i n a l R e p o r t -

COMPARISON OF HIGH PURITY FINE GRAIN GRAPHITES FROM DIFFERENT SUPPLIERS WITH REGARD TO PHYSICAL, MECHANICAL AND THERMAL PROPERTIES

The following KFA personnel contributed to experiments and report:

Task	Name	KFA-Department
Project Coordination	W. Delle	IRW
Coordination of Machining and Examinations of Specimens	F. Meuser	IRW
Measurements of Density, Porosity, Electrical Resistivity (room temp.), Dynamic Young's Modulus, Coefficient of Thermal Expansion	G. Haag H. Görtz	IRW IRW
Measurements of High Temperature Thermal Conductivity and Electrical Resistivity	L. Binkele	IRW
Measurements of Bending Strength	H. Schiffers	IRW
Chemical Analysis	H. Beske G. Wolff	ZCH ZCH
Thermal Shock and High Heat Flux Testing	J. Linke F. Meuser P. Schlebusch E. Sigismund	IRW IRW ZAT ZAT
Ceramography	H. Hoven	IRW
Scanning Electron Microscopy Investigations	E. Wallura F. Els	IRW IRW
Quantitative Image Analysis	J. Linke G. Gutzeit	IRW IRW

IRW: Institut für Reaktorwerkstoffe
(Department of Reactor Materials)

ZAT: Zentralabteilung Allgemeine Technologie
(Central Department of Technology)

ZCH: Zentralabteilung für Chemische Analyse
(Central Department of Chemical Analysis)

Contents

		Page
1.	INTRODUCTION	1
2.	MATERIALS	2
3.	PROGRAMME OF INVESTIGATIONS	4
3.1	Determination of physical, thermal and mechanical properties	4
3.1.1	Apparent density and porosity	4
3.1.2	Electrical resistivity at room temperature	6
3.1.3	Dynamic Young's modulus	6
3.1.4	Linear thermal expansion, CTE	9
3.1.5	High temperature thermal conductivity and electrical resistivity	19
3.1.6	Bending Strength	55
3.1.7	Summary	77
3.2	Determination of impurity contents	79
3.3	Thermal shock and high heat flux testing	88
3.3.1	Introduction	88
3.3.2	Experimental equipment	88
3.3.3	Heat flux conditions	90
3.3.4	Results	91
3.3.4.1	Reproducibility	91
3.3.4.2	Crater dimensions and weight loss	92
3.3.4.3	Crack formation	93
3.3.4.4	Structure of the eroded surface	97
3.3.4.5	Summary	99
4.	REFERENCES	147

LIST OF TABLES

Table		Page
1	Graphites investigated in the frame of the programme described	3
2 - 10	Properties of various grades of graphites	10 - 18
11 - 18	High temperature electrical resistivity and thermal conductivity	23 - 30
19	Results of bending experiments on various grades of graphites	58
20	Results of bending experiments on the carbon fibre composite	59
21 - 25	Bending strength and fracture deflexion measured on individual specimens of various graphites	60 - 64
26	Comparison of property values provided by data sets of the producers with those measured in the frame of this study	78
27 - 33	Results of chemical analysis of various grades of graphites	80 - 86
34	Impurities detected in various grades of graphites	87
35	Number of experiments in series 1 through 4 in dependence on the heat loading conditions	100
36	Sample numbers and weight loss data for 3 test series	101

LIST OF FIGURES

Figure		Page
1	Plan of specimen positions in graphite blocks investigated	3
2	Schematic diagramme for Young's modulus apparatus	8
3	Schematic diagramme of thermal conductivity equipment	19
4 - 11	Temperature dependent thermal conductivity and electrical resistivity of various graphites	30 - 53
12	Fractional change of electrical resistivity caused by heating up from room temperature to 1000^{o}C	22
13	Scheme of specimen cutting and bending strength measurement of carbon fibre composite	56
14	Correlation between mean values of fracture deflexion and bending strength	65
15	Correlation between bending strength and dynamic Young's modulus for various grades of graphite	66
16 - 34	Correlation between bending strength and fracture deflexion for intervals of expectation and prediction	67 - 76
35	Electron beam welding machine for thermal shock testing	102
36	Spatial distribution of current density in a focussed electron beam	103
37	Curves of constant current density at 20, 40, 60 and 80 % of the peak density	103
38	Weight loss of fine grain graphite EK 98 and stainless steel 1.4311 due to electron beam pulses with 5 kW cm^{-2} mean power density and 1 s duration	104
39	Macroscopic appearance of the electron beam damage due to a 5 kW cm^{-2} pulse of 1 s duration	105

Figure		Page
40	Weight loss of graphite tiles due to the single shot electron beam experiment	107
41	Low magnification SEM-images of graphite tiles exposed to an electron beam with 3.5 kW cm^{-2} power density and 1 s pulse duration	110
42	Low magnification SEM-images of graphite tiles exposed to an electron beam with 5.0 kW cm^{-2} power density and 1 s pulse duration	112
43	Low magnification SEM-images of graphite tiles exposed to an electron beam with 10 kW cm^{-2} power density and 0.1 s pulse duration	117
44	High resolution SEM-images of graphite tiles exposed to an electron beam with 3.5 kW cm^{-2} power density and 1 s pulse duration	123
45	High resolution SEM-images of graphite tiles exposed to an electron beam with 5.0 kW cm^{-2} power density and 1 s pulse duration	125
46	High resolution SEM-images of graphite tiles exposed to an electron beam with 10 kW cm^{-2} power density and 0.1 s pulse duration	129
47	Ceramographic sections of graphite samples after a 5.0 kW cm^{-2} electron beam pulse of 1 s duration	131
48	Ceramographic sections of graphite samples after a 5.0 kW cm^{-2} electron beam pulse of 1 s duration	134
49	Ceramographic sections of graphite samples after a 10 kW cm^{-2} electron beam experiment of 100 ms duration	136
50	Ceramographic sections of graphite samples after a 10 kW cm^{-2} electron beam experiment of 100 ms pulse duration	139
51	Evaluation of crack formation after 5 kW cm^{-2} - 1 s pulses	140
52	Thermal conductivity of various graphites	141
53	Young's modulus of various graphites	142
54	Mean bending strength of various graphites	143

Figure		Page
55	Coefficient of linear thermal expansion of various graphites	144
56	Mean value of pore section area for various graphites determined by quantitative optical microscopy	145
57	Macroporosity of various graphites determined by quantitative optical microscopy	146

1. Introduction

Among the low Z materials, graphite appears to be one of the most attractive materials for limiter and wall protection against run-away electrons, disruptions and NB shine through in the JET equipment. Also for the protection of the RF antenna, graphite is felt to be a suitable material.

Polycrystalline graphite is produced by procedures as used in ceramic industry. Various cokes and binders are the basis for the final product. After grinding, different amounts of coke particles are mixed with a binder. The mixture is then pressed at about 100°C, either by moulding, extrusion, vibration or isostatic pressing. The so-called green body is heat-treated at about 1000°C to crack the hydrocarbon binder. To increase the density, the artifact can additionally be pitch impregnated.

The final step is the graphitization at temperatures between 2500 and 3000°C. It is very important for the properties and purity of the particular graphite. Depending upon the particular requirements, an additional purification can follow.

It is evident that the various raw materials and the production parameters will influence the properties of the final product. Therefore it was the purpose of the contract between The Joint European Torus JET Joint Undertaking and The EURATOM/KFA Association to compare some high purity fine grain graphites delivered from different suppliers with regard to physical, thermal and mechanical properties and to determine the impurity content.

Furthermore, the knowledge of the behaviour of these materials under irregular plasma operating conditions, i.e., the behaviour during plasma disruptions or high heat-fluxes to the first wall due to particle bombardment from the neutral beam injector during the absence of the plasma is of significant importance. Both types of accident will - under certain circumstances - cause damages on the limiters and on the first wall, resp.. To simulate the heat-fluxes to the graphite and to study the resulting damage, laboratory tests were carried out using an electron beam (welding machine) with power densities and exposure times similar to those expected in the JET machine. The exposed graphite tiles were analysed with respect to erosion and cracking behaviour using optical and scanning electron microscopy

in addition to the conventional ceramographic methods. An attempt was made to correlate these results with the thermo-mechanical properties and the structural parameters of the various materials.

This report is devided into three parts:

- Determination of physical, thermal and mechanical properties.
- Determination of impurity contents.
- Thermal shock and high heat flux testing.

2. Materials

The experiments to be described in the following chapters were carried out on several fine grain graphites from different manufacturers. The maximum grain sizes of the particular graphites were in the range between 4 and 1000 µm. In the set-up phase of the investigations, only 6 various graphites were foreseen to be tested. In later stages, the number of graphites was increased to 8 plus an additional 2-dimensionally interweaved carbon fibre composite. All graphites based on petroleum coke as filler.

With the only exception of POCO graphite, which is a so-called binderless one, they were all pitch bonded. The materials investigated are listed up in table 1. They were selected and ordered by JET. The particular blocks were delivered to KFA (Kernforschungsanlage Jülich GbmH). The specimens were taken and machined in the graphite workshop of the Institute of Reactor Materials (IRW, Institut für Reaktorwerkstoffe) of KFA.

The principle of sample selection is demonstrated in fig. 1 showing that the specimens were taken from three regions of the block, bottom - middle - top, in three directions (AC, BD, XY, were A, B, C, D, X, Y are areas, i.e., specimen AC was taken in the direction of area A to area C etc.).

Material	Manufacturer
EK 98	Ringsdorff-Werke GmbH, Bonn/D
5890/PT	Le Carbone-Lorraine, Gennevilliers/F
AXF-5Q	POCO Graphite, Inc. Decatur, TX/USA
EY-306	Morganite Spec. Carbons Ltd., London/GB
FP-219	Schunk Kohlenstoff GmbH, Gießen/D
H-490	Great Lakes Carbon Corp., Niagara Falls, NY/USA
ATJ	Union Carbide Corp., Parma, OH/USA
FE-289	Schunk Kohlenstoff GmbH, Gießen/D
E 5923P	Dunlop/GB

Tab. 1: Graphites investigated in the frame of the programme described

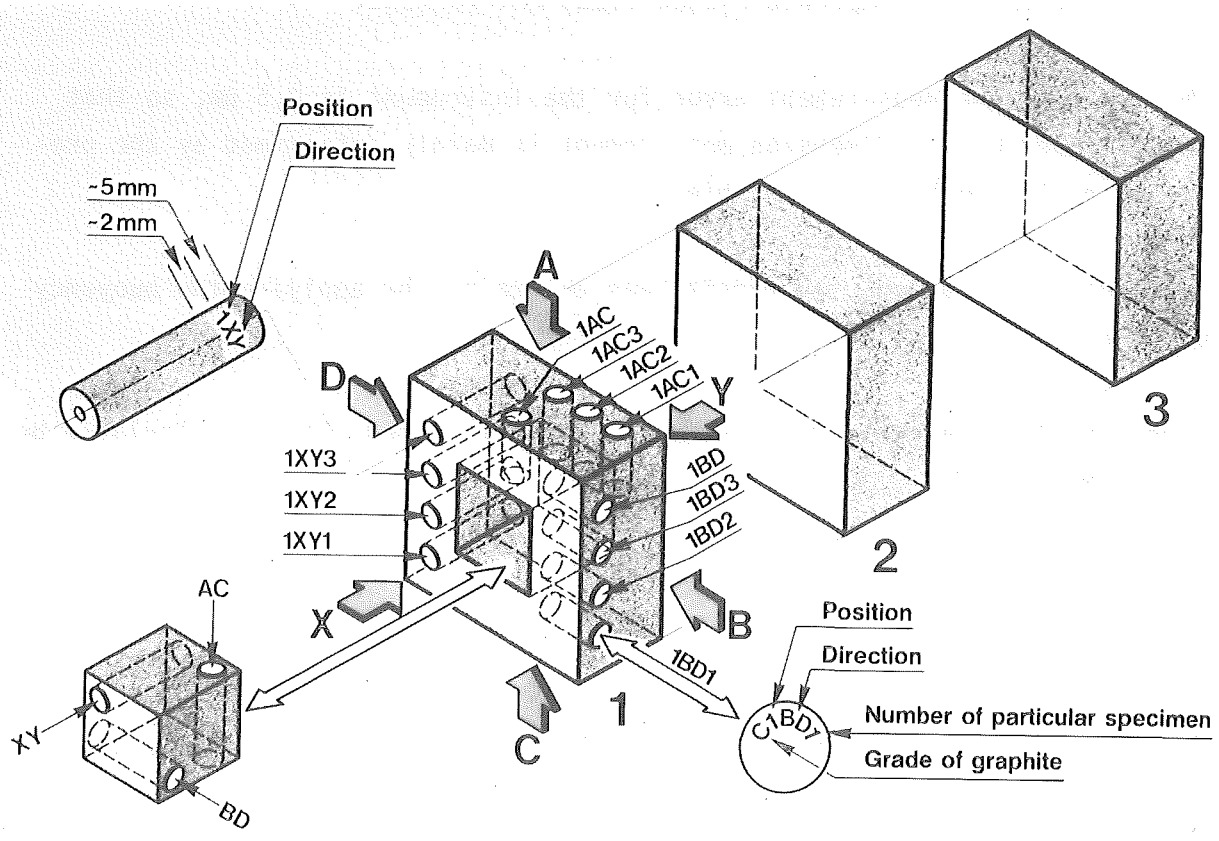

Fig. 1: Plan of specimen positions in graphite blocks investigated

3. Programme of investigations

3.1 Determination of Physical, Thermal and Mechanical Properties

3.1.1 Apparent Density and Porosity

The ratio of the mass of a body to its geometrical volume is defined as the apparent density. For the actual measurements, the mass was determined with an analytical balance H 10 P delivered by the METTLER Company. The dimensions were determined applying the vertical length measuring device delivered by the LEITZ company. After the test specimen is laid on the instrument table, a probe is brought into contact with a constant force of 0.6 N. The vertical length is measured electrically, registered digitally and stored in a data system. The movement of the probe is electrically triggered so that no hand heat is transfered to the specimen. As an extra safeguard, the instrument is in a temperature-stabilized environment.

The limit of the measurement error for the instrument is 0.5 µm, so that the accuracy of the dimension measurement is mainly determined by the precision of the mechanical finishing.

As a second procedure, the density was determined by applying the buoyancy methode.

According to elementary physics, the density of a body can be calculated by the formula

$$d = \frac{m\, W_{liq}}{B},$$

where m is the mass of the sample and B the buoyancy which the sample experiences in a liquid with specific weight W_{liq}. It is equal to the difference between the weight of the sample in air and in the liquid neglecting the buoyancy in air. In the case of samples with measurable porosity, however, the liquid penetrates the pores during the measurement and the sample weight in the liquid increases as the volume of the displaced liquid decreases. Thus for the determination of the apparent density the "outer" volume of displacing body must also be known. To this end, the sample is previously impregnated with the same liquid (namely xylene) as used to

determine the displacement. The samples must first be evacuated for two hours at a pressure of 10^{-2} torr before being exposed to the similarly outgassed xylene which then flows into the pores. During the ventilation of the apparatus, the liquid is forced still deeper into the pores by the outside pressure. After about an hour as the temperature of the sample approaches that of the environment, the sample weight in the liquid can be measured. Since xylene evaporates easily at atmosphere pressure and room temperature, the body, which has been freed of surface liquid, is put into a container filled with xylene which has been previously weighed. The container head is opened here for approximately 10 s. From numerous previous investigations it is known how much liquid evaporates in this time in the temperature controlled laboratory.

The volume V of the displaced liquid for the outer volume of the sample is used to calculate the buoyancy

$$B = VW_{liq}.$$

The accuracy of the weight determination is 1 μN. The temperature of the liquid is measured to within 0.1 degrees so that the specific weight W_{liq} can be read from tables with sufficient accuracy.

The increase in weigth of the graphite sample in air by impregnation with a liquid of well-known specific weight is used for the calculation of open pore volume.

Total porosity is calculated from apparent and theoretical (or real) density

$$P = 1 - \frac{d_a}{d_{th}}$$

d_a = apparent density
d_{th} = theoretical density (2.267 g cm^{-3} for graphite).

It includes all irregularities such as defects and imperfections. If these effects are neglected, the real density instead of theoretical density can be used for the calculation. The results of apparent density and open porosity determinations are listed up in tables 2 to 9.

3.1.2 Electrical Resistivity

Electrical resistivity was measured at 20°C applying the four point method. A current of 50 mA was sent through the specimen and the voltage was measured at three points of the surface immediately.
At temperatures between 50°C and 1000°C electrical resistivity was determined in connection with thermal conductivity measurements at high temperatures. Some informations are presented under 3.1.5.

The results of electrical resistivity determinations at room temperature are listed up in tables 2 to 10 and at high temperatures in tables 11 to 19. Electrical resistivity at high temperatures is discussed under 3.1.5.

3.1.3 Dynamic Young's Modulus

If a periodically changing force is applied to the axis of a body of small cross-section and appreciable length, the speed of propagation C_1 of the longitudinal wave can be described by the equation

$$C_1 = \sqrt{\frac{E_s}{d}} \qquad (1)$$

where E_s is the elasticity modulus for the strain and d the density of the sample material. For a sample whose thickness is not small compared to its length, the lateral contraction induces an increase in the speed of propagation for the longitudinal waves. In the extreme case of a boundless solid body,

$$C_1 = K\sqrt{\frac{E_s}{d}}$$

where

$$K^2 = \frac{1 - \mu}{(1 + \mu)(1 - 2\mu)} .$$

For transversal excitation the following applies for the propagation velocity

$$C_t = \sqrt{\frac{G}{d}}$$

independent of the laterial contraction. Here G is the shearing or torsion modulus. The strain modulus and torsion modulus are connected by the Poisson's constant μ:

$$E_s = 2\ (1 + \mu)\ G. \qquad (2)$$

Since Poisson's constant is normally unknown, one in general determines the strain modulus E_s according to equation (1) by measuring the velocity of sound in samples whose diameters are small in relation to their length. The measurements are carried out using an automatically funtioning apparatus connected to a data system. A synthesizer produces an alternating voltage whose frequency can be continuously varied between 500 Hz and 200 kHz. This alternating voltage triggers an electromechanical oscillator O which transmits the oscillations through direct contact with the sample. Longitudinal as well as transverse oscillations are produced in the sample. At the other end of the sample, the oscillations are taken up by the pickup VP, again through direct contact being measured using a digital voltmeter. For a body whose cross-section is small compared to its length l and which is moveably fixed at both ends, standing waves are produced when the condition

$$l = \frac{\lambda}{2} \qquad (3)$$

is fulfilled. λ is the wave length in the sample and n = 1, 2, 3... the degree of the oscillation. The following relationship applies between the wave length λ, the strain frequency f_s and the propagation velocity C_1:

$$C_1 = f_s \lambda \qquad (4)$$

From the equations (1), (3) and (4) the equation for the determination of the elasticity modulus can be deduced

$$E_s = \frac{4l^2 f_s^2 d}{n^2} .$$

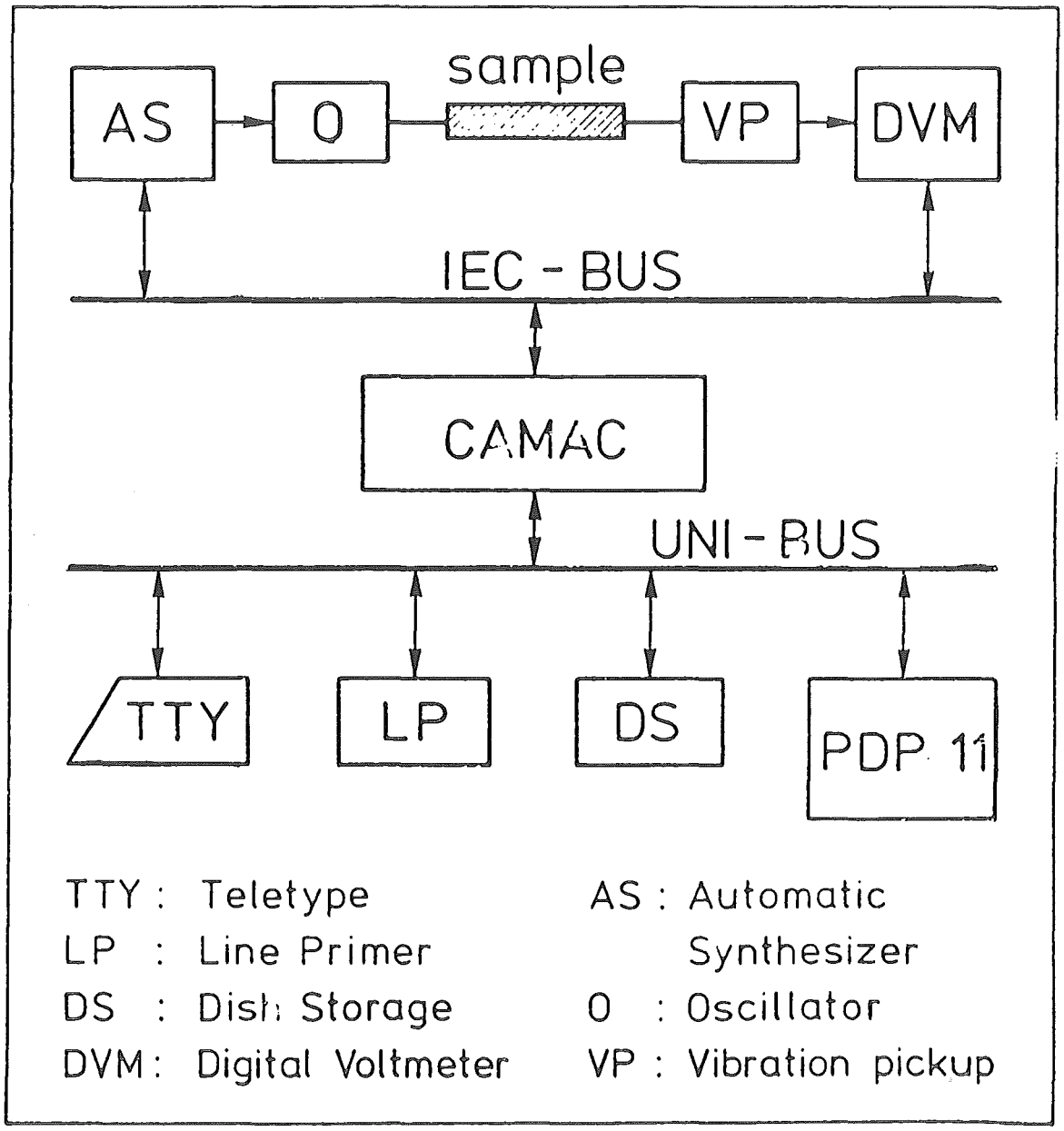

Fig. 2: Schematic Diagramme for Young's Modulus Apparatus

3.1.4 Linear Thermal Expansion, CTE

The linear thermal expansion coefficient is determined as a function of temperature by means of a pushrod dilatometer from the BAEHR company.

The test specimen is put into a vacuum furnace achieving temperatures between room temperature and 900°C. The temperature profile varies less than 2 K over the length of the test specimen. The electronic temperature programmer is set to have a constant heating rate of about 3 K/min.

The length change of the specimen is transduced mechanically to a measuring head which converts the variation in length into an electrical signal. Thus the length change can be plotted directly vs. the temperature of the specimen measured by a thermocouple. In the present case, the equipment has been modified to store the experimental results in a computer for further evaluation.

In case of thermal expansivity measurements on graphitic materials, the dilatometer is calibrated with a tungsten specimen that has been measured very precisely by the "Physikalisch Technische Bundesanstalt" which is the national bureau of standards of the Federal Republic of Germany. After that correction, the data are fitted by a 2nd order polynominal to perform an inter- or extrapolation with respect to the actual temperature required.

The final result is the M e a n Thermal Expansion Coefficient defined by the equation

$$CTE\ (20\ to\ t) = \frac{l\ (t) - l\ (20°C)}{l\ (20°C) * (t-20°C)}$$

where t is the actual temperature (°C),
CTE (20 to t) is the mean thermal expansion coefficient between 20°C and t,
l is the length of the test specimen at the temperature indicated by the argument.

In tables 2 to 10 the CTE's between 20°C and 400°C as well as 20°C and 1000°C are listed up.

Specimen	Length (mm)	Diam. (mm)	Density (g/cm^{-3})	Open Por. (%)	El.Res. ($Ohm \cdot mm^{-2}/m$)	Young's Modulus (kN/mm^{-2})	CTE ($10^{-6}/K$) betw. 20°C and 400°C	CTE ($10^{-6}/K$) betw. 20°C and 1000°C
R1-1AC	25.0062	5.9958	1.865	7.9	16.15	11.59	3.44	4.48
R1-2AC	25.0040	5.9922	1.867	8.0	16.04	11.73	3.81	4.80
R1-3AC	25.0017	5.9937	1.867	8.0	16.08	11.65	3.37	4.57
R1-1BD	25.0068	5.9910	1.862	8.4	16.05	11.72	3.36	4.50
R1-2BD	25.0177	5.9924	1.860	8.3	16.09	11.67	3.27	4.60
R1-3BD	25.0162	5.9899	1.864	8.2	16.10	11.64	3.33	4.57
R1-1XY	24.9885	6.0212	1.863	8.2	16.23	11.48	2.94	4.30
R1-2XY	24.9948	6.0019	1.862	8.3	16.16	11.56	3.25	4.66
R1-3XY	25.0403	5.9810	1.863	8.3	16.19	11.46	3.53	4.63
R2-1AC	24.9960	6.0053	1.864	8.3	16.34	11.38	3.47	4.44
R2-2AC	24.9762	6.0133	1.864	8.2	16.24	11.51	3.36	4.60
R2-3AC	24.9876	6.0068	1.863	8.3	16.38	11.40	3.44	4.61
R2-1BD	24.9760	6.0083	1.864	8.3	16.29	11.61	3.30	4.47
R2-2BD	24.9853	6.0082	1.863	8.3	16.30	11.58	3.35	4.62
R2-3BD	24.9930	6.0103	1.863	8.2	16.28	11.53	3.31	4.55
R2-1XY	25.0012	6.0040	1.866	8.1	16.08	11.59	3.35	4.43
R2-2XY	25.0000	6.0009	1.862	8.2	16.26	11.56	3.42	4.61
R2-3XY	25.0092	5.9993	1.864	8.3	16.38	11.33	3.41	4.55
R3-1AC	24.9898	6.0054	1.865	8.0	16.20	11.31	3.35	4.32
R3-2AC	24.9918	6.0017	1.871	8.0	16.00	11.41	3.45	4.62
R3-3AC	24.9882	6.0076	1.864	8.0	16.19	11.34	3.36	4.52
R3-1BD	25.0110	5.9978	1.862	8.0	15.82	11.66	3.27	4.39
R3-2BD	24.9910	6.0061	1.866	8.0	15.72	11.65	3.53	4.69
R3-3BD	24.9921	6.0043	1.866	8.0	15.86	11.63	3.25	4.49
R3-1XY	24.9901	6.0053	1.865	8.0	15.95	11.49	3.46	4.61
R3-2XY	24.9879	6.0045	1.864	8.2	15.96	11.47	3.38	4.61
R3-3XY	24.9846	6.0069	1.862	8.1	15.92	11.47	3.42	4.57

Tab. 2: Properties of graphite grade Ringsdorff EK 98

Specimen	Length (mm)	Diam. (mm)	Density (g/cm^{-3})	Open Por. (%)	El.Res. ($Ohm \cdot mm^{-2}/m$)	Young's Modulus (kN/mm^{-2})	CTE ($10^{-6}/K$) betw. 20°C and 400°C	CTE ($10^{-6}/K$) betw. 20°C and 1000°C
C1-1AC	25.0066	5.9897	1.798	10.7	17.34	10.76	4.90	5.94
C1-2AC	25.0026	5.9997	1.809	10.1	17.27	10.86	4.92	5.86
C1-3AC	25.0228	5.9892	1.805	10.4	17.24	10.88	4.93	5.92
C1-1BD	25.0190	5.9930	1.811	9.8	15.48	12.47	4.53	5.53
C1-2BD	25.0140	5.9934	1.810	10.0	15.51	12.52	4.58	5.52
C1-3BD	25.0172	5.9930	1.807	10.2	15.71	12.37	4.38	5.44
C1-1XY	24.9950	6.0061	1.819	9.2	15.47	12.56	4.33	5.39
C1-2XY	24.9846	6.0059	1.812	9.7	15.51	12.44	4.41	5.20
C1-3XY	24.9972	6.0061	1.749	13.0	16.83	11.53	4.43	5.37
C2-1AC	24.9906	5.9970	1.796	10.7	17.17	10.78	4.95	5.93
C2-2AC	24.9856	5.9968	1.806	10.2	17.09	10.90	4.92	5.86
C2-3AC	24.9916	5.9981	1.791	11.1	17.07	10.78	5.01	5.97
C2-1BD	24.9760	6.0014	1.789	10.9	15.95	12.08	4.48	5.47
C2-2BD	24.9738	6.0020	1.775	11.6	15.95	11.97	4.78	5.55
C2-3BD	24.9870	6.0015	1.784	11.3	15.61	12.15	4.61	5.63
C2-1XY	25.0280	5.9948	1.813	10.1	15.04	12.53	4.32	5.42
C2-2XY	24.9958	5.9954	1.756	12.7	16.36	11.66	4.28	5.37
C2-3XY	25.0026	5.9947	1.755	12.9	16.30	11.77	4.36	5.45
C3-1AC	24.9960	6.0066	1.804	10.2	17.52	10.89	5.06	5.98
C3-2AC	24.9936	6.0045	1.762	12.3	18.47	10.34	5.09	6.04
C3-3AC	25.0152	6.0057	1.791	11.0	17.66	10.88	5.02	5.97
C3-1BD	24.9818	6.0093	1.770	12.0	16.68	11.95	4.50	5.49
C3-2BD	24.9958	6.0111	1.787	11.2	16.60	12.10	4.61	5.57
C3-3BD	24.9862	6.0092	1.785	11.3	16.33	12.15	4.48	5.50
C3-1XY	24.9926	6.0044	1.797	10.6	16.46	11.95	4.36	5.37
C3-2XY	24.9884	6.0042	1.732	13.6	17.76	11.16	4.48	5.46
C3-3XY	24.9696	6.0053	1.747	13.2	17.98	10.88	4.48	5.49

Tab. 3: Properties of graphite grade Carbone-Lorraine 5890/PT

Specimen	Length (mm)	Diam. (mm)	Density (g/cm^{-3})	Open Por. (%)	El.Res. (Ohm mm^{-2}/m)	Young's Modulus (kN/mm^{-2})	CTE ($10^{-6}/K$) betw. 20°C and 400°C	CTE ($10^{-6}/K$) betw. 20°C and 1000°C
P1-1AC	25.0120	5.9979	1.756	19.6	19.98	13.22	8.30	9.12
P1-2AC	24.9870	6.0151	1.760	19.3	20.02	13.38	8.18	9.10
P1-3AC	25.0098	5.9980	1.762	19.1	19.98	13.42	8.29	9.13
P1-1BD	25.0368	5.9828	1.788	18.0	18.69	14.21	8.49	9.11
P1-2BD	25.0312	5.9853	1.787	17.8	18.78	14.15	8.08	9.13
P1-3BD	25.0332	5.9838	1.791	17.7	18.66	14.28	8.26	9.02
P1-1XY	25.0108	5.9980	1.780	18.5	19.92	13.51	8.57	9.40
P1-2XY	25.0064	5.9985	1.771	18.7	20.42	13.30	8.60	9.36
P1-3XY	25.0182	5.9964	1.786	18.1	19.68	13.69	8.53	9.47
P2-1AC	25.0202	5.9822	1.805	16.9	17.98	14.24	8.24	9.17
P2-2AC	25.0502	5.9828	1.803	17.1	18.04	14.20	8.64	9.31
P2-3AC	25.0214	5.9837	1.804	17.0	17.92	14.34	8.20	9.26
P2-1BD	25.0328	5.9821	1.802	17.1	18.02	14.21	8.40	9.26
P2-2BD	25.0306	5.9837	1.803	17.2	18.10	14.18	8.42	9.28
P2-3BD	25.0298	5.9826	1.805	16.9	18.09	14.28	8.32	9.43
P2-1XY	25.0370	5.9825	1.808	16.9	18.12	14.44	8.78	9.35
P2-2XY	25.0292	5.9831	1.807	17.0	18.23	14.38	8.46	9.35
P2-3XY	25.0262	5.9816	1.807	17.3	18.19	14.29	8.39	8.91
P3-1AC	25.0194	5.9946	1.781	18.3	18.25	13.47	8.93	9.41
P3-2AC	25.0192	5.9972	1.781	18.3	18.39	13.56	8.58	9.36
P3-3AC	25.0052	5.9981	1.781	18.3	18.41	13.52	8.52	9.24
P3-1BD	25.0102	5.9934	1.776	18.6	18.28	13.59	8.18	9.01
P3-2BD	25.0084	5.9933	1.776	18.5	18.10	13.73	8.43	9.01
P3-3BD	25.0162	5.9940	1.775	18.5	18.05	13.79	8.25	9.04
P3-1XY	25.0240	5.9847	1.762	19.4	19.43	13.02	8.40	9.16
P3-2XY	25.0284	5.9826	1.766	19.2	19.13	13.14	8.57	9.23
P3-3XY	25.0248	5.9831	1.765	19.1	19.29	13.04	8.45	9.18

Tab. 4: Properties of graphite grade POCO AXF-5Q

Specimen	Length (mm)	Diam. (mm)	Density (g/cm^{-3})	Open Por. (%)	El.Res. (Ohm mm^{-2}/m)	Young's Modulus (kN/mm^{-2})	CTE ($10^{-6}/K$) betw. 20°C and 400°C	CTE ($10^{-6}/K$) betw. 20°C and 1000°C
M1-1AC	25.0094	5.9984	1.755	17.5	18.43	11.94	5.56	6.61
M1-2AC	24.9984	5.9928	1.754	17.6	19.00	11.81	5.64	6.72
M1-3AC	25.0082	5.9935	1.757	17.4	18.92	11.69	5.74	6.88
M1-1BD	25.0274	5.9869	1.752	17.8	17.99	11.73	5.40	6.54
M1-2BD	25.0260	5.9879	1.751	17.8	17.84	11.68	5.46	6.36
M1-3BD	25.0182	5.9867	1.751	17.9	18.04	11.63	5.43	6.51
M1-1XY	24.9928	6.0091	1.754	17.6	20.21	10.64	6.04	7.03
M1-2XY	24.9844	6.0067	1.758	17.4	19.61	10.85	5.84	6.90
M1-3XY	24.9896	6.0071	1.755	17.5	19.90	10.76	6.00	7.01
M2-1AC	25.0244	5.9904	1.749	17.9	19.32	11.57	5.51	6.71
M2-2AC	25.0228	5.9882	1.750	17.9	19.13	11.67	5.73	6.80
M2-3AC	25.0114	5.9863	1.752	17.8	19.14	11.65	5.54	6.67
M2-1BD	25.0084	5.9911	1.754	17.6	18.00	11.68	5.51	6.58
M2-2BD	25.0060	5.9905	1.758	17.6	17.98	11.98	5.45	6.62
M2-3BD	25.0190	5.9879	1.756	17.6	18.48	11.44	5.73	6.72
M2-1XY	25.0246	5.9877	1.754	17.8	19.22	11.00	5.80	6.84
M2-2XY	25.0264	5.9881	1.751	18.0	19.38	11.02	5.70	6.77
M2-3XY	25.0094	5.9863	1.751	17.9	19.44	11.07	6.03	7.08
M3-1AC	25.0048	5.9949	1.757	17.5	18.13	11.93	5.60	6.68
M3-2AC	25.0048	5.9947	1.758	17.5	18.02	12.07	5.59	6.75
M3-3AC	25.0018	5.9939	1.759	17.4	18.39	11.84	5.66	6.67
M3-1BD	25.0080	5.9961	1.760	17.3	17.53	12.08	5.40	6.56
M3-2BD	25.0218	5.9940	1.758	17.4	18.18	11.91	5.45	6.63
M3-3BD	25.0020	5.9963	1.755	17.4	18.30	11.70	5.38	6.44
M3-1XY	24.9996	5.9972	1.755	17.5	18.85	11.05	5.91	6.92
M3-2XY	25.0040	5.9916	1.759	17.6	19.03	10.95	5.82	6.86
M3-3XY	25.0076	5.9915	1.759	17.5	19.05	11.08	5.98	6.98

Tab. 5: Properties of graphite grade Morganite EY-306

Specimen	Length (mm)	Diam. (mm)	Density (g/cm^{-3})	Open Por. (%)	El.Res. (Ohm mm^{-2}/m)	Young's Modulus (kN/mm^{-2})	CTE ($10^{-6}/K$) betw. 20°C and 400°C	CTE ($10^{-6}/K$) betw. 20°C and 1000°C
J1-1XY	24.9962	5.9896	1.826	11.0	8.73	14.36	2.13	3.46
J1-2XY	24.9972	5.9941	1.823	11.4	8.80	14.30	2.10	3.42
J1-3XY	24.9984	5.9862	1.836	10.2	8.42	14.75	2.30	3.73
J2-1XY	24.9854	5.9915	1.836	10.3	8.49	14.35	2.32	3.54
J2-2XY	25.0240	5.9874	1.832	10.4	8.72	14.08	2.22	3.61
J2-3XY	25.0030	5.9885	1.814	11.2	9.01	13.83	2.38	3.67
J3-1XY	24.9854	5.9864	1.837	10.4	8.49	14.40	2.32	3.64
J3-2XY	25.0070	5.9889	1.837	9.8	8.73	14.47	2.37	3.70
J3-3XY	24.9748	5.9874	1.830	10.4	9.01	14.01	2.35	3.60
J1-1AC	24.9896	5.9946	1.820	11.3	9.10	13.06	2.59	3.84
J1-2AC	24.9800	5.9932	1.834	10.6	8.74	14.10	2.27	3.57
J1-3AC	25.0030	5.9860	1.826	11.1	8.60	14.17	2.12	3.38
J2-1AC	24.9930	5.9901	1.762	14.6	9.76	12.00	2.44	3.74
J2-2AC	24.9914	5.9899	1.792	12.9	9.51	12.31	2.50	3.86
J2-3AC	25.0216	5.9895	1.768	13.9	9.77	12.03	2.46	3.67
J3-1AC	25.0004	5.9873	1.782	13.2	9.63	12.51	2.33	3.68
J3-2AC	25.0126	5.9759	1.784	12.8	9.66	12.11	2.57	3.75
J3-3AC	25.0038	5.9877	1.777	13.1	9.70	12.22	2.41	3.77
J1-1BD	24.9630	6.0230	1.814	11.5	12.07	9.31	4.02	5.18
J1-2BD	24.9820	5.9960	1.814	11.5	12.12	9.50	4.10	5.18
J1-3BD	24.9842	6.0002	1.824	10.9	11.94	9.54	4.12	5.22
J2-1BD	24.9996	5.9915	1.795	12.2	12.24	9.00	4.10	5.07
J2-2BD	24.9996	5.9885	1.797	11.8	12.16	9.14	4.15	5.17
J2-3BD	25.0012	5.9931	1.796	11.8	12.36	9.01	4.09	5.22
J3-1BD	24.9924	5.9919	1.825	10.8	11.68	9.25	3.96	5.12
J3-2BD	24.9870	5.9931	1.815	11.0	11.97	9.25	4.17	5.23
J3-3BD	24.9924	5.9871	1.811	11.2	11.87	9.32	4.05	5.11

Tab. 8: Properties of graphite grade Union Carbide ATJ

Probe	Länge (mm)	Durchm. (mm)	Dichte (g/cm^3)	Off.Por. (%)	El.Wid. (Ohm*mm^2/m)	E-Modul (kN/mm^2)	CTE (10^6/K) bei 400 C	1000 C
S1-AC1	25.0184	5.9997	1.786	15.0	15.69	0.00	5.18	5.87
S1-AC2	25.0082	5.9945	1.793	15.0	15.95	0.00	5.18	5.93
S1-AC3	25.0046	5.9864	1.796	14.9	15.55	0.00	0.00	0.00
S2-AC1	24.9824	5.9976	1.796	15.1	15.59	0.00	5.34	5.95
S2-AC2	24.9764	6.0082	1.791	15.2	15.68	0.00	5.38	5.96
S2-AC3	24.9868	5.9992	1.791	15.2	15.70	0.00	0.00	0.00
S3-AC1	24.9986	5.9996	1.793	15.0	15.60	0.00	5.28	5.99
S3-AC2	24.9942	6.0005	1.793	15.1	15.64	0.00	5.27	5.97
S3-AC3	24.9906	6.0027	1.794	15.0	15.56	0.00	0.00	0.00
S1-BD1	25.0280	5.9838	1.789	15.1	15.43	0.00	5.14	5.90
S1-BD2	24.9882	6.0056	1.795	14.9	15.49	0.00	5.19	5.93
S1-BD3	24.9956	6.0021	1.791	15.0	15.59	0.00	0.00	0.00
S2-BD1	25.0074	5.9961	1.775	16.0	15.92	0.00	5.06	5.84
S2-BD2	24.9798	6.0058	1.772	16.2	15.88	0.00	5.30	6.00
S2-BD3	24.9884	6.0074	1.770	16.4	15.96	0.00	0.00	0.00
S3-BD1	24.9980	5.9950	1.774	16.1	15.84	0.00	5.25	5.92
S3-BD2	25.0078	6.0014	1.773	16.2	15.84	0.00	5.37	6.02
S3-BD3	24.9786	6.0077	1.771	16.3	15.96	0.00	0.00	0.00
S1-XY1	24.9976	6.0029	1.797	14.7	15.58	0.00	5.13	5.84
S1-XY2	25.0128	5.9938	1.797	14.8	15.60	0.00	5.28	6.05
S1-XY3	25.0216	5.9948	1.797	14.7	15.54	0.00	0.00	0.00
S2-XY1	25.0088	5.9980	1.797	14.8	15.31	0.00	5.30	5.85
S2-XY2	25.0024	5.9974	1.796	14.7	15.29	0.00	0.00	0.00
S2-XY3	25.0004	5.9960	1.798	14.7	15.33	0.00	0.00	0.00
S3-XY1	24.9968	6.0034	1.800	14.6	15.16	0.00	5.25	5.86
S3-XY2	24.9862	6.0054	1.801	14.5	15.15	0.00	5.26	5.92
S3-XY3	25.0038	5.9990	1.801	14.5	15.29	0.00	0.00	0.00

Tab. 9: Properties of graphite grade Schunk FE-289

Specimen	Length (mm)	Diam. (mm)	Density (g/cm^{-3})	Open Por. (%)	El.Res. (Ohm mm^{-2}/m)	Young's Modulus (kN/mm^{-2})
K-1	22.0312	6.0070	1.966	7.7	16.64	3.83
K-2	22.0486	6.0120	1.910	9.8	18.50	2.95
K-3	22.0348	6.0078	1.962	8.3	16.94	3.65
L-1	25.0098	6.0060	1.864	10.8	4.26	0.00
L-2	24.9654	6.0088	1.866	11.3	4.13	0.00
L-3	25.0332	5.9970	1.914	9.6	3.59	0.00

Tab. 10: Properties of carbon fibre composite Dunlop 5923P

3.1.5 High Temperature Thermal Conductivity and Electrical Resistivity

Thermal conductivity measurements were carried out by applying a modified KOHLRAUSCH method (1). Fig. 3 is a schematic diagramme of the setup used. It shows a water-cooled copper tube with a black coating on the vacuum side. The tube contains the cylindrical graphite specimen held between spring-loaded upper and lower electrodes and centred in position by a multi-junction thermocouple with ceramic insulation that protrudes from the lower electrode.

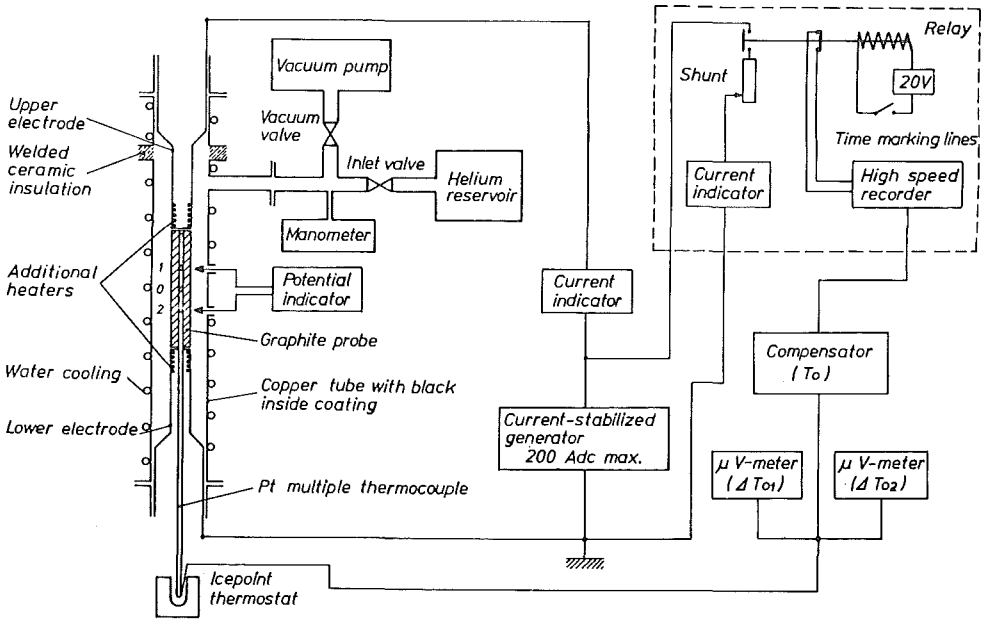

Fig. 3: Schematic Diagramme of Thermal Conductivity Equipment (1)

Special design of the thermocouple permits (after filling the copper tube with helium (~300 torr)) measurements of the temperature T_0 at the centre of the specimen (point 0 in fig. 3) as well as of the temperature differences ΔT_{01} and ΔT_{02} between the centre of the specimen and points 1 and 2 a fixed distance l away from the centre.

The current flowing through this arrangement and the simultaneous operation of two additional heaters at the electrode tips may generate greatly differing temperature profiles. However, only profiles which are symmetric with respect to the centre of the specimen and with small or disappearing tempe-

rature decrease along the test sections 0-1 and 0-2, are of interest for thermal conductivity measurement. For such measurements to be carried out at a given temperature T, the current I flowing through the specimen and the current through the two additional heaters were manually adjusted so as to give

$$T = T_0; \quad \Delta T_{01} = \Delta T_{02} = \Delta T \approx 5 \text{ K}$$

Then the current I was reduced and the currents in the additional heaters were simultaneously increased to achieve the state

$$T = T_0; \quad \Delta T_{01} = \Delta T_{02} = 0 \tag{5}$$

characterized by specimen current I_0. It is in this state that the resistivity R (Ω/cm) was determined in the central zone of the specimen by a rapid measurement of potential difference. The results were used to compute the thermal conductivity from the relationship

$$\lambda(T) = \frac{I^2 R \left(I^2 - I_0^2\right)}{2F \ \Delta T} (1 + \epsilon), \tag{6}$$

where F is the cross-section area of the specimen, and ϵ is a correction term which in the first approximation can be taken to be equal to zero. To obtain the value of ϵ ,further measurements according to equation (5) are required at slightly different temperatures. These measurements are used to derive the differential coefficient $d(RI^2)/dT$ and then to calculate ϵ from the expression

$$\epsilon \simeq \frac{I^2}{12F\lambda'} \cdot \frac{d\left(RI_0^2\right)}{dT} \tag{7}$$

where λ' is the thermal conductivity computed from equation (6) with $\epsilon = 0$.

In tables 11 to 19, the results of thermal conductivity and electrical resistivity measurements at temperatures between 100°C and 1000°C are listed up. Thermal conductivity and electrical resistivity values at particular temperatures can be taken from figures 4 to 11.

With increasing temperature, electrical resistivity decreased to a limit value of temperature. This value is known to be in the range of about 700°C. With increasing temperatures, the specific resistance again increases in contrast to thermal conductivity which continously decreases down to temperatures of about 2000°C. In the investigation programme described here, the behaviour of electrical resistivity under increasing temperatures was found to be different for particular graphites. The very fine-grained materials revealed a minimum in electrical resistivity at about 1000°C whereas the more coarse-grained ones had their minimum at about 600°C (ATJ) and 700°C (H-490), respectively. The fractional temperature dependent decrease in electrical resistivity was the more significant the higher the room temperature value for the particular grade of graphite (fig. 12). High dense and coarse grain materials revealed a lower specific resistance than low dense and fine grain ones. For example, the ultra fine-grain POCO graphite had the highest electrical resistivity of all materials investigated in this study.

The decrease in electrical resistivity described above is due to the band structure of graphite. With increasing temperature, more and more electrons are lifted to the conduction band which leads to the observed decrease in specific resistance. At temperatures above 1000°C, the electrons are scattered by lattice vibrations which increase electrical resistivity and decrease thermal conductivity (3,4).

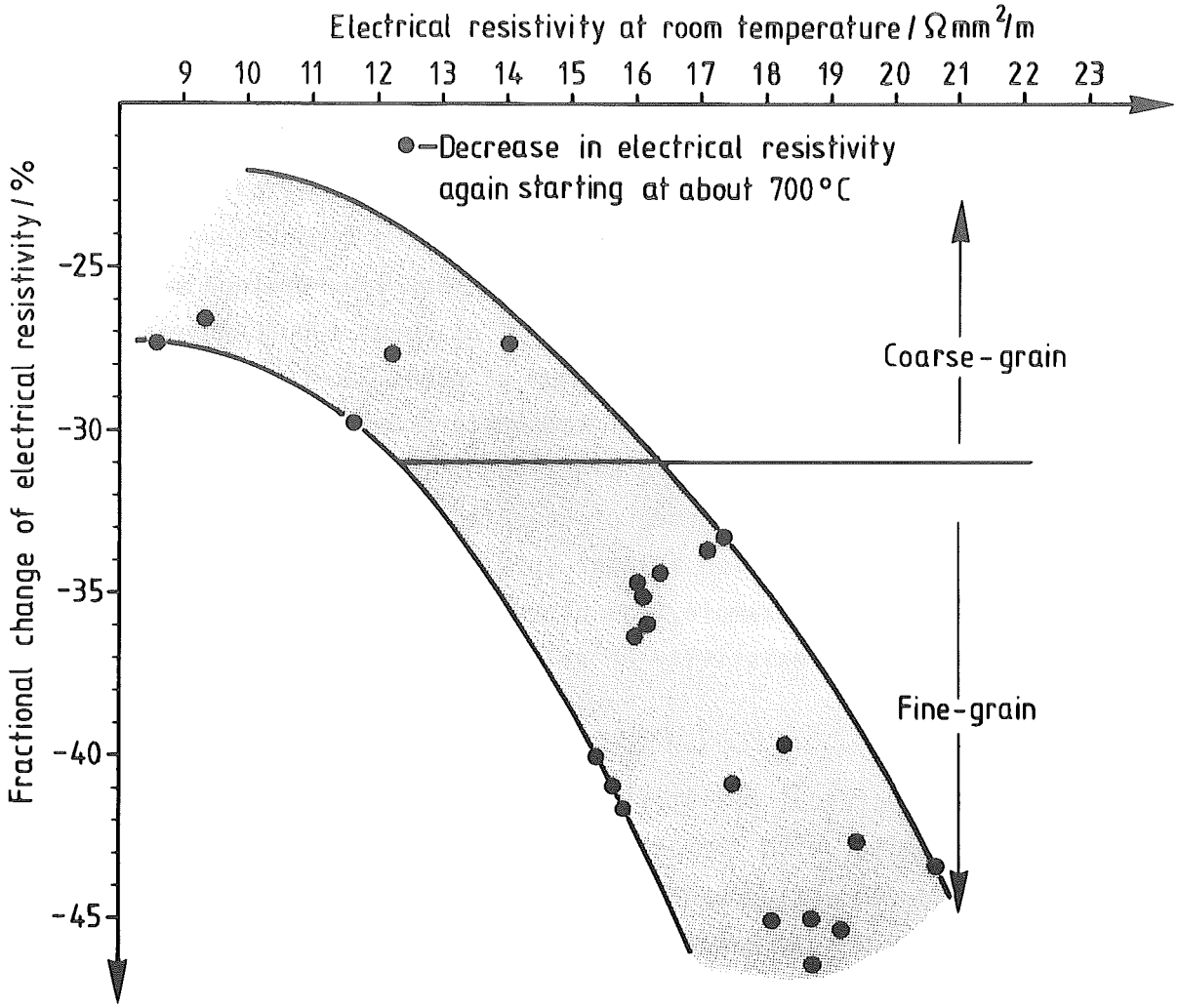

Fig. 12: Fractional change of electrical resistivity caused by heating up from room temperature to 1000°C

Table 11

Ringsdorff EK 98

High Temperature Electrical Resistivity (ρ) and Thermal Conductivity (λ)

	AC		BD		XY		AC		BD		XY		AC		BD		XY	
T	ρ	λ	ρ	λ	ρ	λ	ρ	λ	ρ	λ	ρ	λ	ρ	λ	ρ	λ	ρ	λ
°C	mΩcm	W/cm°C	mΩcm	W/cm°C	mΩcm	W/cm°C	mΩcm	W/cm°C	mΩcm	W/cm°C	mΩcm	W/cm°C	mΩcm	W/cm°C	mΩcm	W/cm°C	mΩcm	W/cm°C
100	1.451	0.672	1.448	0.693	1.523	0.692	1.447	0.733	1.444	0.680	1.457	0.614	1.436	0.660	1.473	0.748	1.436	0.699
200	1.321	0.654	1.324	0.661	1.390	0.636	1.320	0.691	1.317	0.668	1.331	0.573	1.312	0.646	1.345	0.715	1.312	0.660
300	1.233	0.607	1.233	0.605	1.295	0.591	1.228	0.627	1.230	0.623	1.241	0.588	1.222	0.613	1.256	0.679	1.222	0.603
400	1.168	0.555	1.168	0.552	1.225	0.535	1.163	0.582	1.165	0.563	1.176	0.549	1.157	0.594	1.191	0.588	1.160	0.593
500	1.119	0.511	1.119	0.524	1.175	0.493	1.119	0.512	1.119	0.526	1.129	0.496	1.111	0.560	1.142	0.510	1.114	0.545
600	1.085	0.480	1.084	0.468	1.137	0.440	1.084	0.466	1.083	0.499	1.093	0.444	1.078	0.483	1.135	0.480	1.078	0.456
700	1.058	0.441	1.060	0.436	1.111	0.414	1.060	0.447	1.076	0.464	1.069	0.412	1.054	0.444	1.083	0.462	1.054	0.442
800	1.042	0.418	1.041	0.415	1.092	0.384	1.043	0.429	1.041	0.401	1.051	0.399	1.038	0.414	1.064	0.446	1.036	0.425
900	1.031	0.411	1.028	0.402	1.070	0.363	1.032	0.410	1.030	0.357	1.041	0.420	1.027	0.385	1.063	0.422	1.027	0.389
1000	1.023	0.397	1.022	0.397	1.072	0.354	1.022	0.388	1.023	0.347								

Table 14

Morganite EY-306

High Temperature Electrical Resistivity (ρ) and Thermal Conductivity (λ)

	AC		BD		XY		AC		BD		XY		AC		BD		XY	
T	ρ	λ	ρ	λ	ρ	λ	ρ	λ	ρ	λ	ρ	λ	ρ	λ	ρ	λ	ρ	λ
°C	mΩcm	W/cm°C	mΩcm	W/cm°C	mΩcm	W/cm°C	mΩcm	W/cm°C	mΩcm	W/cm°C	mΩcm	W/cm°C	mΩcm	W/cm°C	mΩcm	W/cm°C	mΩcm	W/cm°C
100	1.031	1.026	1.588	0.649	1.713	0.645	1.677	0.662	1.556	0.716	1.682	0.664	1.622	0.685	1.613	0.671	1.684	0.690
200	0.947	0.896	1.417	0.633	1.526	0.627	1.450	0.627	1.389	0.694	1.504	0.625	1.447	0.673	1.428	0.644	1.504	0.660
300	0.893	0.756	1.295	0.570	1.394	0.579	1.366	0.589	1.274	0.626	1.377	0.584	1.322	0.641	1.313	0.618	1.375	0.607
400	0.860	0.730	1.207	0.561	1.299	0.518	1.272	0.532	1.191	0.590	1.284	0.548	1.230	0.599	1.221	0.568	1.279	0.538
500	0.843	0.645	1.146	0.508	1.230	0.483	1.201	0.485	1.130	0.560	1.218	0.494	1.165	0.539	1.156	0.522	1.214	0.499
600	0.825	0.584	1.102	0.459	1.204	0.472	1.150	0.465	1.088	0.528	1.169	0.442	1.118	0.478	1.110	0.500	1.167	0.466
700	0.833	0.527	1.070	0.425	1.146	0.420	1.114	0.423	1.060	0.497	1.138	0.404	1.085	0.464	1.076	0.478	1.134	0.430
800	0.837	0.500	1.050	0.428	1.123	0.386	1.092	0.390	1.039	0.434	1.112	0.394	1.064	0.402	1.054	0.433	1.108	0.395
900	0.847	0.448	1.108	0.413	1.147	0.347	1.077	0.367	1.030	0.420	1.096	0.386	1.049	0.402	1.041	0.398	1.095	0.387

Table 15

Schunk FP 219

High Temperature Electrical Resistivity (ρ) and Thermal Conductivity (λ)

	AC		BD		XY		AC		BD		XY		AC		BD		XY	
T	ρ	λ	ρ	λ	ρ	λ	ρ	λ	ρ	λ	ρ	λ	ρ	λ	ρ	λ	ρ	λ
°C	mΩcm	W/cm°C	mΩcm	W/cm°C	mΩcm	W/cm°C	mΩcm	W/cm°C	mΩcm	W/cm°C	mΩcm	W/cm°C	mΩcm	W/cm°C	mΩcm	W/cm°C	mΩcm	W/cm°C
100	1.573	0.695	2.038	0.577	1.496	0.732	1.564	0.667	1.916	0.596	1.529	0.761	1.545	0.707	1.807	0.666	1.550	0.732
200	1.443	0.657	1.874	0.534	1.377	0.680	1.434	0.629	1.756	0.567	1.398	0.688	1.420	0.660	1.658	0.596	1.423	0.662
300	1.351	0.579	1.747	0.483	1.287	0.615	1.344	0.580	1.639	0.518	1.313	0.620	1.333	0.611	1.555	0.523	1.339	0.591
400	1.295	0.530	1.660	0.437	1.228	0.553	1.284	0.532	1.564	0.446	1.253	0.555	1.274	0.542	1.485	0.475	1.280	0.531
500	1.238	0.484	1.596	0.393	1.182	0.504	1.241	0.499	1.507	0.411	1.212	0.517	1.233	0.500	1.433	0.444	1.237	0.472
600	1.206	0.455	1.552	0.367	1.152	0.471	1.211	0.460	1.466	0.385	1.184	0.479	1.203	0.452	1.398	0.425	1.210	0.443
700	1.186	0.431	1.520	0.345	1.130	0.453	1.190	0.433	1.439	0.359	1.163	0.452	1.184	0.420	1.374	0.391	1.188	0.428
800	1.168	0.392	1.496	0.336	1.116	0.424	1.173	0.396	1.420	0.338	1.149	0.424	1.171	0.395	1.358	0.369	1.177	0.403
900	1.160	0.374	1.480	0.313	1.108	0.400	1.163	0.366	1.406	0.324	1.141	0.404	1.165	0.370	1.347	0.343	1.166	0.387
1000	1.153	0.355	1.469	0.298	1.103	0.387	1.160	0.337	1.398	0.306	1.138	0.377	1.163	0.357	1.339	0.336	1.164	0.374

Table 16

Anglo Great Lakes H490

High Temperature Electrical Resistivity (ρ) and Thermal Conductivity (λ)

	AC		BD		XY		AC		BD		XY		AC		BD	
T °C	ρ mΩcm	λ W/cm°C	ρ mΩcm	λ W/cm°C	ρ mΩcm	λ W/cm°C	ρ mΩcm	λ W/cm°C	ρ mΩcm	λ W/cm°C	ρ mΩcm	λ W/cm°C	ρ mΩcm	λ W/cm°C	ρ mΩcm	λ W/cm°C
100	0.995	0.980	0.994	1.055	1.260	0.919	0.973	1.112	1.199	1.074	1.335	0.949	1.082	0.986	1.076	1.060
200	0.927	0.912	0.909	1.016	1.157	0.837	0.893	1.045	1.100	0.944	1.218	0.829	0.990	0.922	0.986	0.952
300	0.875	0.853	0.861	0.922	1.087	0.724	0.841	0.920	1.034	0.789	1.145	0.720	0.933	0.854	0.926	0.837
400	0.843	0.789	0.825	0.814	1.043	0.649	0.810	0.802	0.990	0.699	1.099	0.656	0.896	0.781	0.891	0.748
500	0.821	0.722	0.806	0.728	1.016	0.589	0.791	0.712	0.966	0.625	1.072	0.567	0.873	0.693	0.868	0.667
600	0.810	0.661	0.797	0.685	1.003	0.547	0.780	0.662	0.952	0.573	1.053	0.521	0.862	0.626	0.857	0.628
700	0.808	0.594	0.794	0.631	0.995	0.511	0.778	0.623	0.946	0.525	1.044	0.476	0.858	0.579	0.851	0.586
800	0.810	0.548	0.797	0.595	0.995	0.481	0.779	0.576	0.946	0.488	1.042	0.444	0.858	0.532	0.854	0.556
900	0.816	0.527	0.802	0.558	0.997	0.457	0.784	0.556	0.952	0.478	1.047	0.434	0.864	0.507	0.858	0.524
1000	0.824	0.494	0.811	0.531	1.005	0.440	0.793	0.536	0.959	0.433	1.055	0.393	0.872	0.485	0.866	0.500

Table 17

Union Carbide ATJ

High Temperature Electrical Resistivity (ρ) and Thermal Conductivity (λ)

	AC		BD		XY		AC		BD		XY		AC		BD		XY	
T	ρ	λ	ρ	λ	ρ	λ	ρ	λ	ρ	λ	ρ	λ	ρ	λ	ρ	λ	ρ	λ
°C	mΩcm	W/cm°C	mΩcm	W/cm°C	mΩcm	W/cm°C	mΩcm	W/cm°C	mΩcm	W/cm°C	mΩcm	W/cm°C	mΩcm	W/cm°C	mΩcm	W/cm°C	mΩcm	W/cm°C
100	0.789	1.327	1.641	0.689	0.818	1.347	0.842	1.243	1.075	1.031	0.753	1.464	0.841	1.323	1.050	1.074	0.758	1.300
200	0.724	1.284	1.465	0.649	0.688	1.174	0.774	1.136	0.985	0.919	0.691	1.237	0.773	1.163	0.958	0.947	0.696	1.148
300	0.685	1.059	1.339	0.639	0.651	1.057	0.733	1.028	0.928	0.807	0.653	1.102	0.730	1.021	0.904	0.816	0.659	1.055
400	0.662	0.910	1.249	0.565	0.630	0.984	0.709	0.891	0.894	0.712	0.632	0.988	0.705	0.935	0.870	0.732	0.639	0.906
500	0.648	0.834	1.182	0.531	0.619	0.845	0.695	0.784	0.875	0.641	0.621	0.864	0.690	0.792	0.854	0.650	0.627	0.865
600	0.646	0.761	1.132	0.511	0.613	0.779	0.690	0.732	0.866	0.613	0.618	0.808	0.689	0.749	0.847	0.611	0.623	0.780
700	0.647	0.666	1.099	0.457	0.616	0.745	0.690	0.655	0.864	0.539	0.619	0.708	0.688	0.641	0.846	0.522	0.623	0.723
800	0.652	0.608	1.076	0.439	0.623	0.672	0.699	0.602	0.871	0.501	0.625	0.677	0.693	0.631	0.850	0.510	0.625	0.639
900	0.655	0.562	1.061	0.384	0.628	0.582	0.706	0.559	0.880	0.473	0.637	0.655	0.703	0.551	0.859	0.482	0.635	0.584

Table 18

Schunk FE 289

High Temperature Electrical Resistivity (ρ) and Thermal Conductivity (λ)

	AC		AC		AC		BD		BD		BD		XY		XY		XY	
T	ρ	λ	ρ	λ	ρ	λ	ρ	λ	ρ	λ	ρ	λ	ρ	λ	ρ	λ	ρ	λ
°C	mΩcm	W/cm°C	mΩcm	W/cm°C	mΩcm	W/cm°C	mΩcm	W/cm°C	mΩcm	W/cm°C	mΩcm	W/cm°C	mΩcm	W/cm°C	mΩcm	W/cm°C	mΩcm	W/cm°C
100	1.347	0.814	1.350	0.828	1.356	0.853	1.377	0.805	1.354	0.799	1.346	0.791	1.308	0.822	1.315	0.798	1.315	0.811
200	1.209	0.753	1.219	0.761	1.209	0.777	1.232	0.743	1.221	0.747	1.182	0.746	1.173	0.770	1.180	0.760	1.181	0.753
300	1.112	0.678	1.109	0.686	1.110	0.704	1.132	0.667	1.118	0.682	1.103	0.699	1.078	0.721	1.083	0.696	1.084	0.690
400	1.041	0.620	1.044	0.644	1.041	0.639	1.062	0.624	1.050	0.621	1.034	0.644	1.010	0.663	1.015	0.646	1.017	0.635
500	0.998	0.578	0.998	0.602	0.995	0.583	1.016	0.580	1.004	0.574	0.985	0.602	0.961	0.621	0.969	0.626	0.972	0.607
600	0.963	0.549	0.966	0.572	0.962	0.544	0.986	0.543	0.972	0.523	0.954	0.538	0.931	0.570	0.940	0.572	0.942	0.559
700	0.944	0.508	0.947	0.506	0.938	0.521	0.965	0.499	0.950	0.491	0.936	0.512	0.915	0.515	0.918	0.531	0.922	0.528
800	0.928	0.490	0.933	0.479	0.924	0.479	0.951	0.484	0.936	0.450	0.917	0.477	0.901	0.493	0.905	0.495	0.911	0.492
900	0.928	0.451	0.928	0.458	0.919	0.461	0.946	0.469	0.936	0.430	0.915	0.454	0.898	0.461	0.899	0.468	0.906	0.462

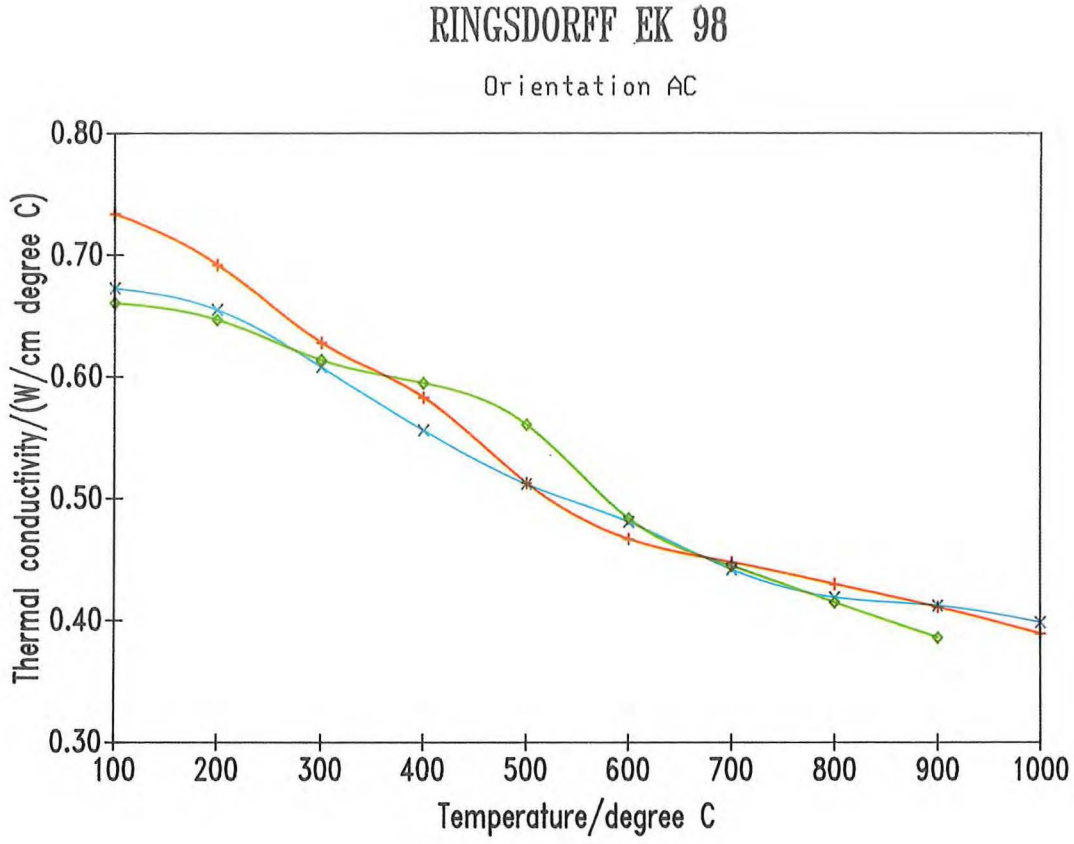

Fig. 4a: Temperature dependent thermal conductivity

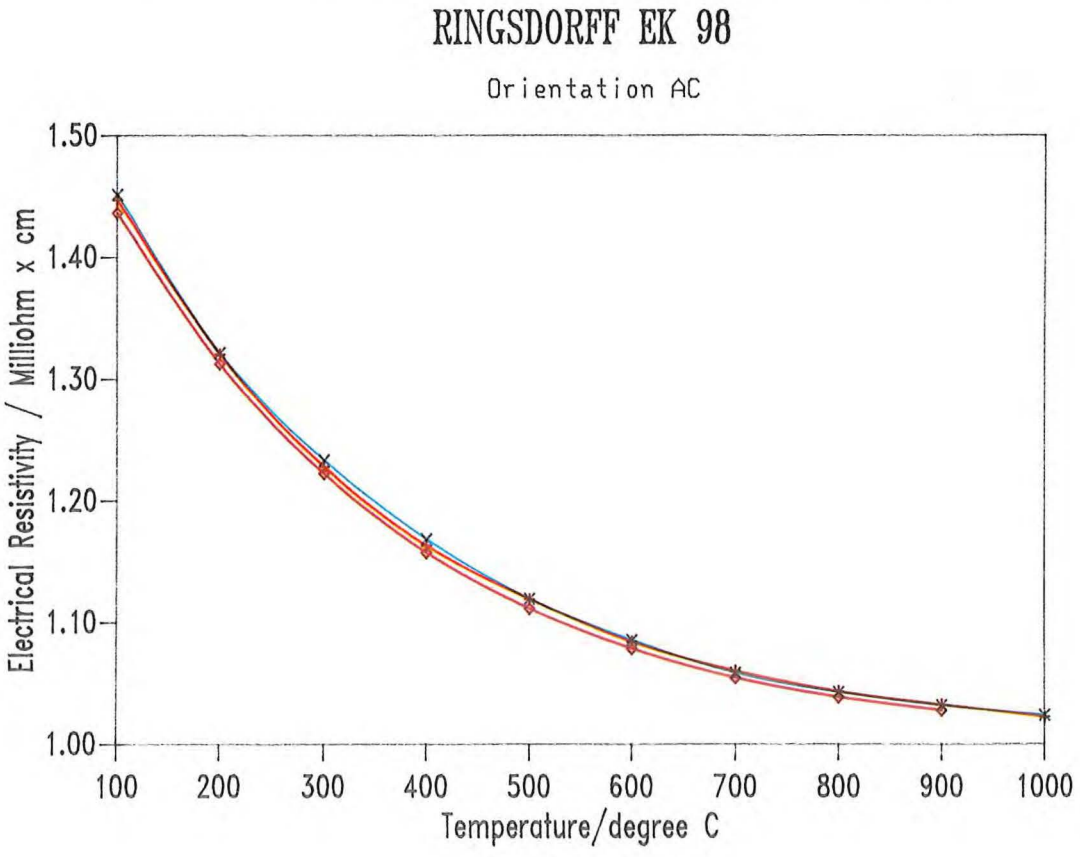

Fig. 4b: Temperature dependent electrical resistivity

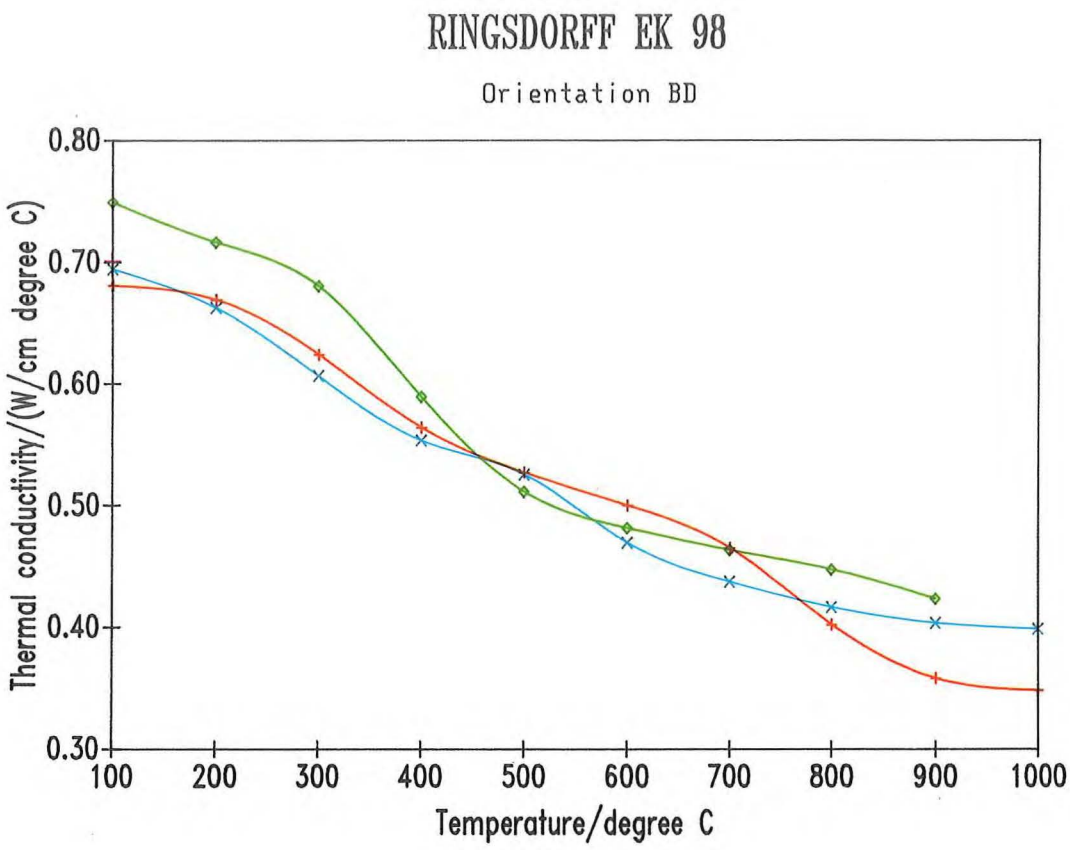

Fig. 4a: Temperature dependent thermal conductivity cont.

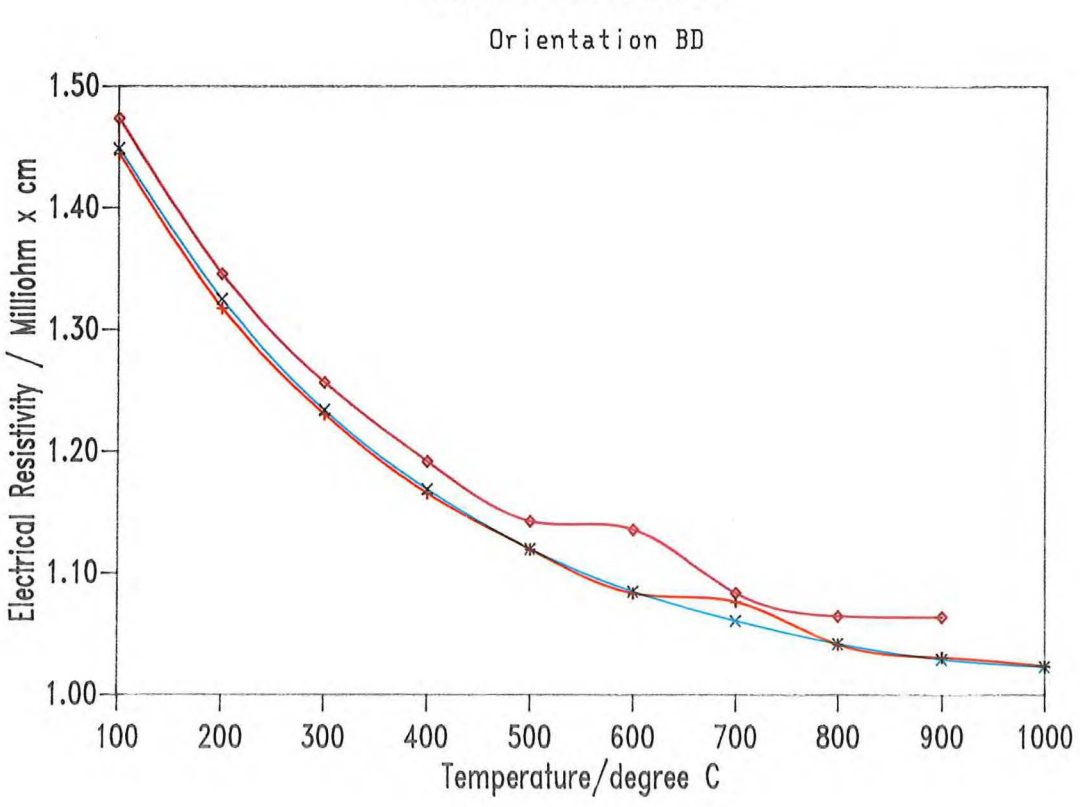

Fig. 4b: Temperature dependent electrical resistivity cont.

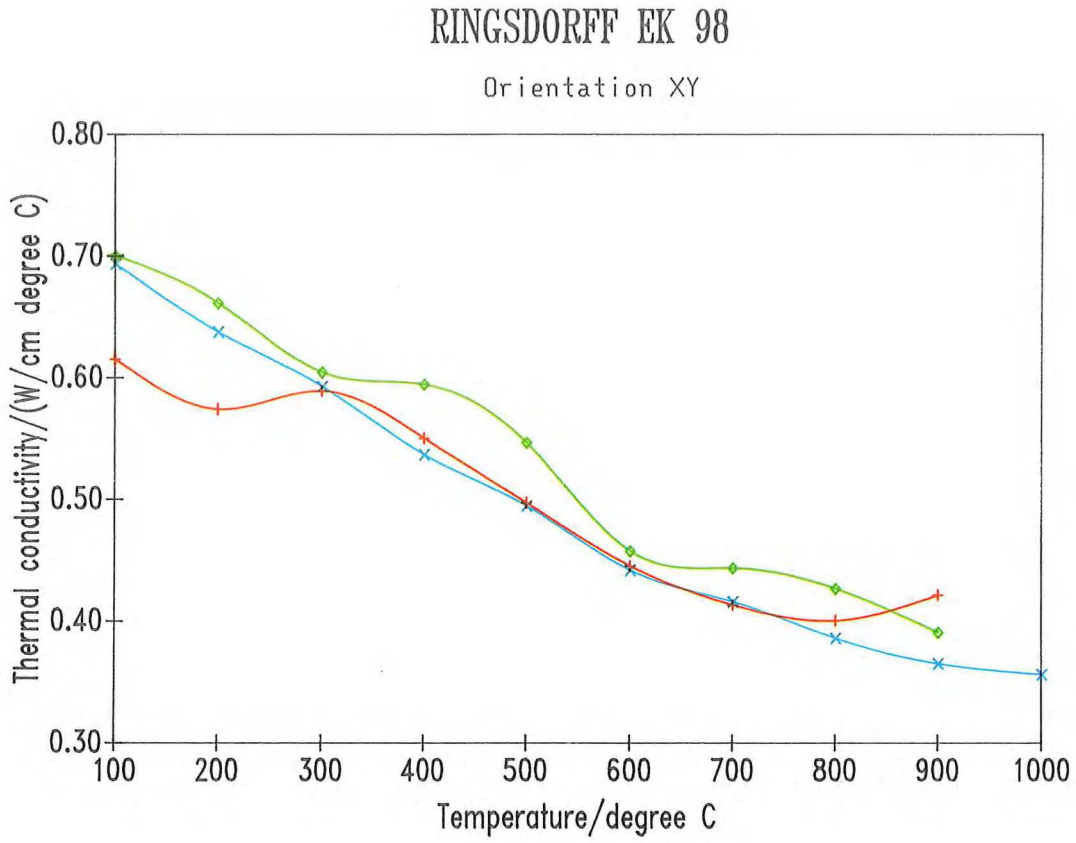

Fig. 4 a: Temperature dependent thermal conductivity cont.

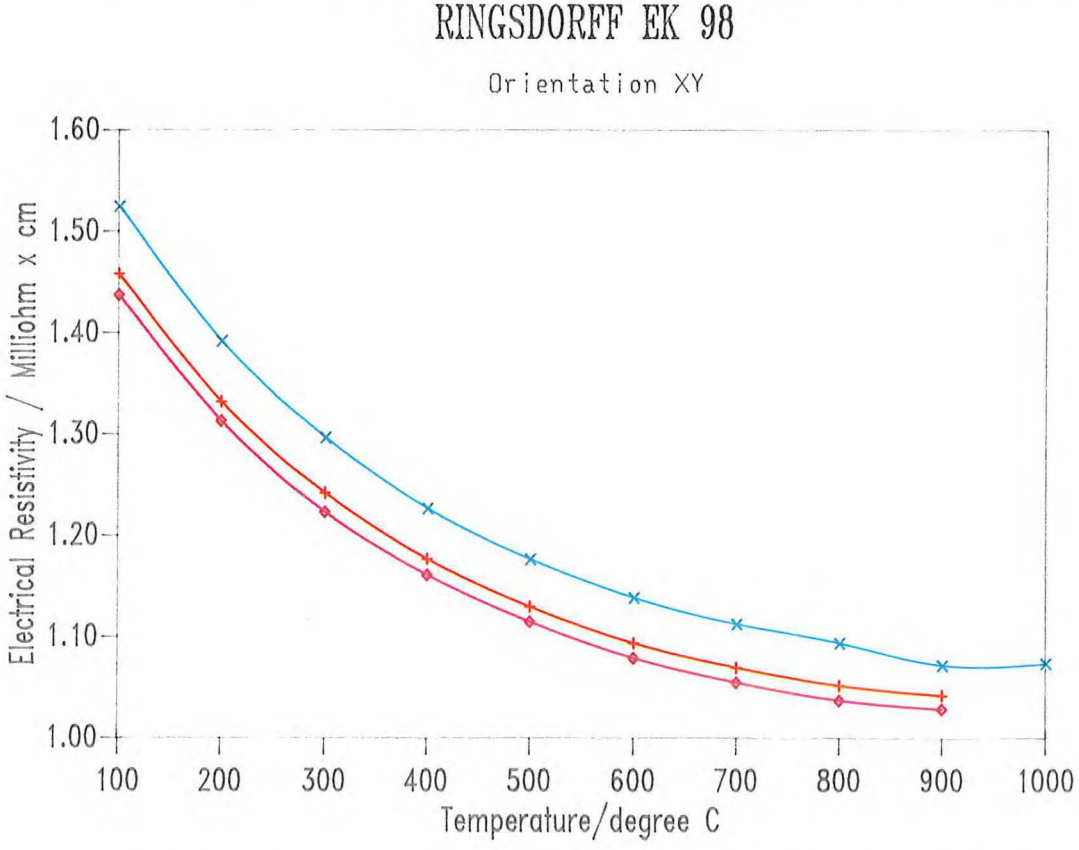

Fig. 4 b: Temperature dependent electrical resistivity cont.

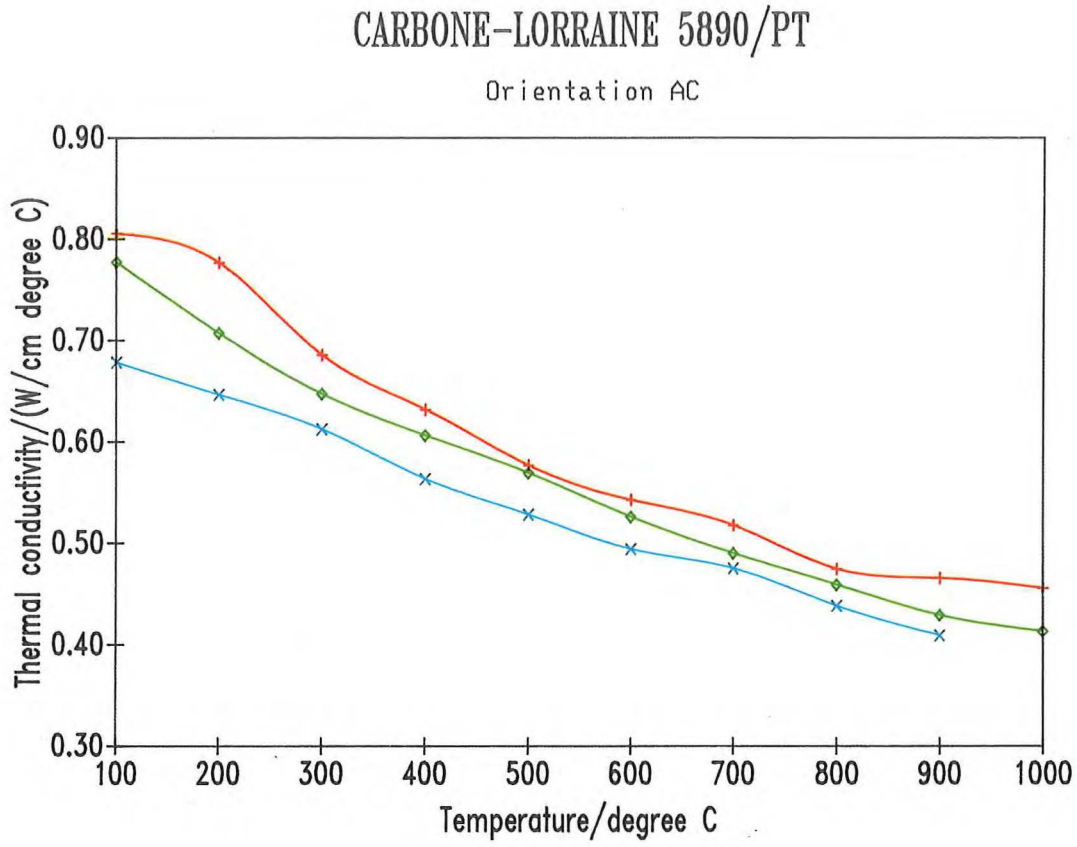

Fig. 5a: Temperature dependent thermal conductivity

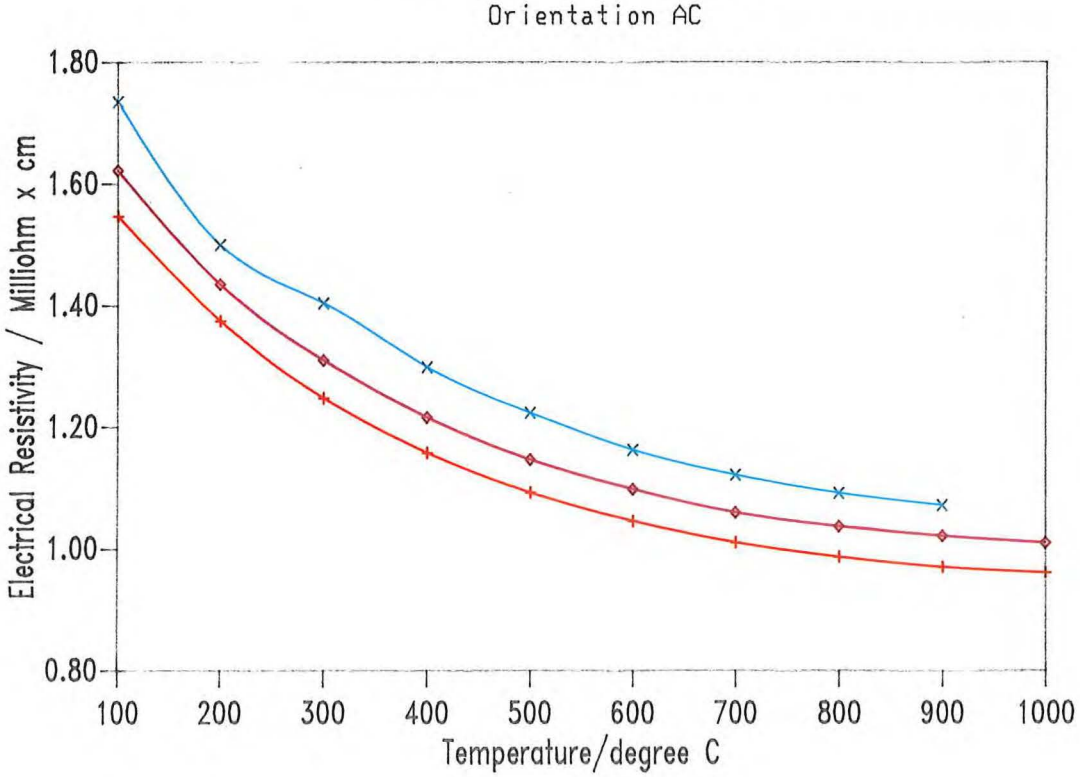

Fig. 5b: Temperature dependent electrical resistivity

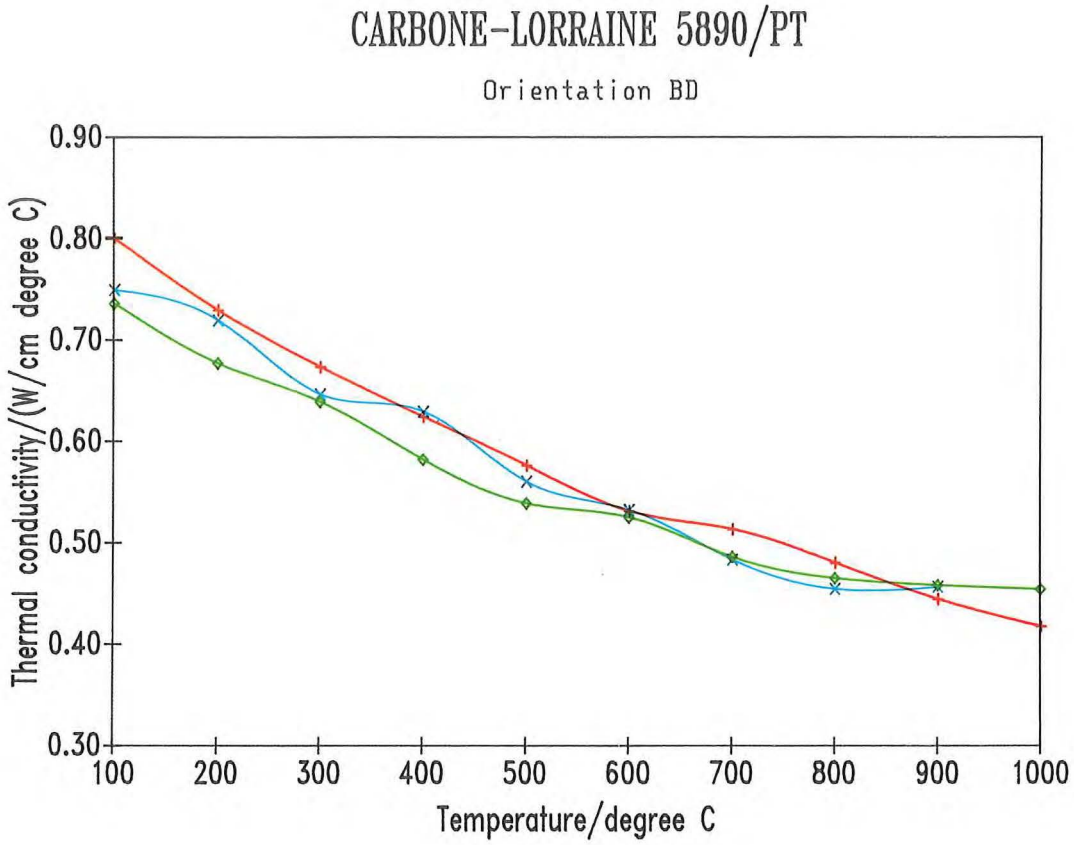

Fig. 5a: Temperature dependent thermal conductivity cont.

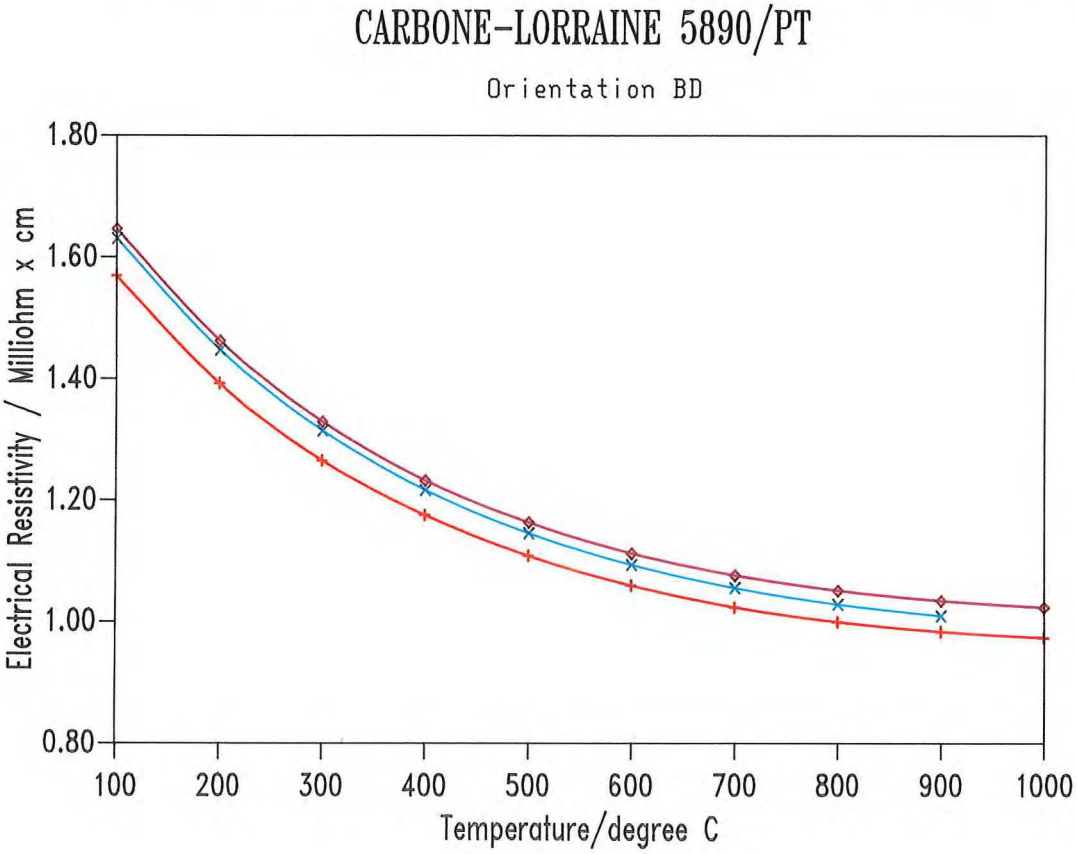

Fig. 5b: Temperature dependent electrical resistivity cont.

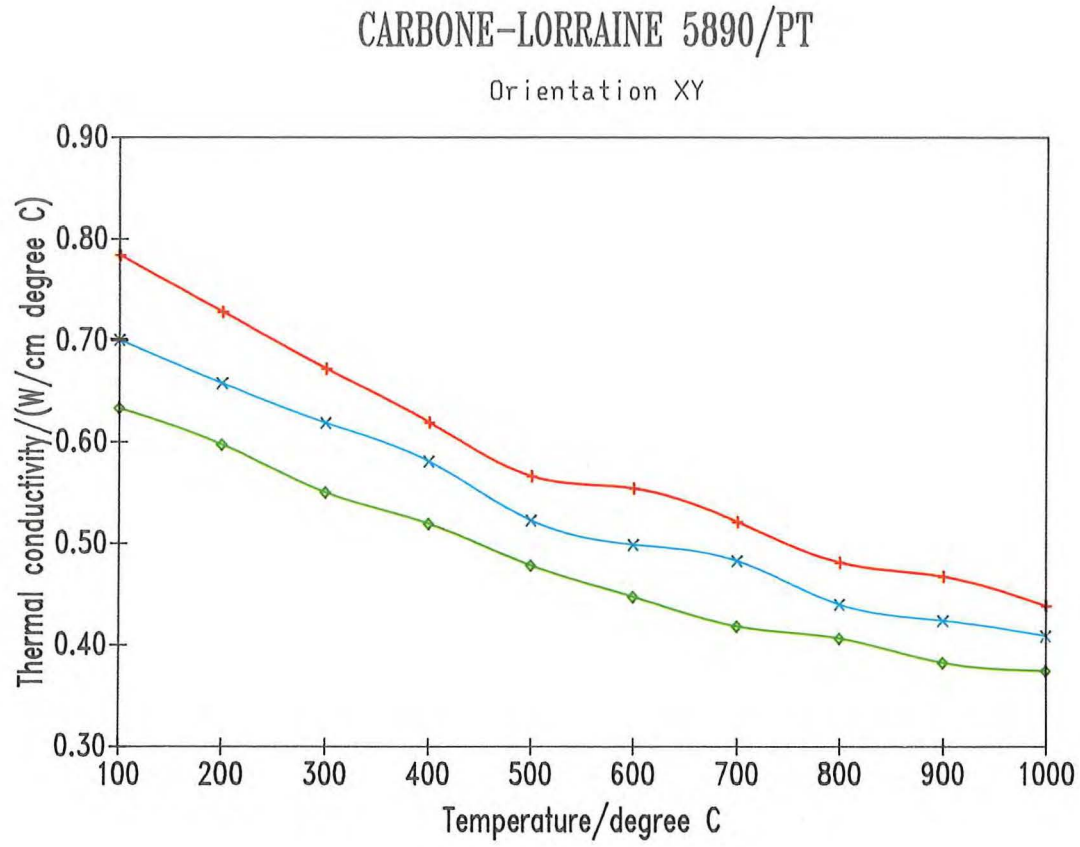

Fig. 5a: Temperature dependent thermal conductivity cont.

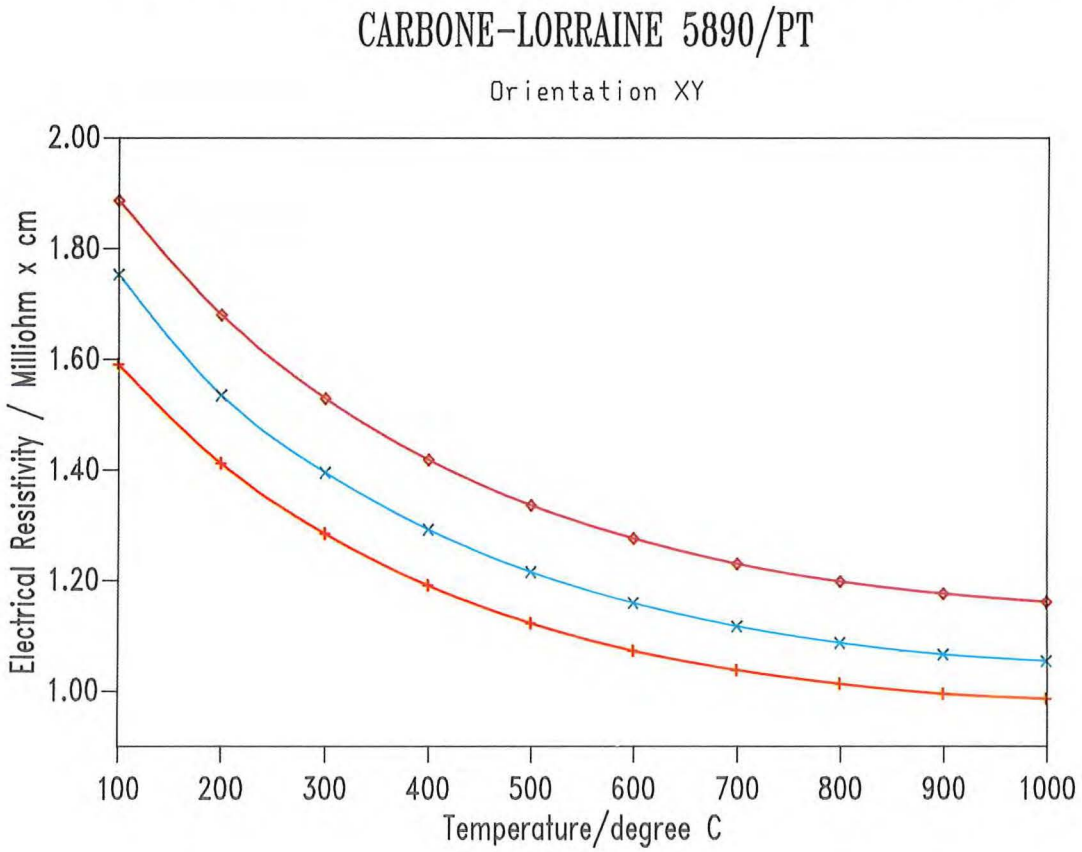

Fig. 5b: Temperature dependent electrical resistivity cont.

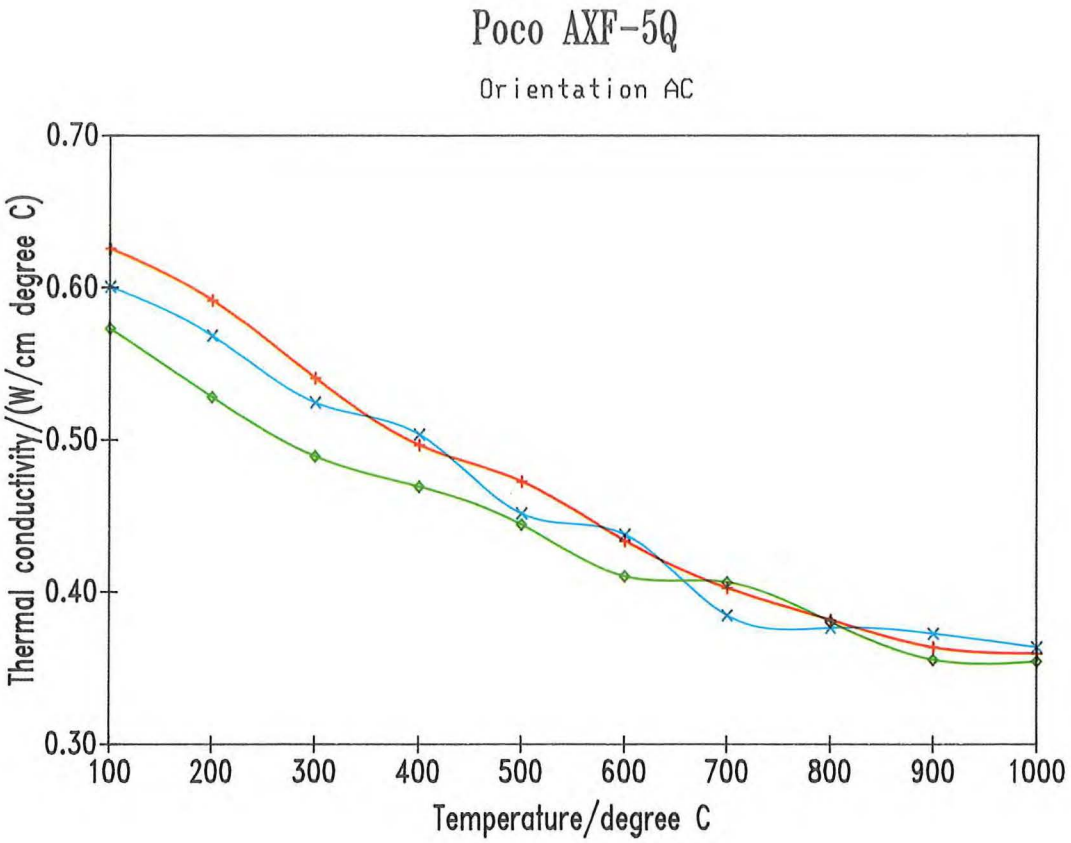

Fig. 6a: Temperature dependent thermal conductivity

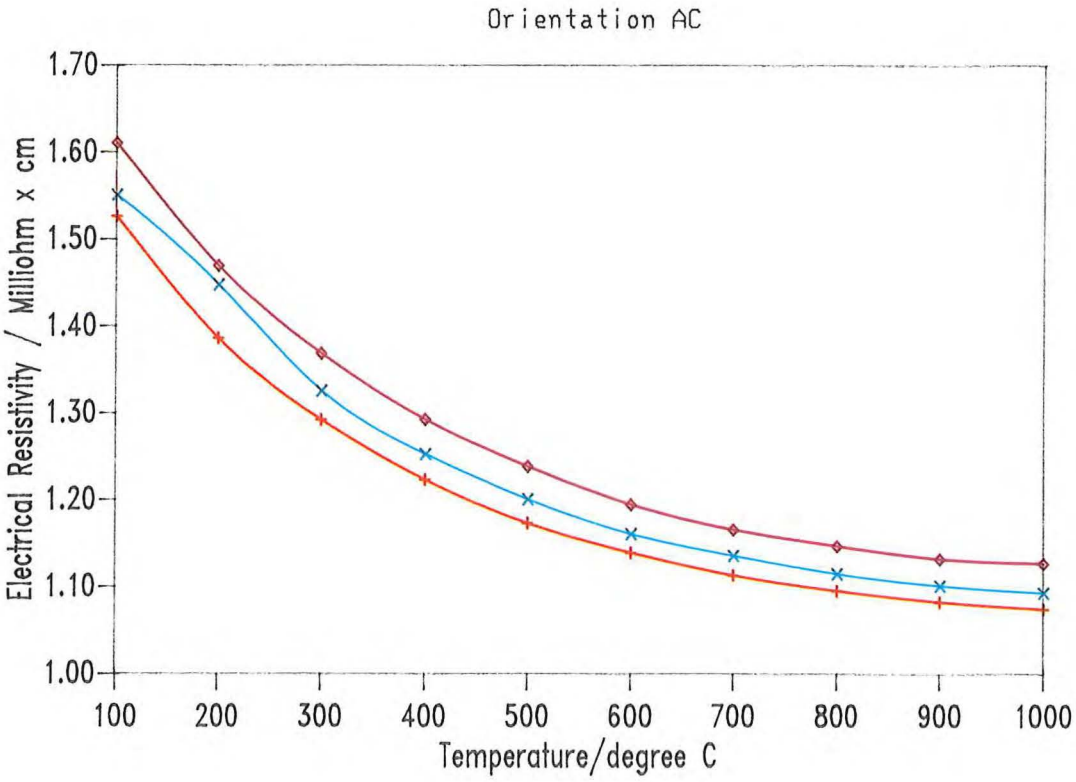

Fig. 6b: Temperature dependent electrical resistivity

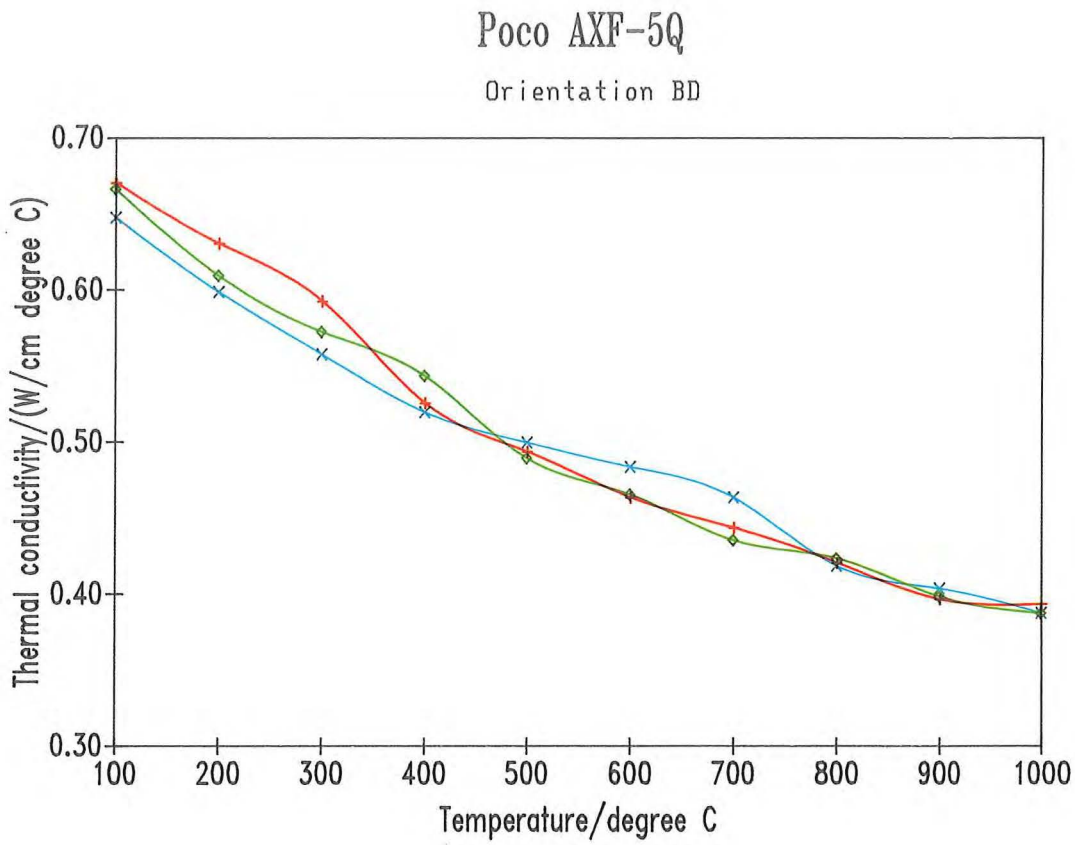

Fig. 6a: Temperature dependent thermal conductivity cont.

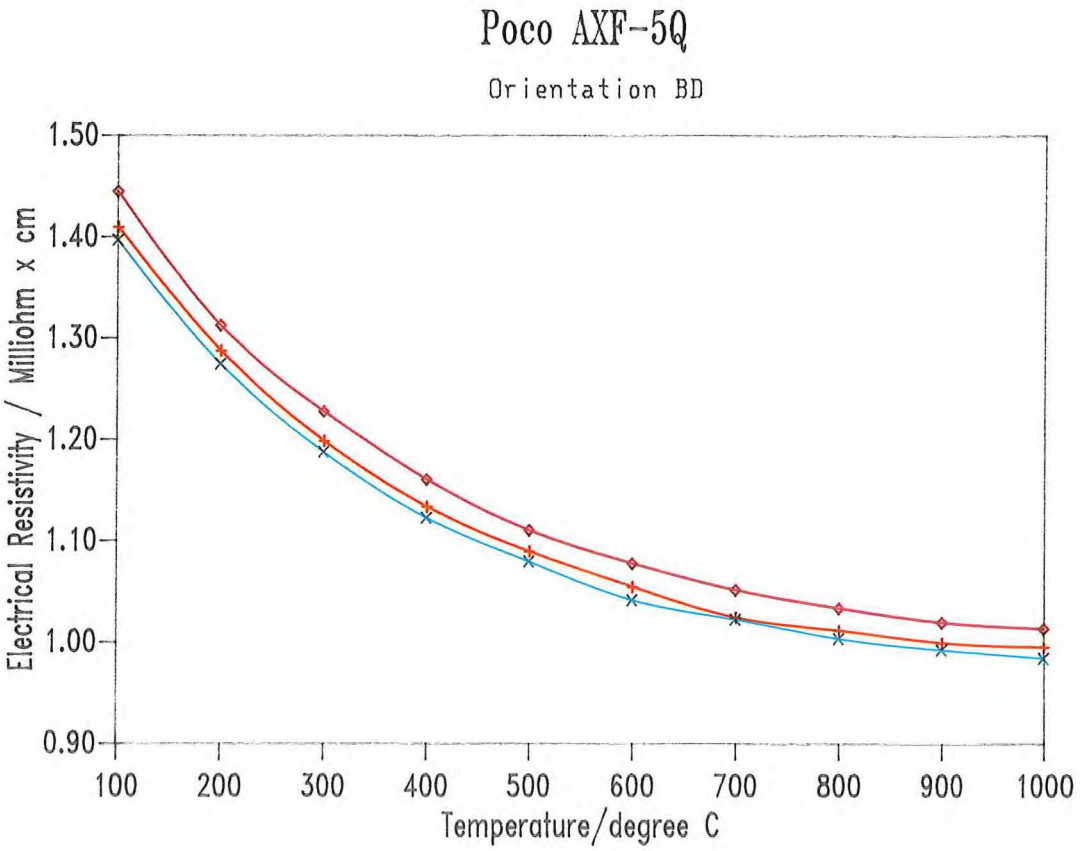

Fig. 6b: Temperature dependent electrical resistivity cont.

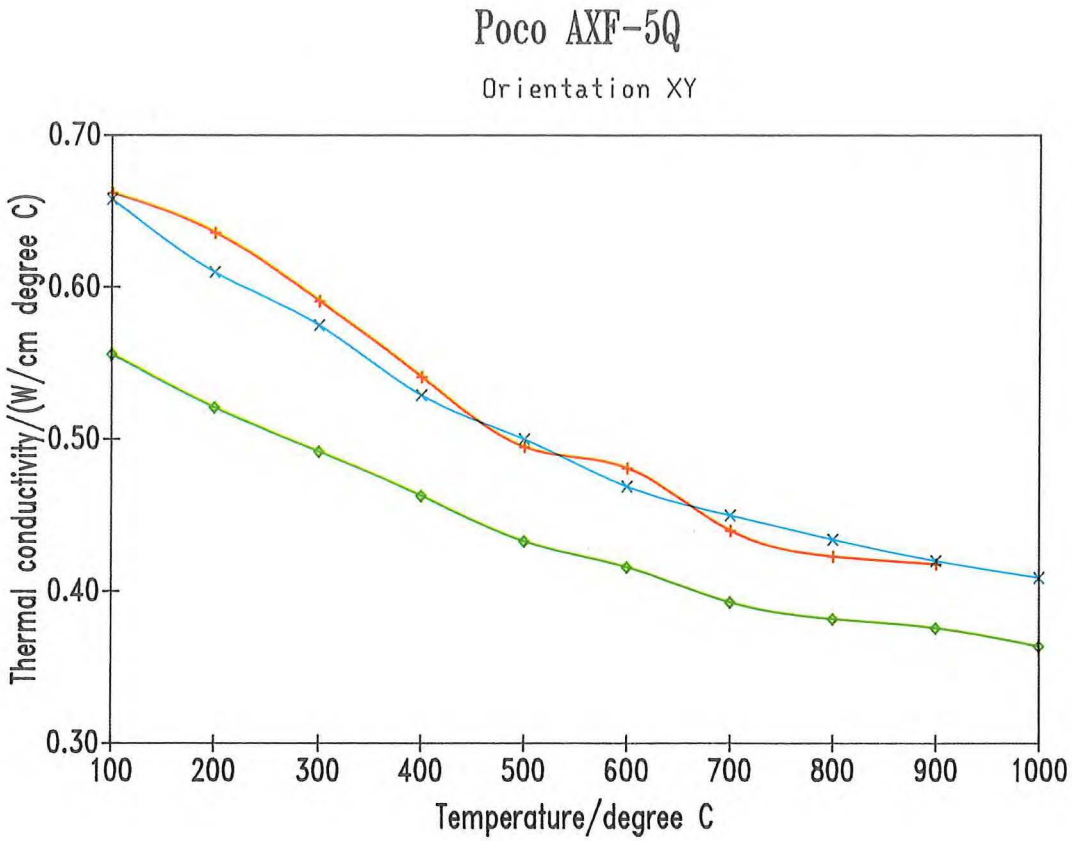

Fig. 6a: Temperature dependent thermal conductivity cont.

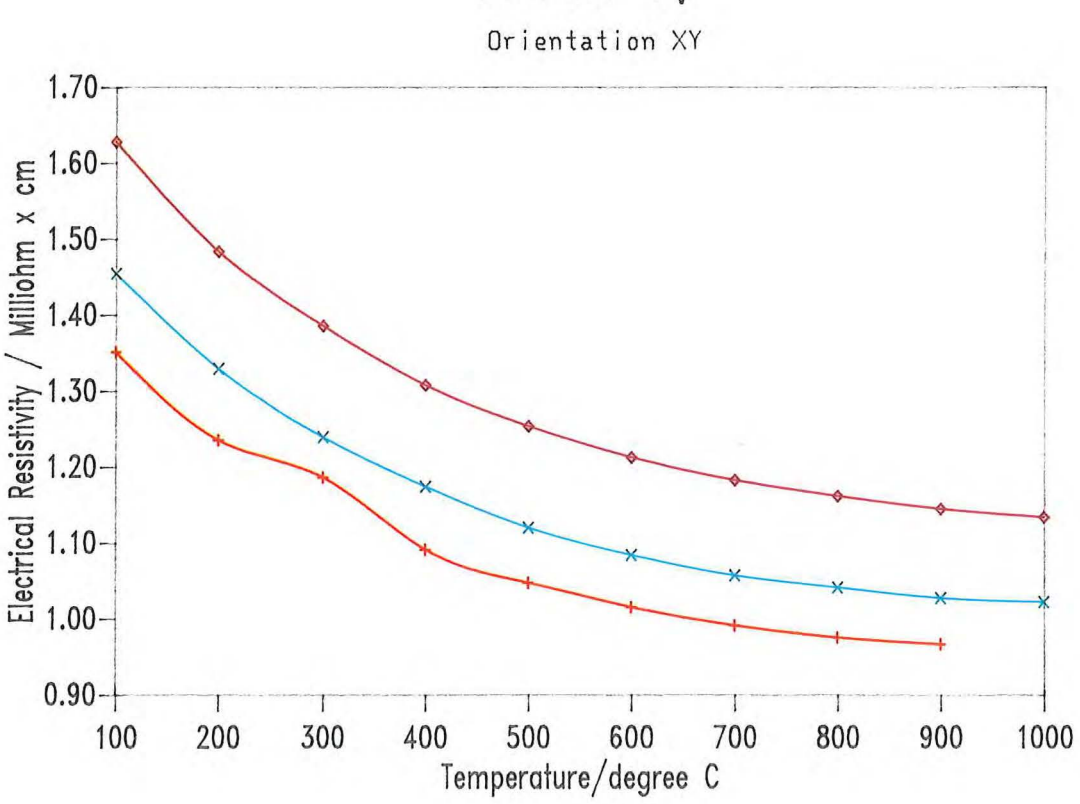

Fig. 6b: Temperature dependent electrical resistivity cont.

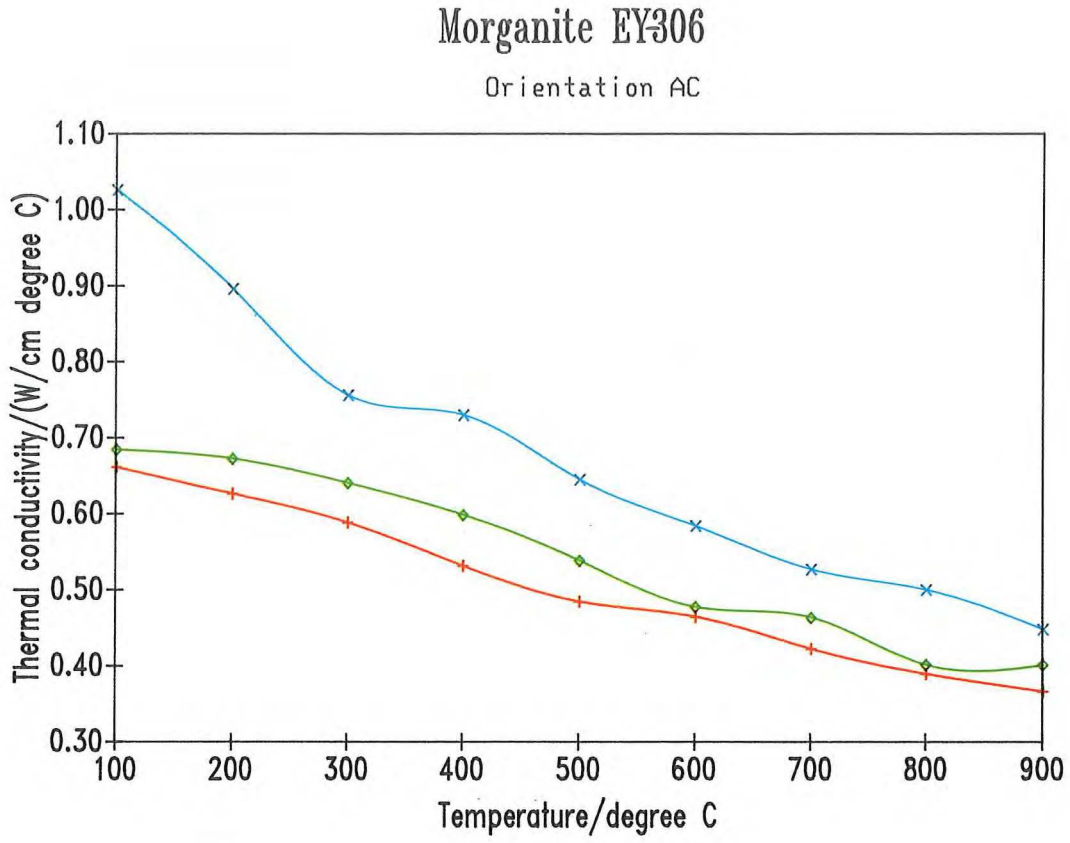

Fig. 7a: Temperature dependent thermal conductivity

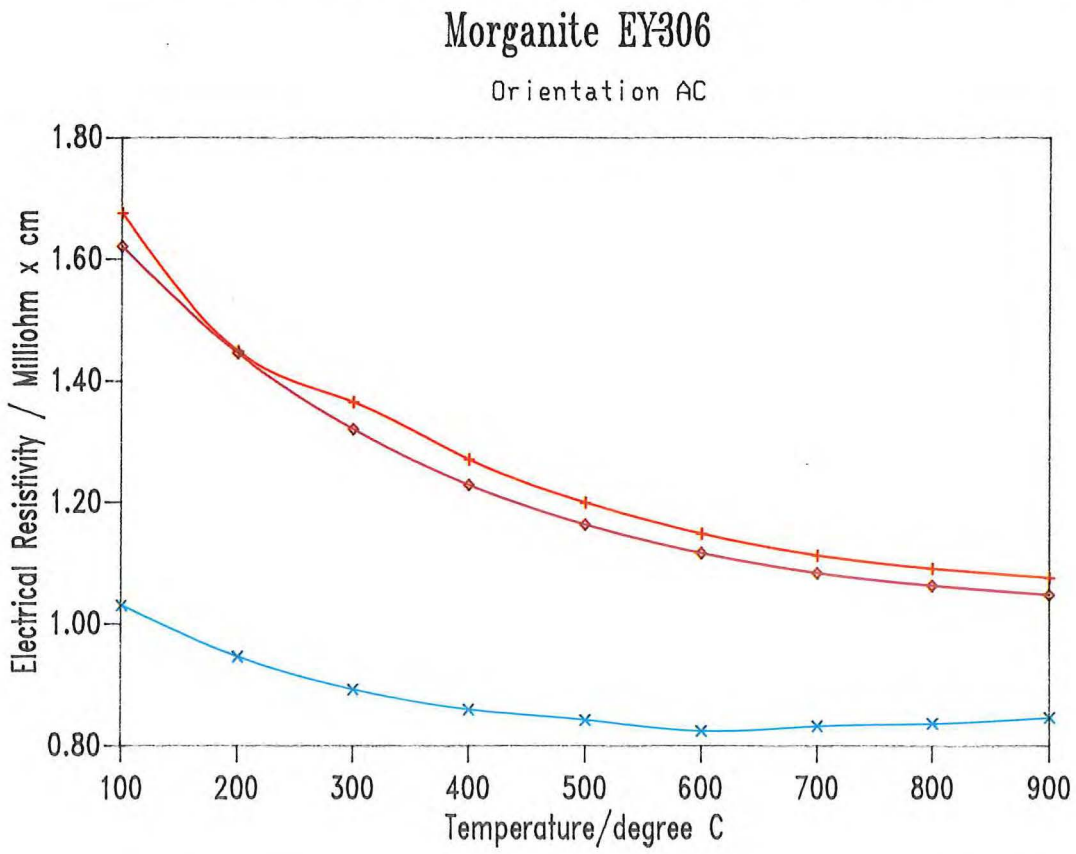

Fig. 7b: Temperature dependent electrical resistivity

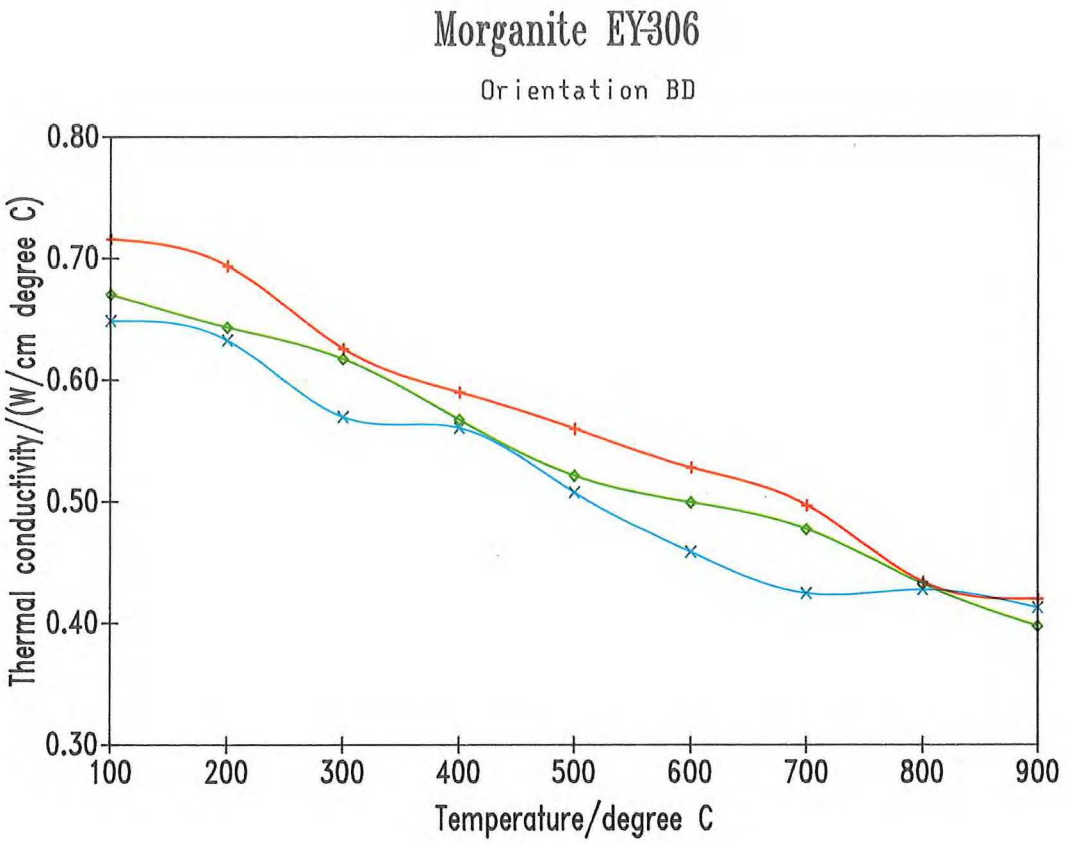

Fig. 7a: Temperature dependent thermal conductivity cont.

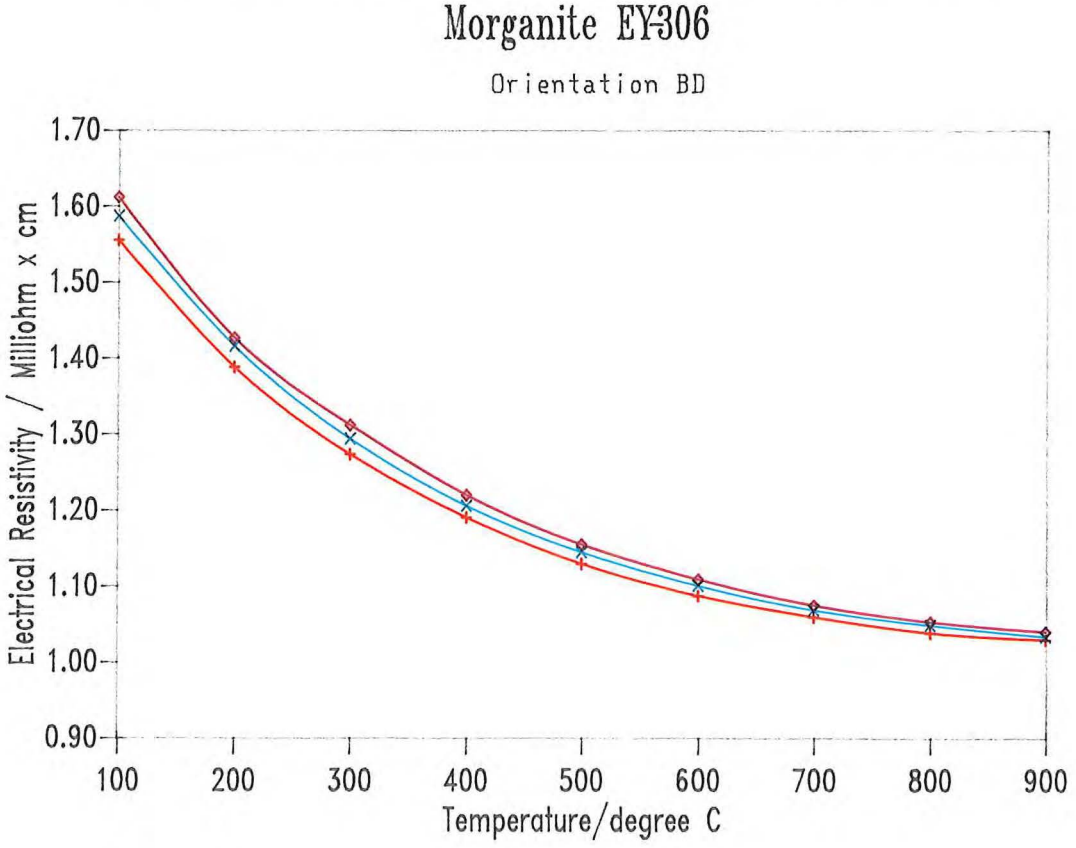

Fig. 7b: Temperature dependent electrical resistivity cont.

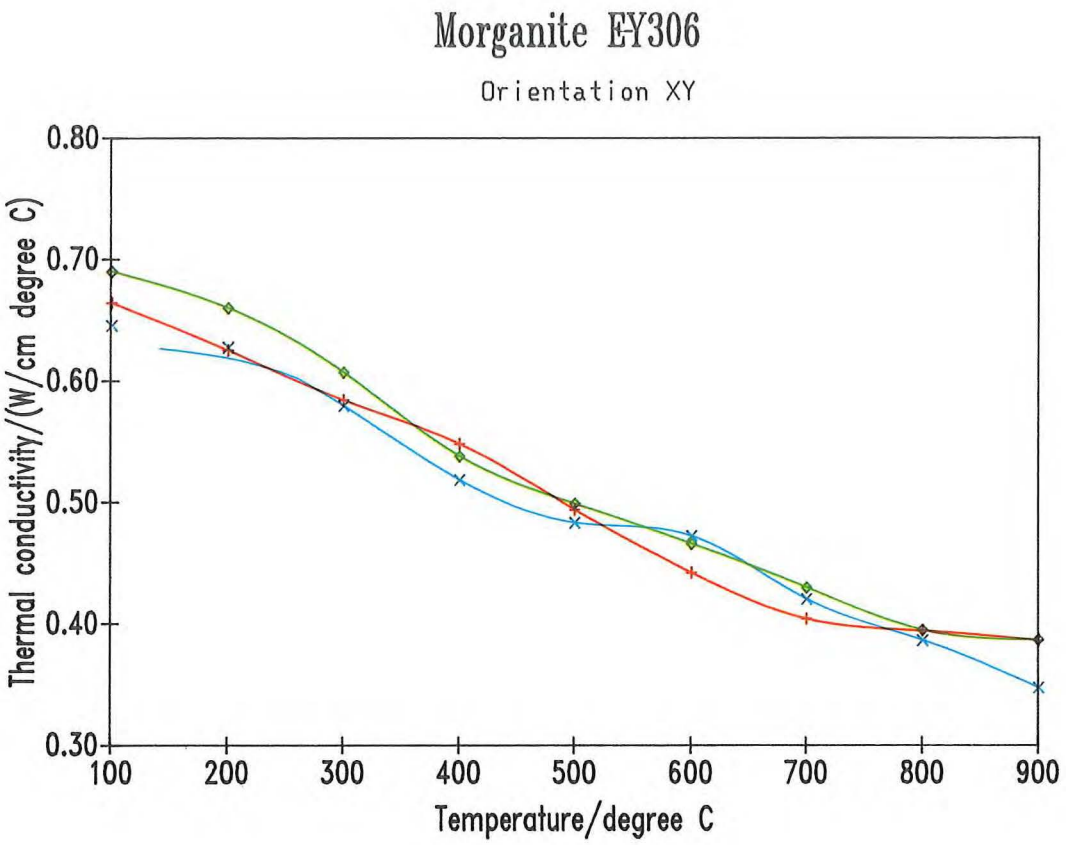

Fig. 7a: Temperature dependent thermal conductivity cont.

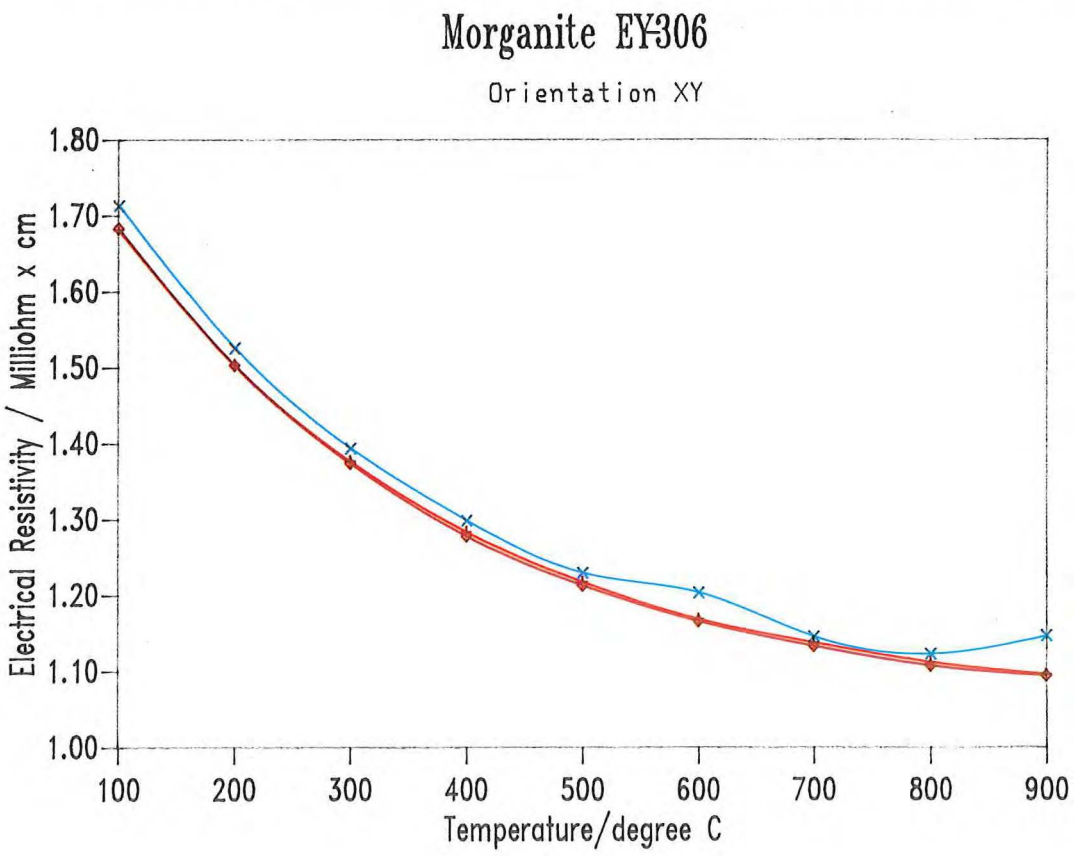

Fig. 7b: Temperature dependent electrical resistivity cont.

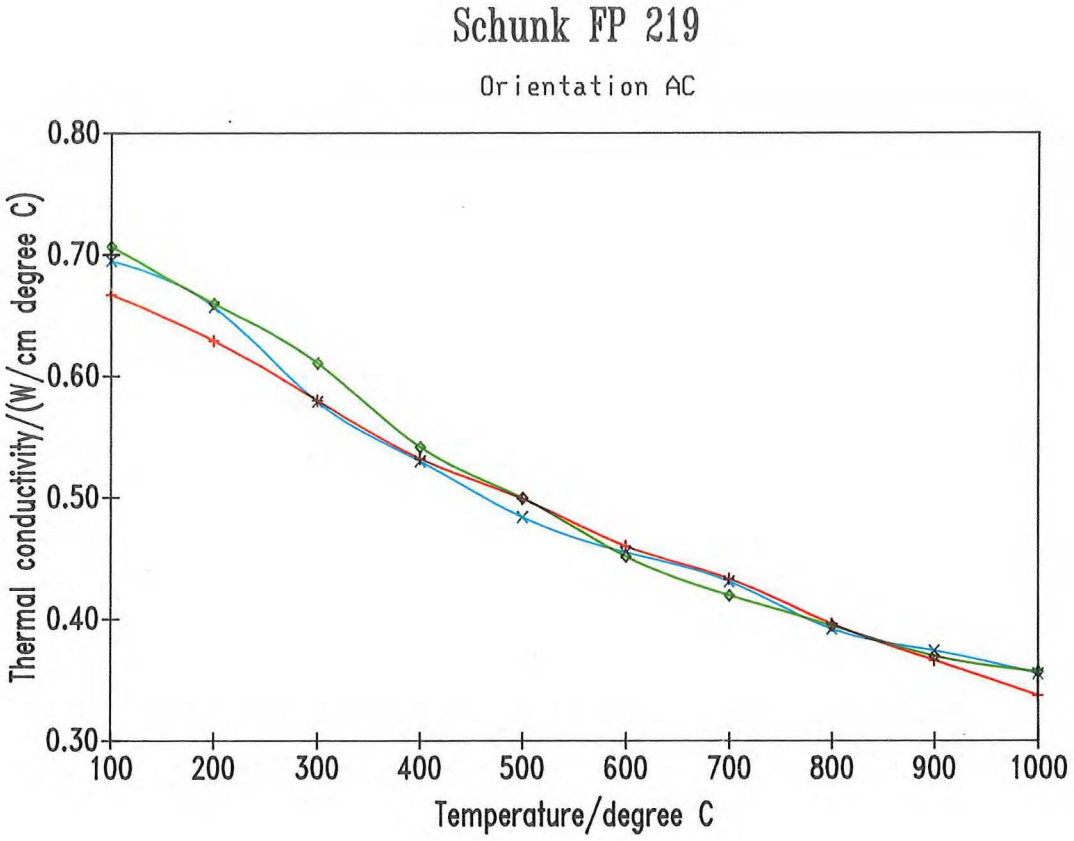

Fig. 8a: Temperature dependent thermal conductivity

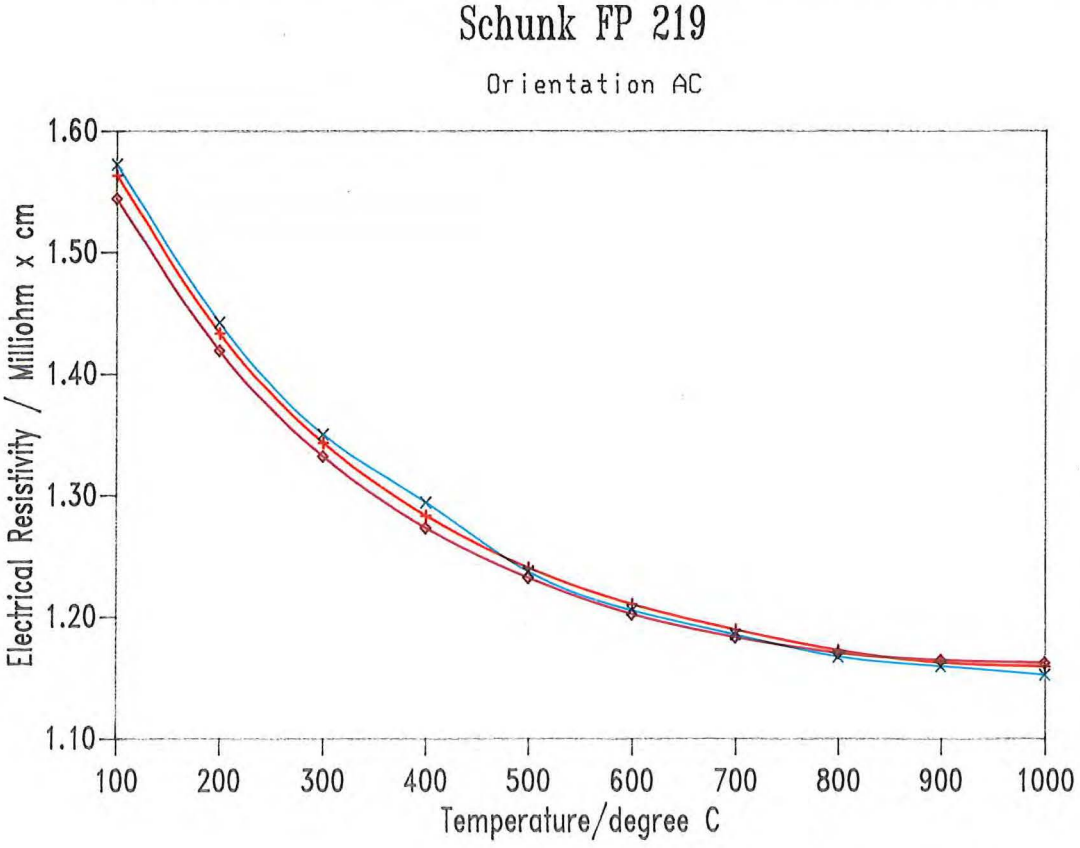

Fig. 8b: Temperature dependent electrical resistivity

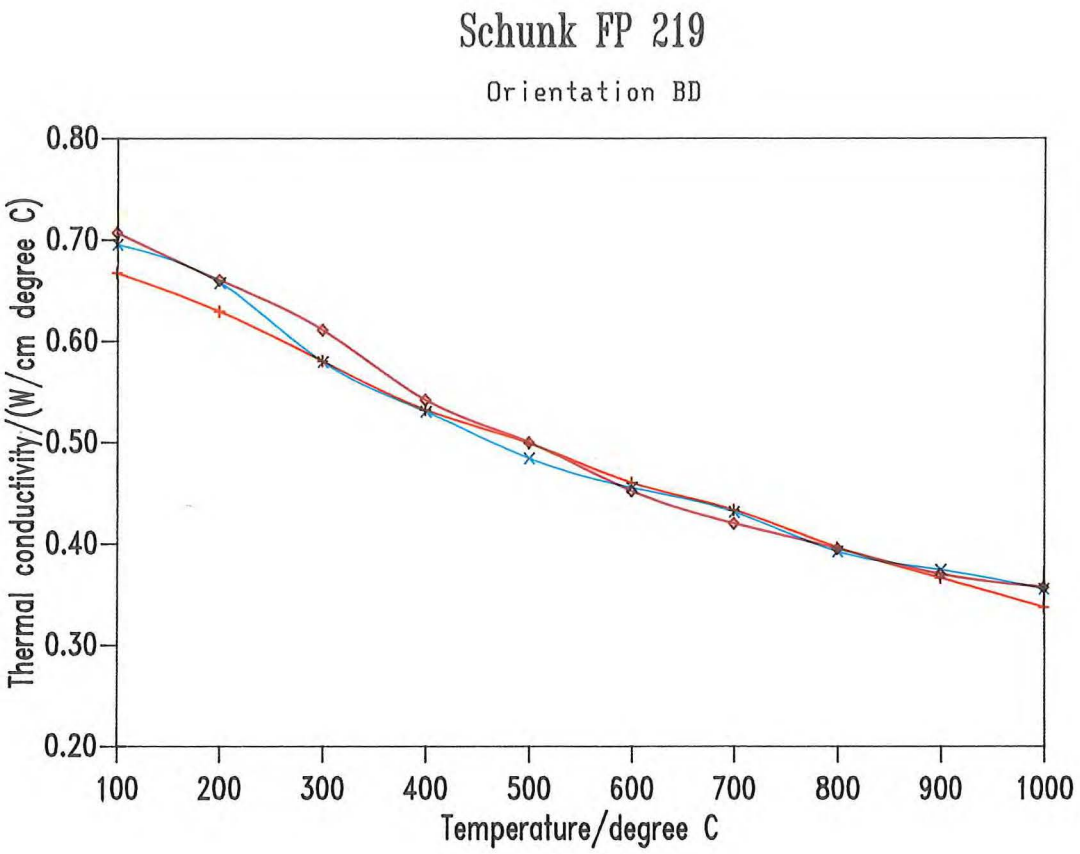

Fig. 8a: Temperature dependent thermal conductivity cont.

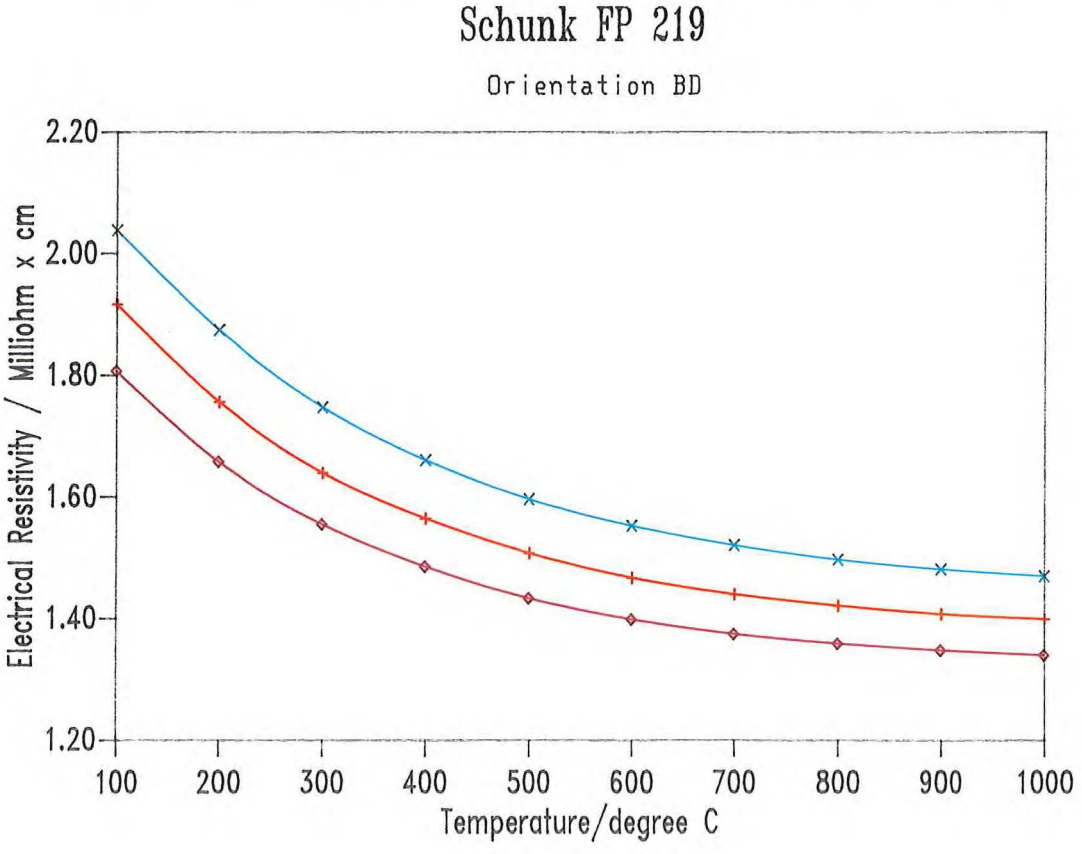

Fig. 8b: Temperature dependent electrical resistivity cont.

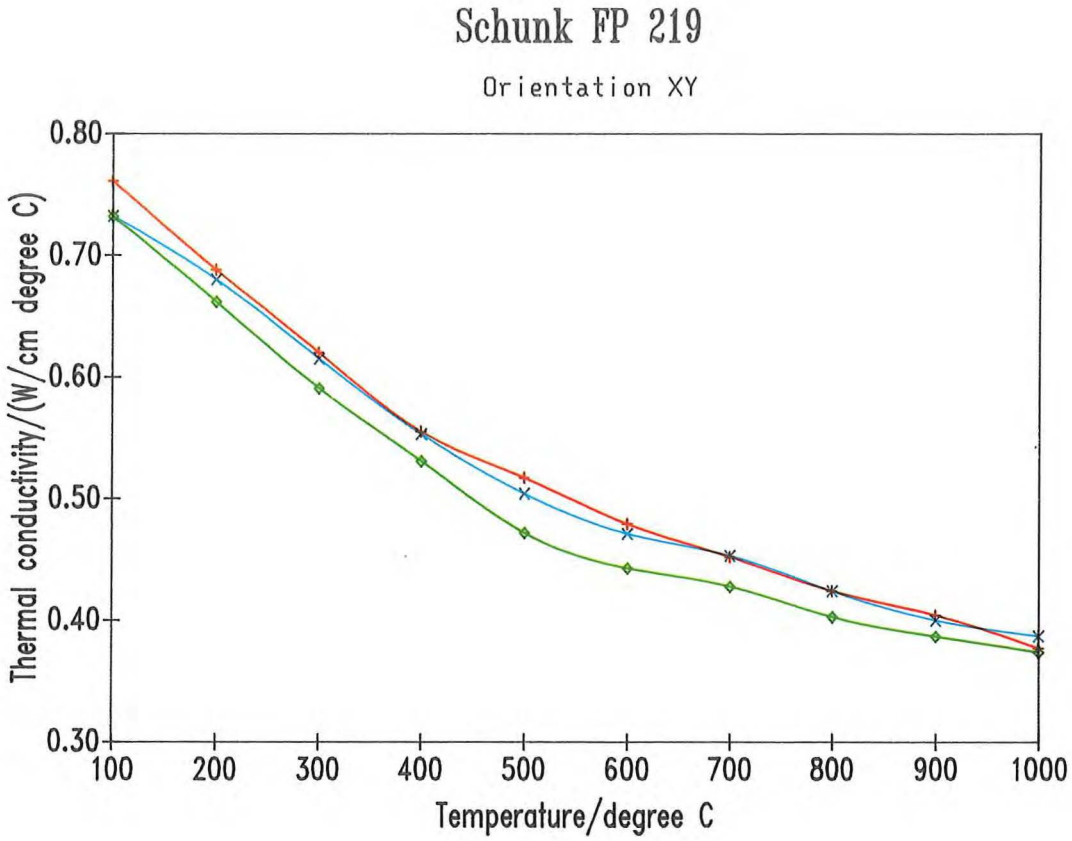

Fig. 8a: Temperature dependent thermal conductivity cont.

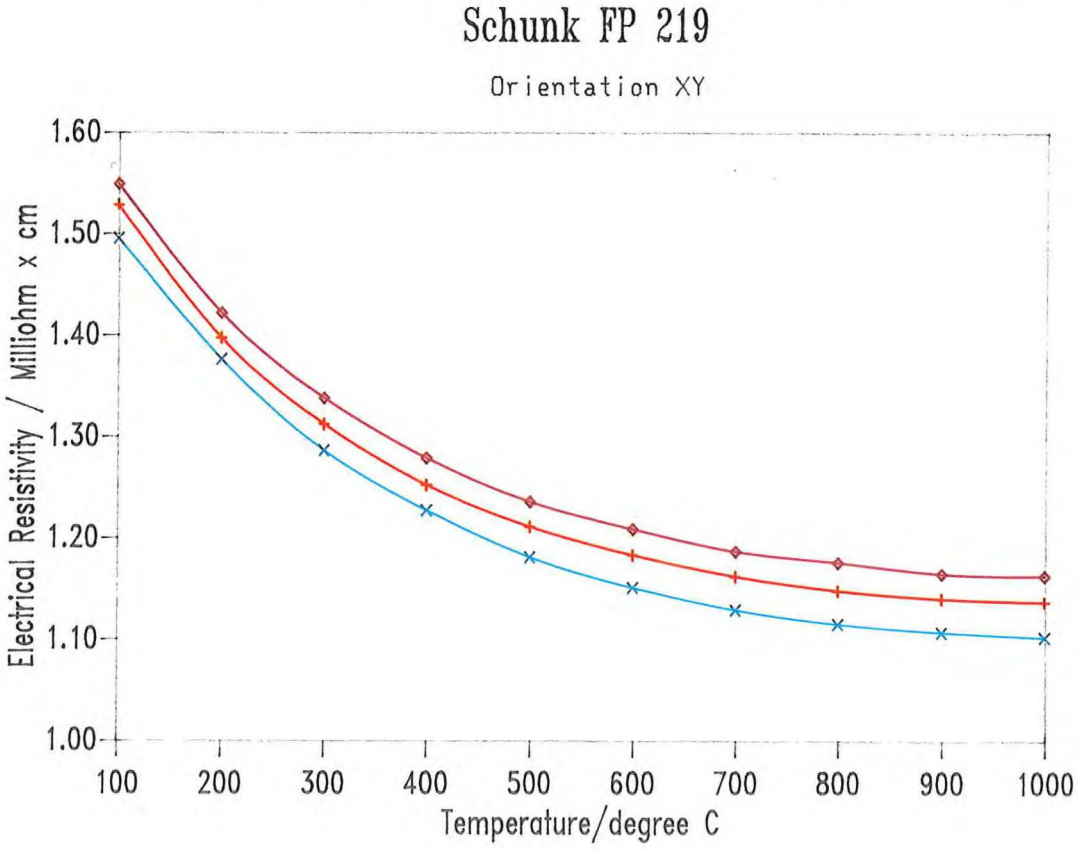

Fig. 8b: Temperature dependent electrical resistivity cont.

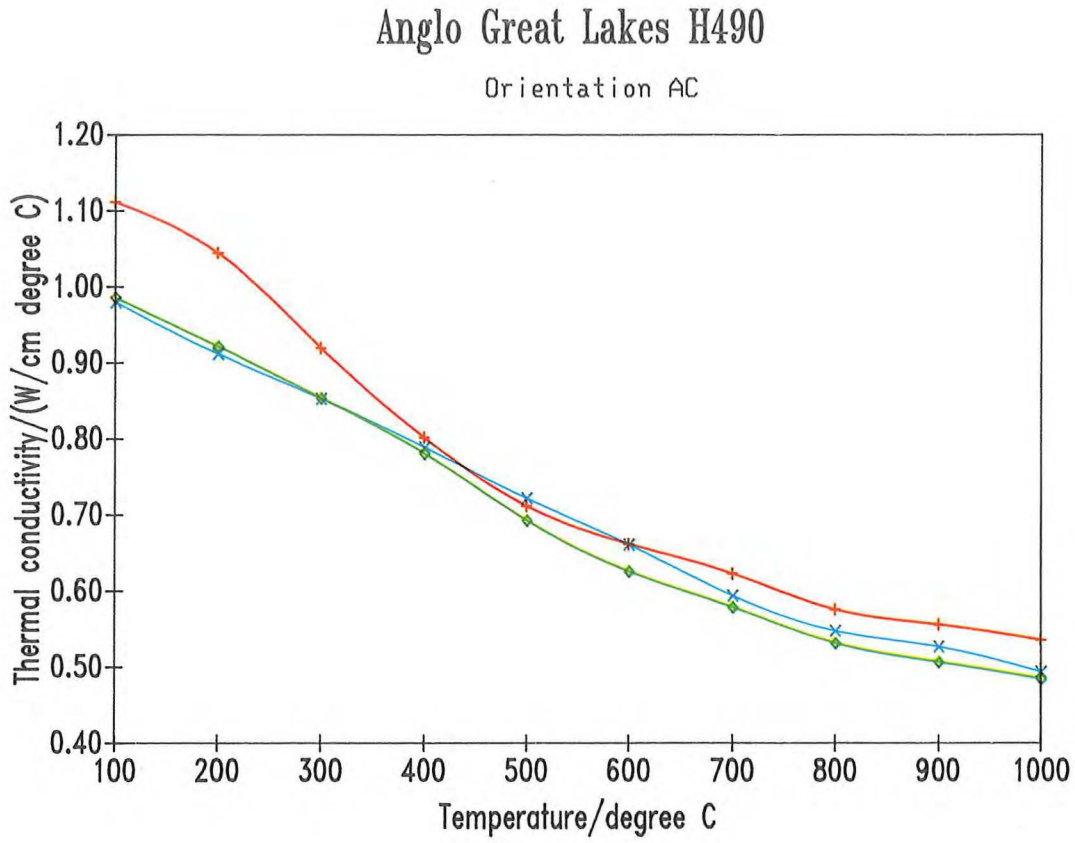

Fig. 9a: Temperature dependent thermal conductivity

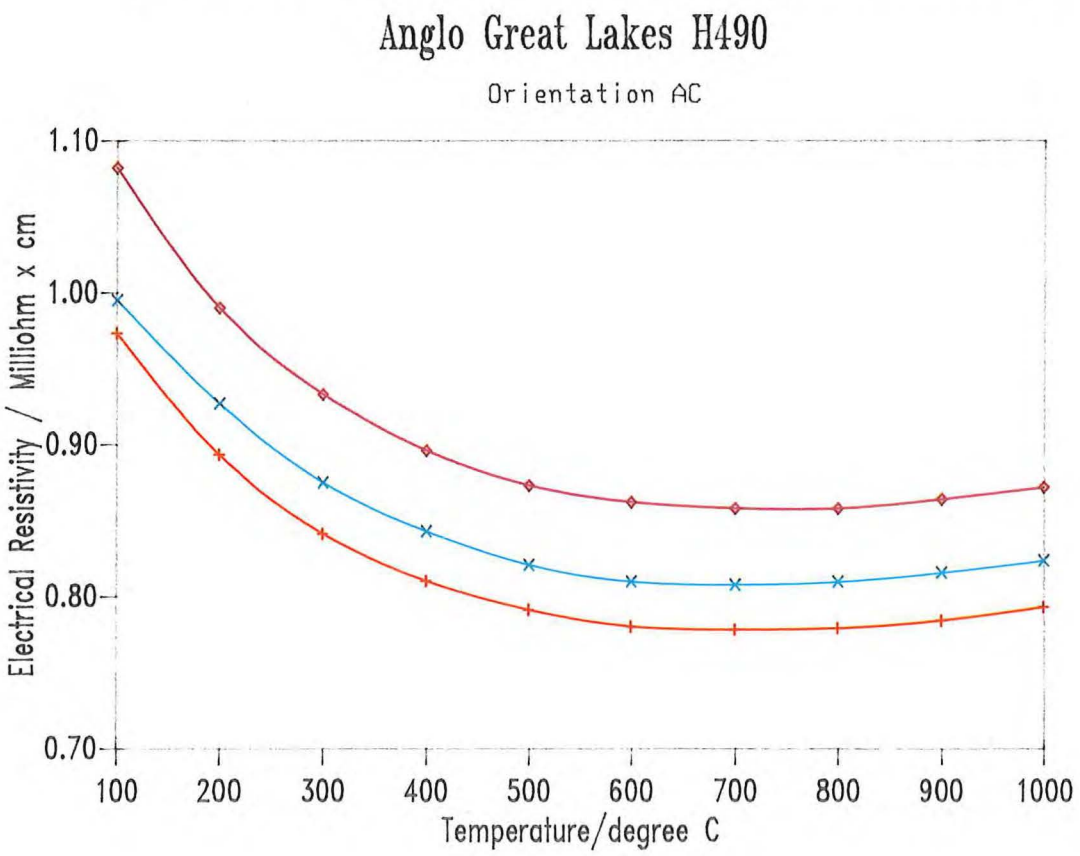

Fig. 9b: Temperature dependent electrical resistivity

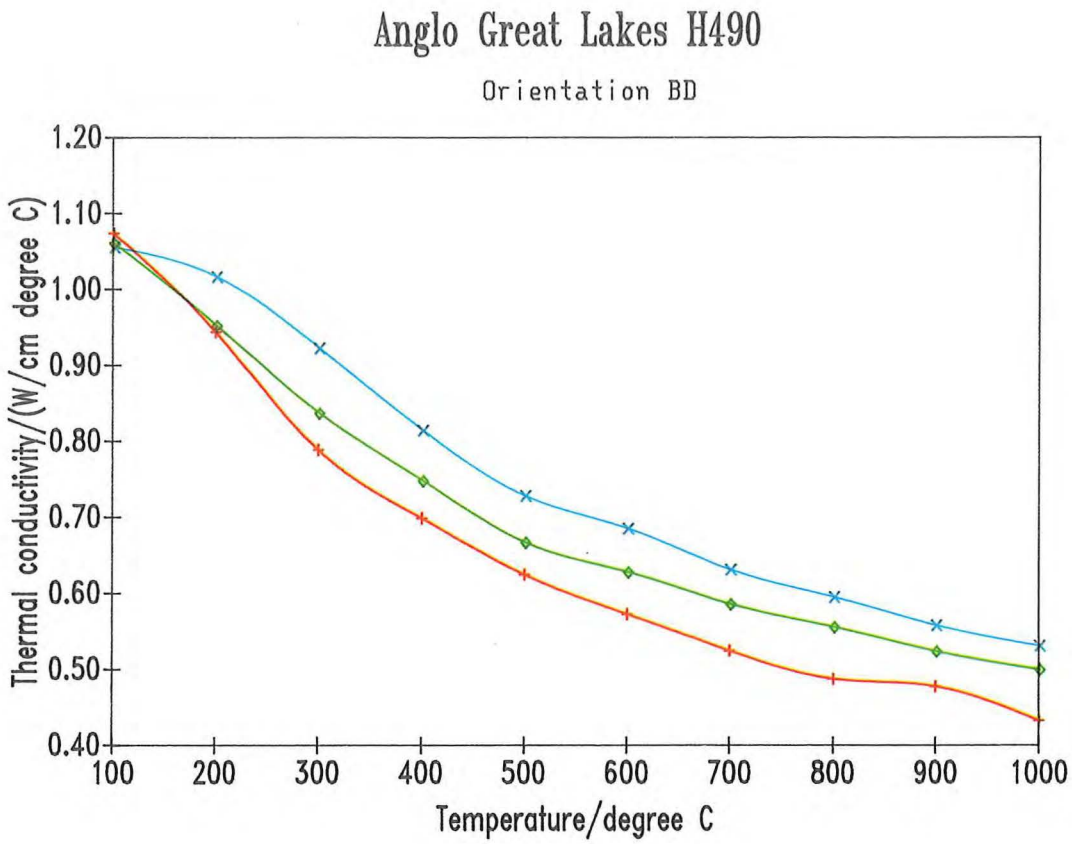

Fig. 9a: Temperature dependent thermal conductivity cont.

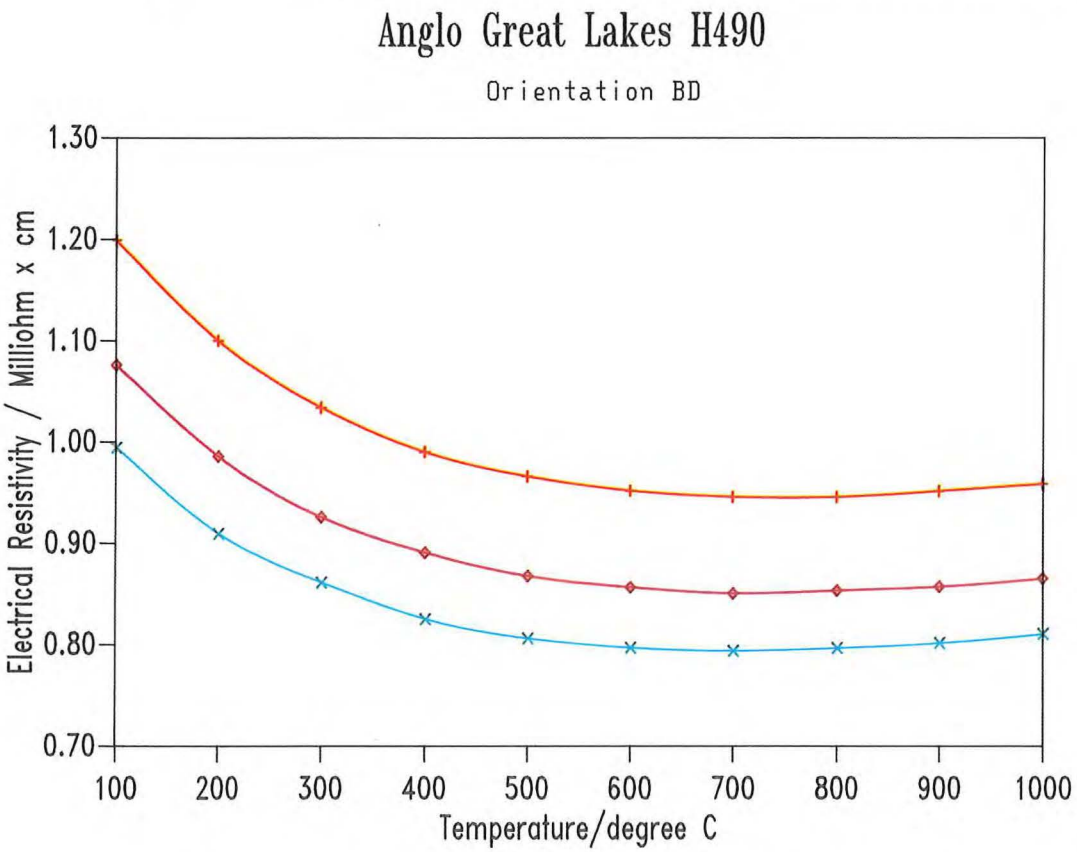

Fig. 9b: Temperature dependent electrical resistivity cont.

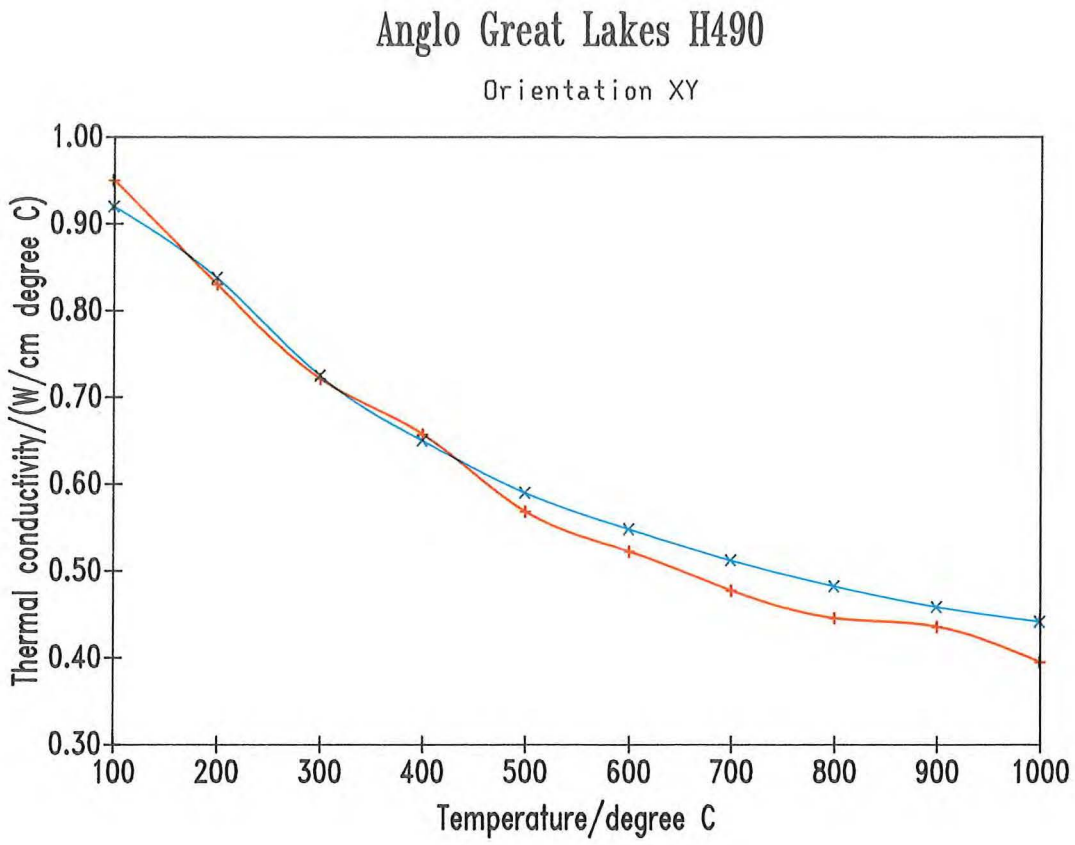

Fig. 9a: Temperature dependent thermal conductivity cont.

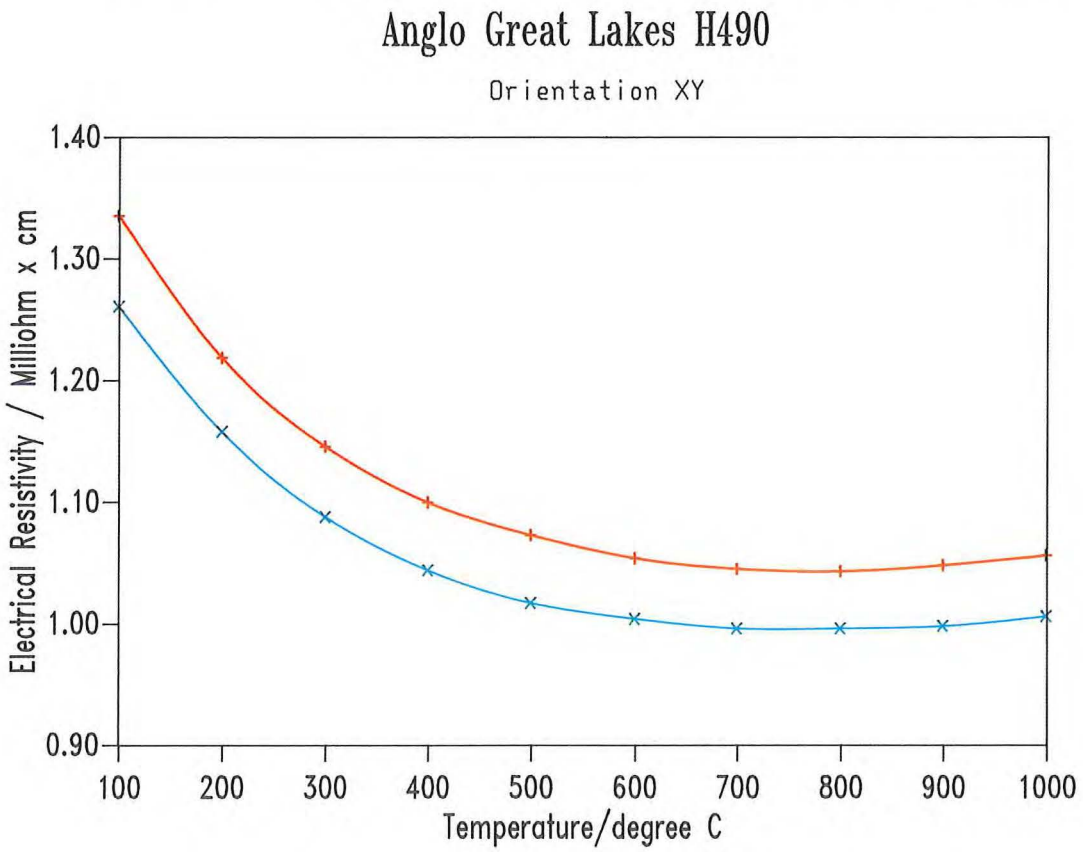

Fig. 9b: Temperature dependent electrical resistivity cont.

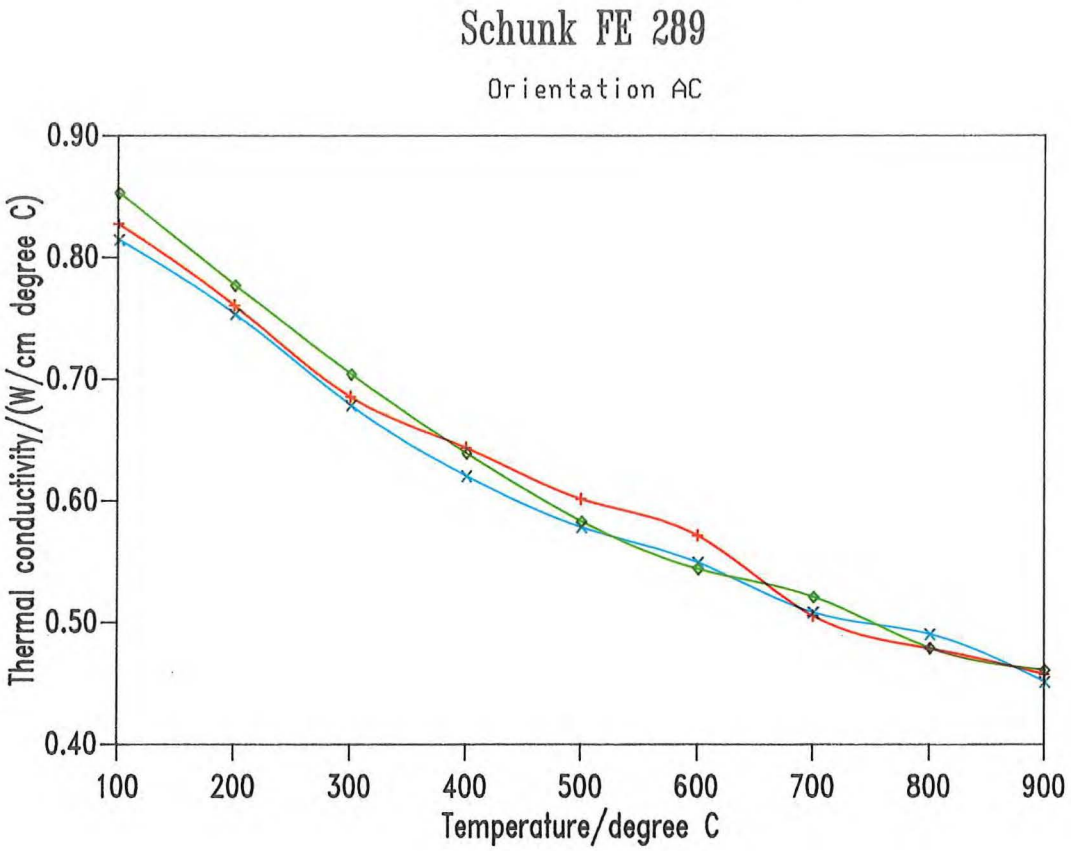

Fig. 10a: Temperature dependent thermal conductivity

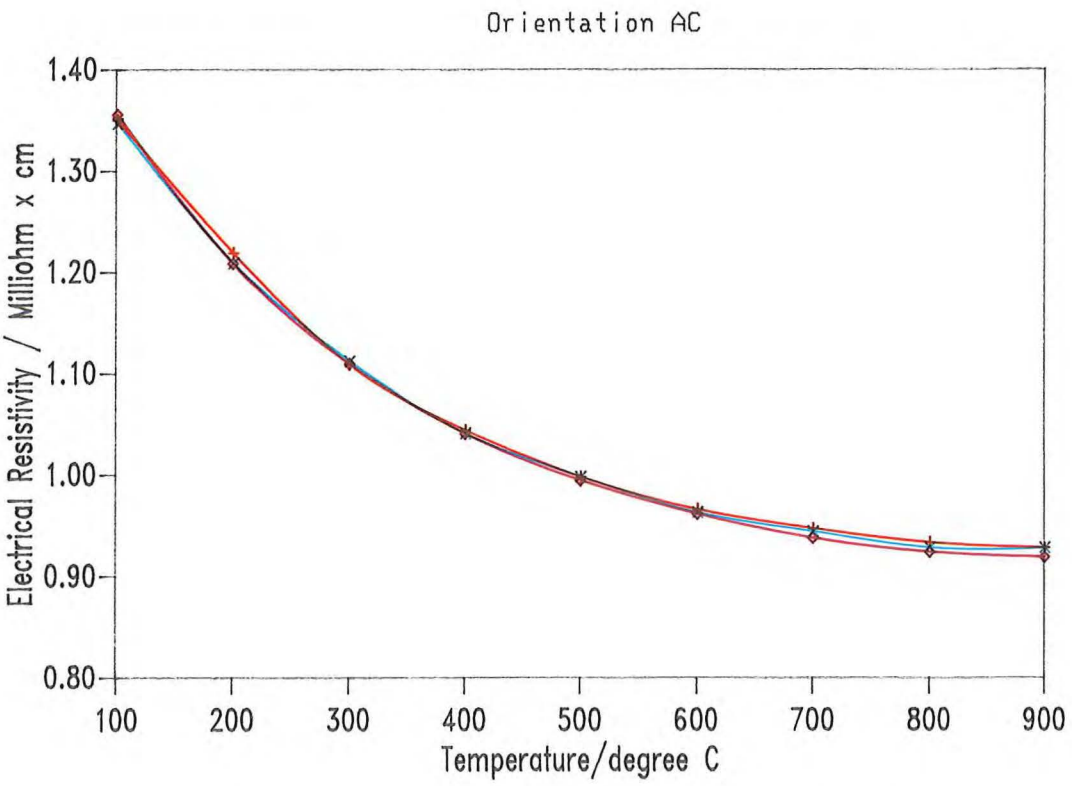

Fig. 10b: Temperature dependent electrical resistivity

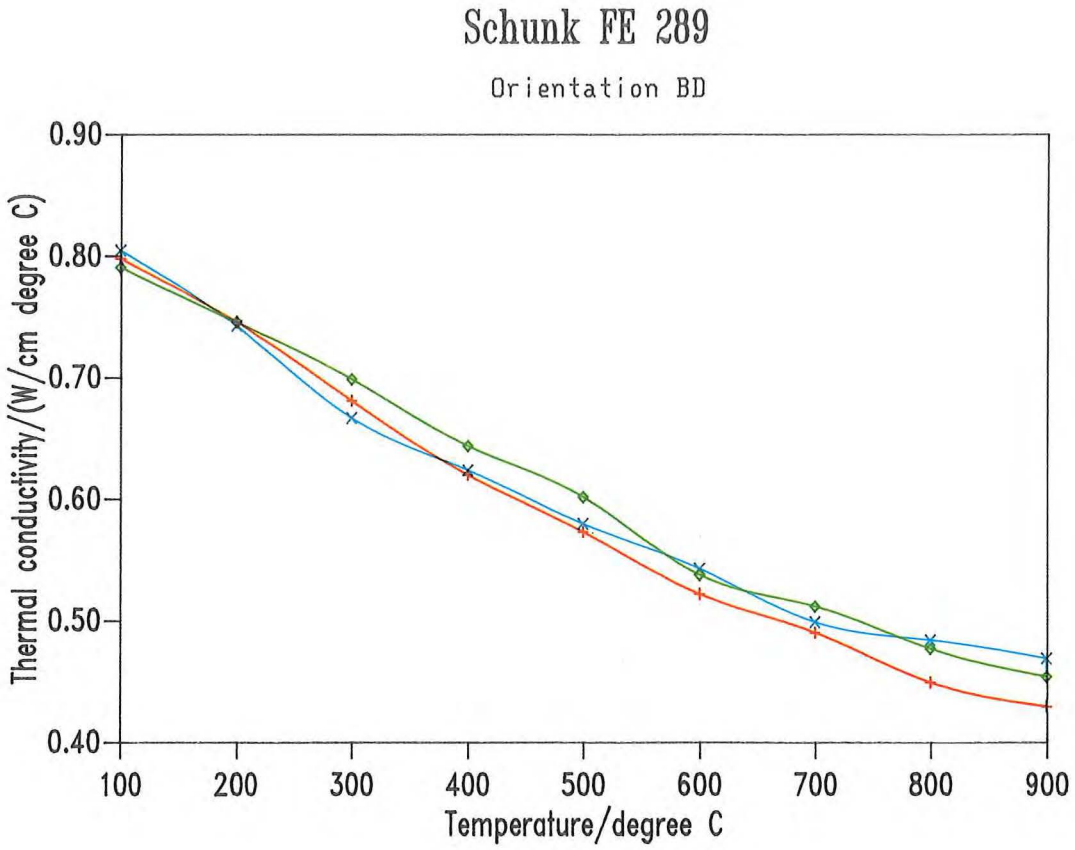

Fig. 10a: Temperature dependent thermal conductivity cont.

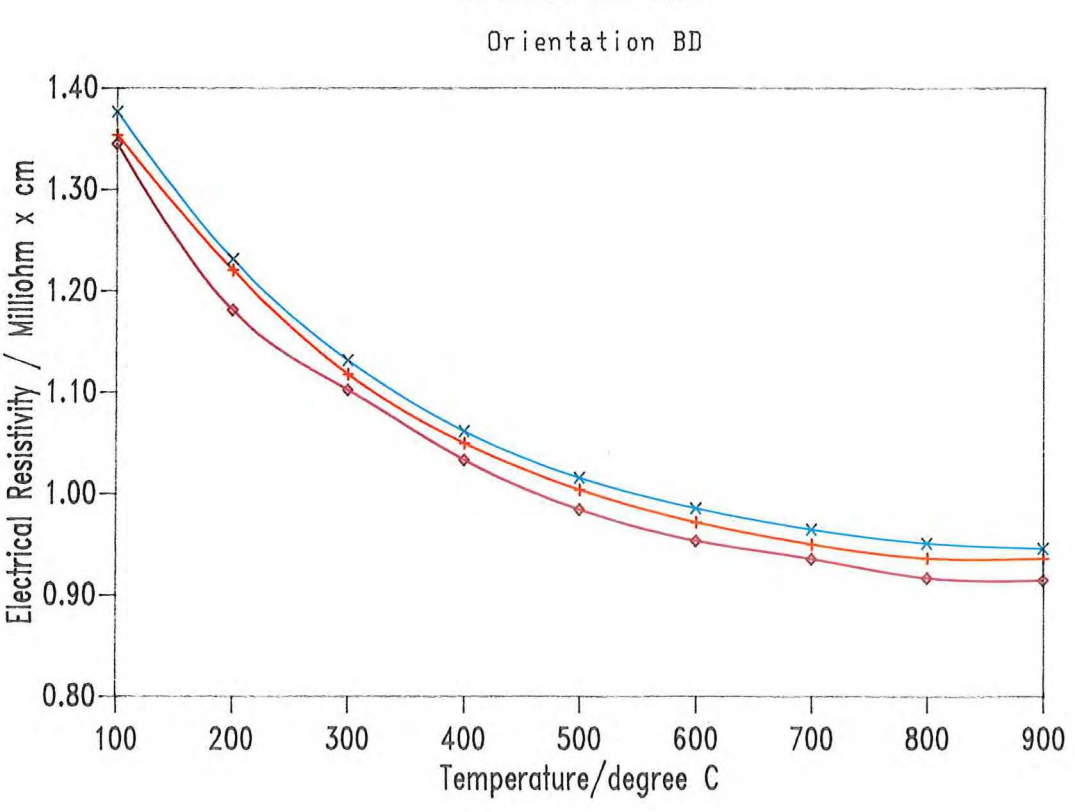

Fig. 10b: Temperature dependent electrical resistivity cont.

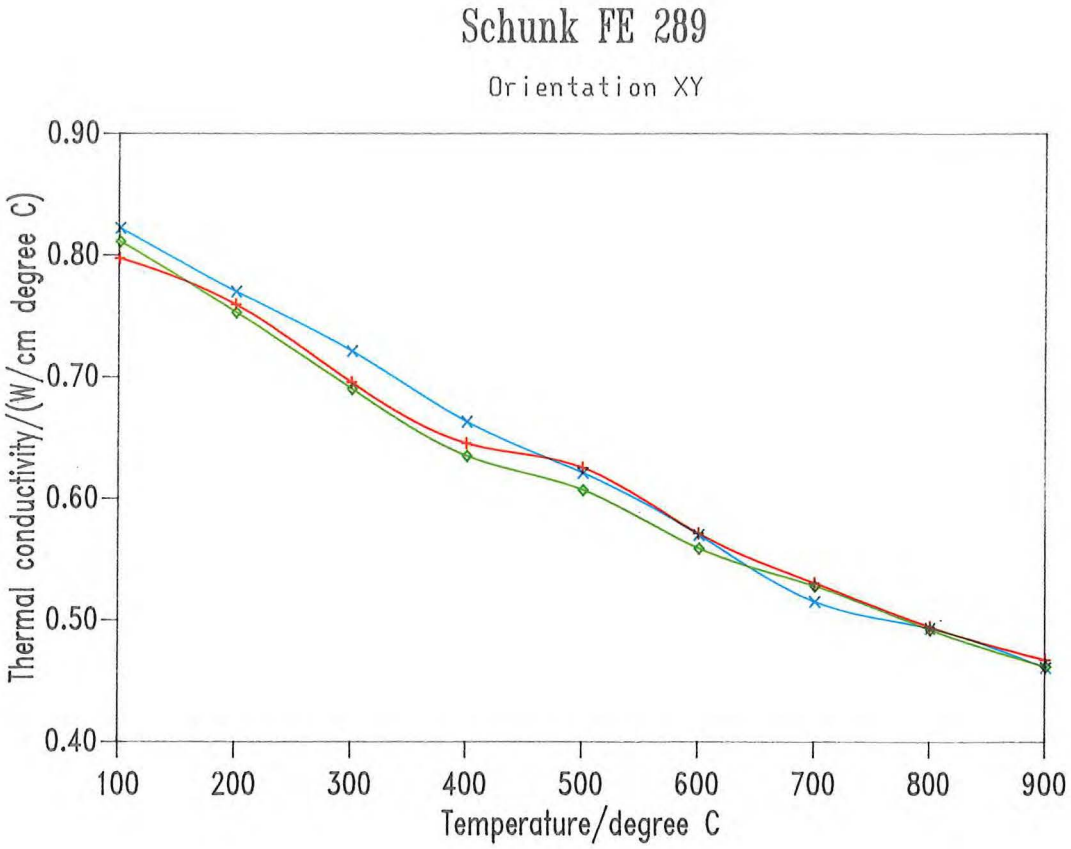

Fig. 10a: Temperature dependent thermal conductivity cont.

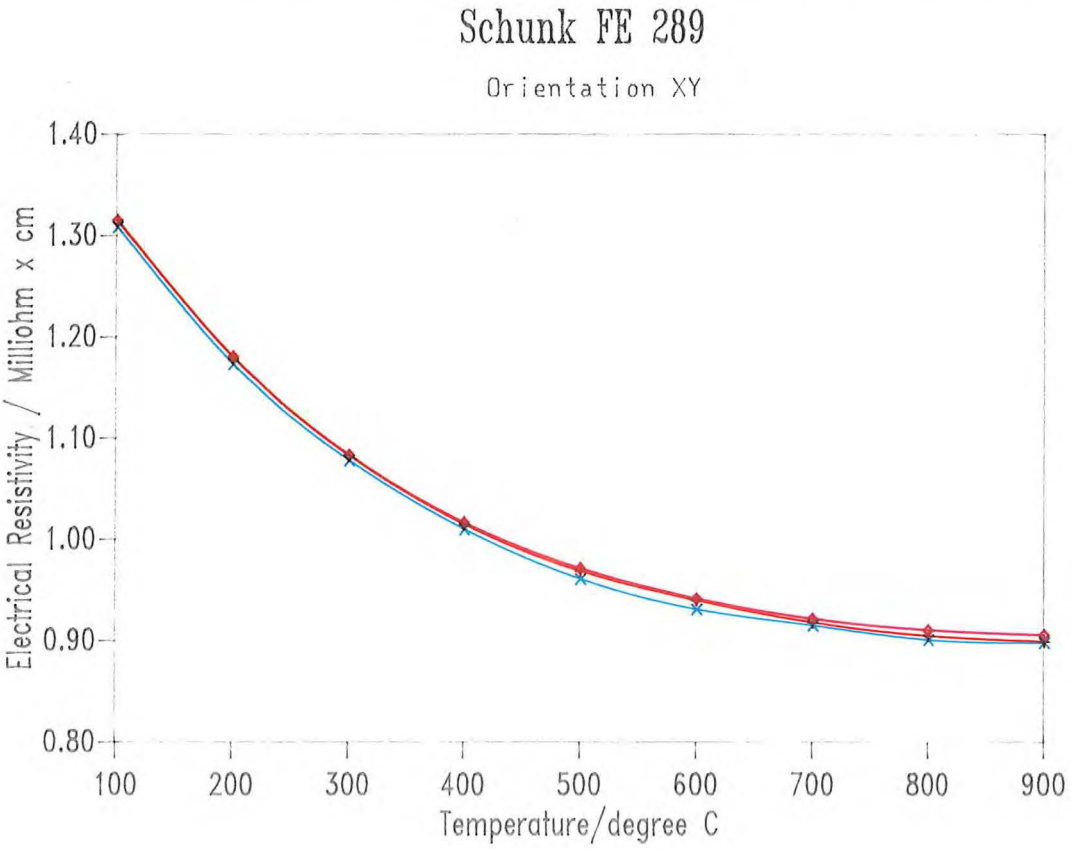

Fig. 10b: Temperature dependent electrical resistivity cont.

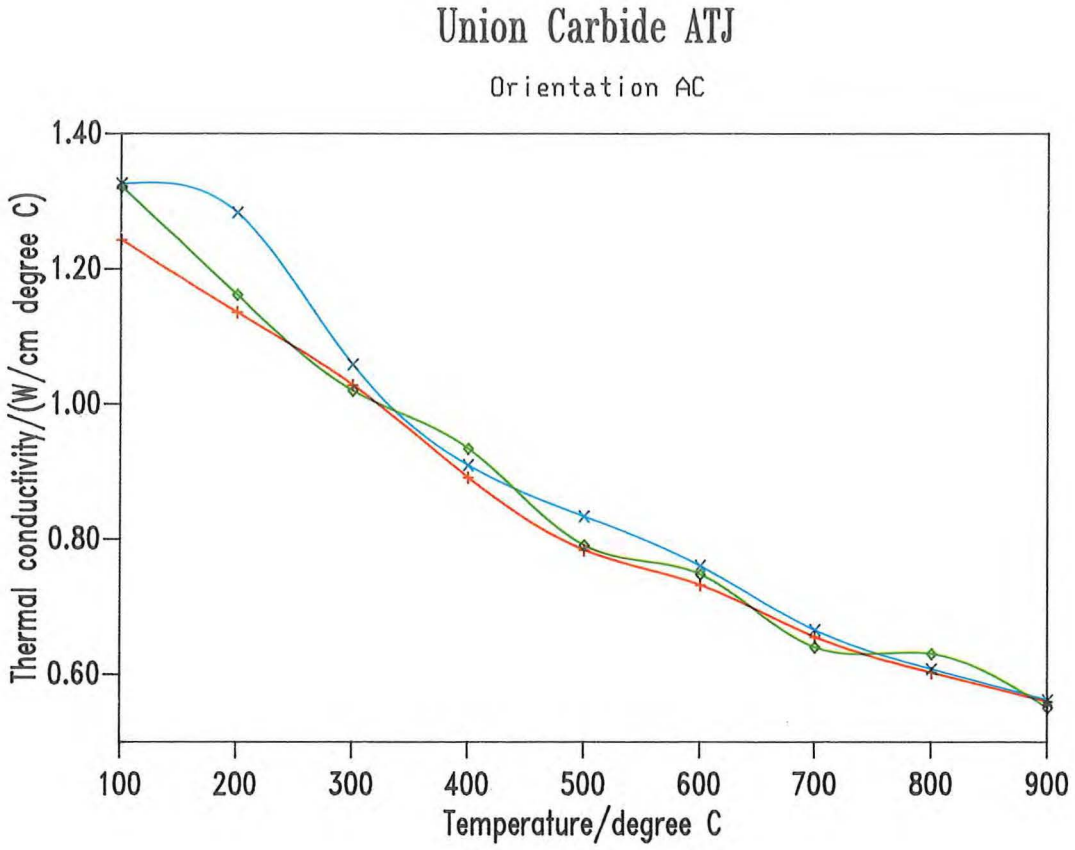

Fig. 11a: Temperature dependent thermal conductivity

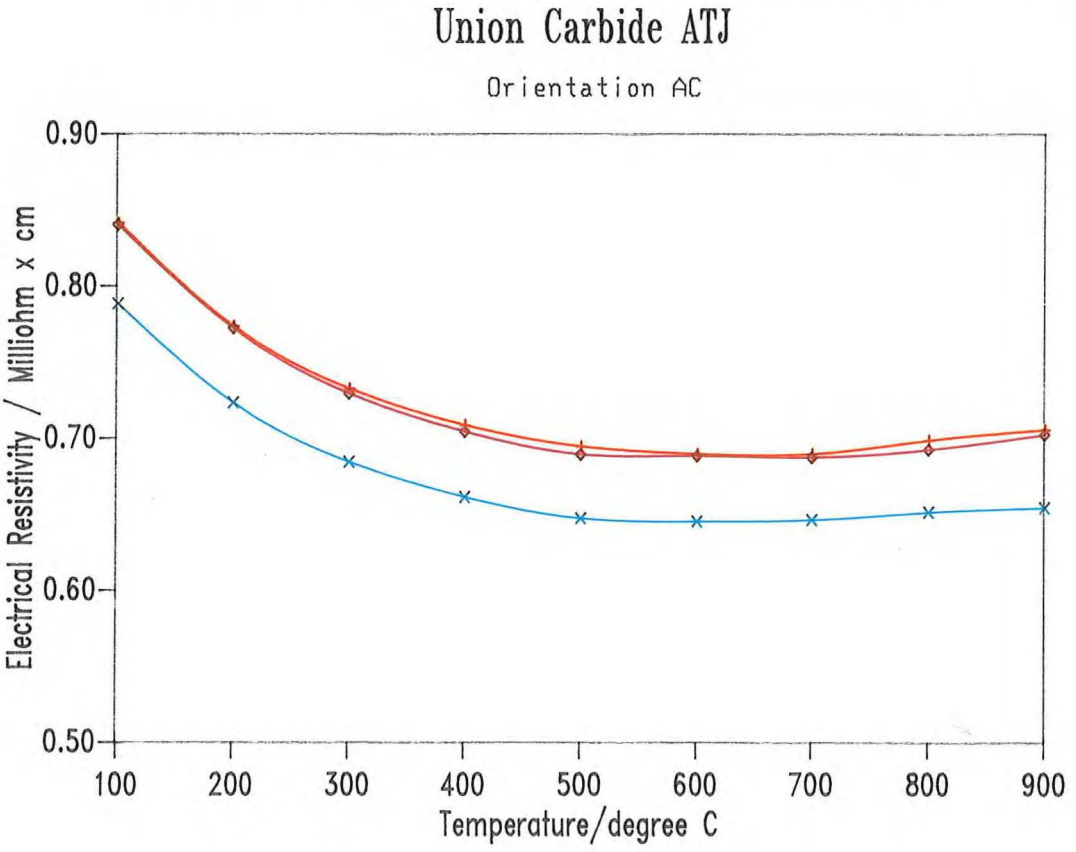

Fig. 11b: Temperature dependent electrical resistivity

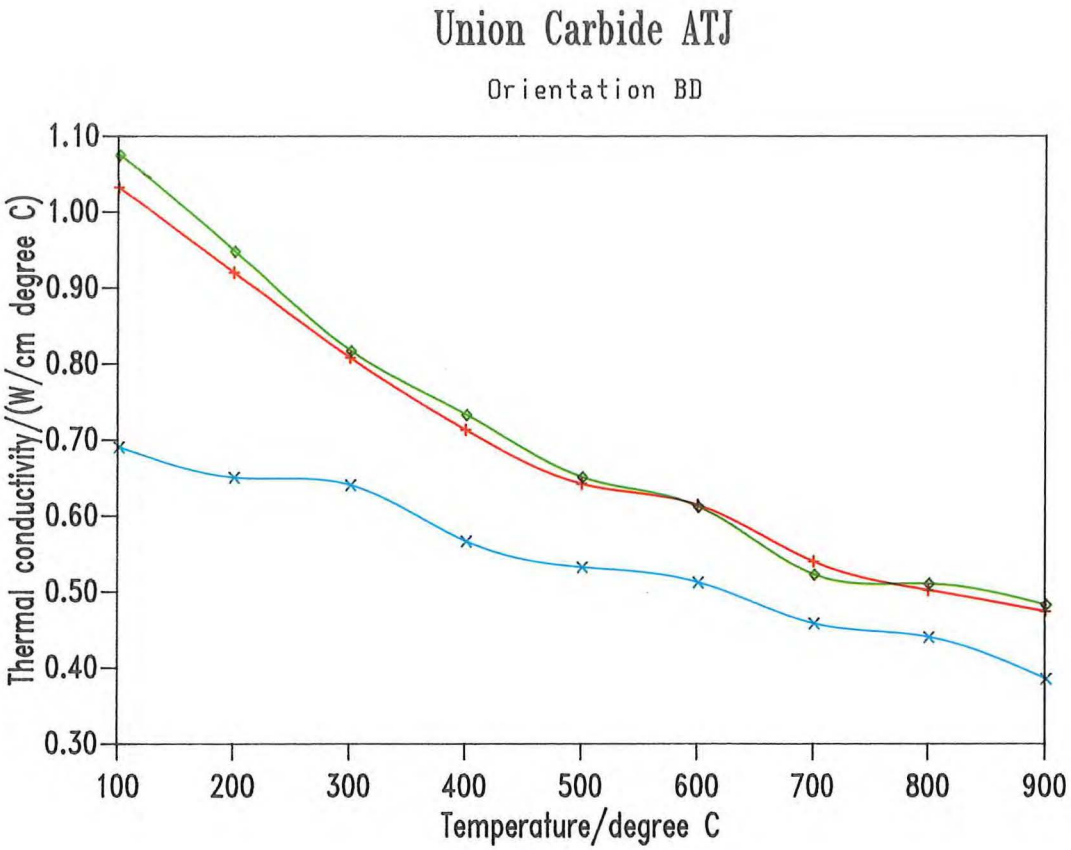

Fig. 11 a: Temperature dependent thermal conductivity cont.

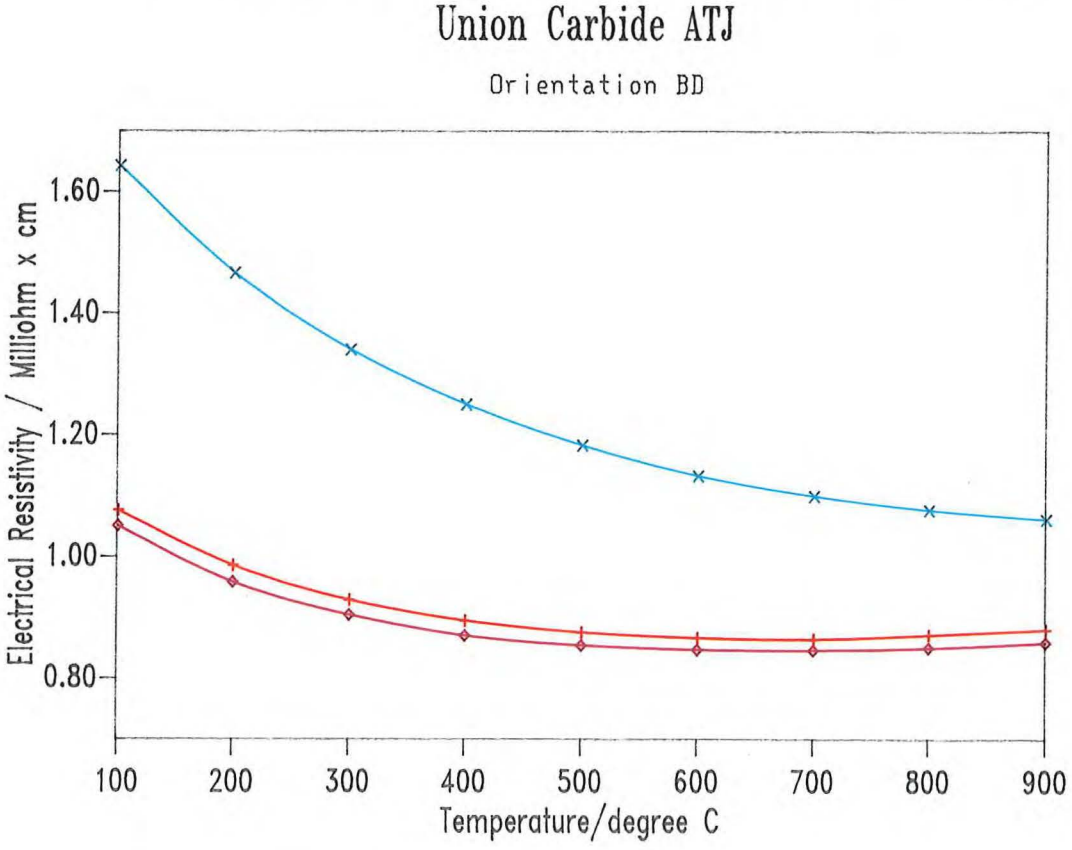

Fig. 11 b: Temperature dependent electrical resistivity cont.

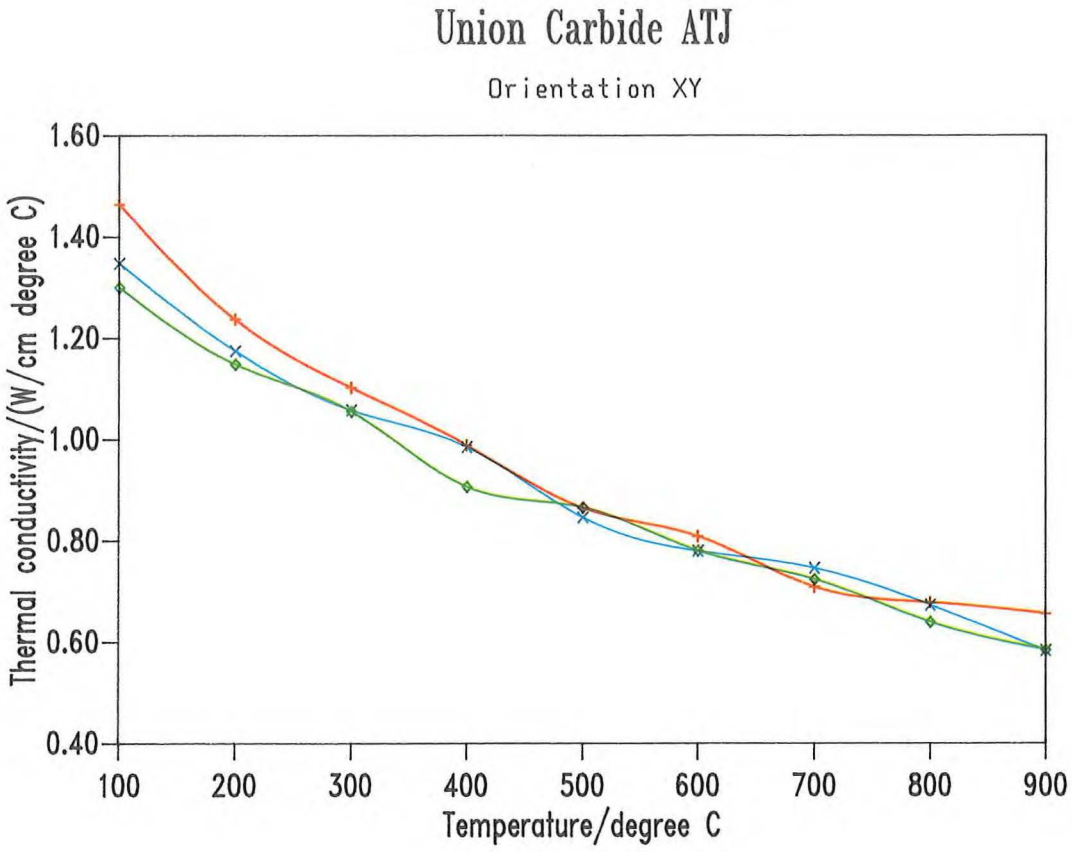

Fig. 11 a: Temperature dependent thermal conductivity cont.

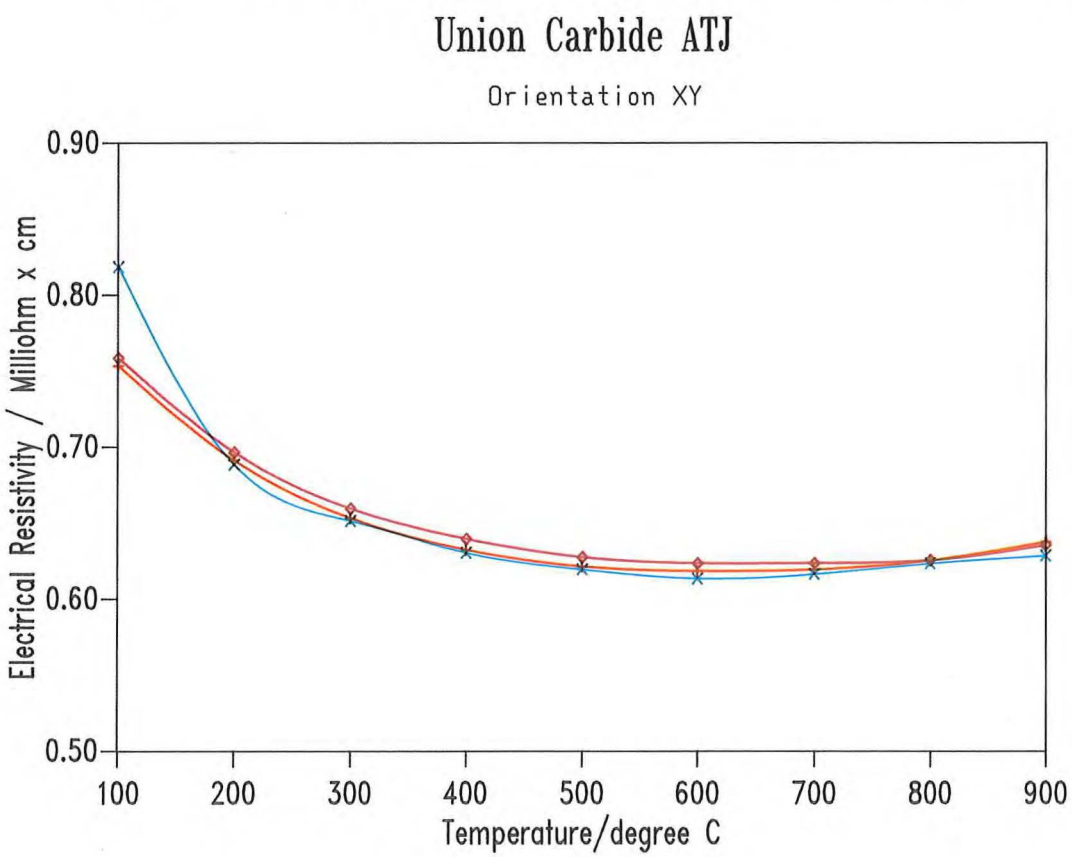

Fig. 11 b: Temperature dependent electrical resistivity cont.

3.1 6 Bending Strength

The samples with the dimensions 6 x 8 x 50 mm were examined in a position with bending forces acting in the stiffest direction of the cross-section to minimize the effect of the bearing forces for the given specimen dimensions. The four-point-equipment used had a moment arm of 10 mm and a distance of the outer bearings of 40.05 mm. To minimize the superimposed torsion stresses, only one of the bearings was kept fixed, the other three bearings were arranged as floating bearings. As bearing rolls, commercally available bearing needles 3 mm in diameter were used.

The bending of the samples was measured by means of a modified extensiometer INSTRON, Typ 2620, series 602. The bending measuring chain was calibrated by means of a "Tesa"-micrometer for measuring depths with an accuracy of 1 µm.

Also the calibration of power was done by using calibrated standard weights and was always examined. All bending experiments were carried out with a constant cross-head speed of 0.1 mm/min.

For the collection of the measured data of force, strain and deflexion, the following equipments were used:

- TEKTRONIX table-computer, type 4052
- TRANSERA ADC, type 752 (12 bit/10 V)
- TRANSERA High-speed Auxiliary Memory (64 K).

The measured and into stress, , and strain, , converted values were presented by using a HEWLETT PACKARD plotter, type 7225 A.

For the calculation of the stress and strain values for the bending experiments, the usual formulas presuming linear elastic behaviour were applied. Because of delay in the delivery, only 6 grades of graphites could be measured:

Ringsdorff EK 98
Carbone-Lorraine 5890/PT
POCO AXF-5Q
Schunk Kohlenstoff FP 219
Anglo Great Lakes H-490.
Morganite EY-306

As far as the near isotropic, isostatically pressed materials are concerned, 10 specimens machined from only one direction of the block were investigated. It was felt to be necessary to measure 10 specimens in the parallel and perpendicular directions of the moulded or extruded grades of graphites.

Furthermore, the carbon fibre composite material E 5923 P produced by the Dunlop company was investigated. Again 10 specimens were examined, 3 cut in main direction of the laminate parallel to the main direction of load (fig. 13 a) and 7 cut in main direction of the laminate perpendicular to the main direction of load (fig. 13 b). There were no samples cut in the third direction (fig. 13 c).

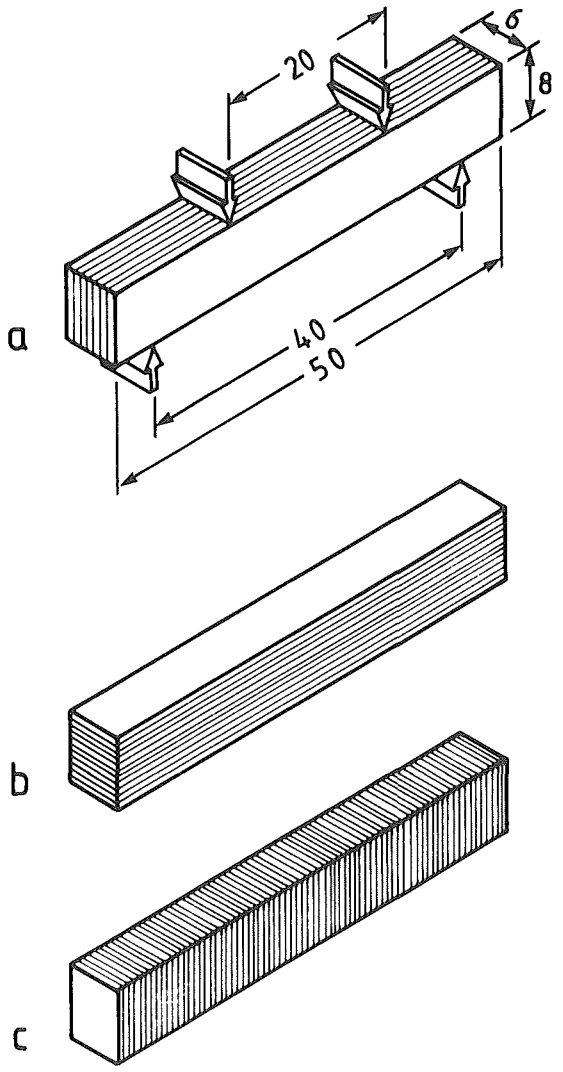

Fig. 13: Scheme of specimen cutting and bending strength measurement of carbon fibre composite

The results of bending experiments are listed up in tables 19 and 20. Fig. 14 demonstrates the correlation between the mean values of fracture deflexion and bending strength for various graphites investigated. The measured values are listed up in tables 21 to 25. Obviously, there is a relationship between Young's modulus of elasticity and bending strength as suggested in fig. 15. Both properties depend upon the grade of graphitization of the filler and binder phases, anisotropy of the artifact and grains, porosity which is influenced by the degree of close-packing of the grains and impregnations, as well as grain size and optimization of binder content (2). The relation demonstrated in fig. 15 allows the estimation of strength by using the measured values of dynamic Young's modulus in comparison with other graphites.

In figures 16 to 35, bendig strength and fracture deflexion are correlated and the intervals of expectation and prediction are plotted.

Producer	POCO	Anglo Great Lakes		Carbone-Lorraine		Schunk	Ringsdorff	Morganite
Grade	AXF-5Q	H-490		5890/PT		FP 219	EK 98	EY-306
Grain orientation	--	∥	⊥	∥	⊥	--	--	--
$\overline{R_B}$ / MPa	87.9	33.6	30.8	53.0	43.0	29.8	47.4	37.0
$\pm$ S / MPa	10.3	4.1	1.1	3.2	2.5	1.0	1.1	3.1
V_p / %	11.7	12.2	3.6	6.0	5.7	3.4	2.3	8.5
$\overline{f_B}$ / mm	0.407	0.253	0.256	0.314	0.28	0.244	0.284	0.244
$\pm$ S / mm	0.051	0.03	0.011	0.016	0.014	0.009	0.007	0.009
V_p / %	12.5	12.0	4.4	5.2	5.0	3.6	2.6	8.7
R	0.9968	0.9876	0.8582	0.9775	0.948	0.9197	0.8392	0.9917
Number of specimens	10	10	10	10	10	10	10	10

$\overline{R_B}$: Mean value of bending strength

$\overline{f_B}$: Mean value of fracture deflexion

S : Standard deviation

R : Correlation coefficient

V_p : Variation coefficient

Tab. 19: Results of bending experiments on various grades of graphite

Direction*)	a	b
$\overline{R_B}$ (MPa)	70,1	56,4
$\pm$ S (MPa)	12,1	9,6
V_p (%)	17,3	17,0
$\overline{f_B}$ (mm)	0,259	0,293
$\pm$ S (mm)	0,042	0,037
V_p (%)	16,0	12,6
R	unsignificant	0,8715
Number of specimens	3	7

*) see fig. 12

$\overline{R_B}$: Mean value of bending strength
S : Standard deviation
V_p : Variation coefficient
$\overline{f_B}$: Mean value of fracture deflexion
R : Correlation coefficient

Tab. 20: Results of bending experiments on carbon fibre composite Dunlop E 5923P

Grade	Ringsdorff EK 98	
Spec. No	Bend. Strength MPa	Fract. Deflexion mm
1	47.01	0.272
2	45.569	0.278
3	48.147	0.292
4	48.133	0.288
5	47.722	0.288
6	46.137	0.277
7	46.553	0.278
8	47.862	0.288
9	47.814	0.284
10	49.326	0.235

Grade	POCO AXF-5Q	
Spec. No	Bend. Strength MPa	Fract. Deflexion mm
1	99.790	0.467
2	95.777	0.442
3	78.844	0.368
4	81.428	0.375
5	81.428	0.375
6	94.609	0.437
7	78.666	0.357
8	72.569	0.332
9	101.283	0.473
10	94.127	0.443

Tab. 21: Bending strength and fracture deflexion measured on individual specimens

Grade	Carbone-Lorraine 5890/PT Parallel to grain orientation	
Spec. No	Bend. Strength MPa	Fract. Deflexion mm
1	55.703	0.327
2	57.002	0.328
3	51.532	0.311
4	46.001	0.278
5	52.794	0.309
6	52.338	0.312
7	49.150	0.297
8	55.000	0.330
9	55.563	0.330
10	54.122	0.320

Grade	Carbone-Lorraine 5890/PT Perpendicular to grain orientation	
Spec. No	Bend. Strength MPa	Fract. Deflexion mm
1	44.601	0.282
2	37.878	0.249
3	40.888	0.267
4	43.975	0.287
5	46.770	0.299
6	43.842	0.288
7	44.721	0.292
8	42.710	0.284
9	42.185	0.277
10	41.384	0.279

Tab. 22: Bending strength and fracture deflexion measured on individual specimens

Grade	Morganite EY-306	
Spec. No	Bend. Strength MPa	Fract. Deflexion mm
1	39.684	0.237
2	39.292	0.233
3	38.925	0.233
4	29.289	0.173
5	34.601	0.203
6	39.468	0.228
7	36.239	0.217
8	36.761	0.215
9	38.942	0.236
10	37.465	0.220

Grade	Schunk FP-219	
Spec. No.	Bend. Strength MPa	Fract. Deflexion mm
1	28.525	0.230
2	30.134	0.242
3	30.349	0.251
4	29.025	0.237
5	31.568	0.257
6	28.992	0.235
7	29.993	0.245
8	29.o25	0.241
9	29.332	0.247
10	31.190	0.255

Tab. 23: Bending strength and fracture deflexion measured on individual specimens

Grade	Anglo Great Lakes H-490 Parallel to grain orientation	
Spec. No	Bend. Strength MPa	Fract. Deflexion mm
1	23.522	0.177
2	33.279	0.248
3	38.586	0.283
4	37.948	0.284
5	33.904	0.250
6	35.104	0.264
7	33.421	0.252
8	34.298	0.260
9	34.233	0.268
10	32.054	0.241

Grade	Anglo Great Lakes H-490 Perpendicular to grain orientation	
Spec. No	Bend. Strength MPa	Fract. Deflexion mm
1	30.215	0.243
2	30.577	0.252
3	29.326	0.238
4	32.217	0.259
5	29.441	0.252
6	32.713	0.275
7	31.538	0.264
8	31.162	0.267
9	30.952	0.258
10	30.202	0.247

Tab. 24: Bending strength and fracture deflexion measured on individual specimens

Grade	Dunlop E 5923 P Laminate perpendicular to load	
Spec. No	Bend. Strength MPa	Fract. Deflexion mm
1	73.875	0.307
2	56.507	0.243
3	79.818	0.228

Grade	Dunlop E 5923 P Laminate perpendicular to load	
Spec. No	Bend. Strength MPa	Fract. Deflexion mm
1	49.790	0.283
2	42.919	0.241
3	57.974	0.333
4	48.206	0.250
5	67.092	0.322
6	66.876	0.325
7	61.979	0.297

Tab. 25: Bending strength and fracture deflexion measured on individual specimens of carbon fibre composite

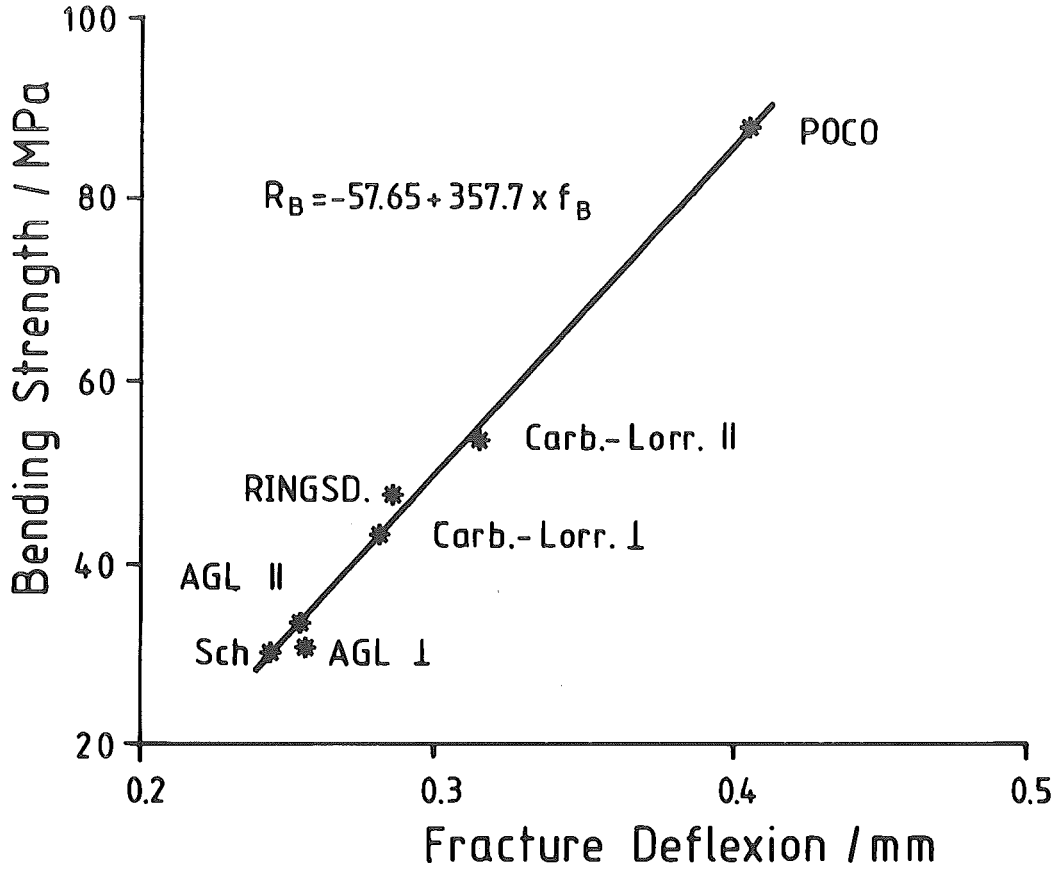

Fig. 14: Correlation between mean values of fracture deflexion and bending strength for various grades of graphite

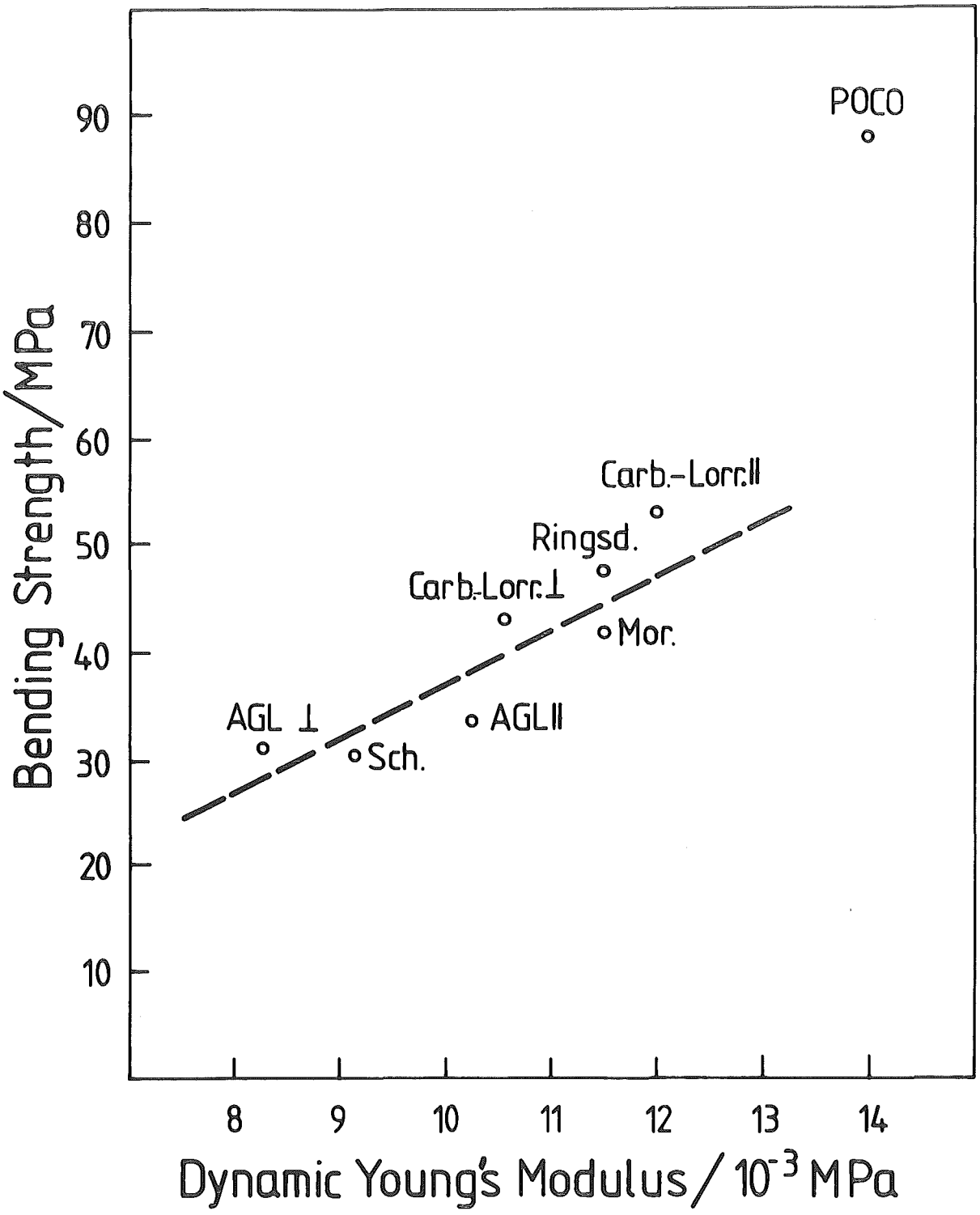

Fig. 15: Correlation between bending strength and dynamic Young's modulus for various grades of graphite

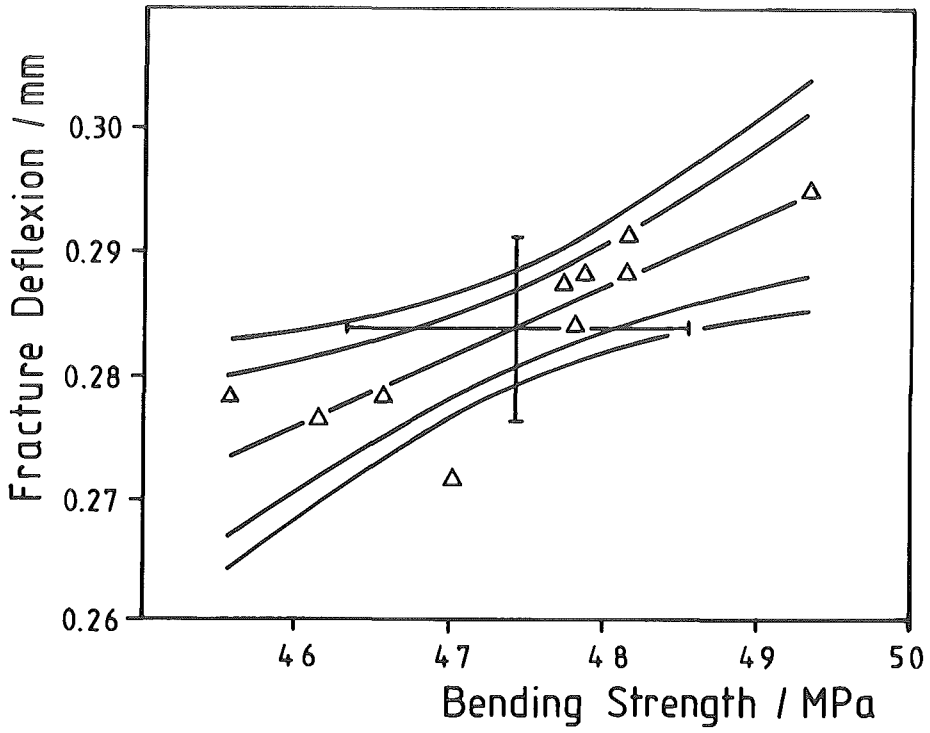

Fig. 16: Correlation between bending strength and fracture deflexion with confidence intervals of 99 and 95 % for intervals of expectation Ringsdorff EK 98

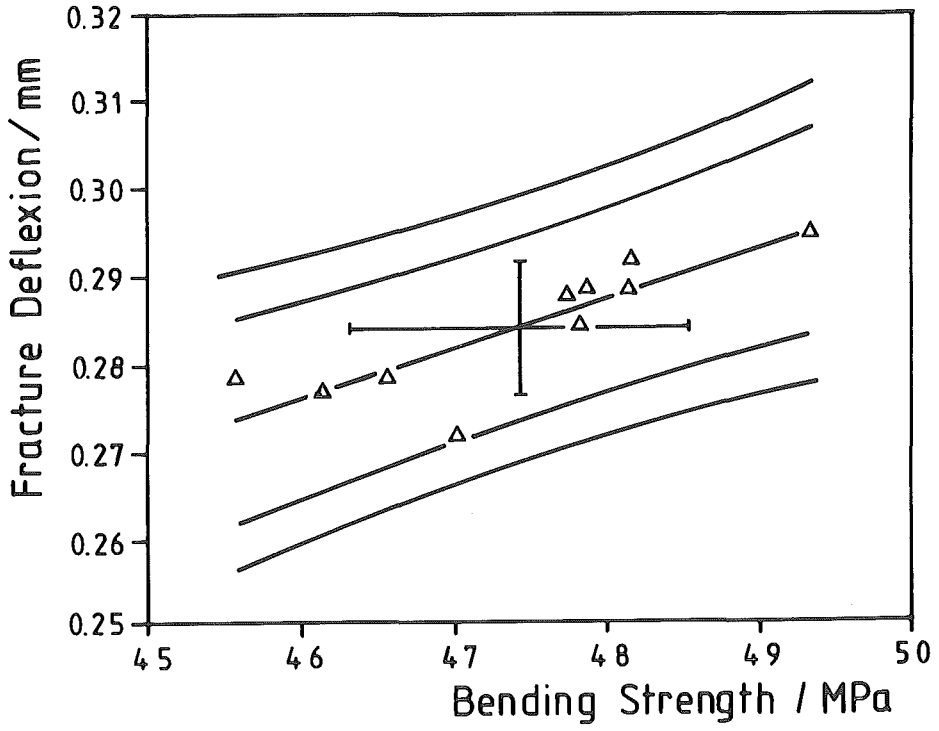

Fig. 17: Correlation between bending strength and fracture deflexion with confidence intervals of 99 and 95 % for intervals of prediction Ringsdorff EK 98

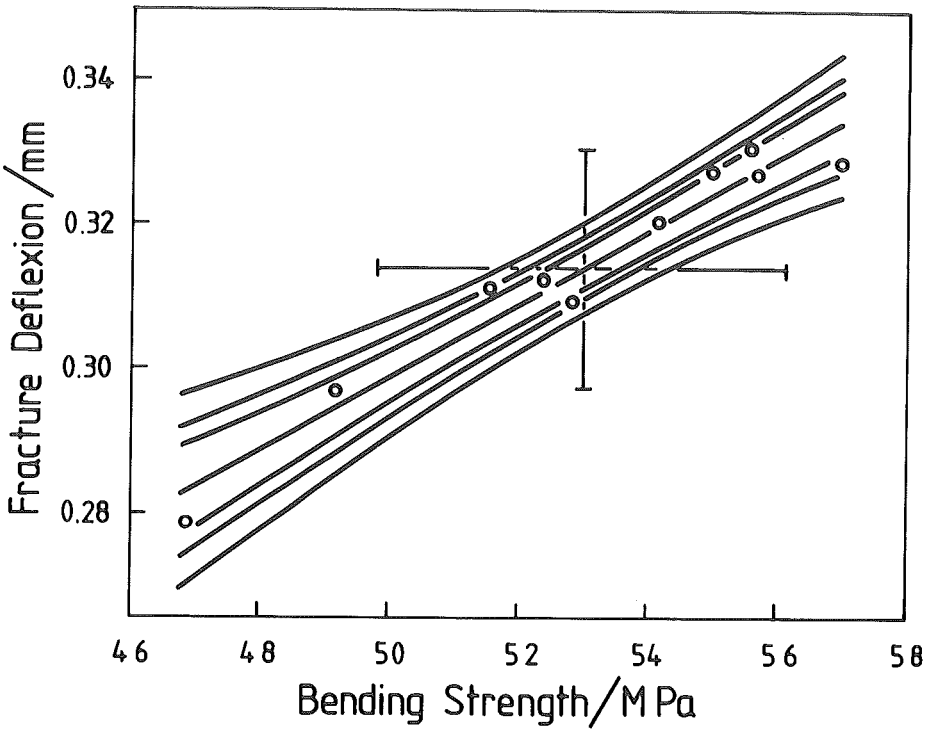

Fig. 18: Correlation between bending strength and fracture deflexion with confidence intervals of 99.9, 99 and 95 % for intervals of expectation
Carbone-Lorraine 5890/PT parallel to grain orientation

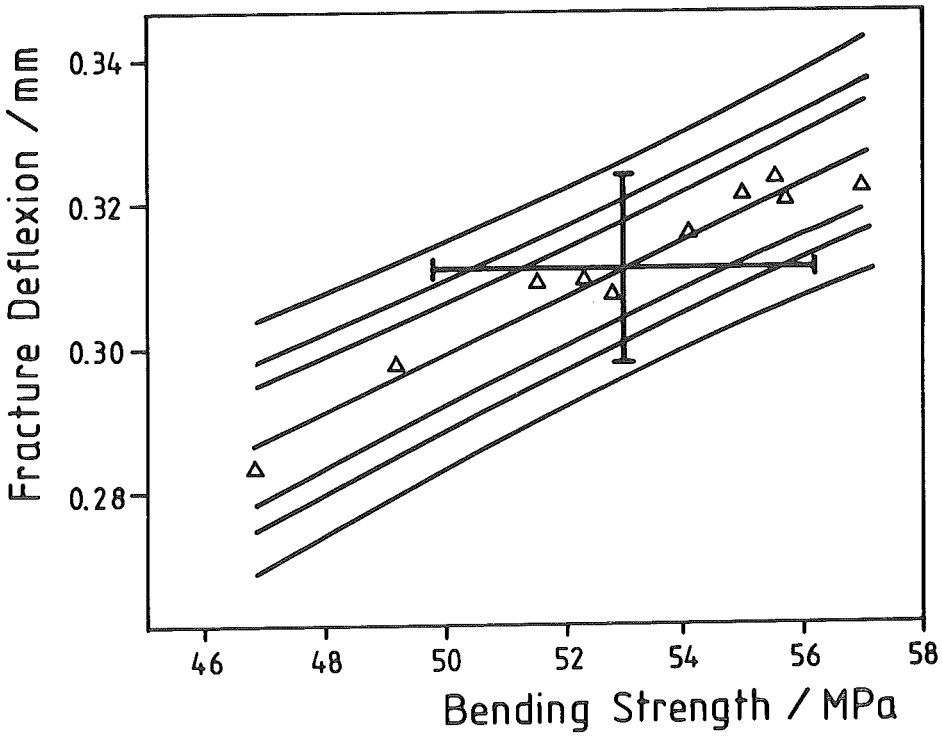

Fig. 19: Correlation between bending strength and fracture deflexion with confidence intervals of 99.9, 99 and 95 % for intervals of prediction
Carbone-Lorraine 5890/PT parallel to grain orientation

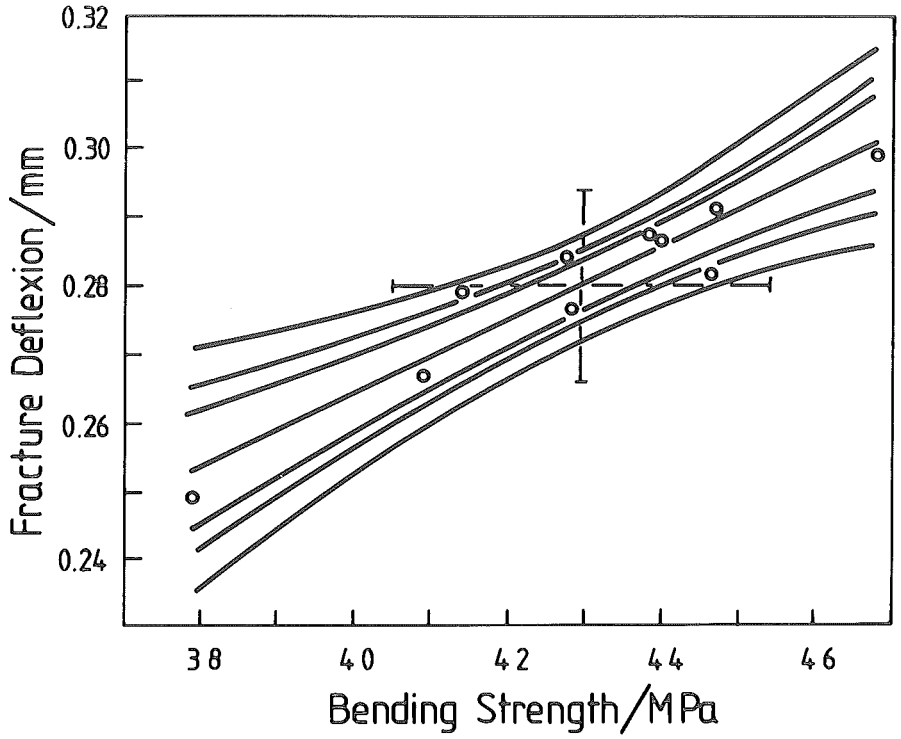

Fig. 20: Correlation between bending strength and fracture deflexion with confidence intervals of 99.9, 99 and 95 % for intervals of expectation
Carbone-Lorraine 5890/PT perpendicular to grain orientation

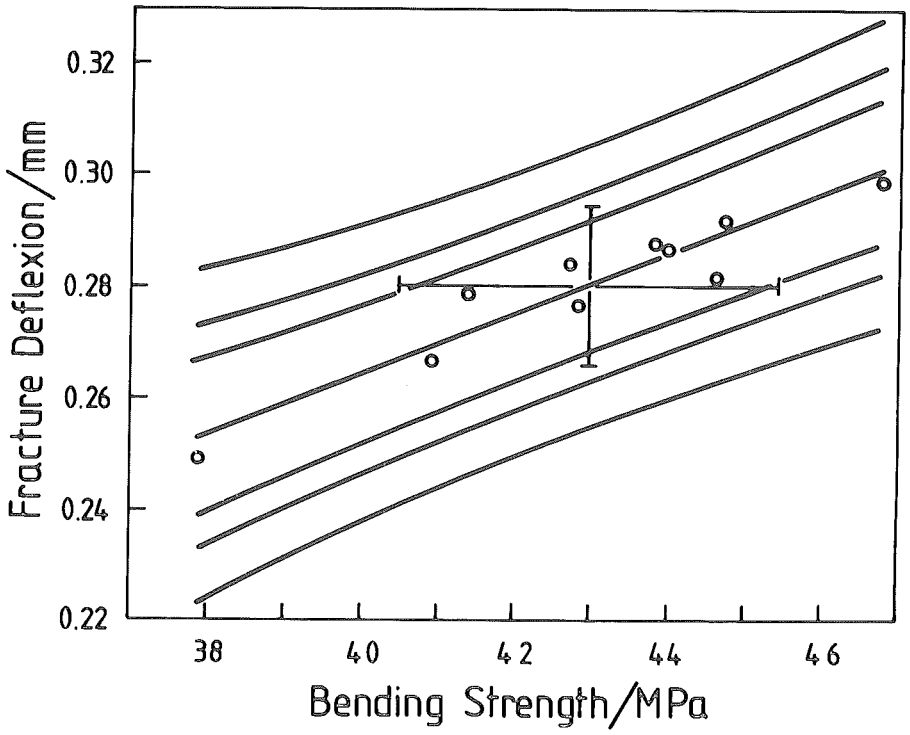

Fig. 21: Correlation between bending strength and fracture deflexion with confidence intervals of 99.9, 99 and 95 % for intervals of prediction
Carbone-Lorraine 5890/PT perpendicular to grain orientation

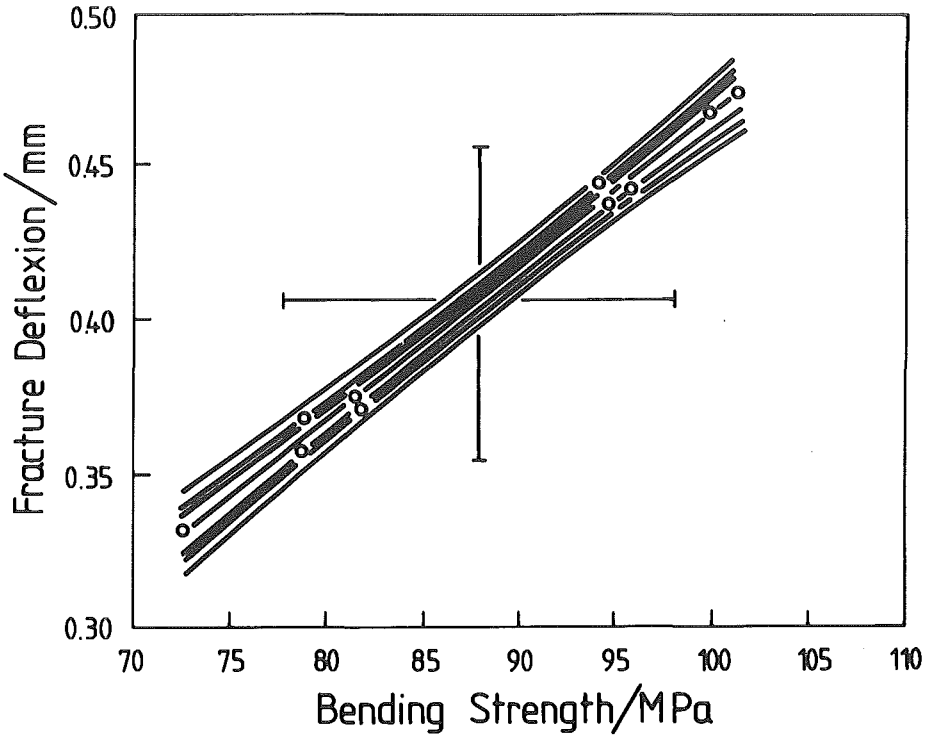

Fig. 22: Correlation between bending strength and fracture deflexion with confidence intervals of 99.9, 99 and 95 % for intervals of expectation
POCO AXF-5Q

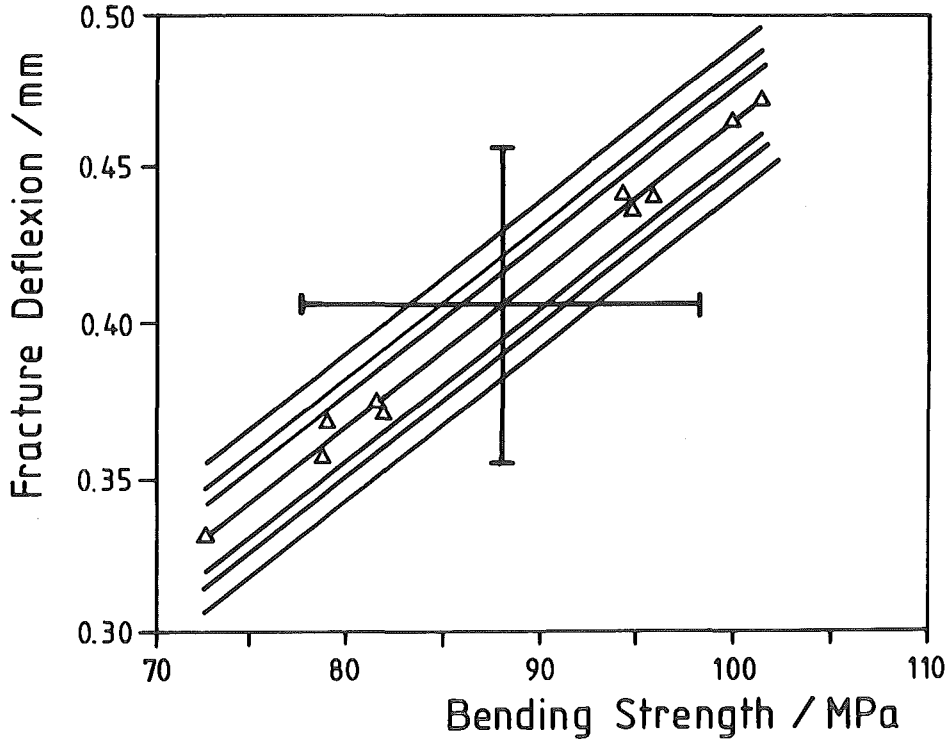

Fig. 23: Correlation between bending strength and fracture deflexion with confidence intervals of 99.9, 99 and 95 % for intervals of prediction
POCO AXF-5Q

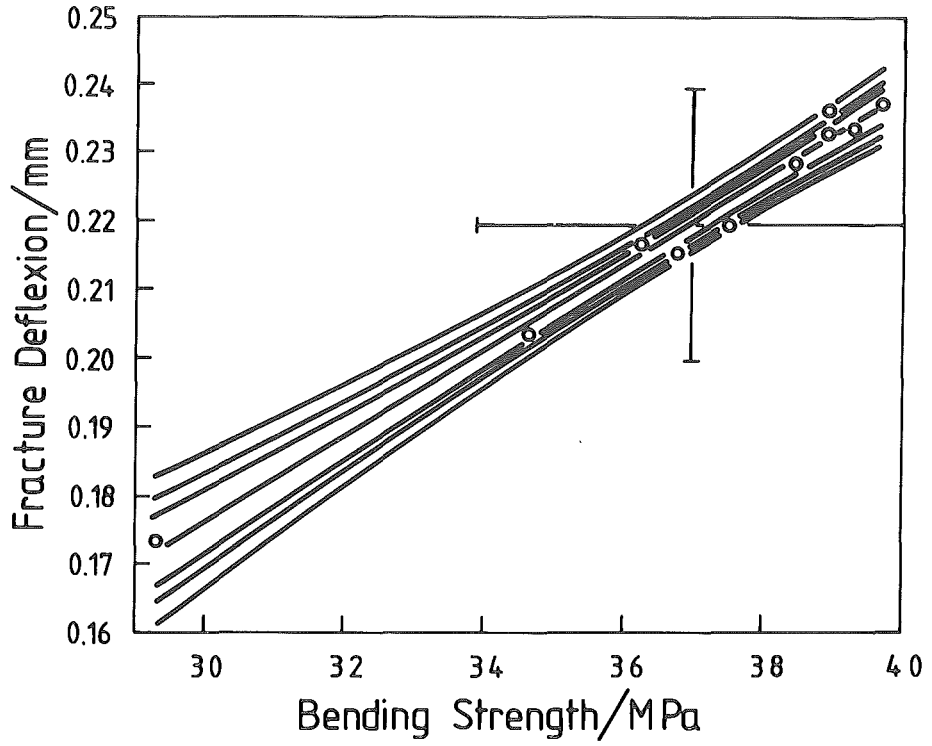

Fig. 24: Correlation between bending strength and fracture deflexion with confidence intervals of 99.9, 99 and 95 % for intervals of expectation
Morganite EY-306

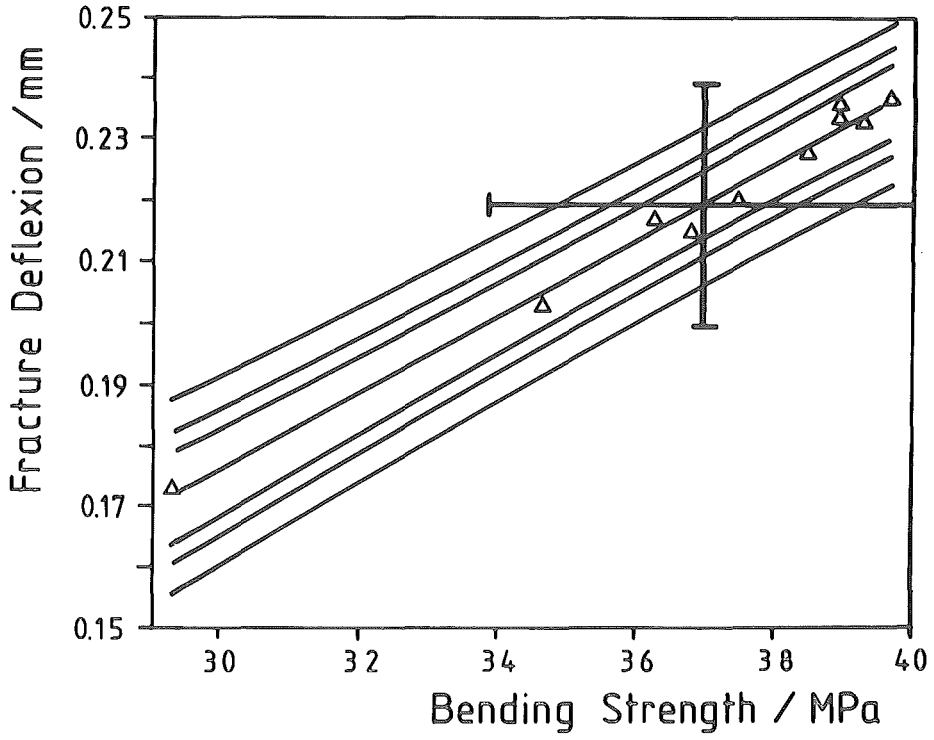

Fig. 25: Correlation between bending strength and fracture deflexion with confidence intervals of 99.9, 99 and 95 % for intervals of prediction
Morganite EY-306

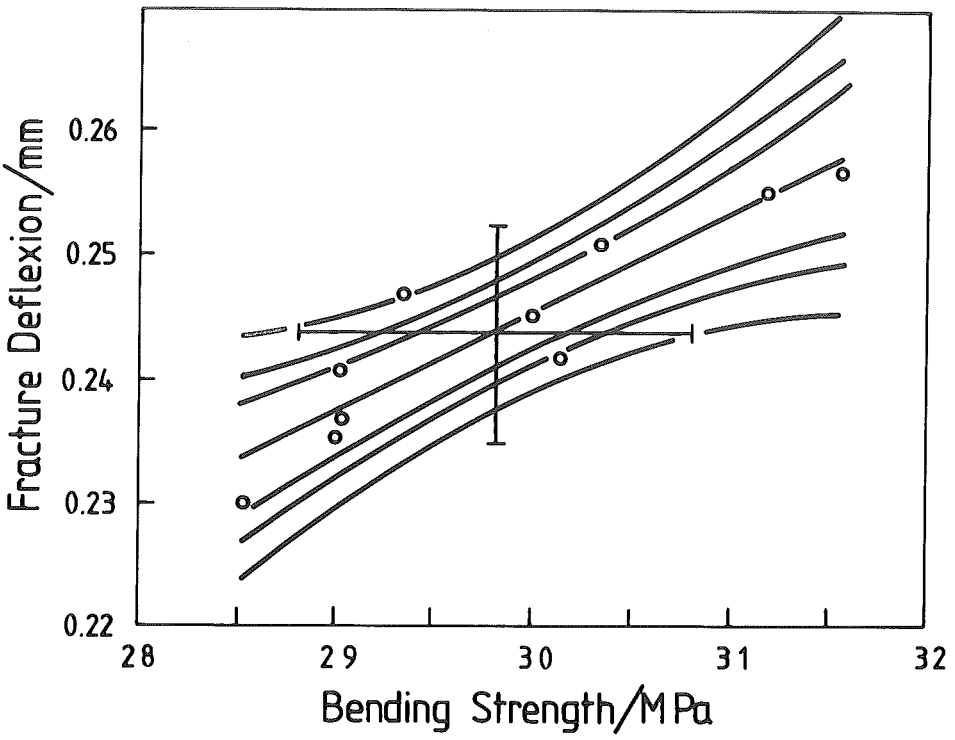

Fig. 26: Correlation between bending strength and fracture deflexion with confidence intervals of 99.9, 99 and 95 % for intervals of expectation
Schunk FP 219

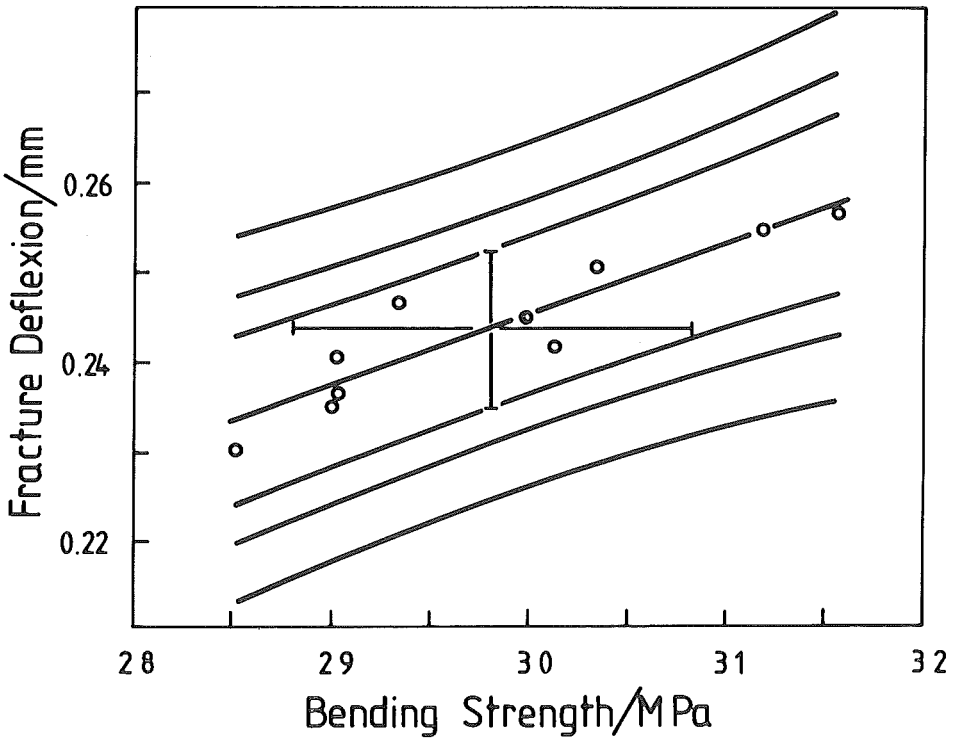

Fig. 27: Correlation between bending strength and fracture deflexion with confidence intervals of 99.9, 99 and 95 % for intervals of prediction
Schunk FP 219

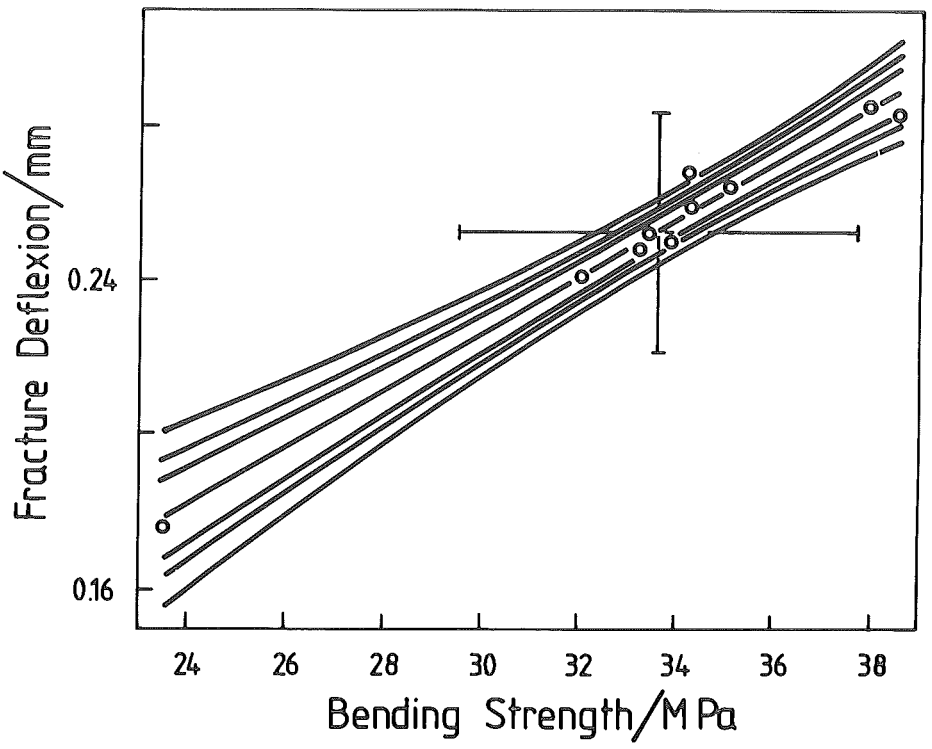

Fig. 28: Correlation between bending strength and fracture deflexion with confidence intervals of 99.9, 99 and 95 % for intervals of expectation
Anglo Great Lakes H-490 parallel to grain orientation

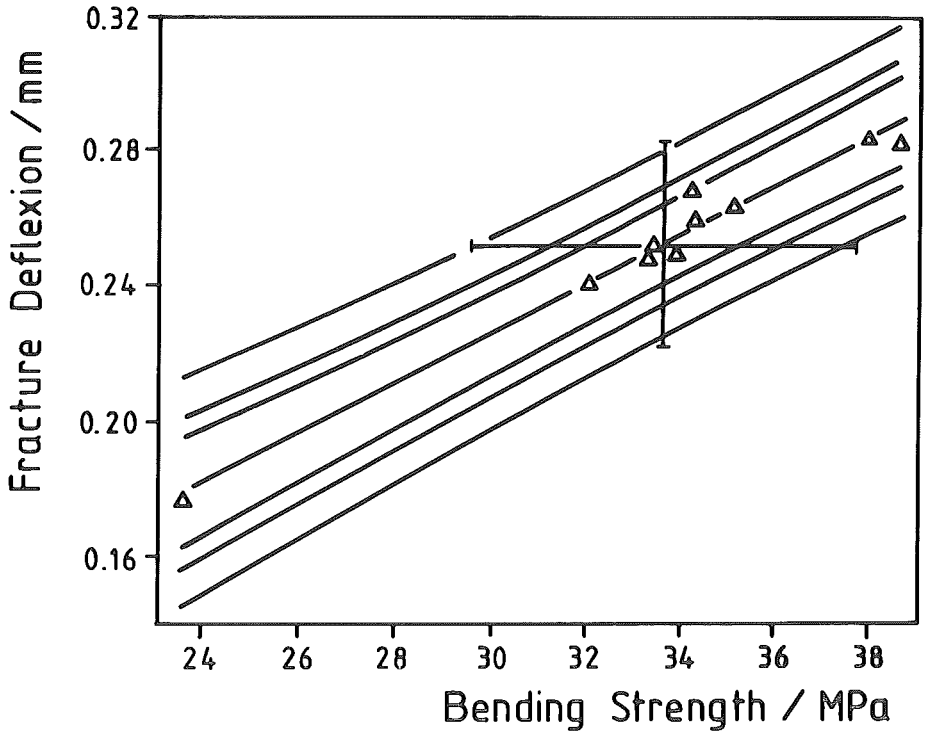

Fig. 29: Correlation between bending strength and fracture deflexion with confidence intervals of 99.9, 99 and 95 % for intervals of prediction
Anglo Great Lakes H-490 parallel to grain orietation

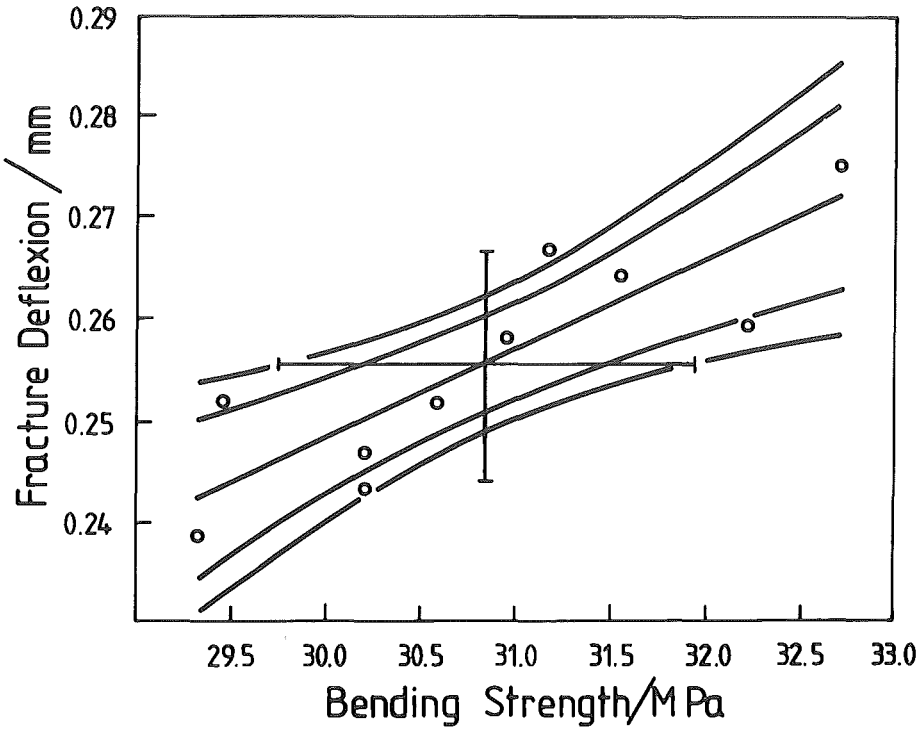

Fig. 30: Correlation between bending strength and fracture deflexion with confidence intervals of 99 and 95 % for intervals of expectation Anglo Great Lakes H-490 perpendicular to grain orientation

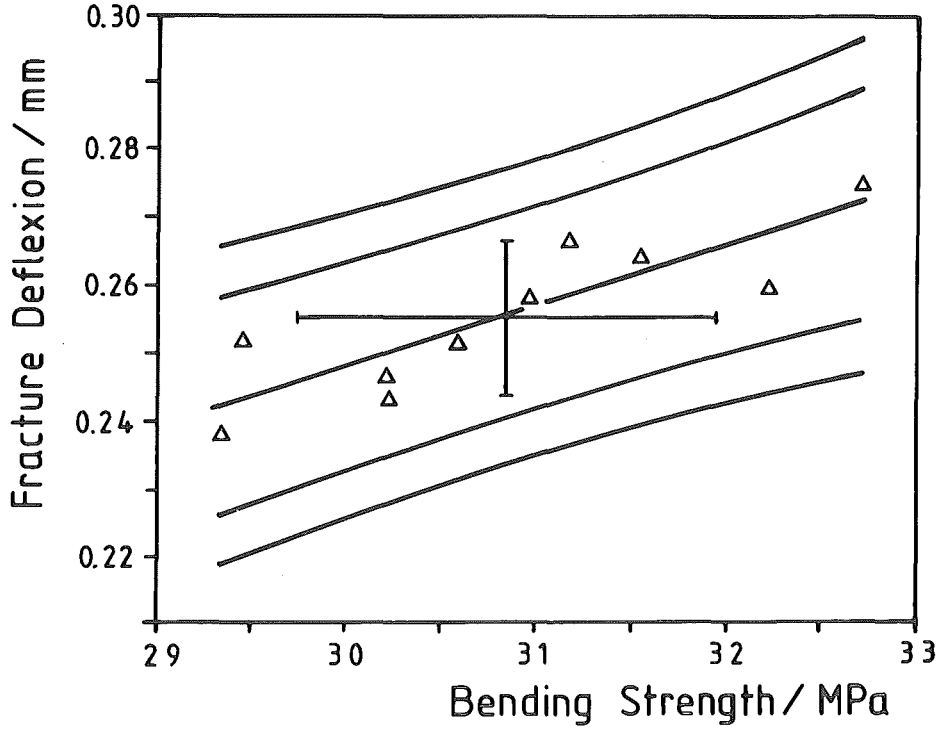

Fig. 31: Correlation between bending strength and fracture deflexion with confidence intervals of 99 and 95 % for intervals of prediction Anglo Great Lakes H-490 perpendicular to grain orientation

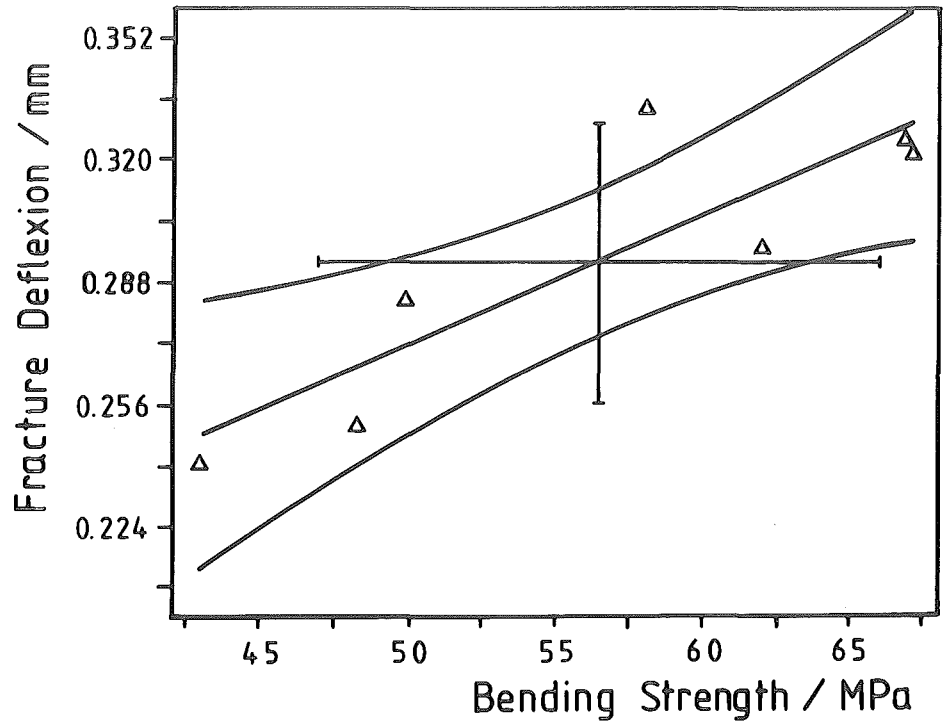

Fig. 32: Correlation between bending strength and fracture deflexion with confidence interval of 95 % for interval of expectation
Dunlop Carbon Fibre Composite E 5923 main laminate orientation perpendicular to direction of load

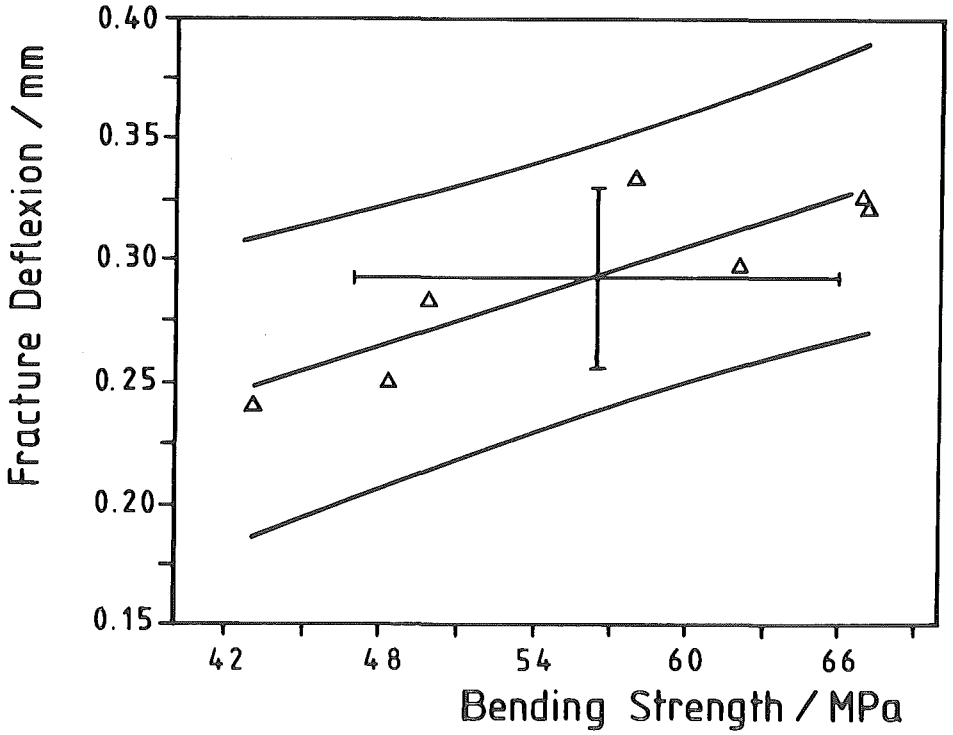

Fig. 33: Correlation between bending strength and fracture deflexion with confidence interval of 95 % for interval of prediction
Dunlop Carbon Fibre Composite E 5923 main laminate orientation to direction of load

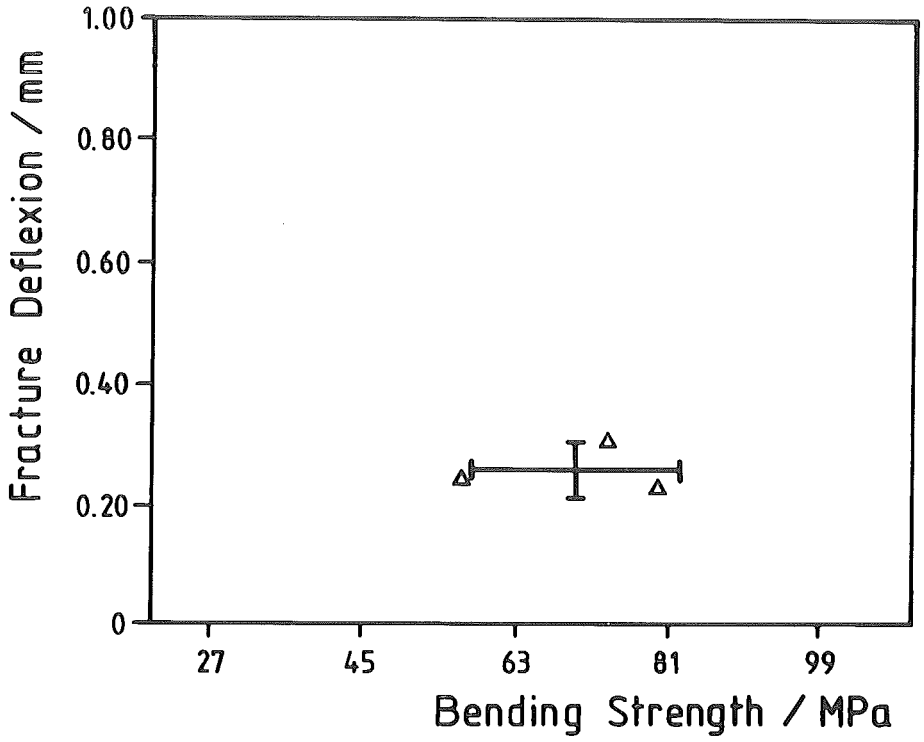

Fig. 34: Correlation between bending strength and fracture deflexion with confidence interval of 95 % for interval of expectation Dunlop Carbon Fibre Composite E 5923 main laminate parallel to direction of load

3.1.7 Summary

One of the purposes of this work was the comparison of property values which are presented in data sets provided by the producers with those measured in the frame of this study.

Significant differences were found in density values for POCO AXF-5Q (tab. 4) and Union Carbide ATJ (tab. 8). While the measured densities of the POCO material was lower than that in the data set, the measured values for the Union Carbide graphite were significantly higher than those in the data set. It seems that ATJ has been improved because all the other properties were changed as a consequence of densification: Porosity and electrical resistivity were decreased, whereas coefficient of thermal expansion (CTE), thermal conductivity and Young's modulus were increased.

There are difficulties in comparing the CTE-values because some producers do not inform about the temperature range applied. All values for thermal conductivity supplied by the producers have been measured at room temperature, whereas KFA started high-temperature investigations at 100°C. Thus, the results of KFA must be lower than those of the manufacturers. This fits well with the only exception of ATJ, surely due to the improvement of the material mentioned above.

Graphite grade	Density/g cm^{-3}		Total porositiy/V–%		Open porosity/V–%		El. resistivity/Ωmm^{2}m^{-1}		CTE/10^{-6}K^{-1}		Thermal cond./W/cmK		Joung's mod./κNmm^2		Bending str./MPa	
	data set	measured	data set	measured	data set	measured	data set[3]	measured[4]	data set	measured	data set[3]	measured[4]	data set	measured	data set	measured
Ringsdorff EK 98	1.85	1.86	–	18.0	–	8.2	13	17.2	3.8[1]	3.4[2]	0.90	0.69	10	11.5	50	47
Carbone-Lorr. 5890/PT II	1.81	1.79	20	21.0	–	11.1	12.5	16.2	5.0	4.5	0.96	0.75	14.5	12.1	56	53
Carbone-Lorr. 5890/PT ⊥							14.5	17.4	5.3	5.0	0.65	0.73	12.5	10.8	51	43
POCO AXF-5Q	1.83	1.78	19	21.5	14.8	18.1	14.8	18.8	8.4[5]	9.2[5] 8.4[2]	1.20	0.63	11.0	13.9	90	88
Morganite EY-306	1.80[7]	1.75	20.6[7]	22.8	14[7]	17.6	–	18.7	4.9	5.7[2]	0.75	0.71	11.8	11.5	59	37
Schunk FP 219	1.73	1.76	23.7	22.4	13	13.7	19	18.4	4.0[5]	4.3[5] 3.1[2]	0.75	0.68	9.0	9.1	36	30
Schunk FE 289	1.78	1.79	21.5	21.0	11	15.2	13	15.6	3.6[5]	5.9[5]	1.00	0.81	10.0	–	42	–
Anglo Great Lakes H-490 II	1.78	1.80	21.5	20.6	–	13.2	12	11.9	2.8[6]	3.2[2]	1.11	1.04	11.1	10.3	33	31
Anglo Great Lakes H-490 ⊥								14.1		4.2[2]	1.11	0.93	11.1	8.3	33	34
Union Carbide ATJ II	1.74[7]	1.81	23.2	20.2	–	11.5	10.5[7]	9.0	2.1[7]	2.3[2]	1.20	1.33	10.4[7]	13.5	30[7]	–
Union Carbide ATJ ⊥							14.3[7]	12.1	3.5[7]	4.1[2]	0.92	0.93	7.7[7]	9.3	25[7]	–

1) 20 – 200° C
2) 20 – 400° C
3) at room temperature
4) at 100° C
5) 20 – 1000° C
6) 0 – 50° C
7) JET information

Table 26: Comparison of property values provided by data sets of the producers with those measured in the frame of this study

3.2 Determination of Impurity Contents

For the determination of impurities in the graphite grades delivered by the producers, various analytical methods were used. Spark source mass spectrometry (SSMS) was applied to detect reliably all elements with detection limits smaller than 1 ppm. The pre-selected range of elements was between masses of 10 (Boron) and 240 (Uranium). That means that hydrogen, lithium and beryllium were not measured. Solid samples were used for the investigations and no chemical preparation was necessary, but mechanical machining. The disadvantage of this method is its insufficient accuracy. To improve the accuracy of the results of SSMS, optical atom emission spectrometry with excitation in an inductively coupled plasma (OES-ICP) was used. This method rendered the simultanious detection of about 45 elements including all which were found with SSMS. Soluted samples were necessary for OES-ICP. In the case of graphite, a mechanically prepared piece of material was burnt to ash and the ashes were decomposed by $Li_2B_4O_7 + LiBO_2$.
The detection limit of most elements is in the range of ppm and smaller. The accuracy is sufficient for such elements for which a calibration has been carried out.

In addition to the multi-element analytical methods mentioned, sulfur was detected by the classical method of burning to SO_2 and application of infrared.

The results of impurity determination are listed up in tables 27 to 34. As far as the contents of impurities were available, a number of differences could be found.

The ash contents of Carbone-Lorraine 5890/PT (tab. 28) and Anglo Great-Lakes H-490 (tab. 30) were much higher than presented in the data sheets, given by the manufacturers, whereas those of Ringsdorff EK 98 were lower (tab. 31). Ashes found in POCO AXF-5Q were lower for the standard quality and significantly higher for the purified version following the information from the data set.

The deviations in particular can be taken from tables 27 to 31.

Specimen	A	B	C	Data set
B	1	1	1	
Mg	1	1	1	
Al	2	2	5	
Si	4	4	4	
S	8	15	15	
Cl	5	2	5	
Ca	25	25	80	
Ti	2	2	4	
V	25	25	60	
Cr	2	1	5	
Fe	30	25	60	
Co	2	1	1	
Ni	15	20	60	
Sr	1	1	6	
Mo	2	2	2	
Ba	3	1	20	
La	1	1	1	
Ashes calculated	150	161	401	Standard: 700
Ashes found	150	180	405	Purified: < 5

Tab. 27: Results of chemical analysis of POCO AXF-5Q, impurities in ppm weight

Specimen	A	B	C	Data set
B	1	1	2	< 2
Mg	1	1	1	0 - 5
Al	2	3	2	0 - 5
Si	1	2	1	0 - 5
S	40	40	25	-
Cl	1	1	1	< 20
Ca	1	1	1	-
Ti	3	3	3	-
V	290	260	220	~ 4
Cr	1	1	1	$\sim 10^{-2}$
Fe	9	8	5	0 - 5
Ni	1	1	1	0.1 - 2
Mo	1	1	1	< 1
Ba	1	1	1	$< 0.5 \cdot 10^{-1}$
La	1	1	1	$0.11 \cdot 10^{-1}$
Ashes calculated	530	480	400	< 20
Ashes found	600	680	540	

Tab. 28: Results of chemical analysis of Carbone-Lorraine 5890/PT, impurities in ppm weight

Specimen	A	B	C	Data set
B	2	1	1	
Mg	1	1	1	
Al	1	1	1	
Si	5	5	6	
S	25	25	15	
Cl	1	1	1	
Ca	10	15	10	
Ti	25	30	25	
V	10	10	10	
Fe	6	5	6	
Cr	1	1	1	
Mo	20	20	20	
Ba	1	2	2	
La	1	1	1	
Ashes calculated	90	99	84	< 50
Ashes found	100	150	100	

Tab. 29: Results of chemical analysis of Schunk FP 219, impurities in ppm weight

Specimen	A	B	Data set
B	1	1	
Mg	1	3	
Al	50	40	
Si	20	25	
S	30	35	
Cl	2	2	
Ca	250	250	
Ti	15	15	
V	190	200	
Cr	35	15	
Fe	540	380	
Co	2	1	
Ni	35	25	
Sr	5	5	
Mo	2	2	
Ba	8	9	
La	3	5	
Ce	3	1	
Ashes calculated	1730	1480	0.5
Ashes found	1960	1510	

Tab. 30: Results of chemical analysis of Anglo Great Lakes H-490, impurities in ppm weight

Specimen	A	B	Data set
B	1	1	2 - 10
Mg	1	1	< 5
Al	1	1	2 - 10
Si	7	7	5 - 20
S	15	15	
Cl	1	1	
Ca	1	1	5 - 20
Ti	1	1	5 - 20
V	1	1	2 - 10
Fe	5	7	2 - 10
Cr	1	1	
Ni	1	1	
Ba	1	1	
Sr	1	1	
Mo	1	1	
Ashes calculated	28	40	< 150
Ashes found	50	50	

Tab. 31: Results of chemical analysis of Ringsdorff EK 98, impurities im ppm weight

Specimen	A	B	C
Al	31	31	28
Ba	0,72	1,3	0,84
Be	0,02	18,2*	0,03
Ca	18	15	10
Ce	0,5	0,5	0,5
Co	0,18	-	0,23
Cr	0,61	0,58	0,43
Fe	36,5	48,2	37,0
La	0,3	0,25	0,2
Mg	0,59	0,46	-
Mn	0,05	0,10	0,05
Mo	0,15	0,11	0,21
Ni	0,63	-	0,20
P	1,8	1,9	1,5
S	6	7	6
Si	0,14	0,14	0,14
Sr	0,42	0,39	0,58
Ti	4,1	3,9	3,6
V	0,95	0,78	1,2
Ashes calculated	209	326	235
Ashes found	247	361	268

* Addition of Be as an internal standard
Data set not available

Tab. 32: Results of chemical analysis of Morganite EY-306, impurities in ppm weight

Specimen	A	B	C
Al	6,8	12	9,6
Ba	9,1	9,3	9,0
Be	0,03	0,05	14,9*
Ca	73,2	159	100
Ce	1,7	0,43	1,6
Co	-	0,49	0,56
Cr	0,80	0,77	0,78
Fe	217	176	195
La	1,2	0,5	1,1
Mg	0,12	0,15	0,11
Mn	0,08	0,12	0,08
Mo	0,31	0,25	0,30
Ni	16,4	14,2	13,2
P	0,8	0,6	0,6
S	65	85	55
Si	28,0	10,9	15,9
Sr	2,4	3,3	2,2
Ti	3,9	7,9	4,4
V	5,8	28	5,4
Ashes calculated	584	663	576
Ashes found	580	761	695

*Addition of Beryllium as an internal standard

Data set not available

Tab. 33: Results of chemical analysis of Union Carbide ATJ, impurities in ppm weight

	Impurities				
Concentration/ppm	10-20	20-50	50-100	100-200	> 1000
POCO AXF-5Q	Ba S	-	Ca,V,Fe, Ni	-	-
Carbone-Lorraine 5890/PT	-	S	-	-	V
Schunk FP 219	Ca,V Mo	Ti S	-	-	-
Great-Lakes H-490	Ti	Al,Si, Cr,Ni S	-	V	Ca,Fe
Ringsdorff EK 98	S	-	-	-	-
Morganite EY-306	Ca	Al,Fe	-	-	-
Union Carbide ATJ	Si,Ni	-	S	Fe,Ca	-

Tab. 34: Impurities detected in various grades of graphite and arranged in five groups of concentrations. Considerable inhomogeneous impurity distributions were found in most of the materials.

3.3 Thermal Shock and High Heat Flux Testing

3.3.1 Introduction

Thermal shock and erosion experiments were carried out on several fine grain graphites from different manufacturers. In the set-up phase of the investigations described in this paper, only 6 various graphites were foreseen to be tested at 3 different heat load conditions with only 1 sample. In later stages, the number of graphites was increased to 8 plus an additional 2-dimensionally interweaved carbon fibre composite material (see table 1). Due to insufficient reproducibility, the number of electron beam experiments per graphite and heat load condition was increased to 4, at least for the 5.0 $kWcm^{-2}$ pulses of 1 s duration (see chapter 3.3.2), which turned out to be most sensitive to the type of material.

In a total, 4 series of experiments were carried out; due to delays in the delivery of the graphites to IRW, only the series 3 and 4 could be accomplished with the whole set of 9 materials. Table 35 gives a survey on the number of experiments in the different series. The sample-numbers are given in table 36. The carbon fibre composite material was tested in two different orientations ($\parallel \triangleq$ electron beam direction parallel to the 2 D-fibre plane; $\perp \triangleq$ electron beam direction vertical to the 2 D-fibre plane).

In order to test the reproducibility of the experiments, identical tests were performed on metal samples (stainless steel 1.4311).

Due to an unprecise adjustment of the electron beam in series 2, the resulting power density in these experiments differed from those in the other series. Therefore the results of series 2 were not taken into consideration.

3.3.2 Experimental equipment

The thermal shock/erosion experiments were carried out in a Leibold-Heraeus-electron beam welding machine (ESW 1000/15), fig. 35. The graphite samples with a size of 25 mm x 25 mm x 10 mm were exposed to a defocussed electron beam of 10 mm diameter. The manually adjusted beam-diameter was controlled by size measurements of the melting spot on stainless steel (1.4311) specimens which were exposed to a 262 mA electron pulse of 1 second duration

(electron energy = 150 keV). In addition, the resulting crater dimensions on identical materials (EK 98 was chosen for a reference) were compared applying the same heat load conditions.

The energy of the electrons was 150 keV; the electron beam was used in a static, i.e., in a not-scanned mode. In contrast to scanned electron beam devices for thermal shock testing, this operation mode guarantees a continuous power input to the surface of the test specimen. For the experiments described in this paper, power density values P/a = 3,5 $kWcm^{-2}$, P/a = 5.0 $kWcm^{-2}$ and P/a = 10 $kWcm^{-2}$ were selected. The value P/a only indicates the mean power density in the substrate surface. P/a does not represent a constant value across the beam diameter; it rather shows a nearly Gaussion distribution in the x- and y-direction, similar to that shown in fig. 36 for a focussed electron beam (5). The Gaussion distribution of the current density is only a rough approximation, since curves of constant current density (fig. 37) show a severe deviation from a circular shape. Similar behaviour was observed in the defocussed electron beam of the welding machine used for the experiments reported in this paper.

The above given P/a values were calculated on the assumption of a homogeneous energy profile across the beam diameter, i.e.,

$$P/a = \frac{4\ U \cdot I}{d^2}$$

where U (kV) = acceleration voltage
I (mA) = beam current
d (mm) = beam diameter.

Thus, the power density is given by the equation

$$P/a\ kWcm^{-2} = 0.191\ \ I\ (I/\ [mA]\ ),$$

when the assumption U = 150 kV and d = 10 mm is valide.

For all 4 series, the experimental procedure was as follows:

- sample preparation
  (manufacturing, polishing, marking of sample orientation)
- ultrasonic cleaning
  (in Inkibisol-solution)
- drying
  (1 h at 200°C)
- weight measurement
- electron beam thermal shock/erosion experiment
- measurement of weight loss
- optical examination and documentation
- scanning electron microscopy (using secondary electron (SE) and back-scatter electron (BE) detectors)
- sectionning of the sample along the maximum crater axis
- ceramographic preparation
- optical microscopy in polarized and not-polarized light.

All experiments carried out in the frame of the work summarized in this paper were single shot tests, i.e., thermal cycling effects remain disregarded.

3.3.3 Heat flux conditions

Beside the beam power density P/a the pulse duration Δt is the most important parameter. All experiments were carried out with the following heat flux conditions:

a) $P/a = 3.5\ kWcm^{-2}$; $\Delta t = 1.0$ s
b) $P/a = 5.0\ kWcm^{-2}$; $\Delta t = 1.0$ s
c) $P/a = 10\ kWcm^{-2}$; $\Delta t = 100$ ms.

The conditions a) and b) were chosen to simulate the material damage due to high particle fluxes from the JET neutral beam injectors when the plasma is absent. Since the time for the detection of such an accident is supposed to be relatively short so that the neutral beam can be switched off in less than 1 second, the experiments were carried out with a pulse length of 1 s.

The power density P/a = 3.5 $kWcm^{-2}$ was chosen in such a way, that the condition a) represents a threshold for material erosion and crack initiation. Increasing P/a to 5.0 $kWcm^{-2}$ with identical pulse lengths (Δt = 1 s) resulted in a significant erosion of the material; deviating resistances of the various materials against crack formation could be observed.

Condition c) was established to test the thermal shock behaviour of the material under plasma disruption events. 100 ms represent the lower limit in pulse duration for the test device used; short pulses could not be realized.

The reproducibility of the experiments was tested at P/a = 5.0 $kWcm^{-2}$ and Δt = 1.0 s by using stainless steel (1.4311) as a reference.

3.3.4 Results

3.3.4.1 Reproducibility

To investigate the reproducibility of the electron beam test, 12 specimens of a reference graphite (EK 98) were loaded with identical pulses (series 4). The weight losses Δm due to erosion of all these experiments are represented in fig. 38 (see also table 36): the mean Δm-value was found to be 1,80 mg; the difference of the individual experiments was significant and varied from 0,65 mg (sample-No. 11/65) to 3,85 mg (sample-No. 11/62), this covering a scatter of a factor about 6. Additional experiments on 10 reference samples in series 3 (see table 35) revealed a similar scatter (factor 7).

The above mentioned reproducibility tests on graphite were repeated under identical heat load condition (and identical beam adjustment) on 5 stainless steel samples. Here a mean weight loss of 22.2 mg was measured, thus representing an increase of approximately one order of magnitude compared to graphite. The scatter within the individual experiments (sample-No. M 14/5 through M 14/9, fig. 38) is reduced to less than 2 % of the mean value.

Hence the severe deviations in the weight loss measurements on graphite are not due to instabilities of the used electron beam device. The real source of these variations has not yet been analyzed; the following effects possibly influence the weight loss of the graphite samples:

- electrostatical charging of the graphite tiles due to the electron bombardment,
- outgassing of the graphites,
- discontinuous erosion of graphite due to its grain structure.

The discontinuous, flickering light emission during the electron beam pulse could be interpreted as a first hint that the third of the above mentioned processes is the dominent one. Electron beam experiments on metallic alloys in general show a continuous, stable light emission (during electron beam welding).

3.3.4.2 Crater dimensions and weight loss

An example for the macroscopical appearance of the graphite surfaces after exposure to an 5 $kWcm^{-2}/1.0$ s - electron beam shot is given in fig. 39 for all materials tested. As outlined in chapter 3.3.2 the resulting craters do not show a circular shape; deviations from circularity are different in the 4 test series. This misfit is due to difficulties in the adjustment of new cathodes.

In a first approximation the crater size is directly correlated to the weight loss of the samples.

In figs. 40 b and c as well as in the following graphical presentations, the carbon fibre composite material E-5923 P is shown in two different orientations:

E-5923 P ($\parallel$): electron beam direction parallel to the 2 D-fibre plane,

E-5923 P ($\perp$): electron beam direction vertical to the 2 D-fibre plane.

The fibres in the (⫴)-oriented sample are clearly visible in fig. 39 i.

Precise measurements on the amount of the eroded material were obtained by weighing on a micro balance before and after exposure to the beam. These results are shown in fig. 40 a through c for the series 1, 3 and 4. The comparison of the results of these three series shows, that there is no clear tendency: on the one hand, the absolute values of the eroded material differ between the experimental series (this might be due to the above mentioned difficulties in beam adjustment), on the other hand, the ratio of the eroded material from one grade of graphite to another is not constant for a few materials (e.g., 5890/PT and AXF-5Q). The latter effect might be due to inhomogenities in the material or to statistic variations of the results (see fig. 38).

A rather good reproducible tendency for the quantity of eroded material was found for the materials EK 98, EY-306, FP-219 and H-490 (in series 1, 3 and 4) as well as for ATJ and the carbon fibre composite material in both orientations (series 3 and 4). It should be noted that the parameter n in figs. 40 b and c indicates the number of experiments performed. At least 4 samples with identical heat load conditions (P/a = 5 kW cm^{-2}, Δt = 1 s) have been made available for all graphites.

3.3.4.3 Crack formation

To visualize the formation of cracks, all samples were inspected in a scanning electron microscope (SEM) using secondary electron (SE)- and backscatter electron (BE)-detectors. Cracks in general are better detectable in the BE-mode while topographical effects are clearly visuable in the SE-image. Figures 41 through 43 show the crater region for the materials tested in a typical experiment at a low magnification. Some selected high resolution SEM-images are shown in figs. 44, 45 and 46.

Beside the SEM-inspection, all samples were investigated by ceramographic methods: ceramographic sections were prepared along a plane vertical to the file surface cutting the crater along its maximum diameter. The resulting optical micrographs are shown in figs. 47 and 49 for the 5 $kWcm^{-2}$ - 1 s and the 10 $kWcm^{-2}$ - 0.1 s heat flux conditions, resp. High resolution micrographs of some minor cracks are given in figs. 48 and 50.

All results are summarized in fig. 51. Here an evaluation of the crack formation is presented in a schematic diagramme. The effect of crack formation was evaluated for all materials in all three series (1, 3 and 4) by SEM-images and by ceramographic sections according to the scale given in the caption of fig. 51:

- 0 = optimum thermal shock behaviour, no cracks detectable
- 4 = worst thermal shock behaviour, severe cracking.

To get an over all "factor of crack formation", F_{cf}, the mean value of the individual tests listed in fig. 51 was calculated. In the following, the behaviour of the various graphite qualities will be discussed briefly:

- EK 98, $F_{cf} = -2.3$

This material shows a very uniform, slight crack formation in all 3 series and for both heat loading conditions (see figs. 42 a, b, 43 a, b, 45 a, 47 a, 49 a). The crack depth is in the range of some hundred microns (fig. 48 a).

After a 3,5 $kWcm^{-2}$ - 1 s - heat pulse, the material surface does not show any effects, the weight loss (see table 35) is insignificant.

- 5890/PT, $F_{cf} = -1.8$

The F_{cf}-factor of this material is only slightly increased compared to EK 98, for both long- (1.0 s) and short (0.1 s)-term pulses. But in contrast to EK 98, the individual series yielded different results, i.e., in series 1 cracking was nearly not observable (fig. 43 c, d), whereas the series 3 and 4 revealed a crack behaviour similar to that of EK 98 (see figs. 42 c, d, 43 e, 45 b, 47 b, 49 b). These deviations in cracking behaviour for the 5890/PT graphite might possibly originate in slight differences in the power density profiles due to the above mentioned adjustment difficulties of the electron beam (see also graphite H-490).

The 3.5 $kWcm^{-2}$ - 1 s - pulses cause only a slight erosion of the graphite at the tiles surface (fig. 41 a). A SEM-image at a higher magnification is shown in fig. 44 a.

- AXF-5Q, F_{cf} = - 3.8

The material AXF-5Q shows the worst cracking behaviour of all graphites tested. In all samples which were analyzed by SEM or by ceramography, a severe cracking was found (figs. 42 e, 43 f). In contrast to all other samples tested, the ceramographic sections show cracks parallel to the crater surface (figs. 47 c, 49 c). These cracks might result in a very significant material erosion by the detachment of the overlying graphite if further electron beam loads would be applied to the sample.

No significant erosion effects are detectable when exposed to a 3.5 $kWcm^{-2}$ - 1 s - electron beam pulse. Reasons for the relativly poor thermal-shock resistance of the AXF-5Q graphite seem to be the extremly high values for the coefficient of thermal expansion compared to the other graphites (see fig. 55) and for the Young's modulus (see fig. 53). On the other hand, a very high bending strengh was measured for this material. Thermal conductivity (fig. 52) and macroporosity (fig. 57) show values similar to those of the other graphite qualities. The mean size of the macropores (fig. 56) is small compared to that of the other materials.

- EY-306, F_{cf} = - 3.1

Graphite grade EY-306 is another material which shows a relatively large scatter in the individual results of crack behaviour. But - compared to 5890/PT - the over all crack formation factor, F_{cf}, is significantly smaller: F_{cf} = - 3.1 (see figs. 42 f, 43 g, h, 45 e, 47 d, 49 d).

Even after exposure to low power density pulses (3.5 $kWcm^{-2}$ - 1 s), the material shows crack initiation (fig. 41 b). Fig. 44 b shows a high magnification image of this crack.

A correlation of the relatively poor crack resistance of this material with the characterization data (figs. 52 through 57) is impossible.

- FP-219, F_{cf} = - 0.4

The FP-219 (together with the carbon fibre composite material) shows the best thermal shock resistance of all graphites tested. Neither in SEM-images (figs. 42 g, h, 43 i, 45 f), nor in the ceramographic sections (figs. 47 e and 49 e), any significant cracking could be observed.

The 3.5 $kWcm^{-2}$ - 1 s - pulses show slight erosion effects at the substrate surface (fig. 41 c). Fig. 44 c shows the eroded area at a higher magnification.

A comparison with other graphites shows that this material has relatively low values of the Young's modulus (fig. 53) and a low coefficient of thermal expansion (fig. 55). This could be interpreted as one reason for the good thermal shock resistance of this material.

- H-490, F_{cf} = - 2.0

The graphite H-490 again is a material which shows no uniform thermal shock behaviour in all series: Here the pulses of series 1 have caused the most significant damage. On the other hand, the erosion and cracking behaviour from series 3 and 4 is similar to that of FP-219 or ATJ. The SEM-images from series 3 are shown in figs. 42 i, 43 j, k. Fig. 45 g gives a high magnification image of a crack found on a tile from series 1.

Figs. 47 f and 49 f represent the ceramographic sections (series 3) - here also no cracks could be found.

3.5 $kWcm^{-2}$ - 1 s - pulse do not result in any detectable erosion or cracking of the material.

- ATJ, F_{cf} = - 0.5

The ATJ material (which was added to the test-materials in a later stage - thus it was only present in series 3 and 4) turned out to have a shock resistance similar to FP-219 (or the carbon fibre material). Only a single crack was found on one SEM-image from series 3 (fig. 43 l). All other SEM-nalysis (see fig. 42 j) and the ceramographic sections did not reveal any cracks (figs. 47 g, 49 g).

The surface of the sample loaded by the 3.5 $kWcm^{-2}$ - 1 s - pulse shows slight erosion effects but no cracking (fig. 41 d).

- FE-289, F_{cf} = - 2.6

The crack formation of this material due to high heat fluxes is similar to that of EK 98 (slightly worse). Cracks are observable in both, the SEM-images (figs. 42 k, l, 43 m, n, 45 i, 46 b) and in the ceramographic sections (figs. 47 h, 49 h, 50 a).

Erosion due to the 3.5 $kWcm^{-2}$ - 1 s - electron beam pulse (series 3) is clearly visuable.

- E-5923 P, F_{cf} = 0...- 0.2

Compared to most of the fine grain graphites, the carbon fibre composite material E-5923 P shows a significantly different behaviour in the thermal shock experiment. According to fig. 51, the evaluation of crack formation reveals a good behaviour ($F_{cf} \approx 0$). It should be noted, that for this material only cracks which destroy the fibre structure were taken into account. Some inter-fibrous cracks (see fig. 48 c) were detected; possibly they originate from the manufacturing process.

In general, the craters are larger for samples of the ($\perp$)-orientation (see weight losses in figs. 40 b, 40 c and figs. 42 m, n, 43 o, p, 47 i, j, 49 i, j).

3.5 $kWcm^{-2}$ - 1 s - pulses (figs. 41 f, 44 d) show a slight erosion of the matrix material; the carbon fibres remained undamaged for the most part.

3.3.4.4 Structure of the eroded surface

The appearance of the graphite surfaces after electron bombardment depends strongly on the grain structure of the individual qualities. In figs. 44 through 46 examples for the eroded surface structures are given.

Fig. 44 shows high magnification SEM-images of graphites after a 3.5 $kWcm^{-2}$ - 1 s - heat pulse. In the micrographs only those samples which reveal a significant erosion (see chapter 3.3.4.3) are shown. The grain structure can be clearly seen since the binder-material was removed during the electron beam pulse. For the examples given here, the grain size increases from 5890/PT (fig. 44 a) via EY-306 (fig. 44 b) to FP-219 (fig. 44 c). The fibres of the E-5923 P-material (fig. 44 d) were only etched at the outermost ends.

Similar results were obtained at the 5.0 $kWcm^{-2}$ - 1 s - electron beam pulse. The materials discussed in fig. 44 reveal a similar grain size (figs. 45 b, e, f). The grain size of the EK 98-graphite (fig. 45 a) is comparable to that of 5890/PT. The materials H-490 (fig. 45 g) and ATJ (fig. 45 h) show a somewhat higher grain size. These grains are slightly plate-shaped. The grain size of the FE-289 material (fig. 45 i) is in the range of the FP-219 material (identical manufacturer).

It should be noted that in general the structure of all these graphites appears similar with the exception of the AXF-5Q-graphite (figs. 45 c, d). The grain size of this material is by approximately one order of magnitude smaller; at lower magnifications this material shows a dimple-like etching structure (see fig. 45 c). This effect might be due to the binder coke-free structure of this graphite quality in comparison to all other materials tested.

The carbon fibre composite material shows etching effects only at the fibre tips (figs. 45 k, l); fibres oriented vertically to the electron beam are reduced in diameter (fig. 45 j).

Under thermal shock heat load conditions of 10 $kWcm^{-2}$ for very short pulse lengths (Δt = 100 ms), the surfaces of the eroded graphites show different structures at very high magnifications (V = 1000...2000 x). The surface of ATJ (fig. 46 a) or FE-289 (fig. 46 b) seems to be coated with a new carbon modification, probably with pyrocarbon. Similar material deposits were observed on the E-5923 P material (figs. 46 c, d).

3.3.4.5 Summary

Thermal shock resistance of eight various fine grain graphites was tested in single shot experiments in an electron beam welding machine. In addition to this, a carbon fibre composite material was tested. All tests were performed under 3 different heat load conditions:

$P/a = 3.5\ kWcm^{-2}$ - $\Delta t = 1.0$ s,
$P/a = 5.0\ kWcm^{-2}$ - $\Delta t = 1.0$ s,
$P/a = 10\ kWcm^{-2}$ - $\Delta t = 100$ ms.

The samples exposed to the electron beam were analyzed by the following methods:

- weight loss,
- optical microscopy,
- scanning electron microscopy,
- ceramography.

The results can be summarized as follows:

- The materials EY-306, FP-219 and E-5923 P ($\perp$, electron beam vertical to the fibre planes) show the highest weight loss values.
- Relatively low amounts of eroded material in all series were found for EK 98, ATJ, FE-289 and E-5923 P ($\parallel$).
- The graphite AXF-5 Q shows the worst cracking behaviour, followed by EY-306.
- Excellent thermal shock behaviour was detected for the materials FP-219, ATJ and the carbon fibre composite E-5923 P.

	series 1			series 2			series 3			series 4		
power density[+]	3,5	5	10	3,5	5	10	3,5	5	10	3,5	5	10
pulse duration[++]	1	1	0.1	1	1	0.1	1	1	0.1	1	1	0.1
EK 98	1	1	1	-	3	3	1	10	1	-	12	-
5890/PT	1	1	1	-	1	1	-	2	1	-	2	-
AXF-5 Q	1	1	1	-	1	1	-	2	1	-	2	-
EY-306	1	1	1	-	1	1	-	1	1	-	2	-
FP-219	1	1	1	-	1	1	-	1	1	-	2	-
H-490	1	1	1	-	1	1	-	1	1	-	2	-
ATJ	-	-	-	1	1	1	1	1	1	-	3	-
FE-289	-	-	-	-	-	-	1	1	1	-	3	-
E 5823 P (∥)	-	-	-	1	1	1	1	1	1	-	2	-
E 5823 P (⊥)	-	-	-	1	1	1	1	1	1	-	2	-

[+] ($kWcm^{-2}$) [++] (s)

Tab. 35: Number of experiments in series 1 through 4 in dependence on the heat loading conditions

	load conditions		series 1		series 3		series 4	
material	P/a	t	sample No.	m	sample No.	m	sample No.	m
	$kWcm^{-2}$	s		mg		mg		mg
EK 98	3.5	1.0	11/32	0.03	11/54	0.14		
	5.0	1.0	11/32	1.97	11/44	2.77	11/56	3.01
					11/45	3.28	11/57	1.33
					11/46	7.50	11/58	2.09
					11/47	3.04	11/59	1.94
					11/48	2.22	11/60	1.91
					11/49	2.47	11/61	2.25
					11/50	2.34	11/62	3.85
					11/51	1.00	11/63	1.93
					11/52	2.32	11/64	2.05
					11/53	2.46	11/65	0.65
							11/66	2.58
							11/67	1.57
	10.0	0.1	11/33	3.57	11/55	4.43		
5890/PT	3.5	1.0	12/6	0.15				
	5.0	1.0	12/5	3.62	12/10	5.24	12/14	1.56
					12/12	3.84	12/15	1.86
	10.0	0.1	12/7	3.35	12/11	4.51		
AXF-5Q	3.5	1.0	17/6	0.14				
	5.0	1.0	17/5	5.62	17/10	3.02	17/14	1.40
					17/12	2.75	17/15	1.59
	10.0	0.1	17/7	3.95				
EY-306	3.5	1.0	34/2	0.40				
	5.0	1.0	34/1	7.87	34/6	4.84	34/8	4.36
							34/9	3.67
	10.0	0.1	34/3	4.25				
FP-219	3.5	1.0	35/2	0.30				
	5.0	1.0	35/1	6.57	35/6	3.38	35/8	4.30
							35/9	3.38
	10.0	0.1	35/3	3.10				
H-490	3.5	1.0	36/2	0.31				
	5.0	1.0	36/1	4.38	36/6	2.94	36/8	2.86
							36/9	3.27
	10.0	0.1	36/3	3.70				
ATJ	3.5	1.0			41/5	0.10		
	5.0	1.0			41/4	2.63	41/7	2.83
							41/8	2.02
							41/9	3.01
	10.0	0.1			41/6	4.24		
FE-289	3.5	1.0			43/2	0.01		
	5.0	1.0			43/1	3.50	43/4	1.18
							43/5	3.04
							43/6	1.97
	10.0	0.1			43/3	4.25		
E-5923 P(II)	3.5	1.0			40/9	0.13		
	5.0	1.0			40/7	2.98	40/15	1.83
							40/16	2.17
	10.0	0.1			40/11	1.82		
E-5923 P(⊥)	3.5	1.0			40/8	0.70		
	5.0	1.0			40/10	5.16	40/13	6.90
							40/14	6.72
	10.0	0.1			40/12	3.71		
1.4311	5.0	1.0					M 14/5	22.21
							M 14/6	22.26
							M 14/7	22.15
							M 14/8	21.92
							M 14/9	22.59

Tab. 36: Sample numbers and weight loss data for 3 test series

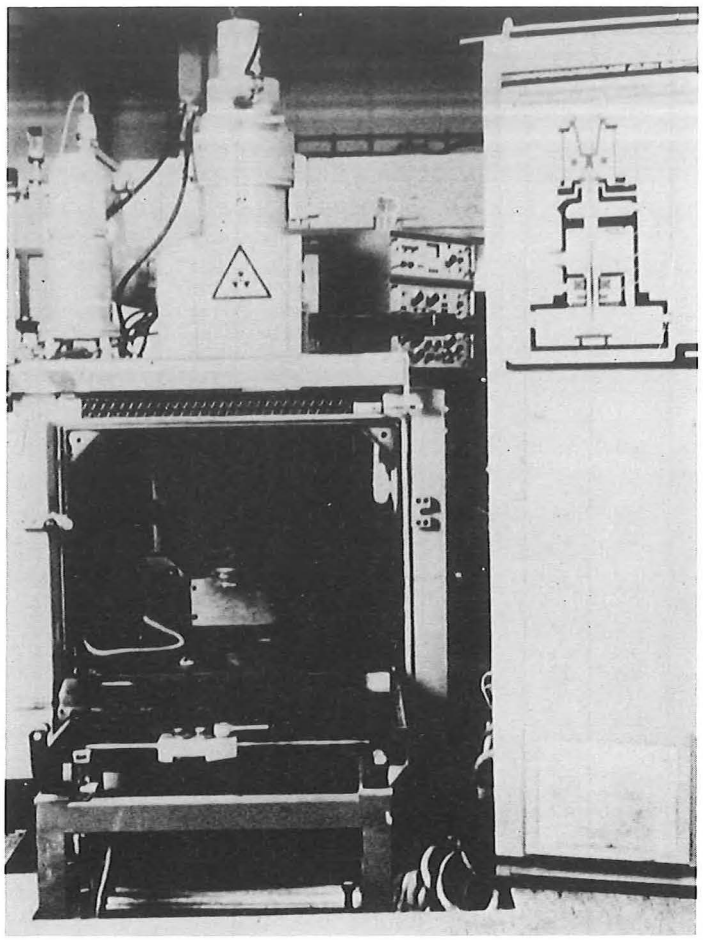

a)

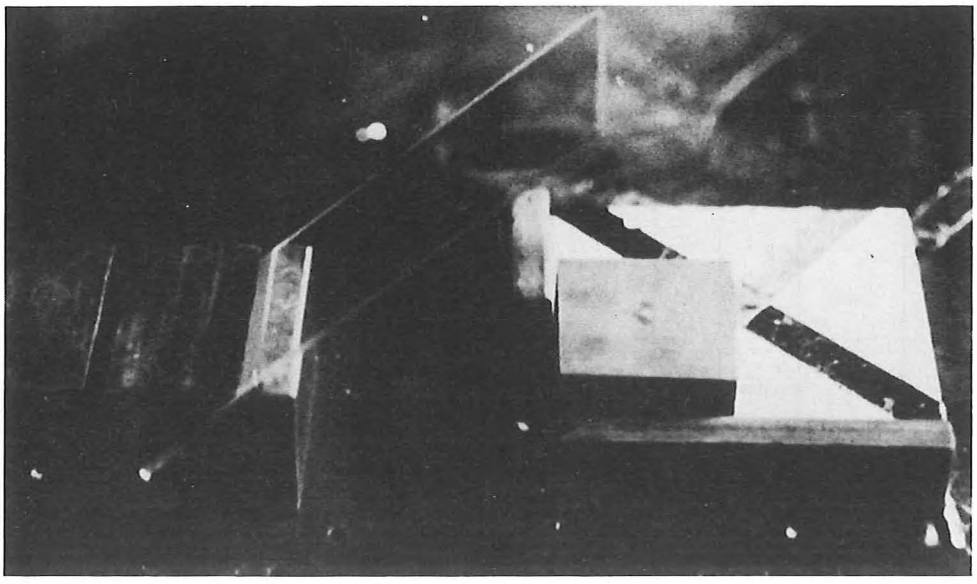

b)

Fig. 35:
Electron beam welding machine for thermal shock testing
a) overall view
b) sample stage with collector probe (glass disk) for evaporated/ eroded material

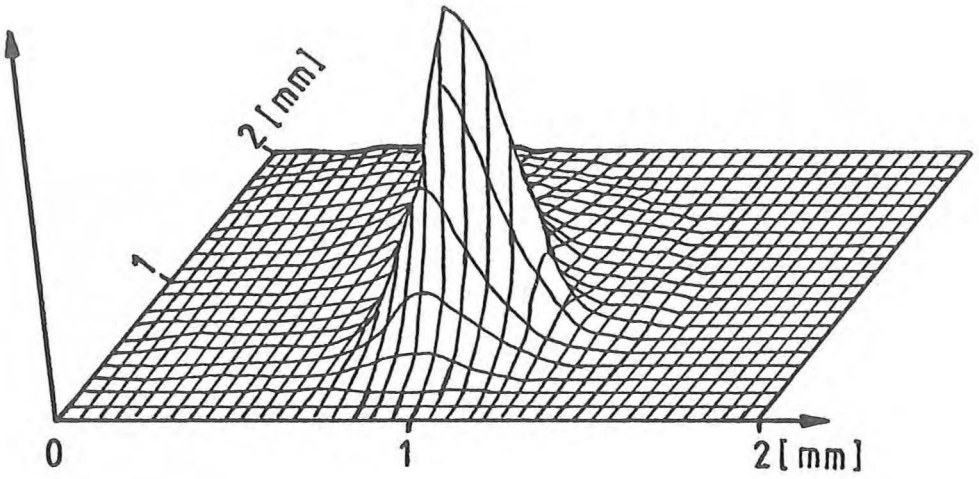

Fig. 36:
Spatial distribution of current density in a focussed electron beam

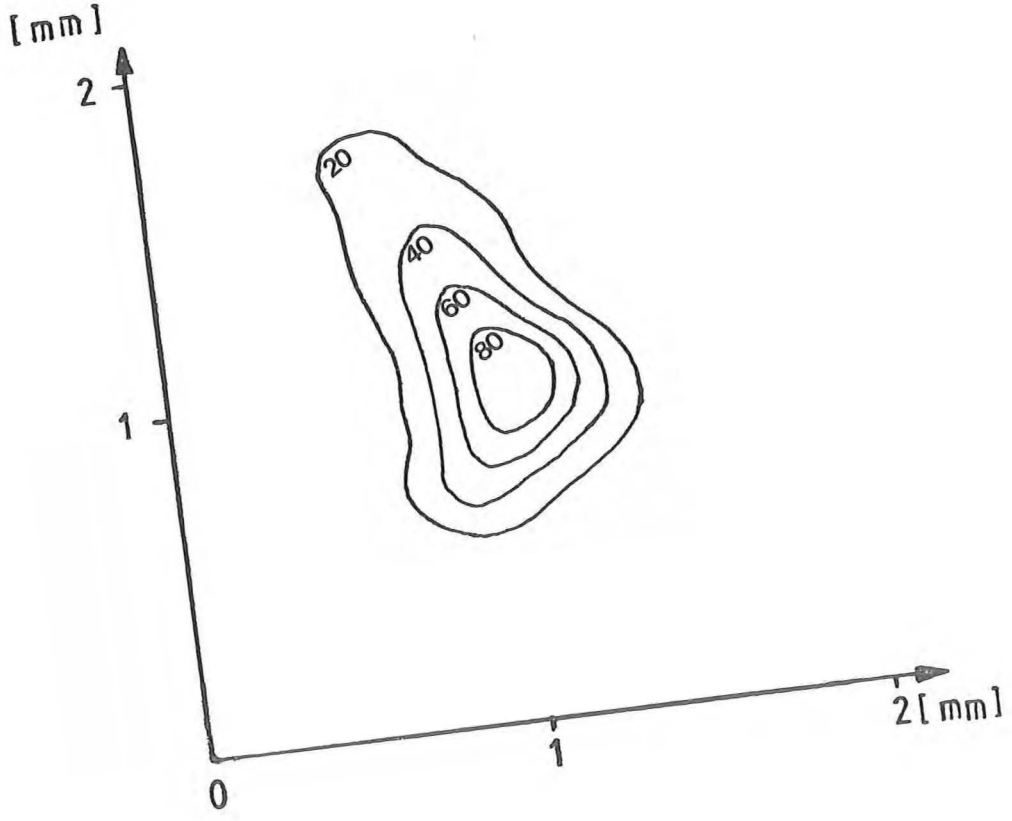

Fig. 37:
Curves of constant current density (for the beam in fig. 2) at 20, 40, 60 and 80 % of the peak density

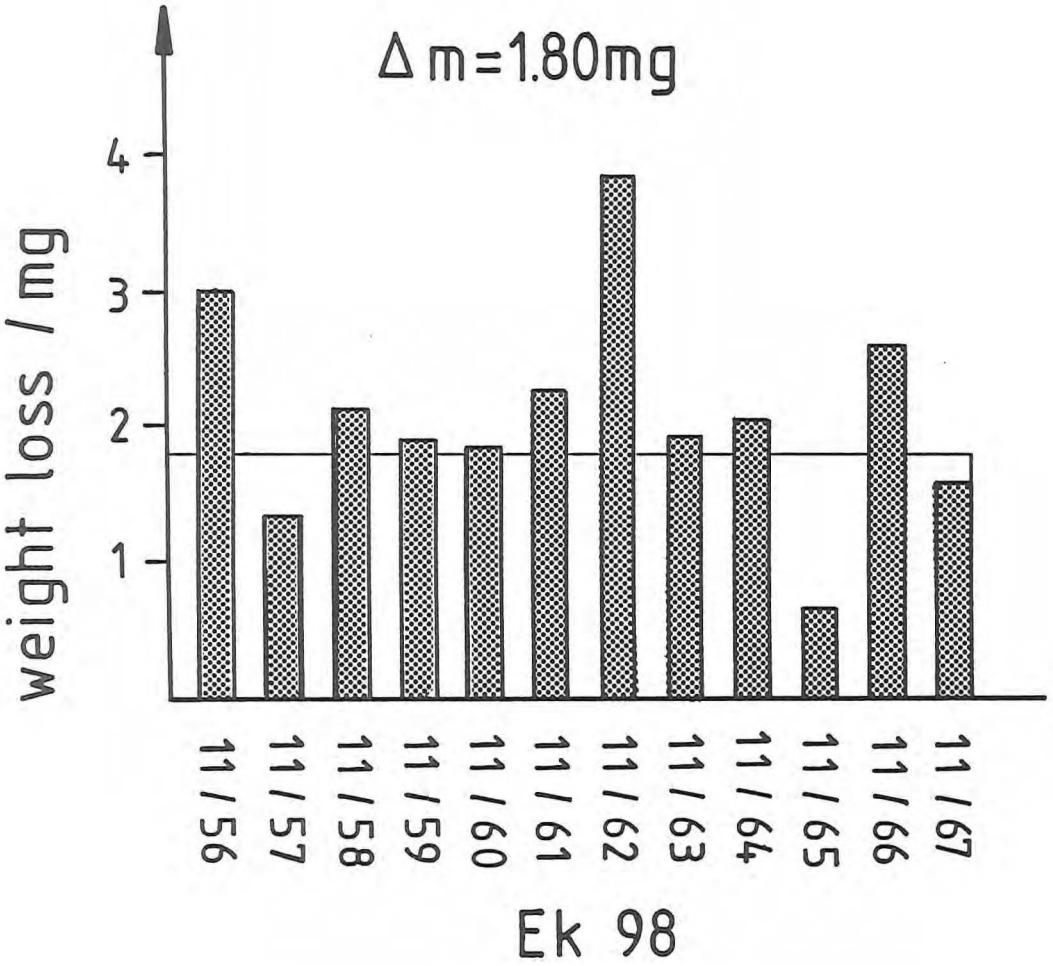

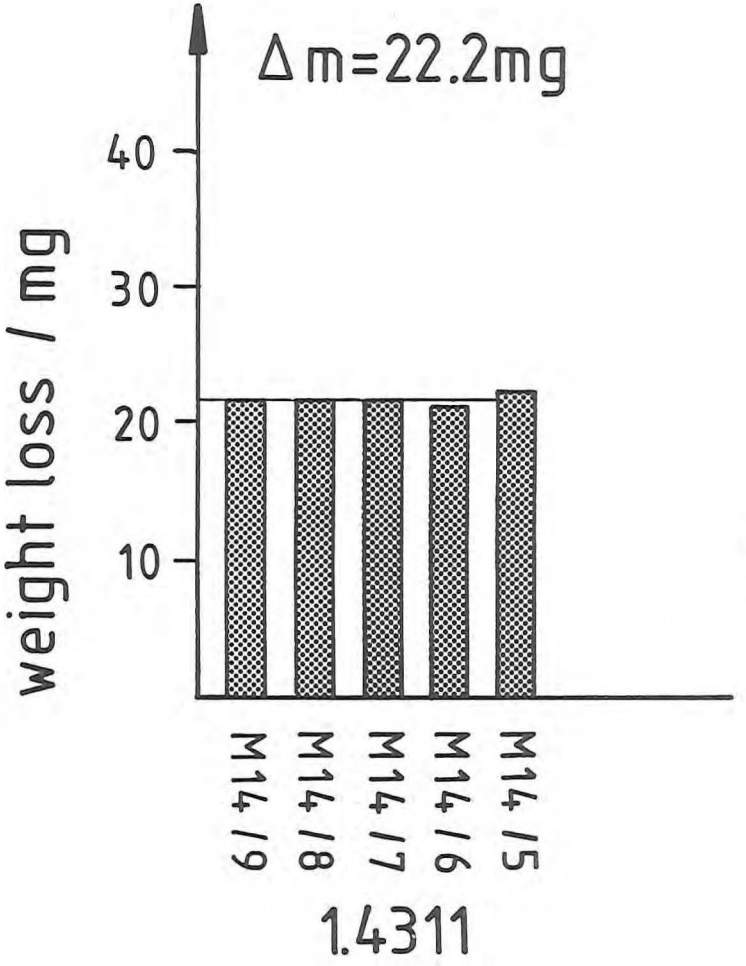

Fig. 38:
Weight loss of the fine grain graphite EK 98 and stainless steel 1.4311 due to electron beam pulses with 5 $kWcm^{-2}$ mean power density and 1 s duration

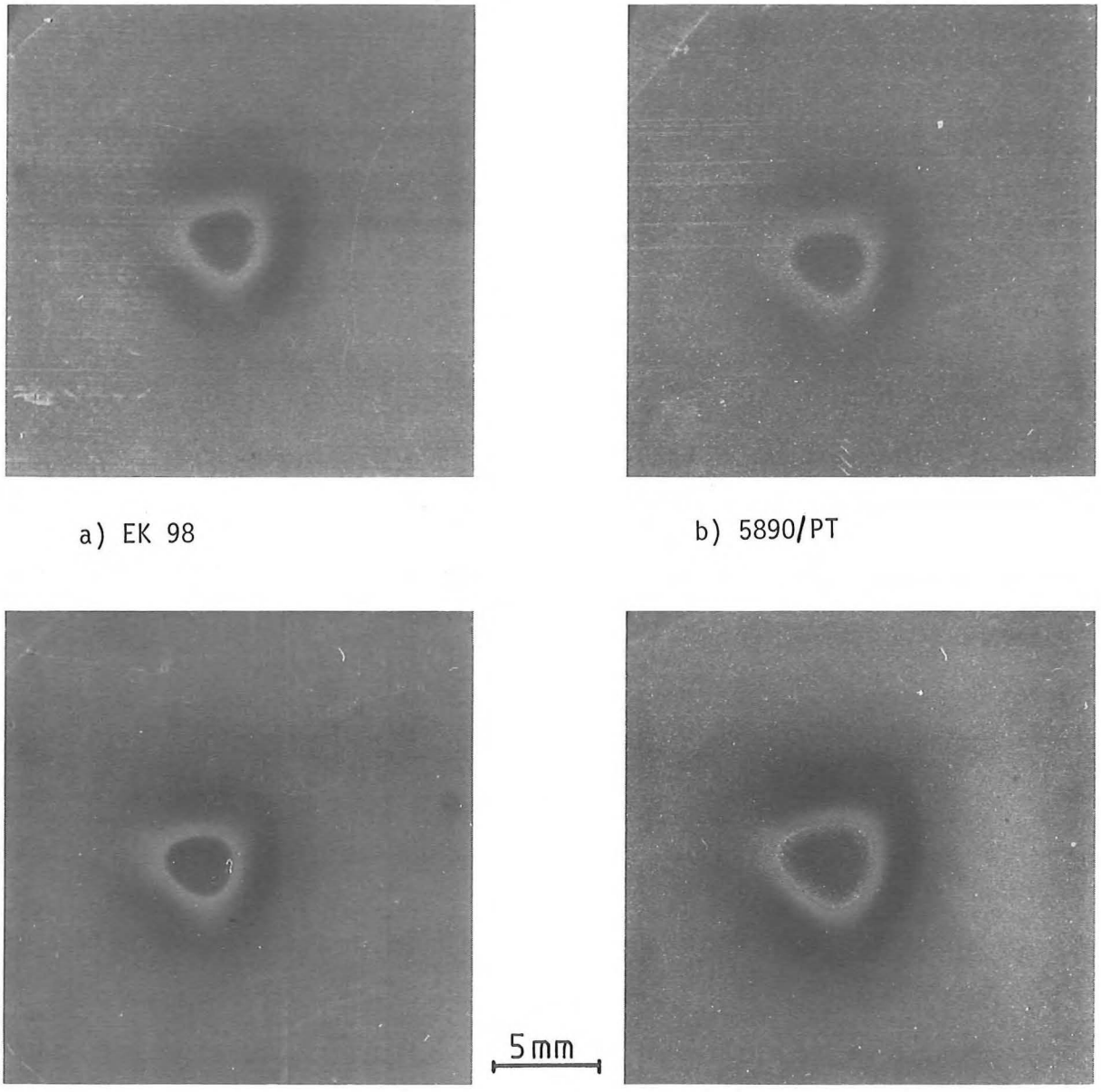

Fig. 39:
Macroscopic appearance of the electron beam damage due to a 5 $kWcm^{-2}$ pulse of 1 s duration (series 4).

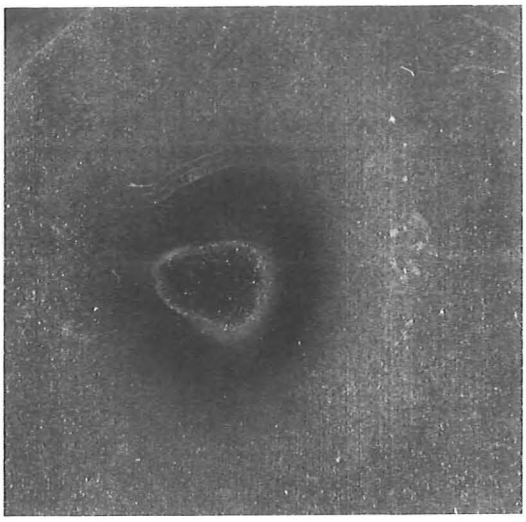

e) FP-219

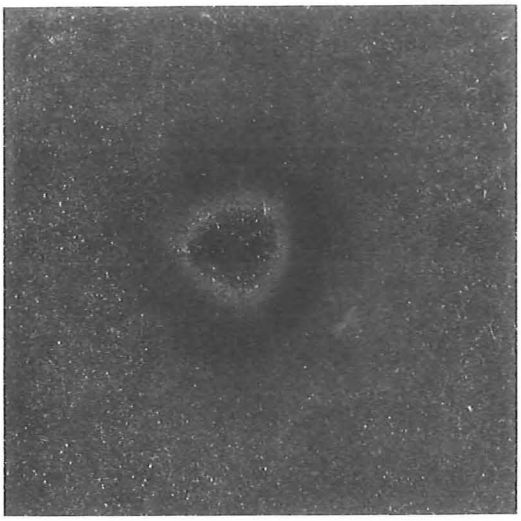

f) H-490

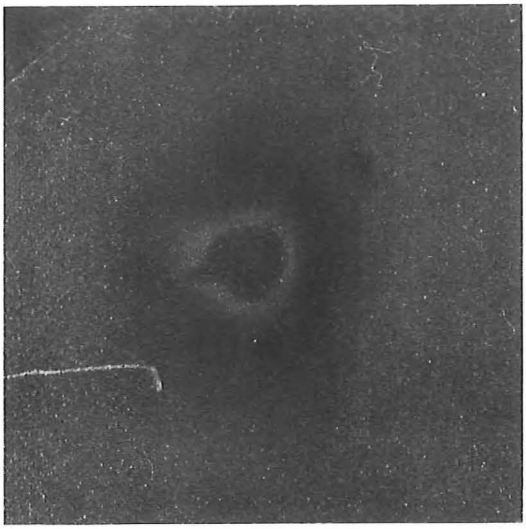

g) ATJ

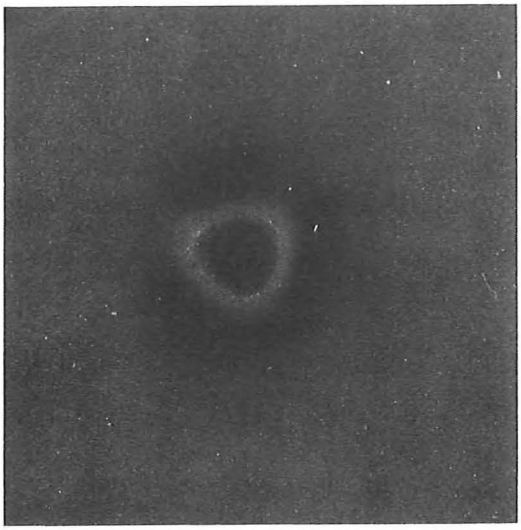

h) FE-289

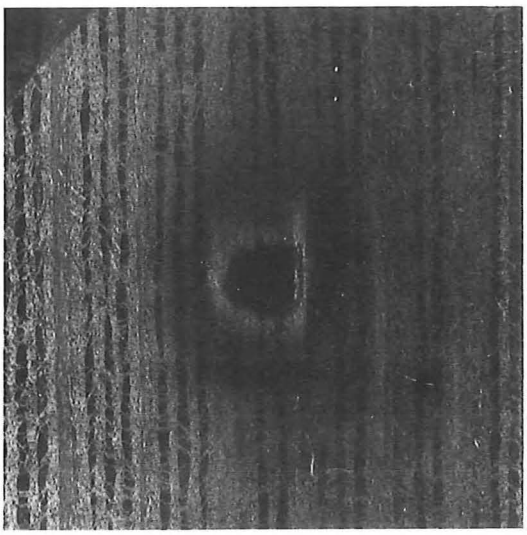

i) E-5923 P (∥)

5 mm

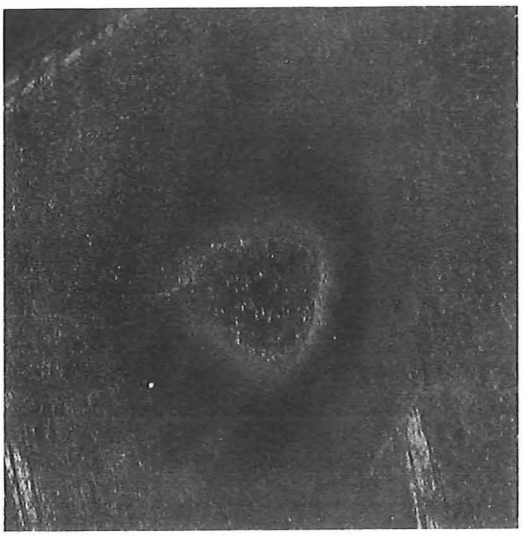

j) E-5923 P (⊥)

Fig. 39:

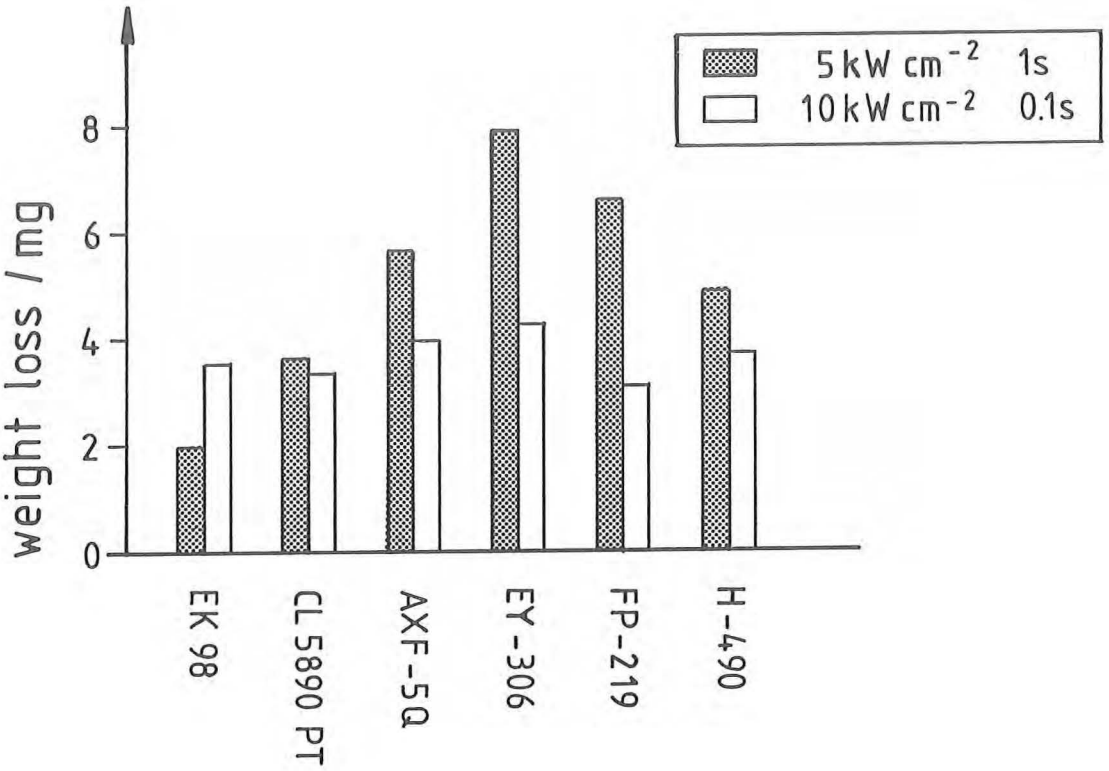

Fig. 40:
Weight loss of the graphite tiles due to the single shot electron beam experiment.
series 1 with 6 graphite qualities at 2 different loading conditions

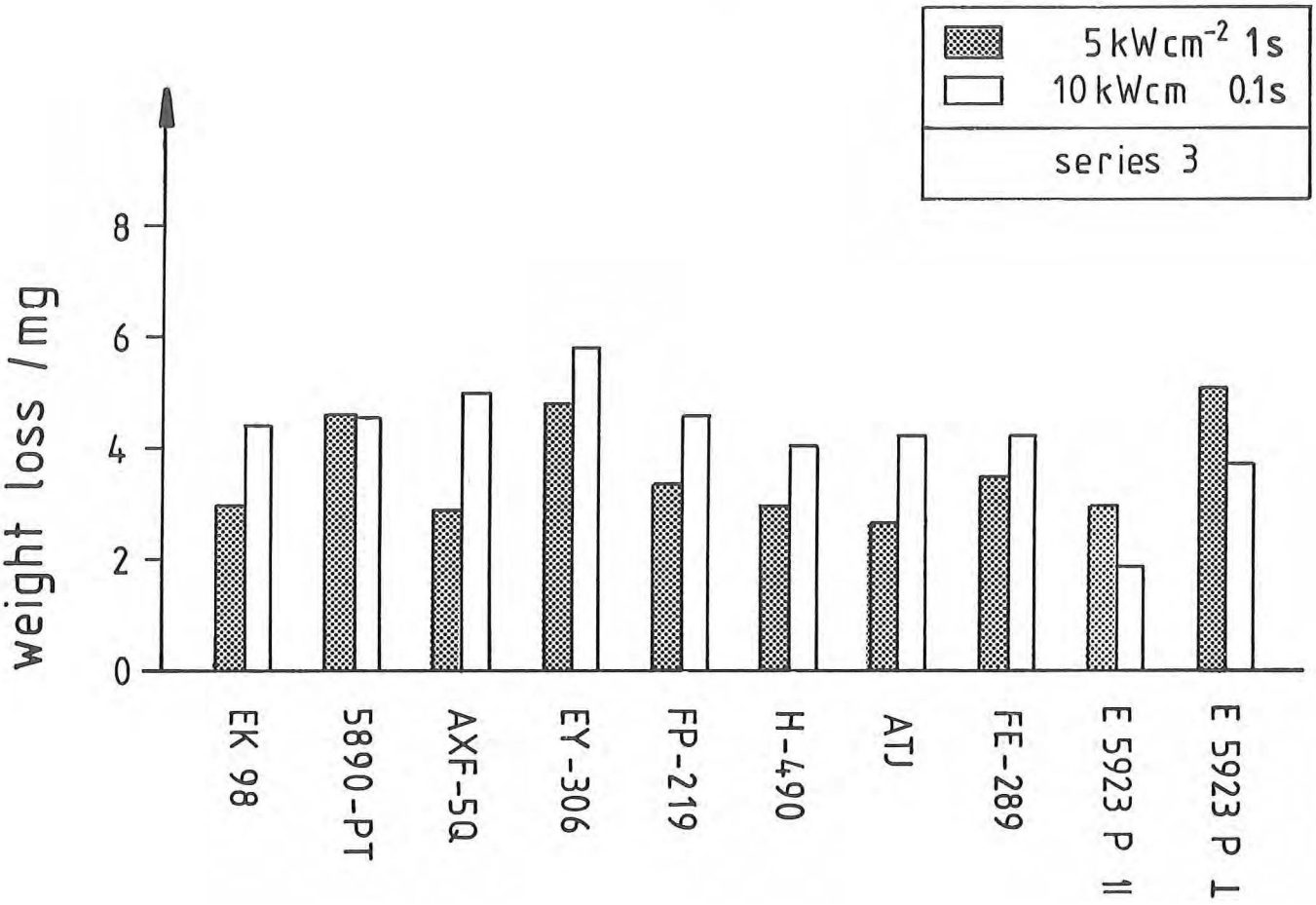

Fig. 40:
Weight loss of the graphite tiles due to the single shot electron beam experiment.
series 3 with 8 graphite qualities plus a carbon-fibre composite (2 loading conditions)

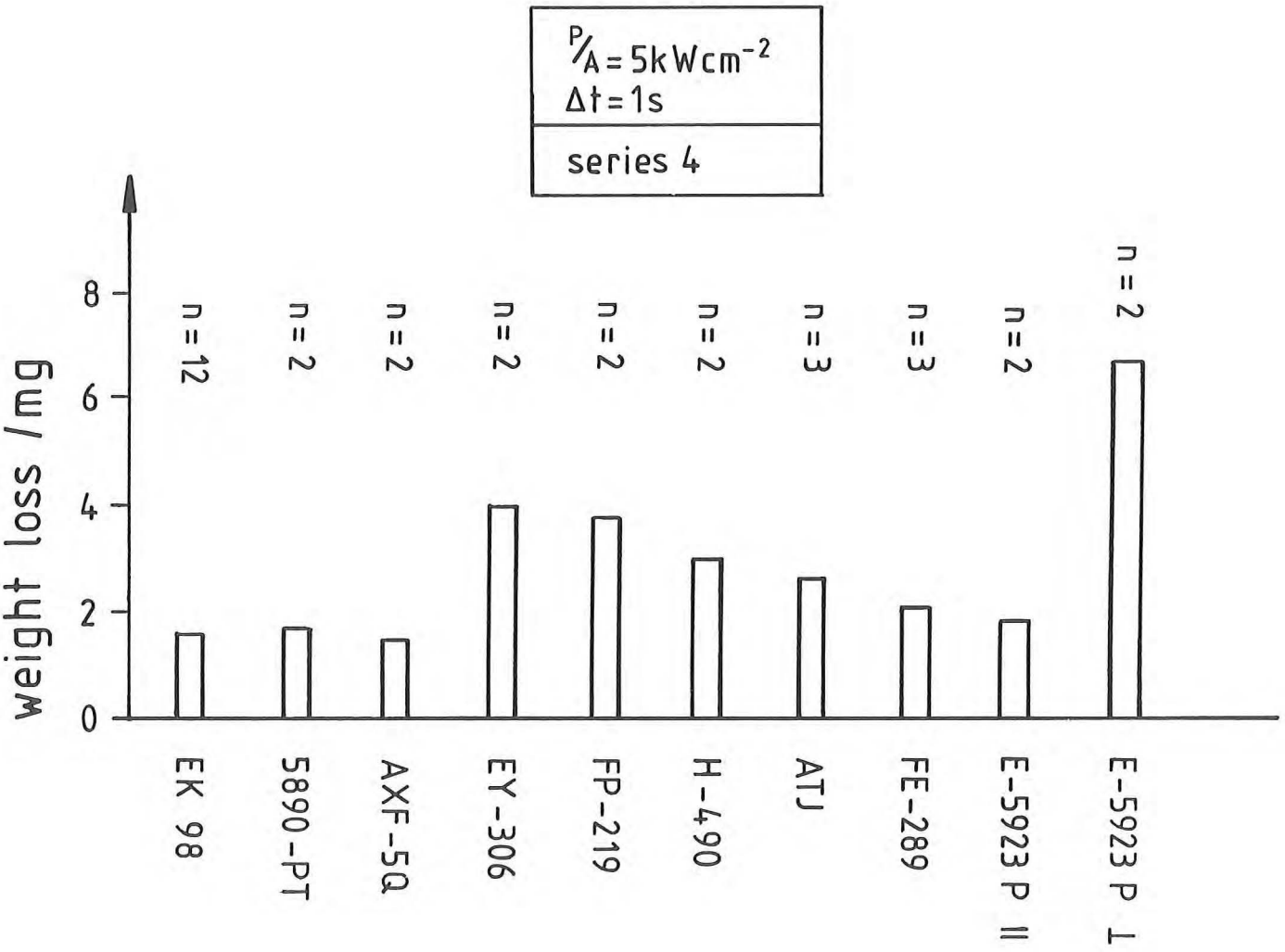

Fig. 40:
Weight loss of the graphite tiles due to the single shot electron beam experiment.
series 4 (similar to series 3, but only 5 $kWcm^{-2}$-pulses)

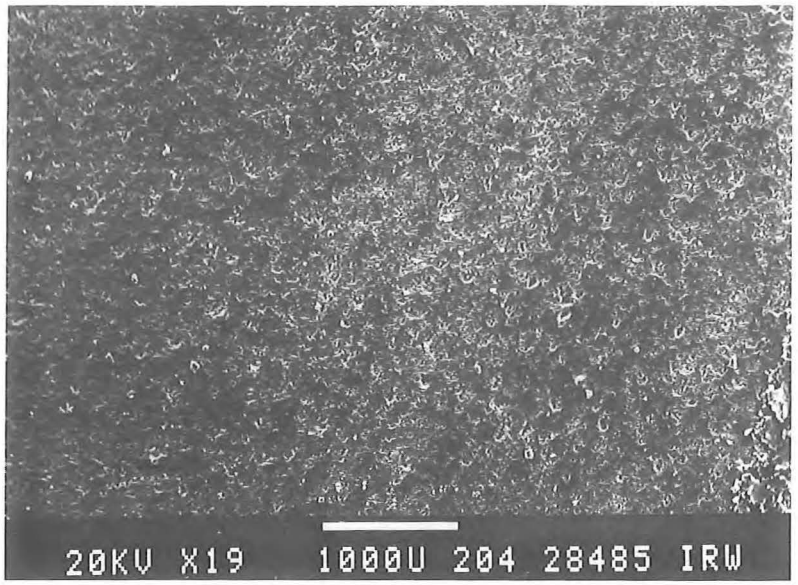

a) 5890/PT

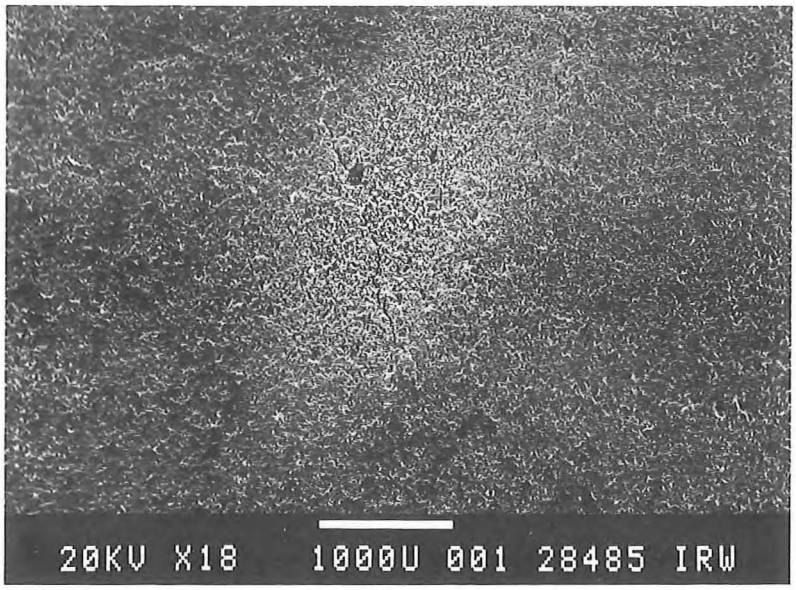

b) EY-306

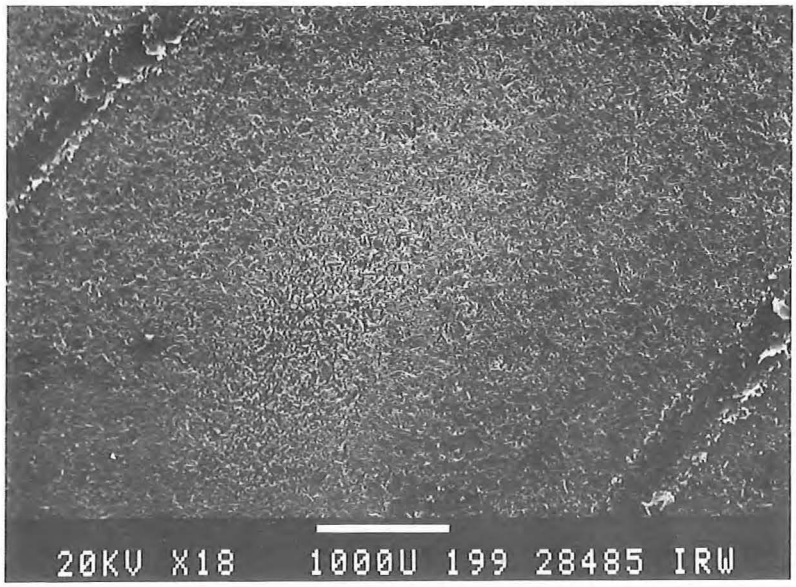

c) FP-219

Fig. 41:
Low magnification SEM-images (secondary electron) of graphite tiles exposed to an electron beam with 3.5 $kWcm^{-2}$ power density and 1 s pulse duration.
- series 1 -

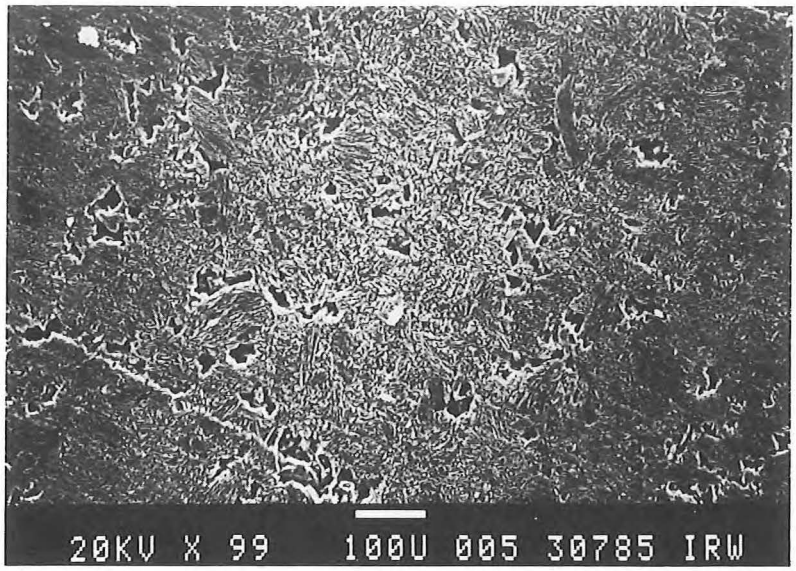

d) ATJ

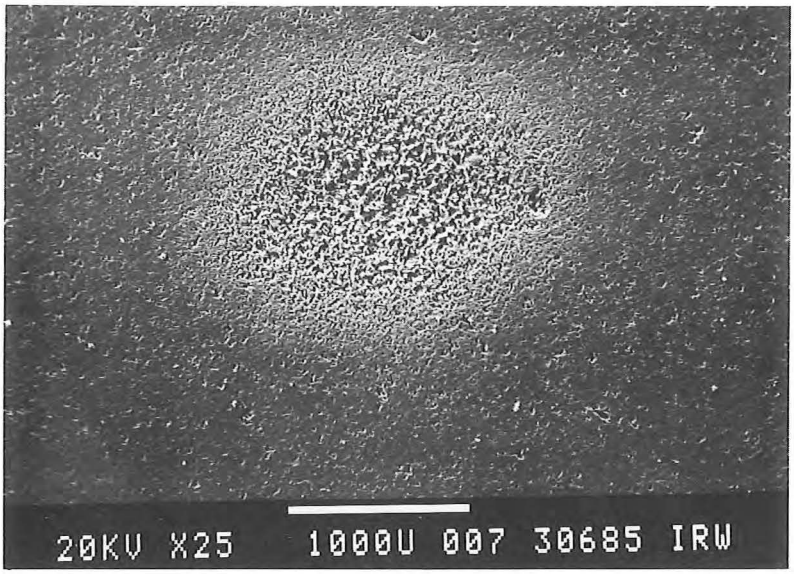

e) FE-289

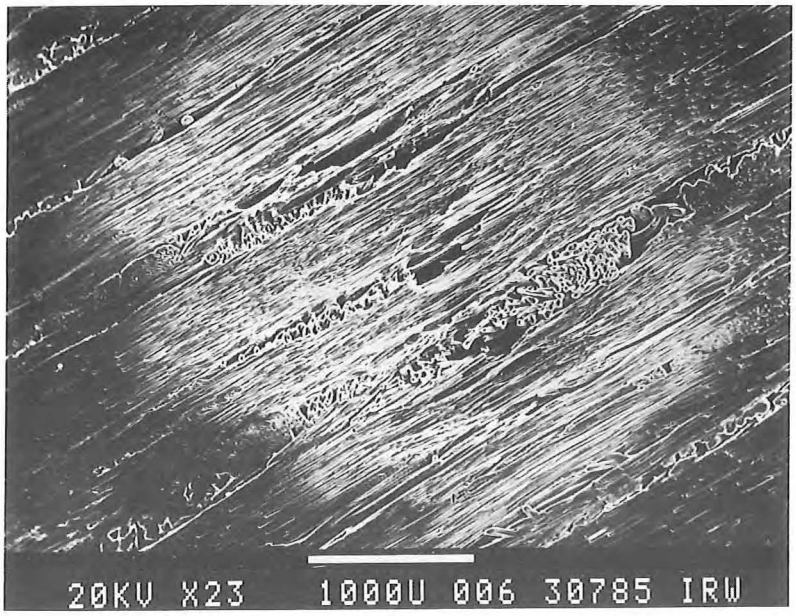

f) E 5923 P (⊥)

Fig. 41:
- series 3-

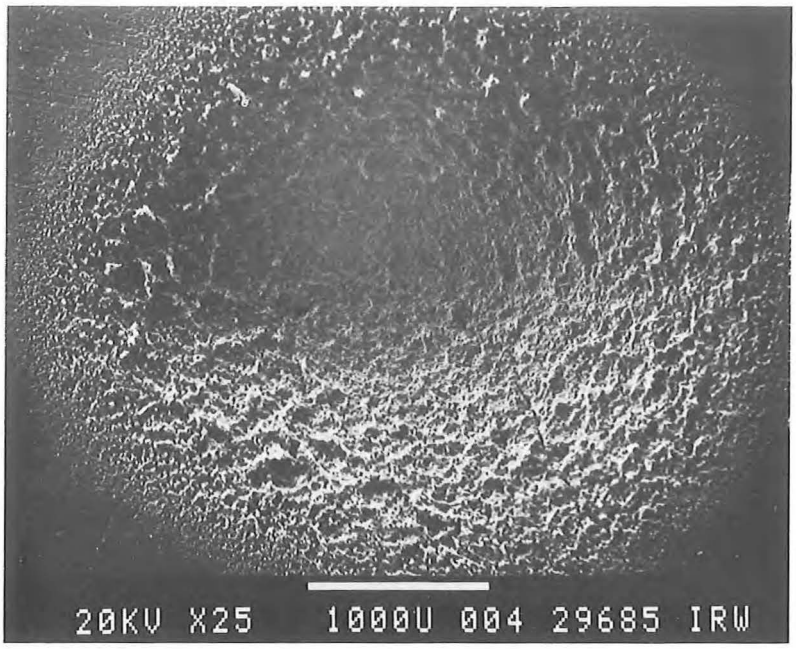

a) EK 98

SE

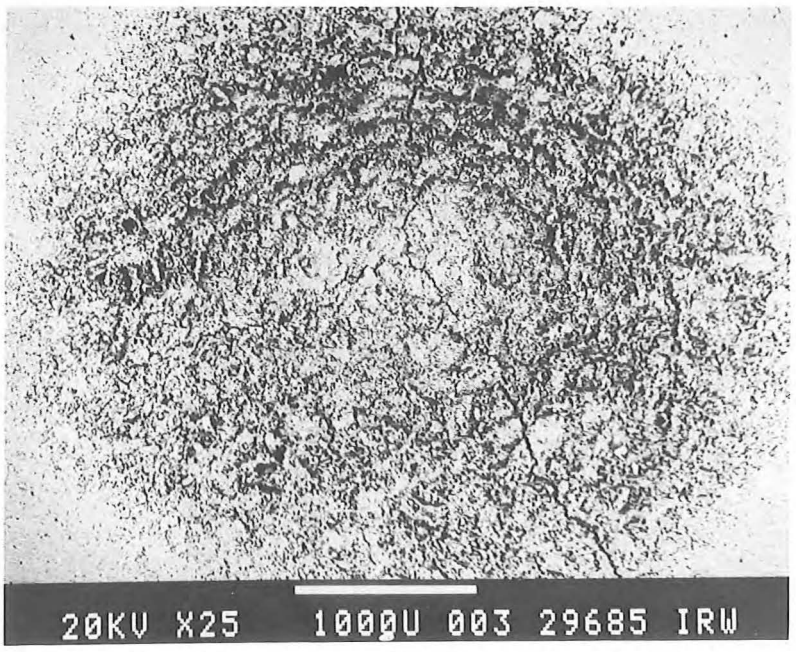

b) EK 98

BE

Fig. 42:
Low magnification SEM-images of graphite tiles exposed to an electron beam with 5.0 $kWcm^{-2}$ power density and 1 s pulse duration (series 3)
SE = secondary electron image
BE = back-scatter electron image

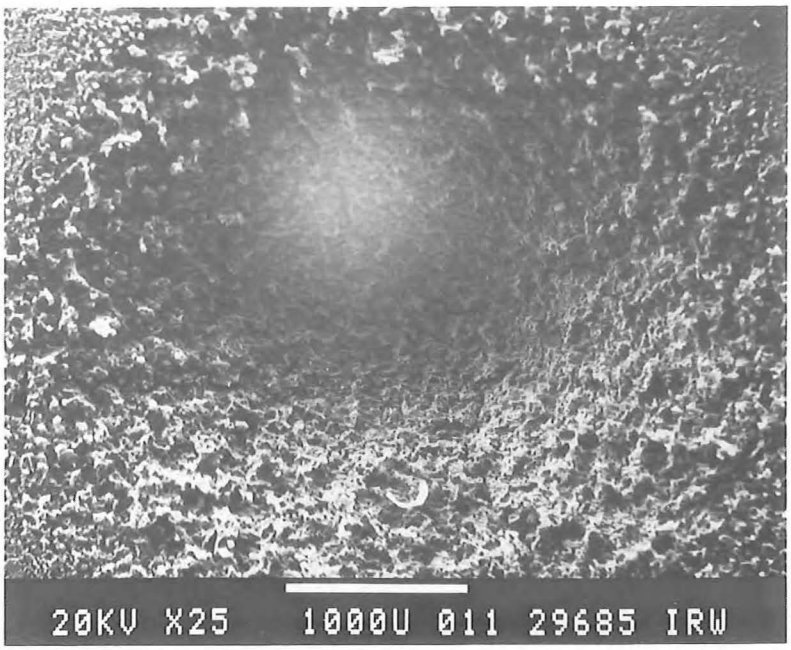

c) 5890/PT SE

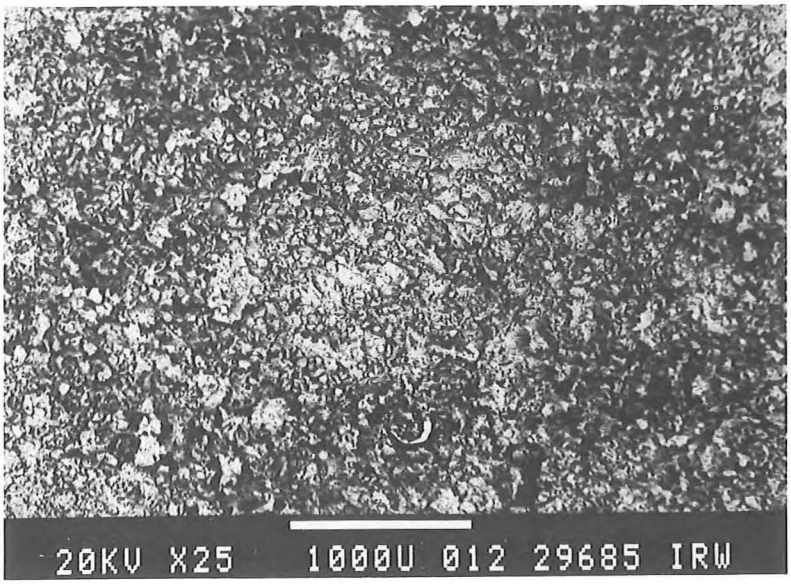

d) 5890/PT BE

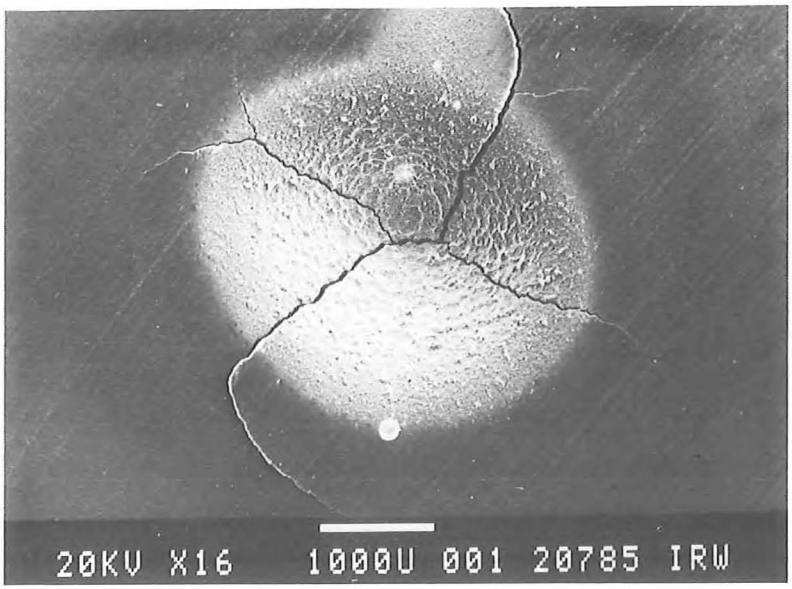

e) AXF-5 Q SE

Fig. 42:

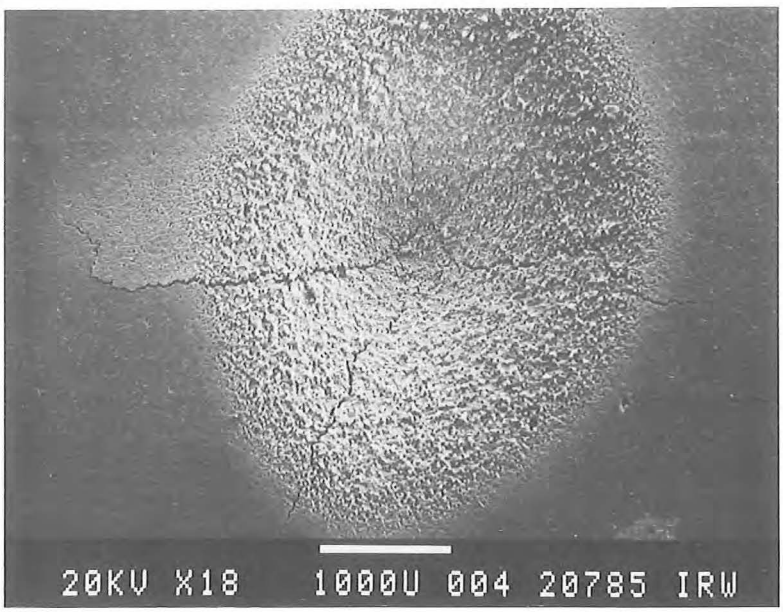

f) EY-306

SE

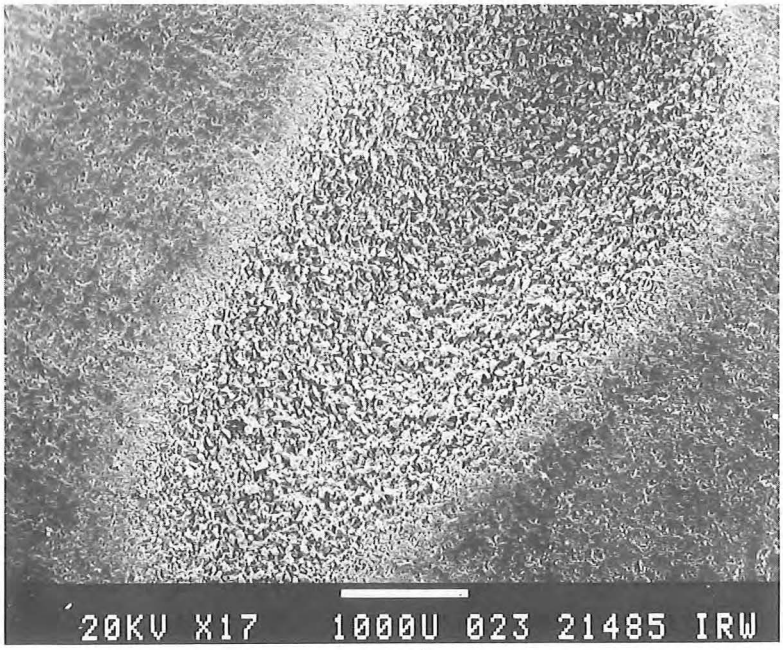

g) FE-219

- series 1 -

SE

h) FE-219

- series 1 -

BE

Fig. 42:

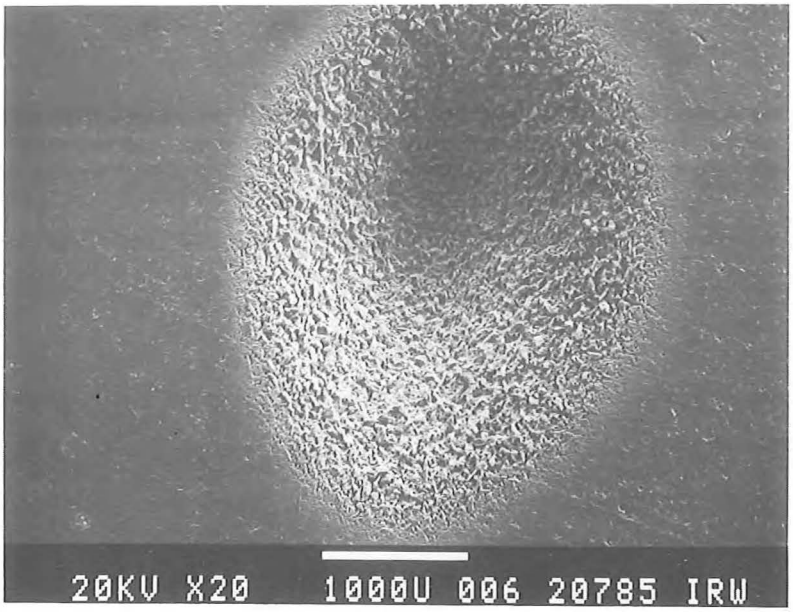

i) H-490 SE

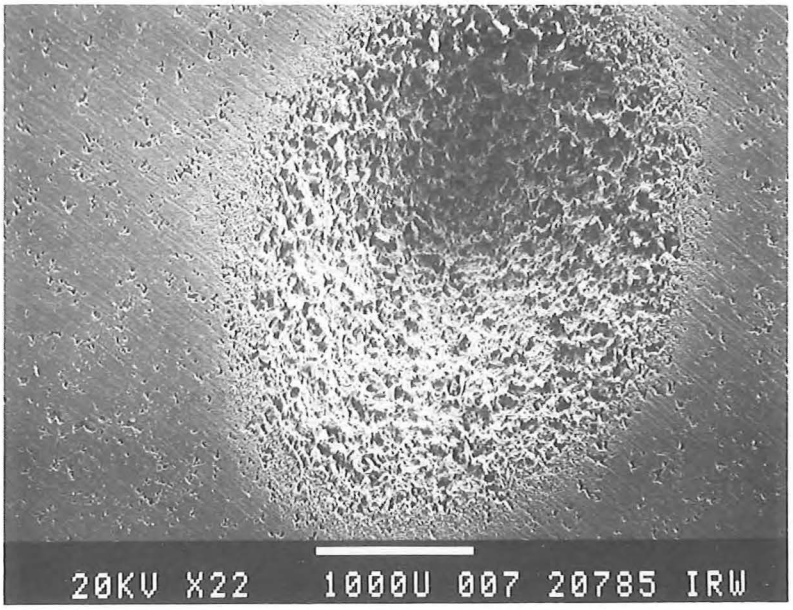

j) ATJ SE

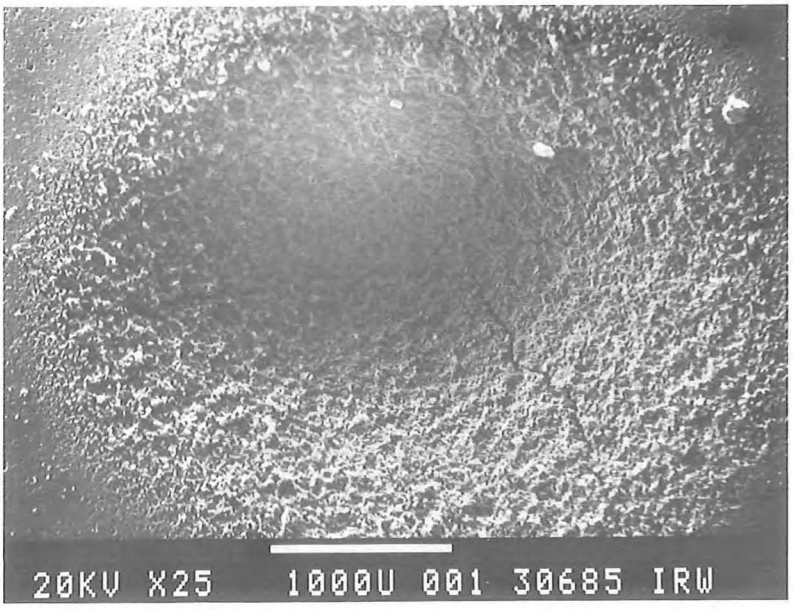

k) FE-289 SE

Fig. 42:

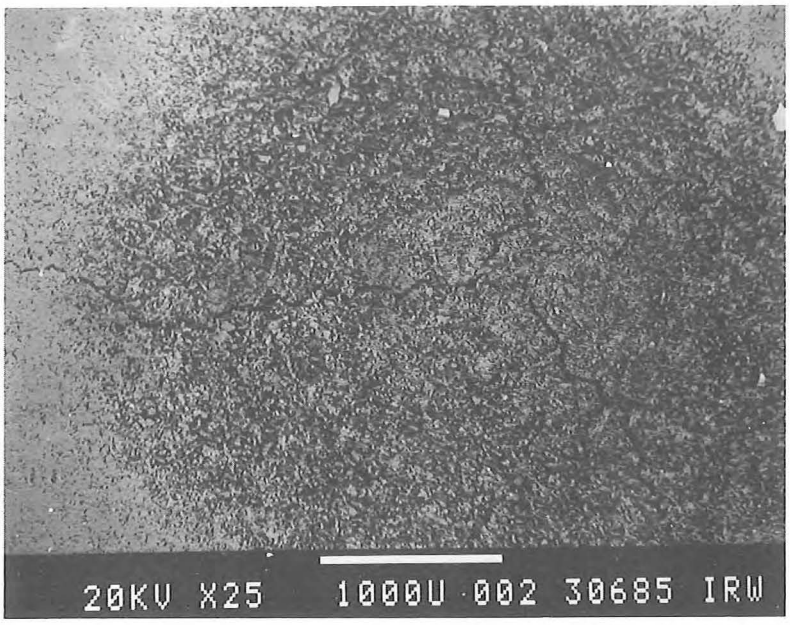

l) FE-289 BE

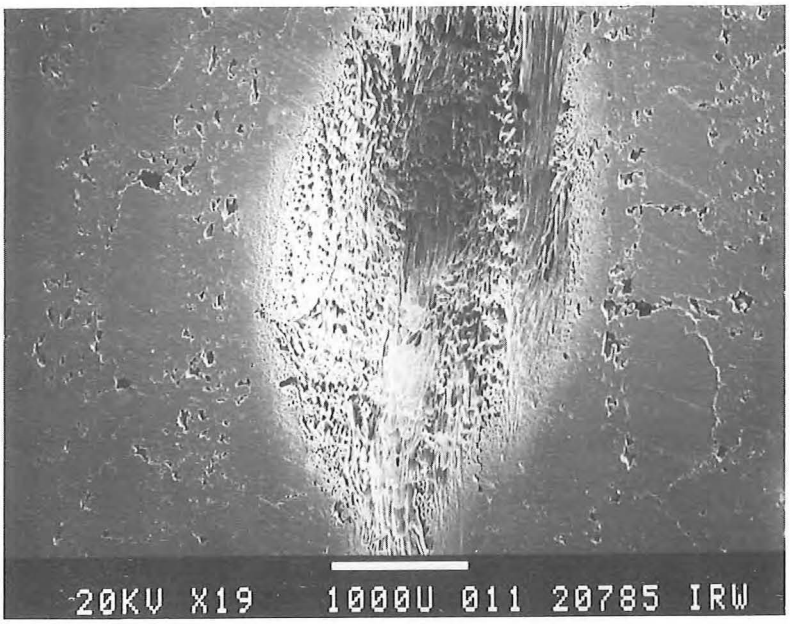

m) E-5923 P (II) SE

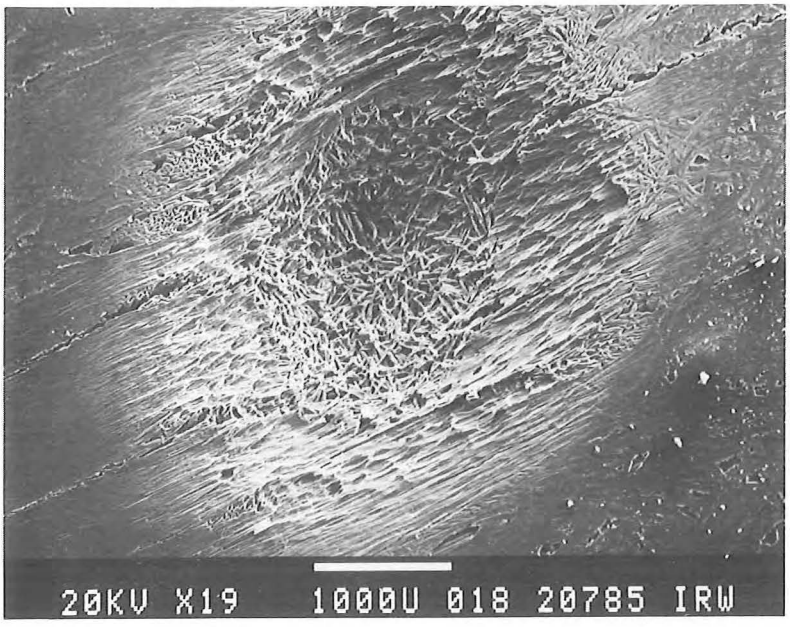

n) E-5923 P (⊥) SE

Fig. 42:

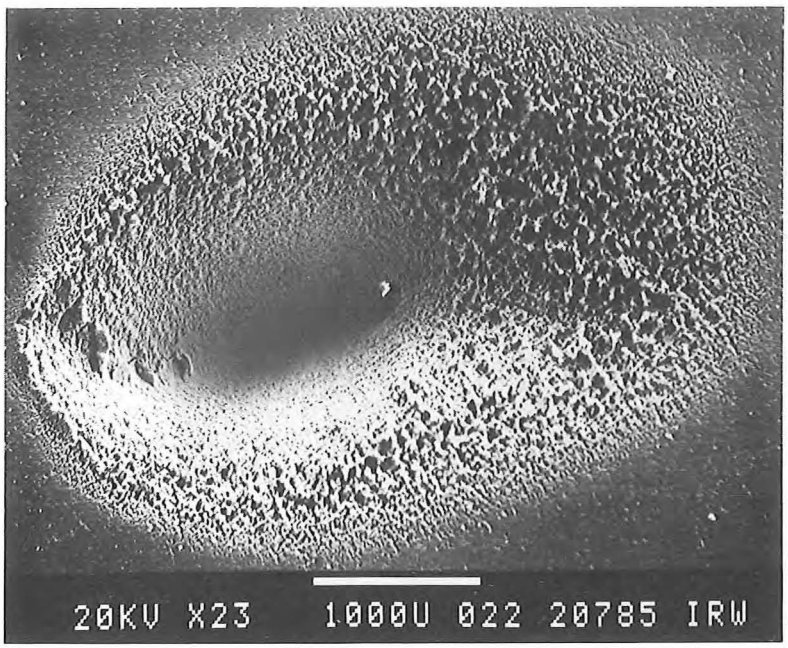

a) EK 98

SE

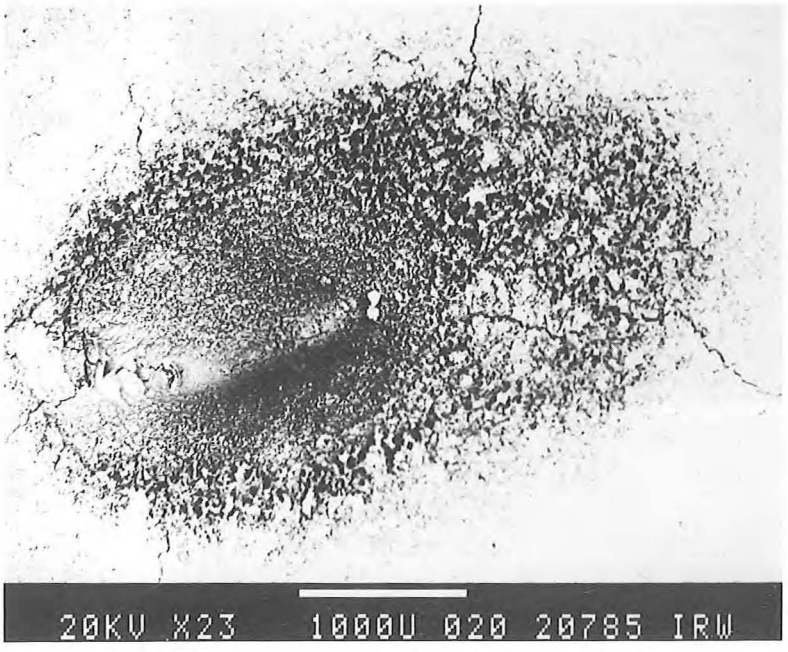

b) EK 98

BE

Fig. 43:
Low magnification SEM-images of graphite tiles exposed to an electron beam with 10 $kWcm^{-2}$ power density and 0.1 s pulse duration (series 3)
SE = secondary electron image
BE = back-scatter electron image

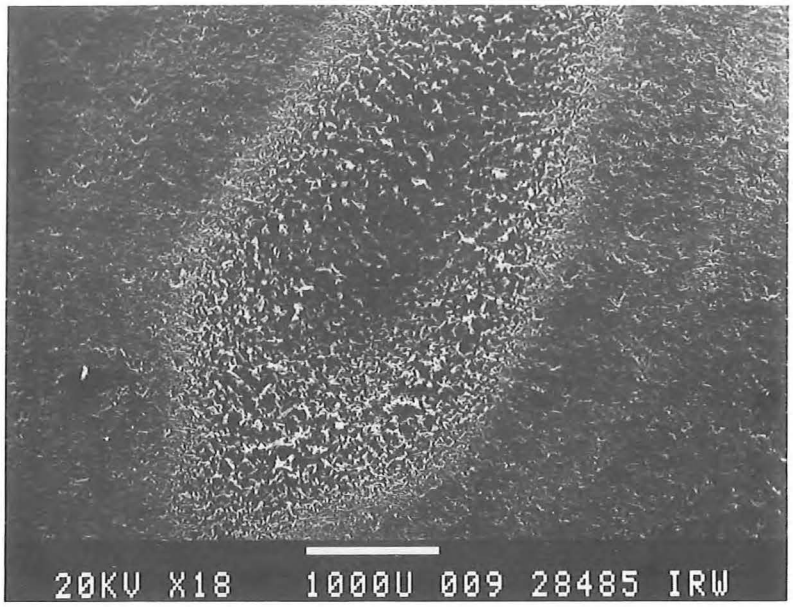

c) 5890/PT

- series 1 -

SE

d) 5890/PT

- series 1 -

BE

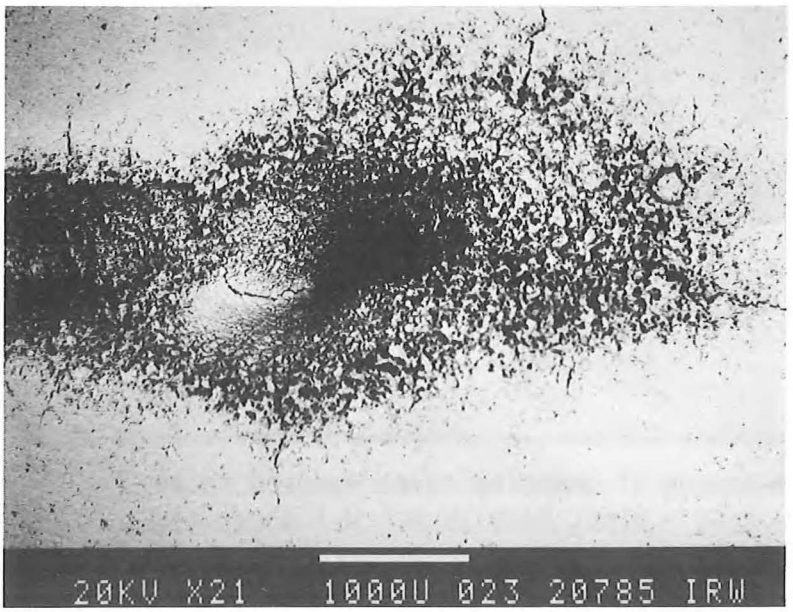

e) 5890/ PT

BE

Fig. 43:

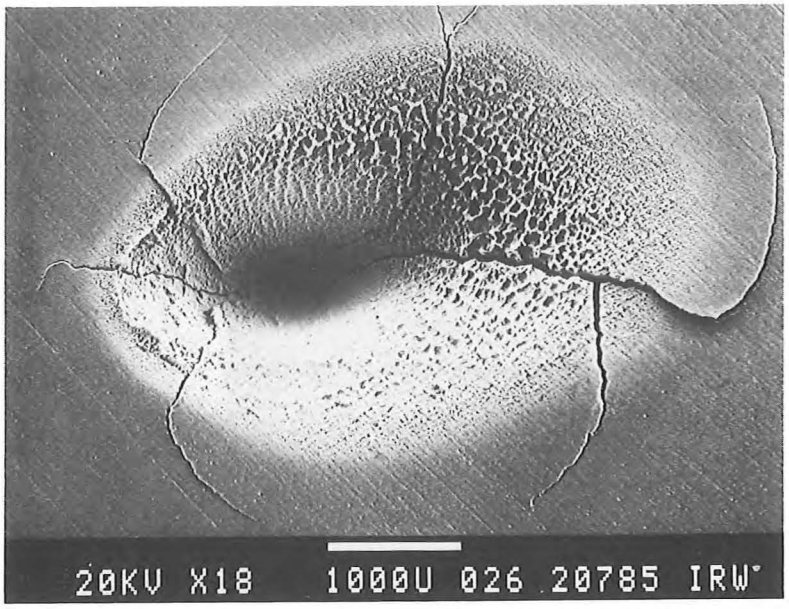

f) AXF-5 Q SE

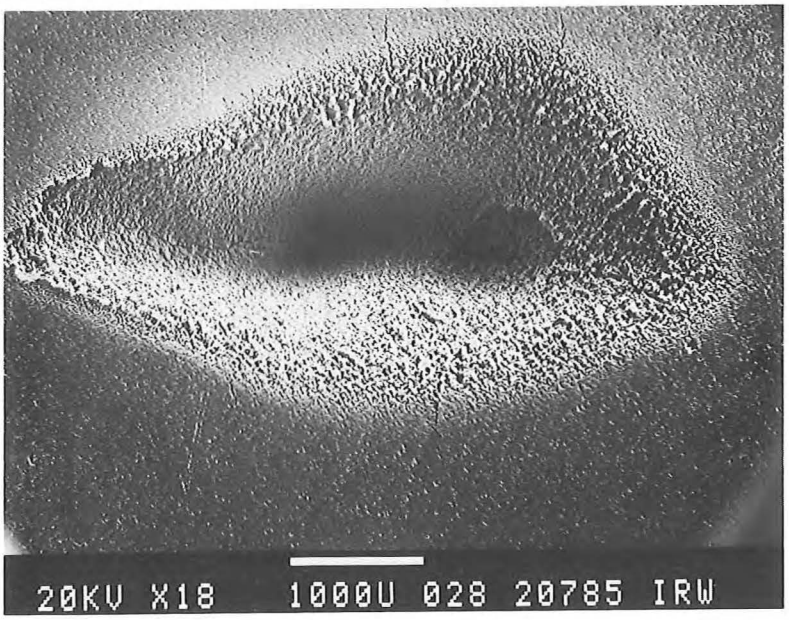

g) EY-306 SE

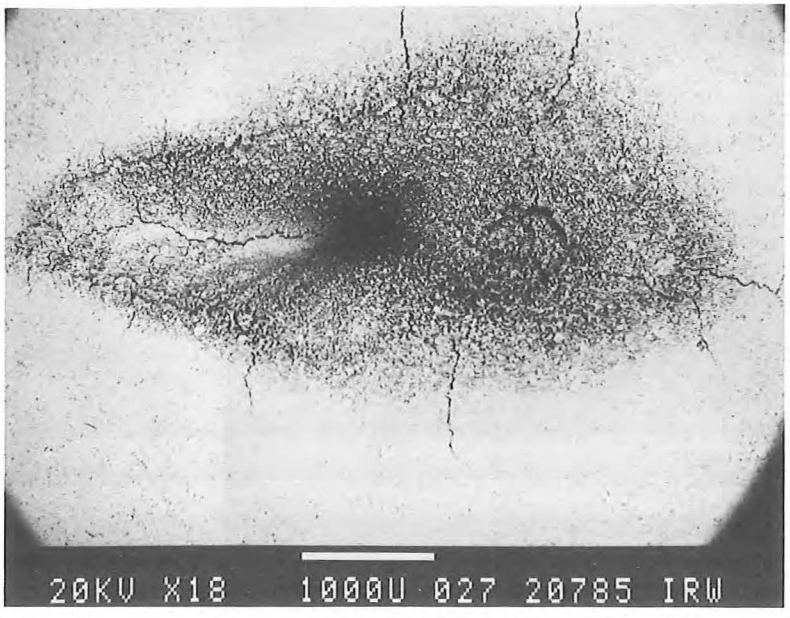

h) EY-306 BE

Fig. 43:

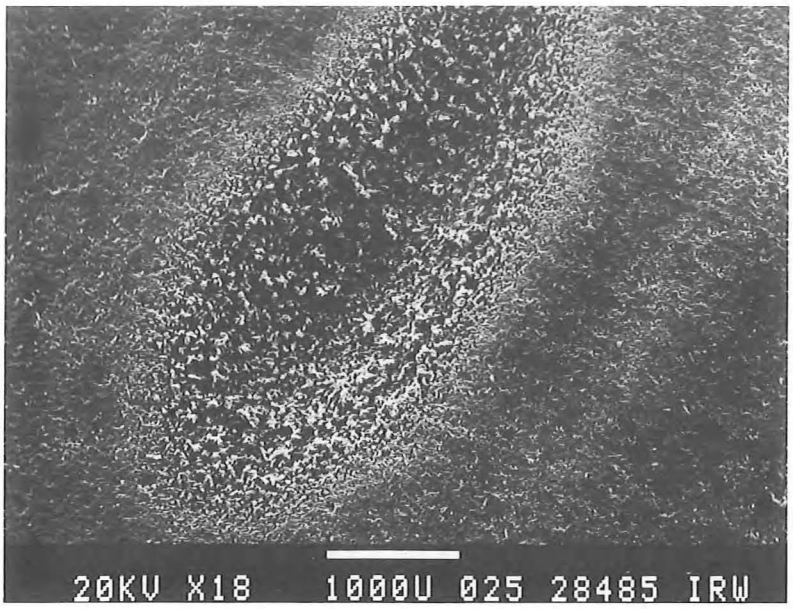

i) FP-219

- series 1 -

SE

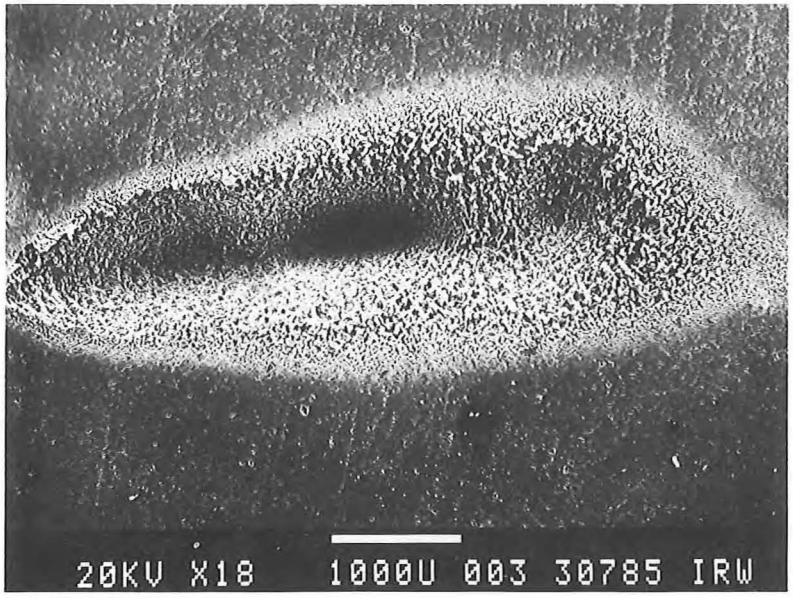

j) H-490

SE

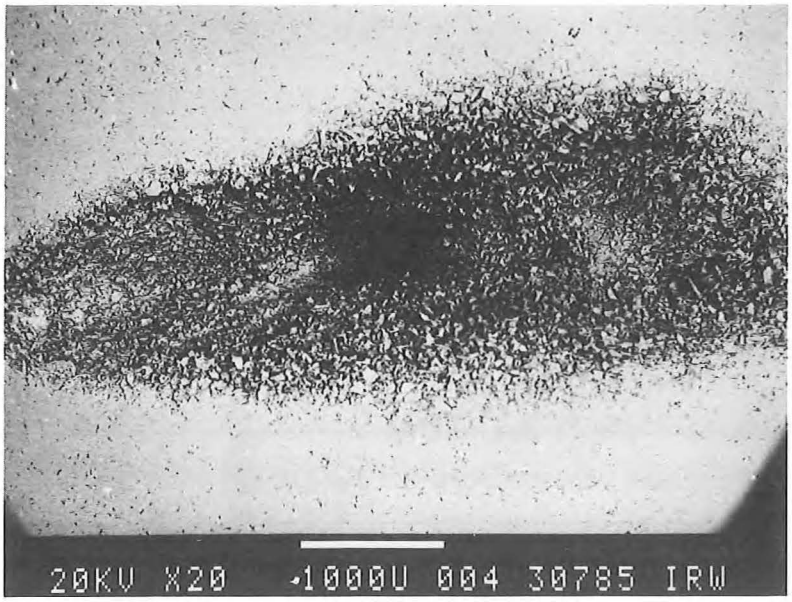

k) H-490

BE

Fig. 43:

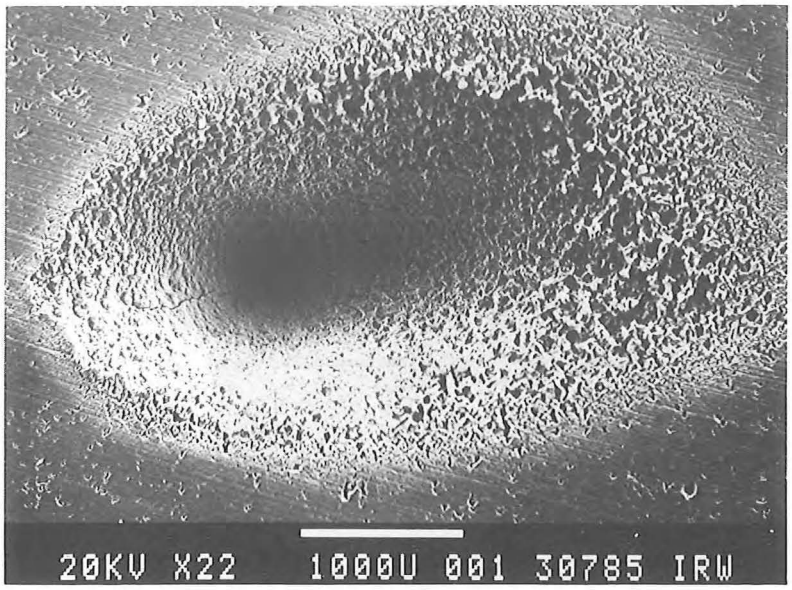

l) ATJ

SE

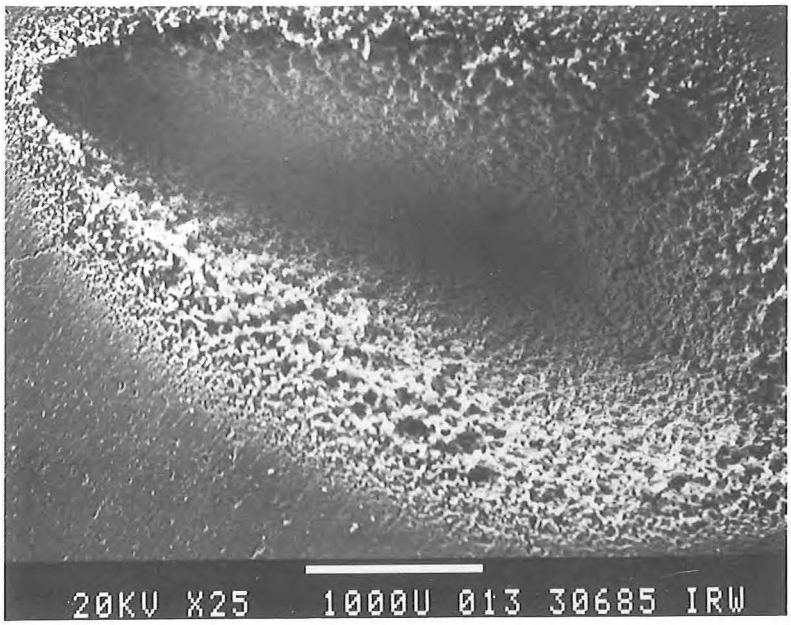

m) FE-289

SE

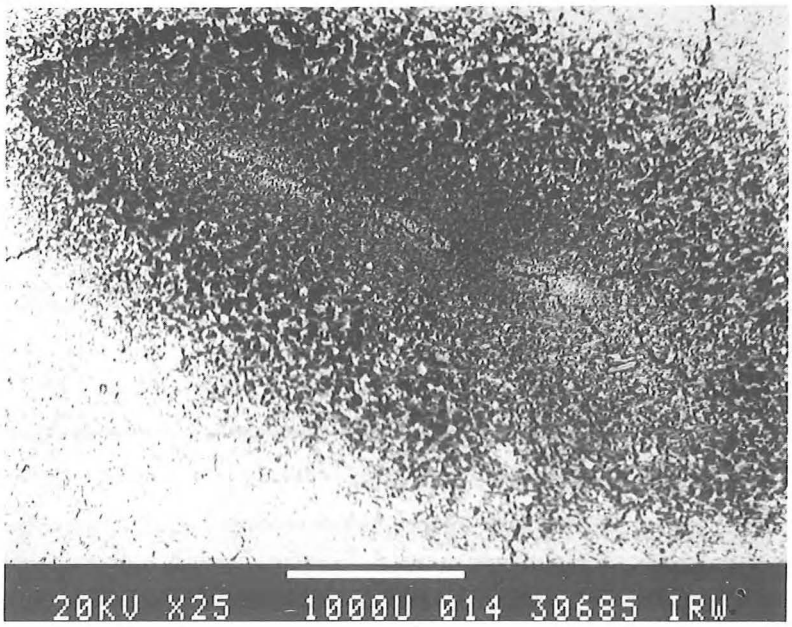

n) FE-289

BE

Fig. 43:

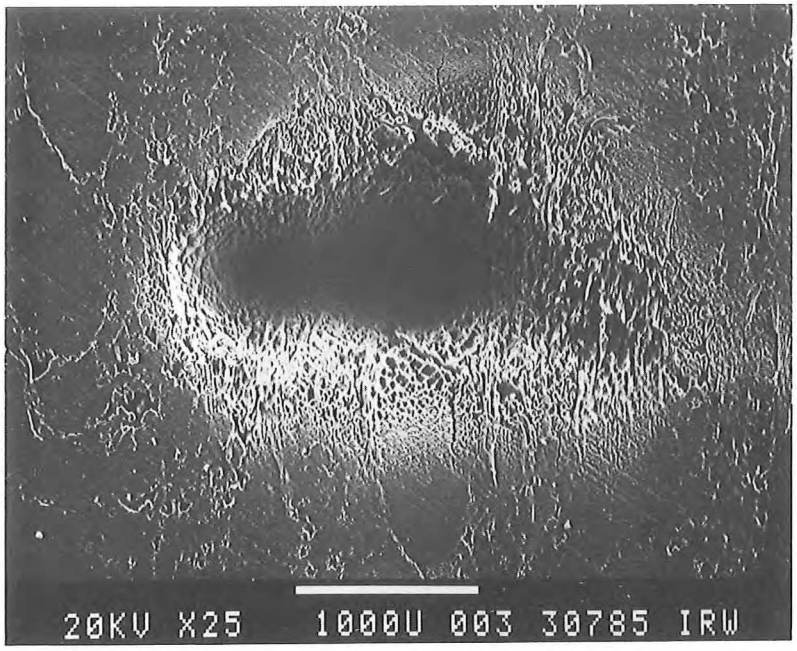

o) E-5923 P (II)

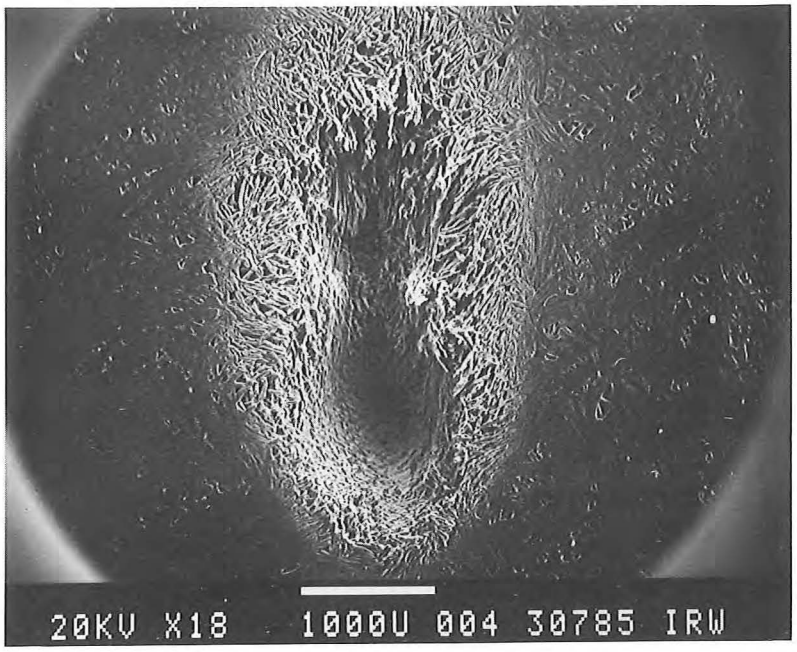

p) E-5923 P (⊥)

Fig. 43:

a) 5890-PT

SE

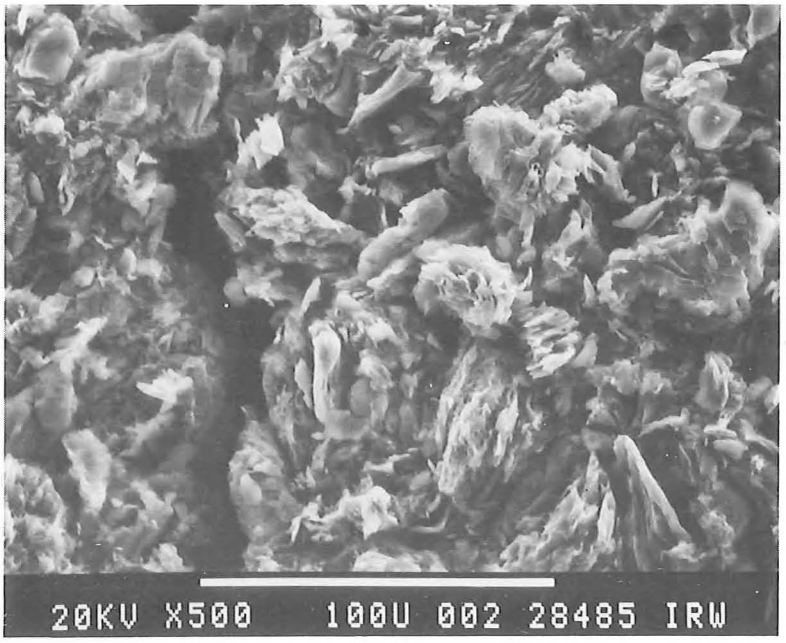

b) EY-306

SE

Fig. 44:
High resolution SEM-images of graphite tiles exposed to an electron beam with 3.5 $kWcm^{-2}$ power density and 1 s pulse duration (series 1)

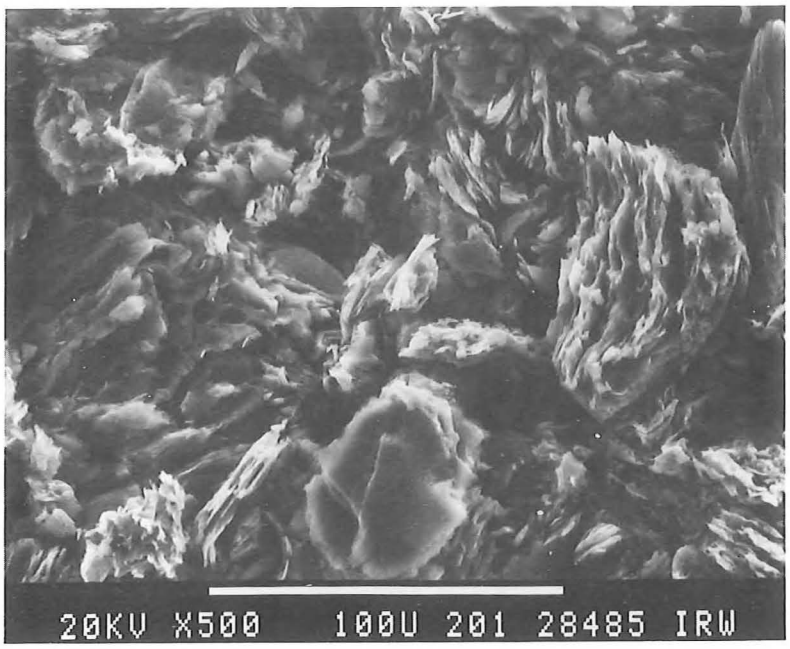

c) FP-219

SE

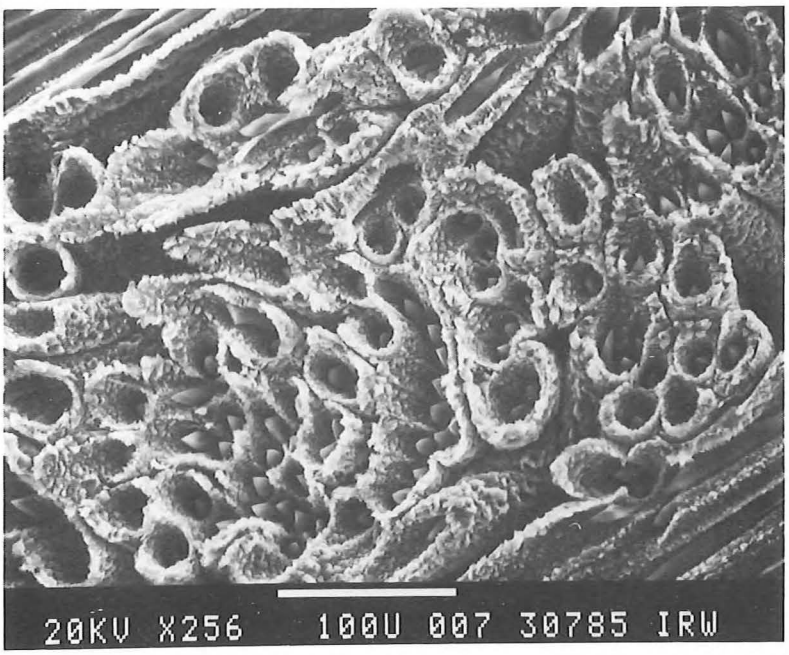

d) E-5923 P (⊥)

SE

Fig. 44:

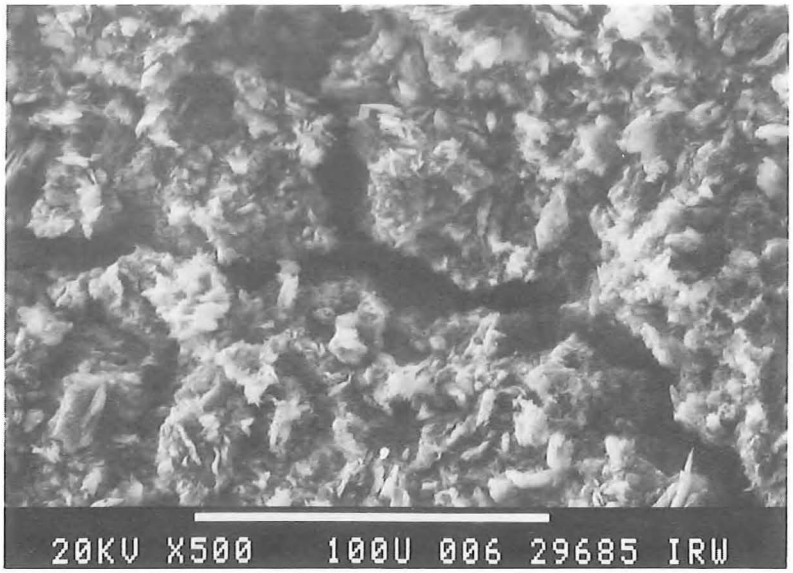

a) EK 98

SE

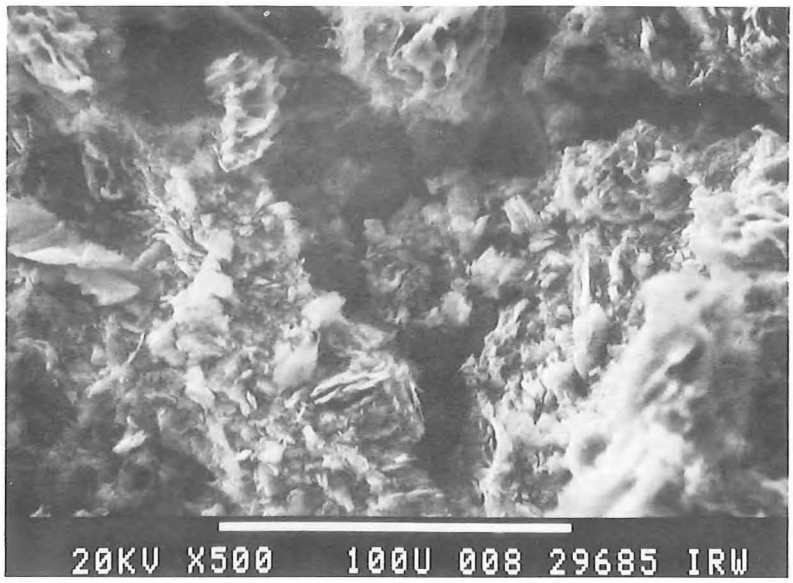

b) 5890/PT

SE

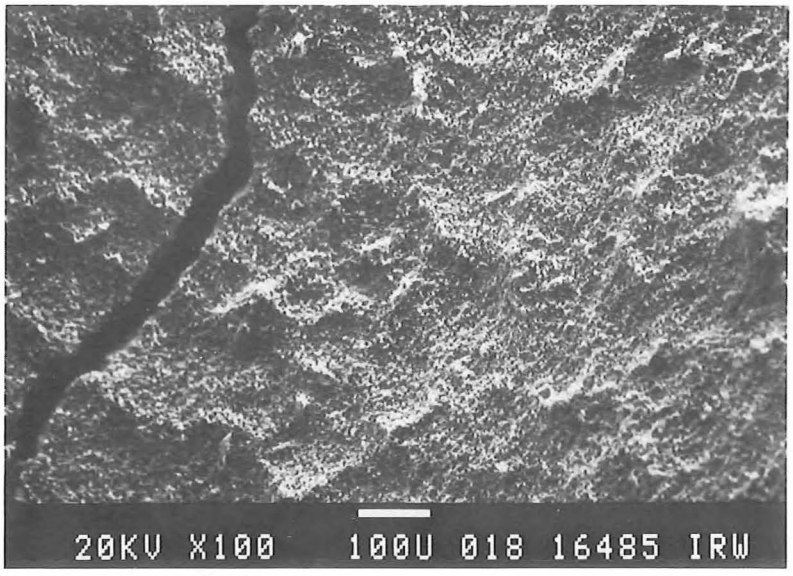

c) AXF-5 Q

SE

Fig. 45:
High resolution SEM-images of graphite tiles exposed to an electron beam with 5.0 $kWcm^{-2}$ power density and 1 pulse duration (series 3)

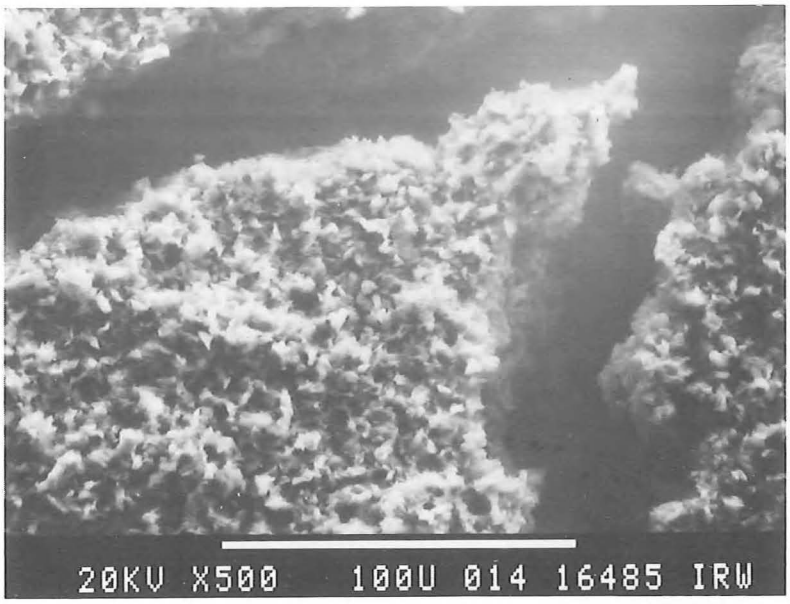

d) AXF-5 Q SE

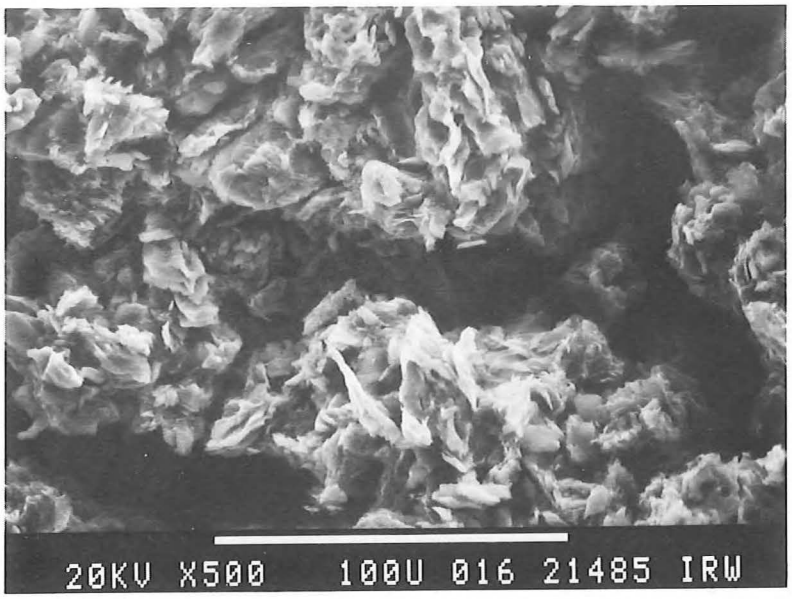

e) EY-306 SE

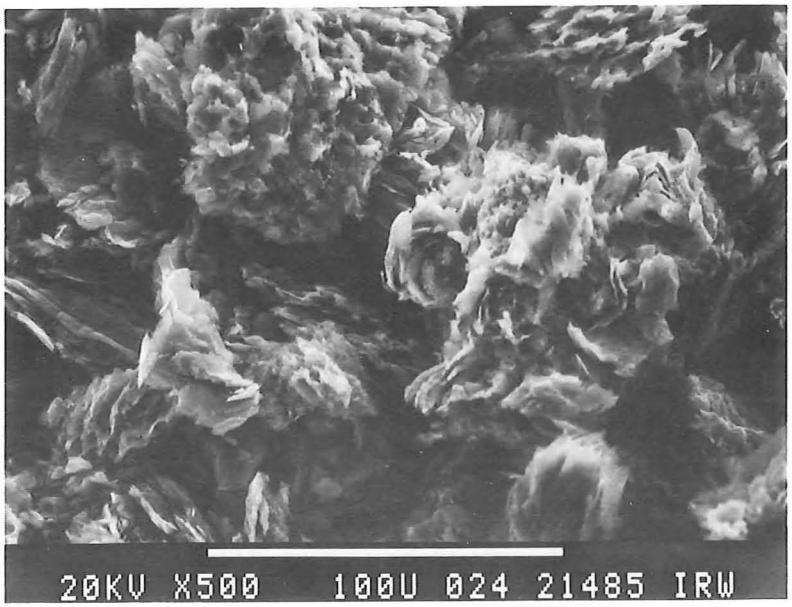

f) FP-219 SE

- series 1 -

Fig. 45:

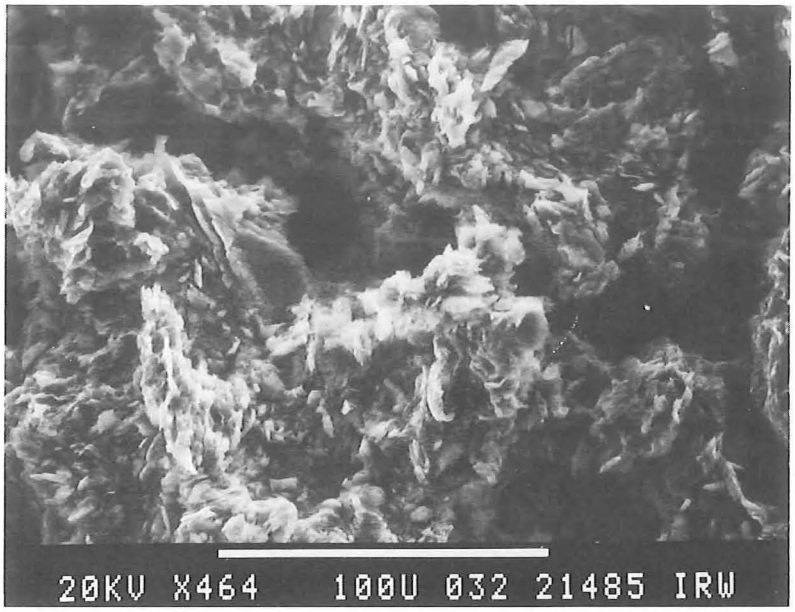

g) H-490

- series 1 -

SE

h) ATJ

SE

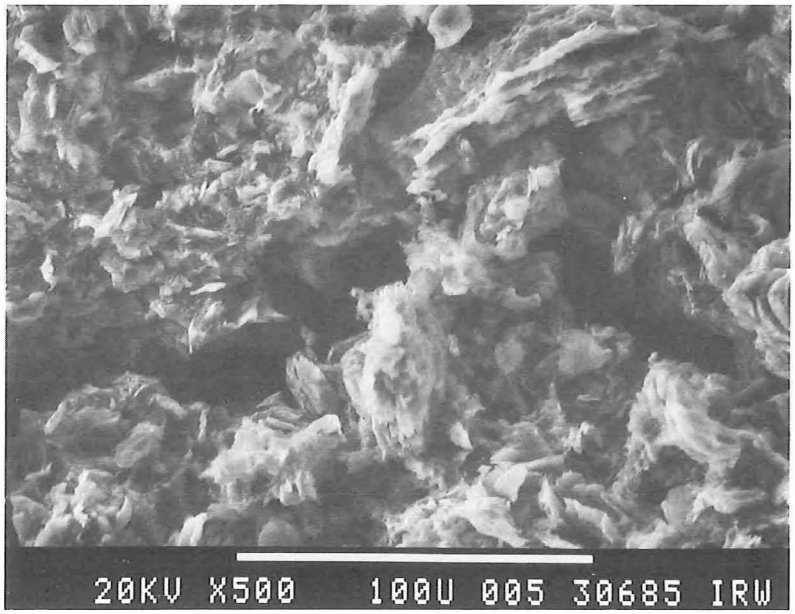

i) FE-289

SE

Fig. 45:

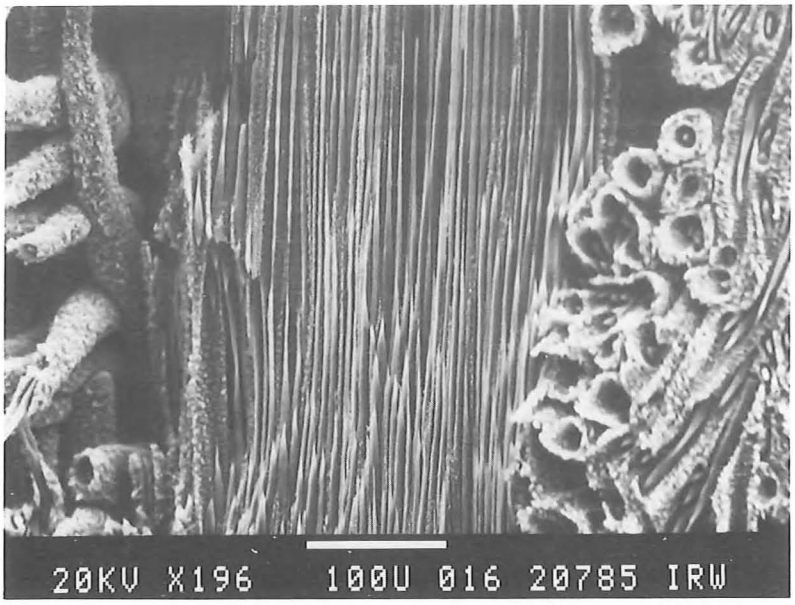

j) E-5923 P (II)

SE

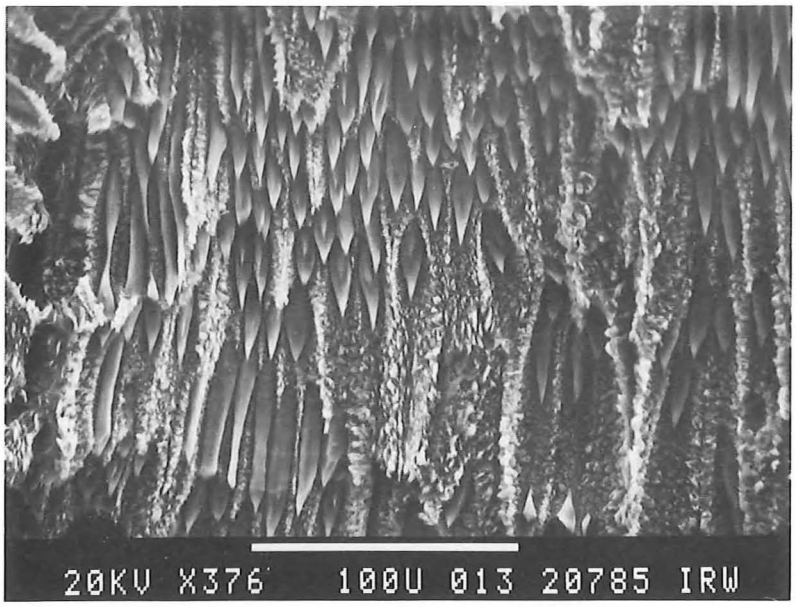

k) E-5923 P (II)

SE

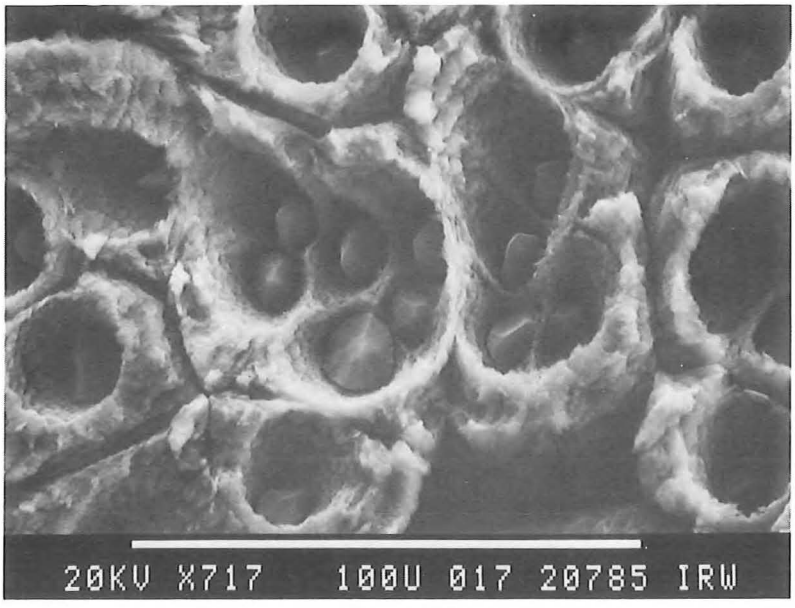

l) E-5923 P (⊥)

SE

Fig. 45:

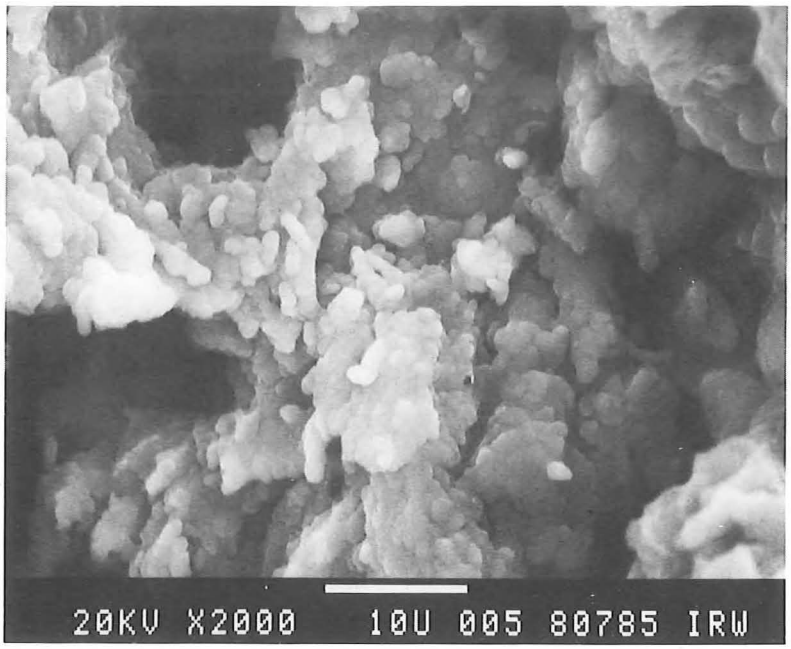

a) ATJ

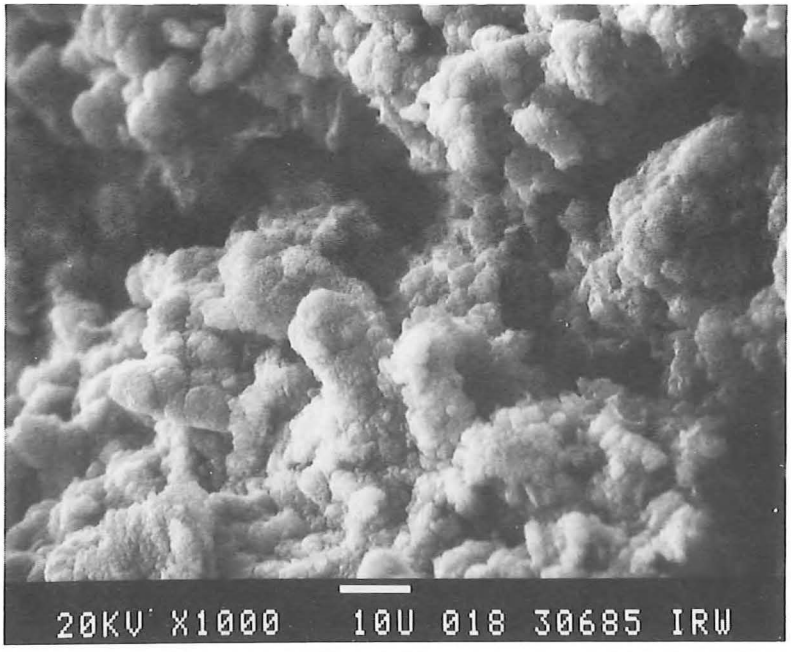

b) FE-289

Fig. 46:
High resolution SEM-images of graphite tiles exposed to an electron beam with 10 $kWcm^{-2}$ power density and 0.1 s pulse duration (series 3)

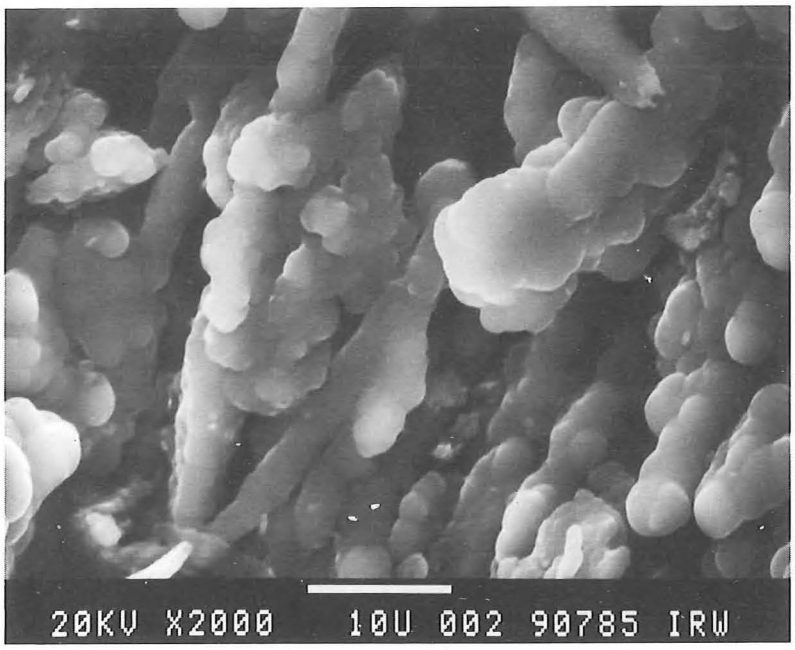

c) E-5923 P (⊥)

SE

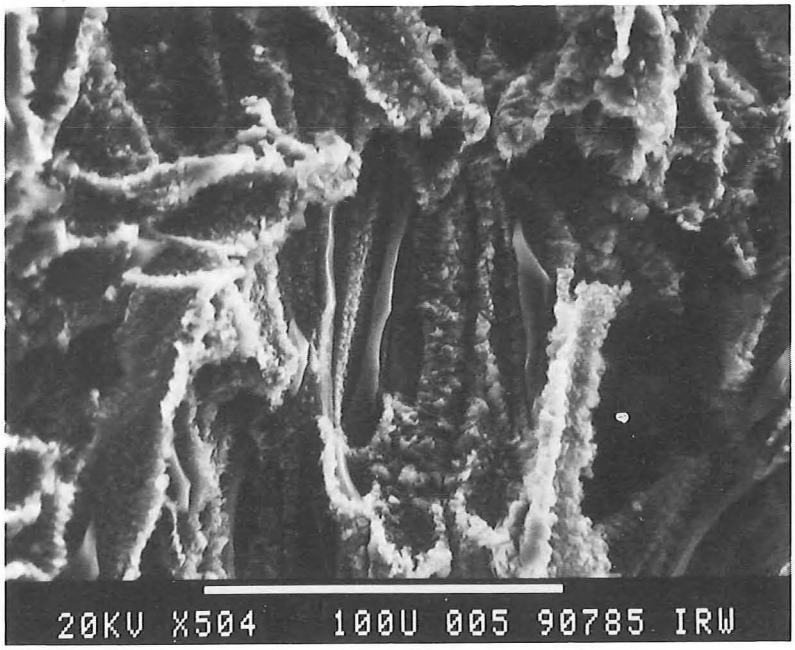

d) E-5923 P (⊥)

SE

Fig. 46:

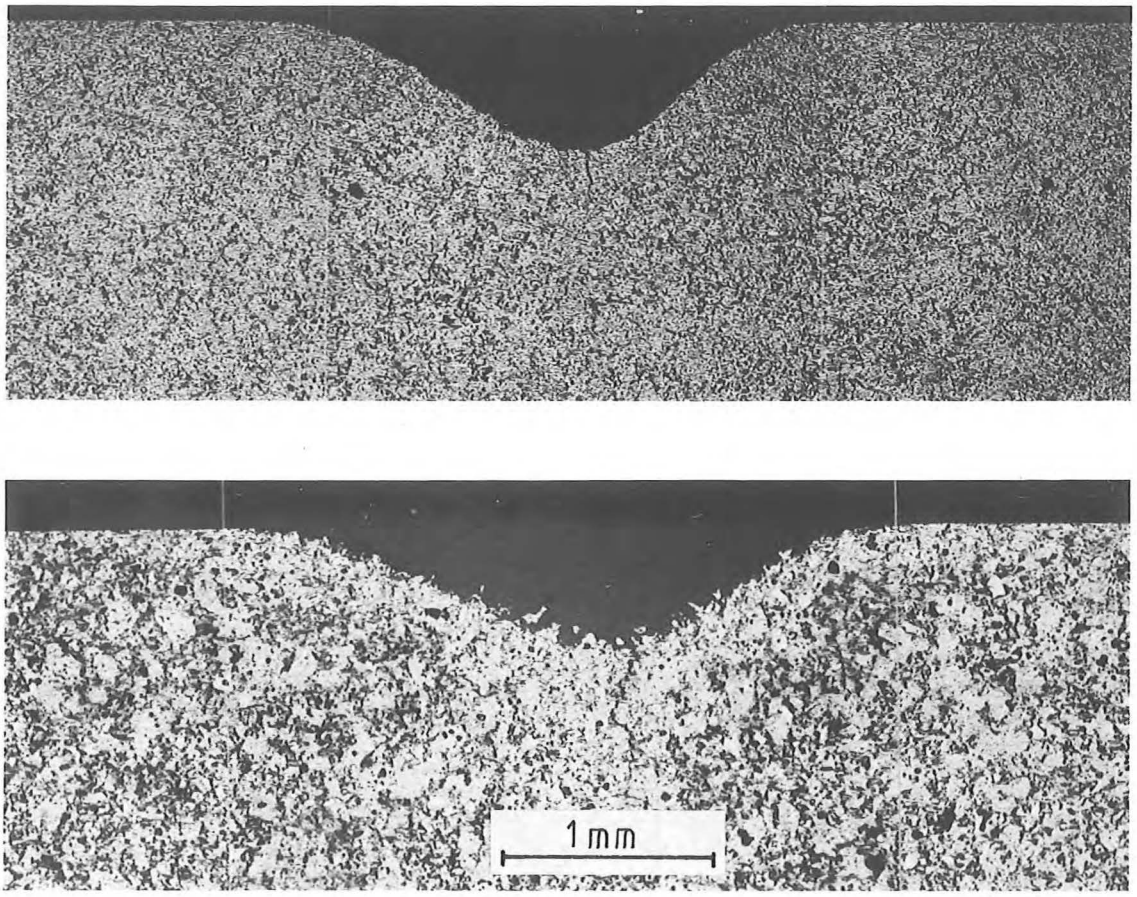

a) EK 98

b) 5890/PT

Fig. 47:
Ceramographic sections of graphite samples after a 5.0 $kWcm^{-2}$ electron beam pulse of 1 s duration (series 3)

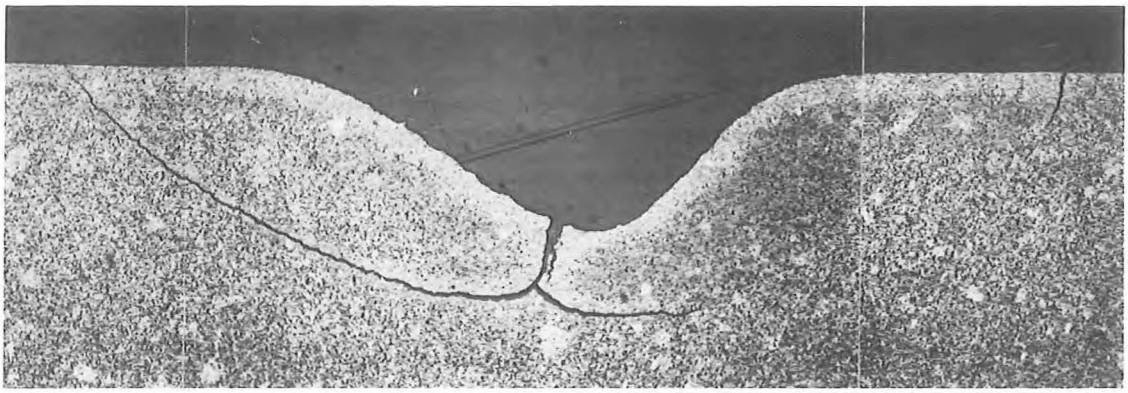

c) AXF-5 Q

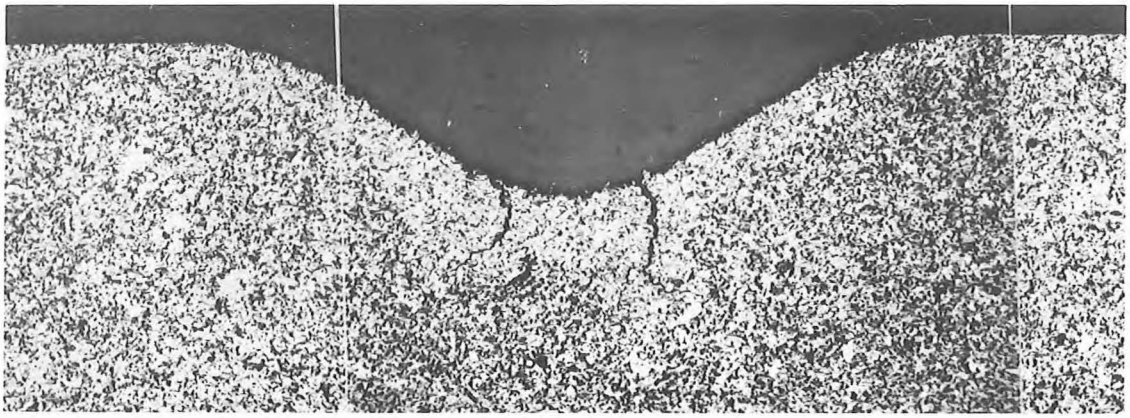

d) EY-306

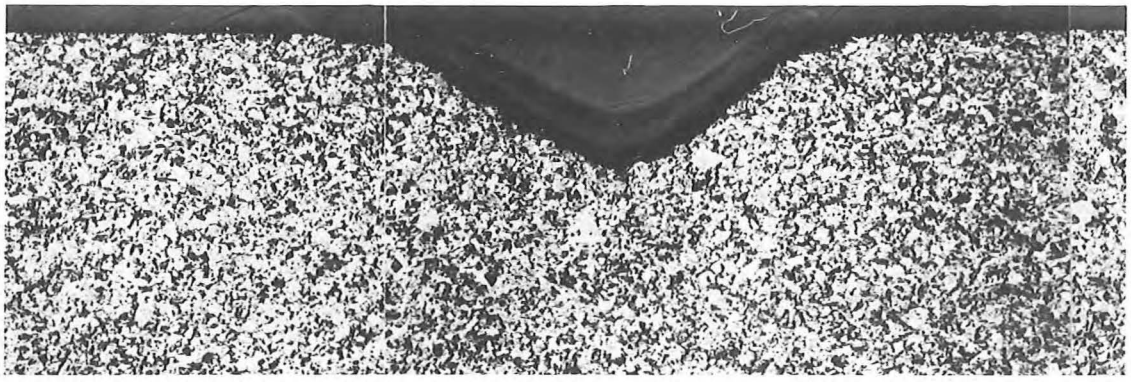

e) FP-219

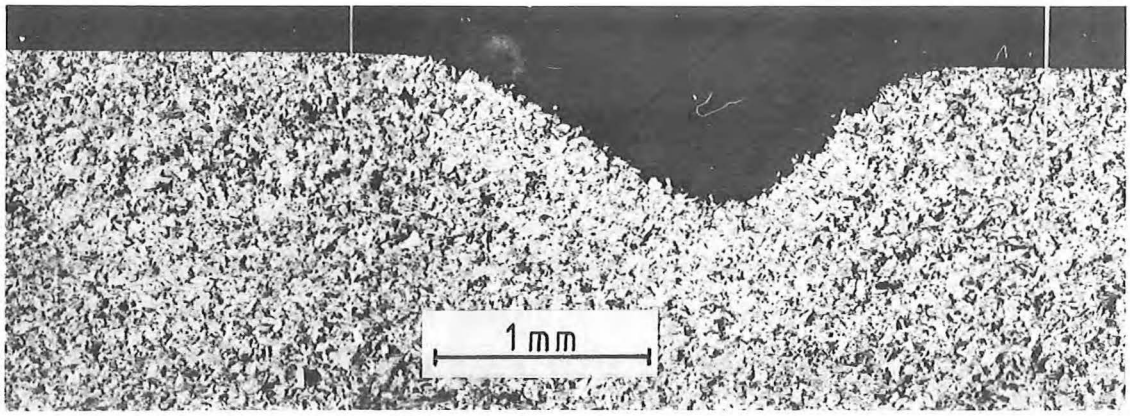

f) H-490

Fig. 47:

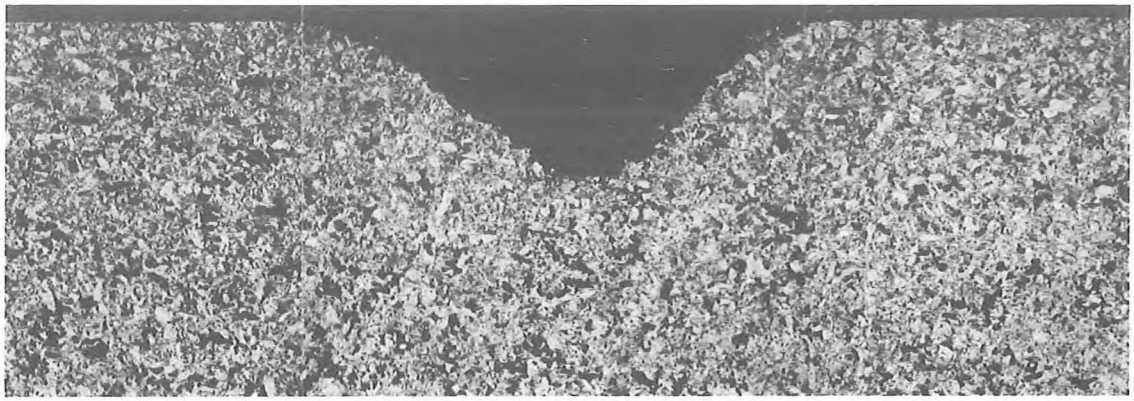

g) ATJ

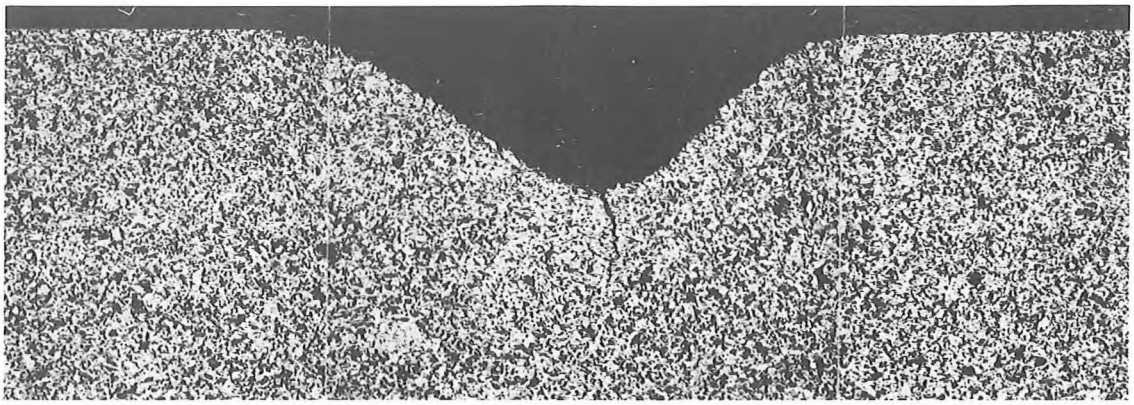

h) FE-289

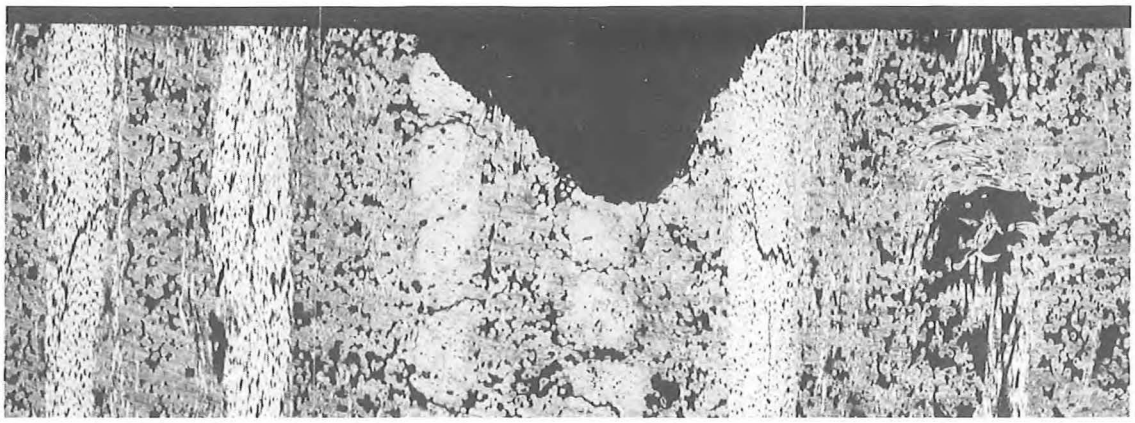

i) E-5923 P (||)

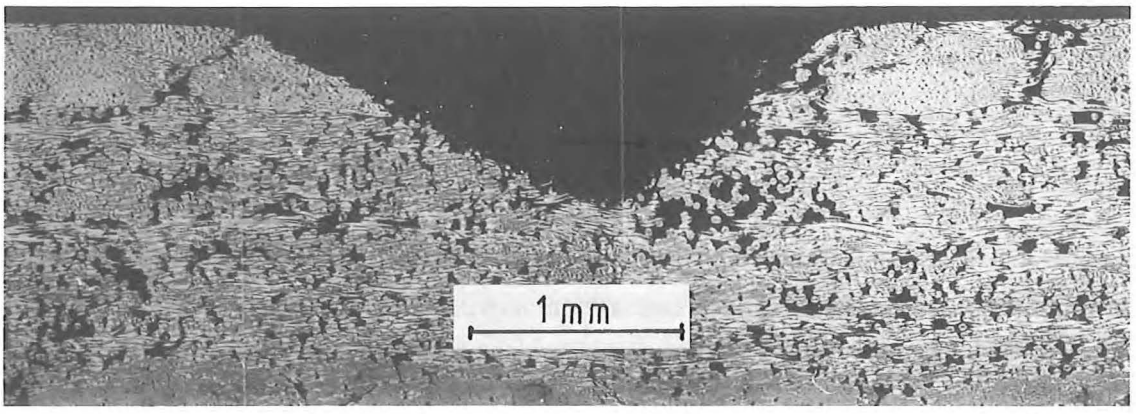

j) E-5923 P (⊥)

Fig. 47:

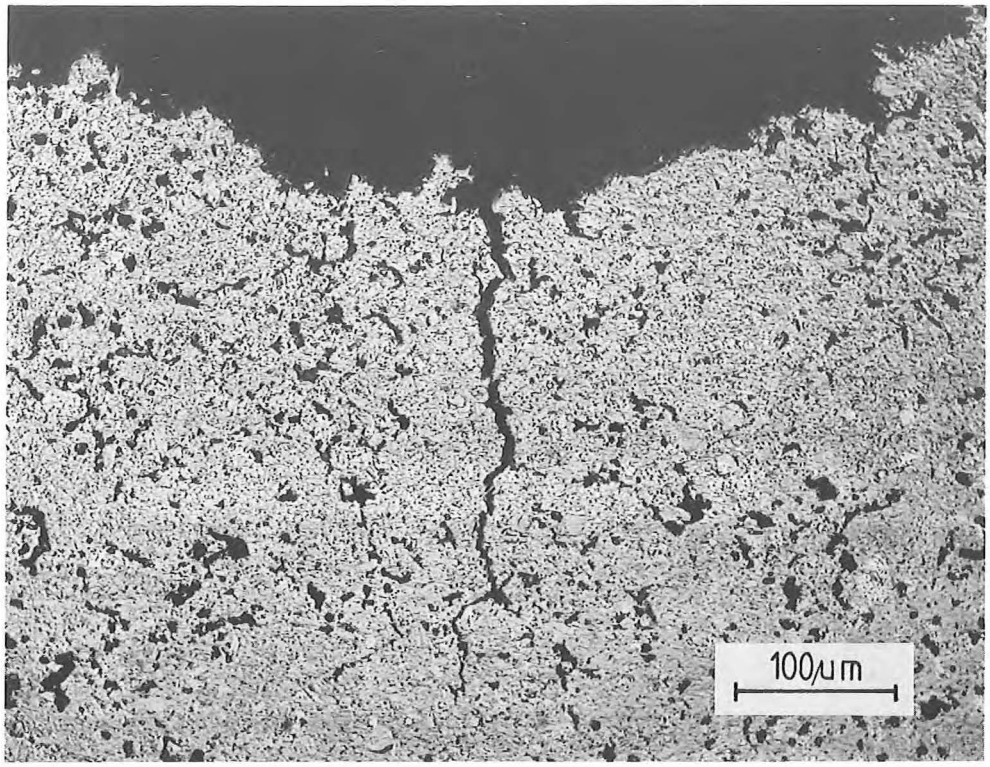

a) EK 98

Fig. 48:
Ceramographic sections of graphite samples after a 5.0 $kWcm^{-2}$ electron beam pulse of 1 s duration (series 3). High magnification micrographs of cracks.

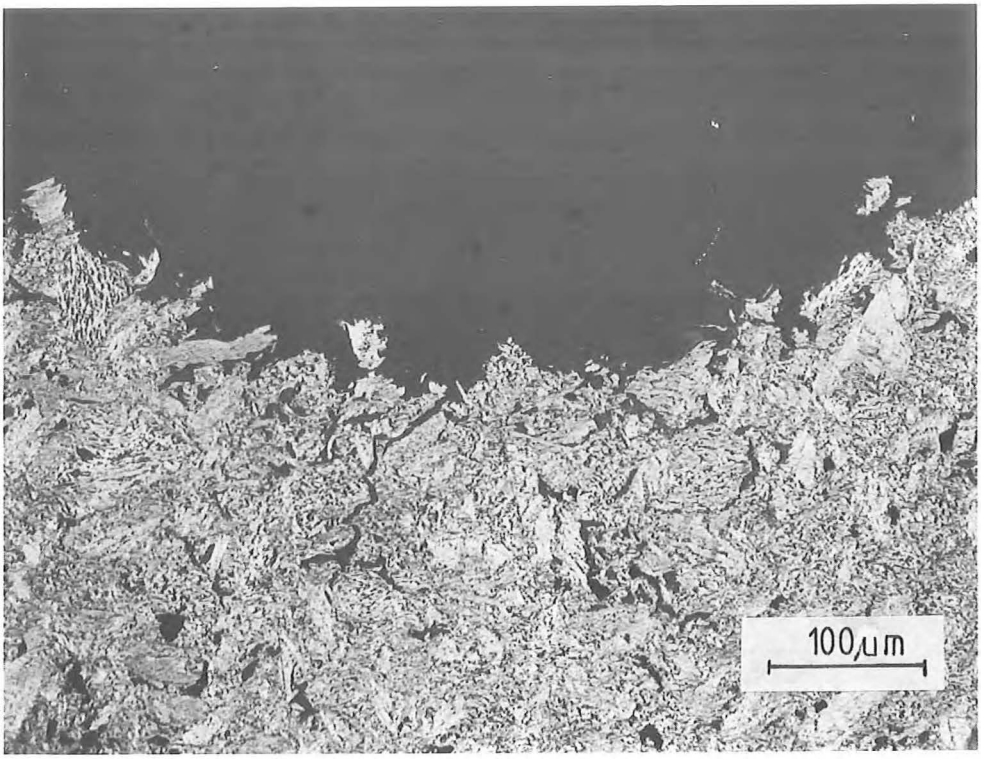

b) H-490

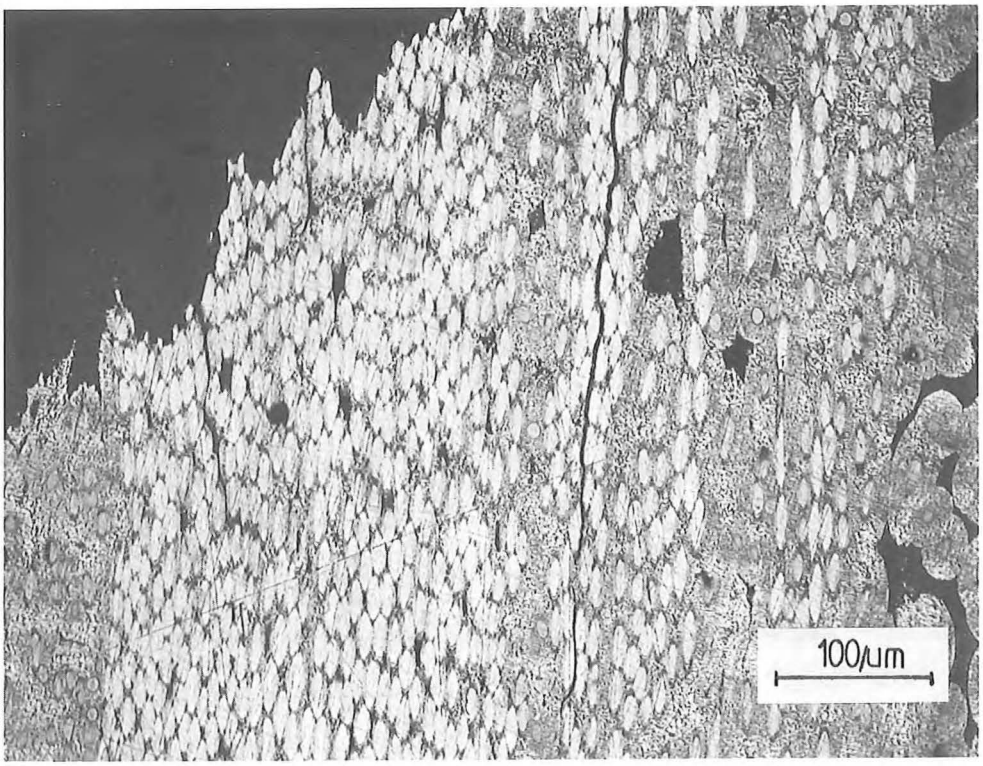

c) E-5923 P (| |)

Fig. 48:

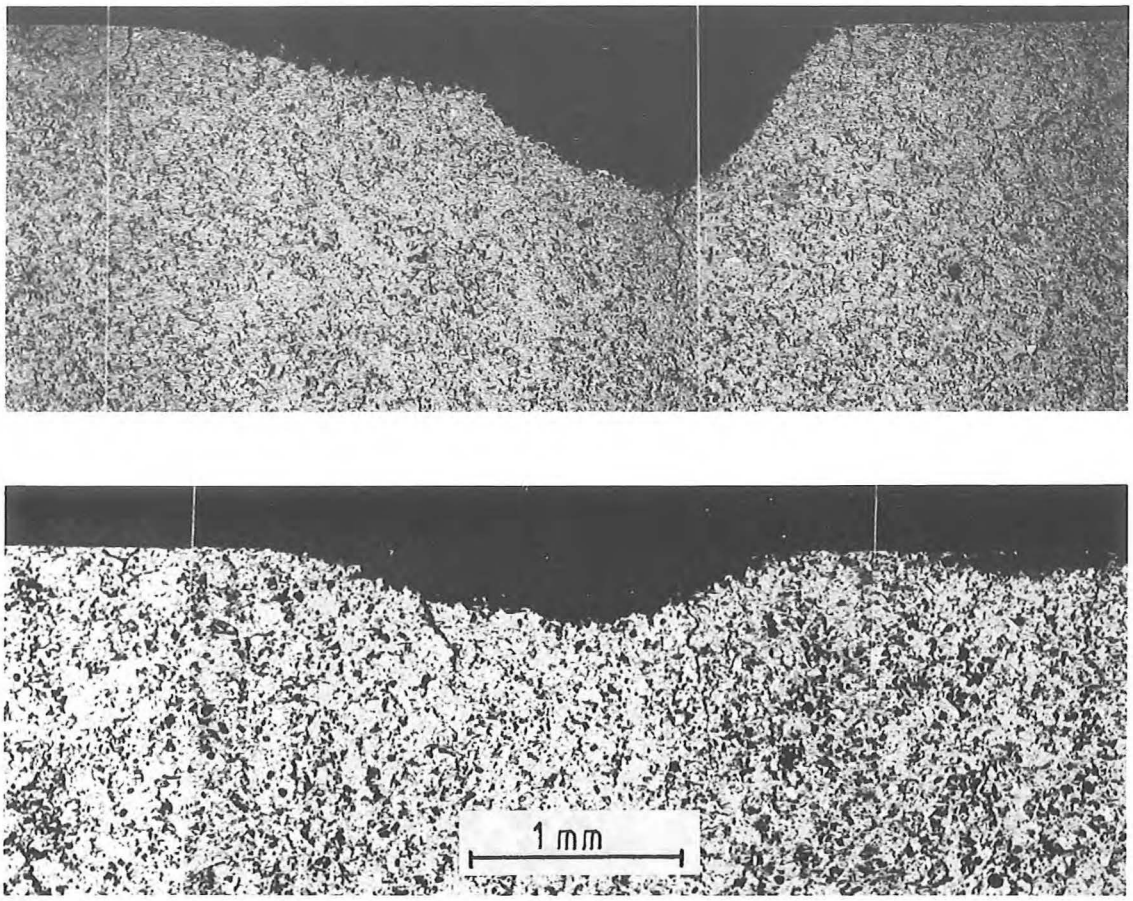

Fig. 49:
Ceramographic sections of graphite samples after a 10 $kWcm^{-2}$ electron beam experiment of 100 ms duration (series 3)

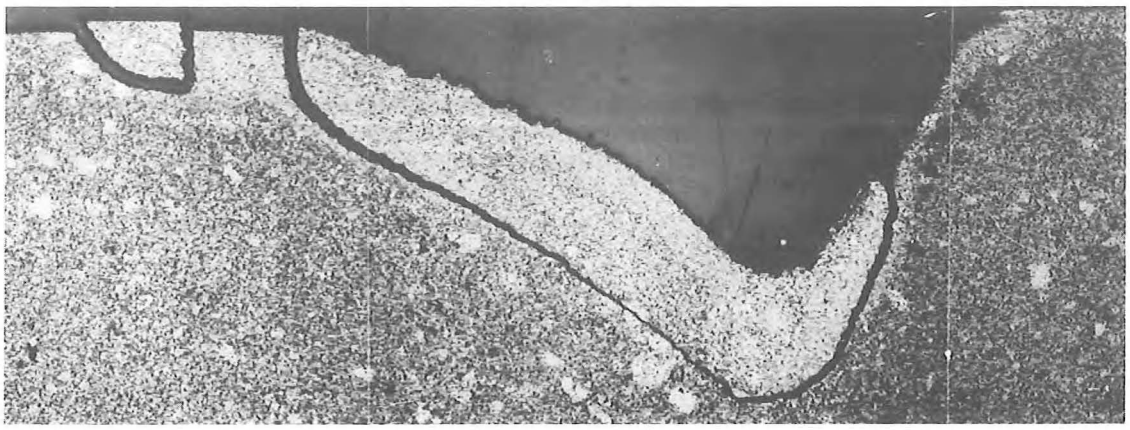

c) AXF-5 Q

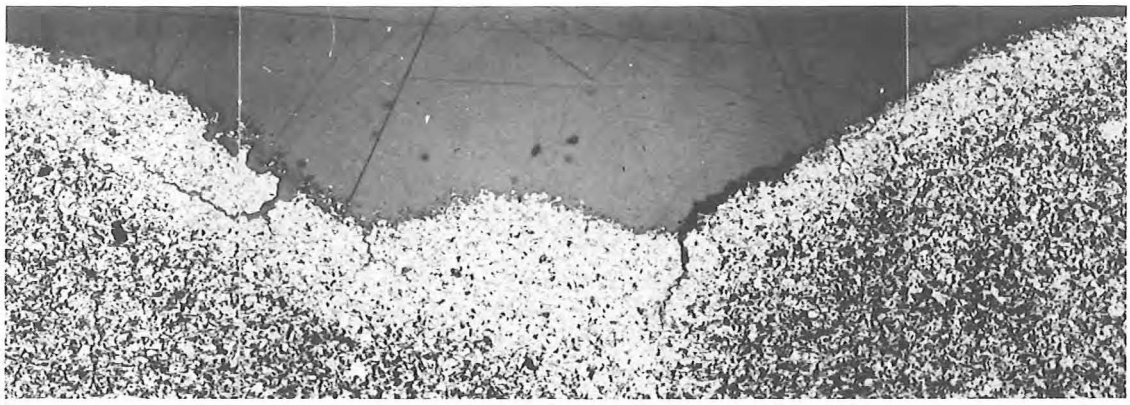

d) EY-306

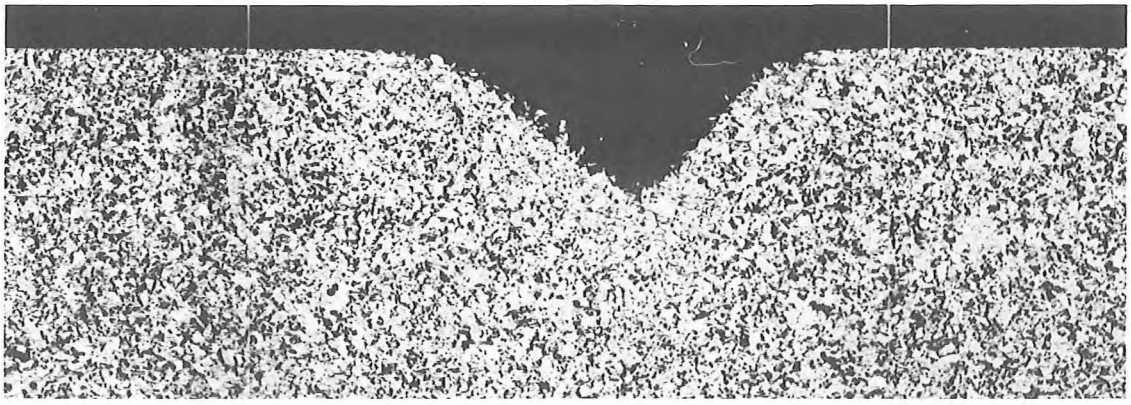

e) FP-219

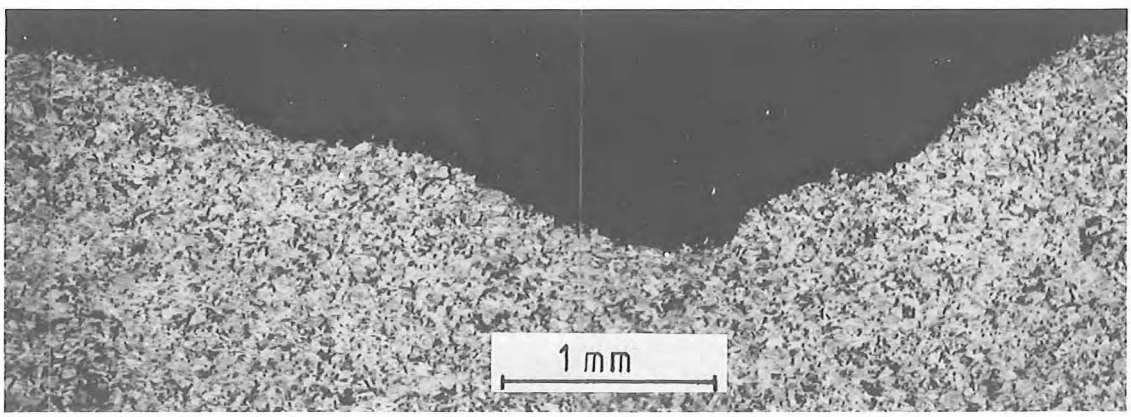

f) H-490

Fig. 49:

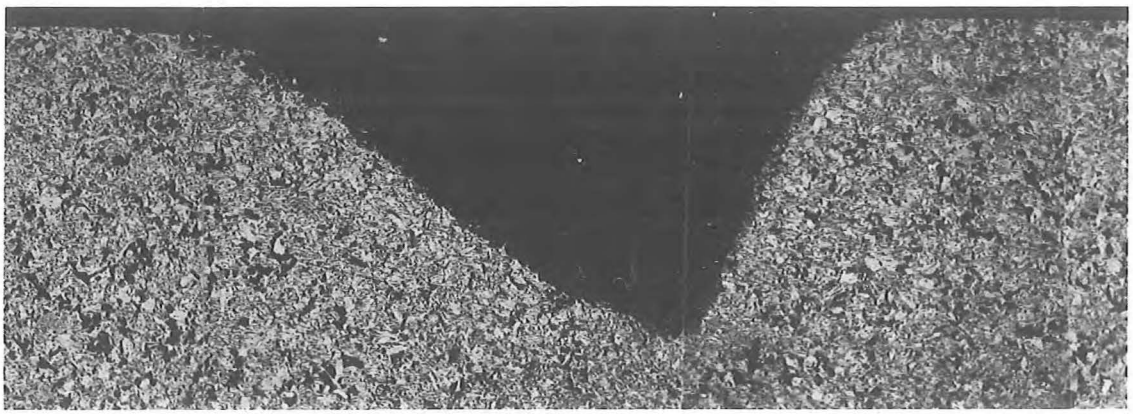

g) ATJ

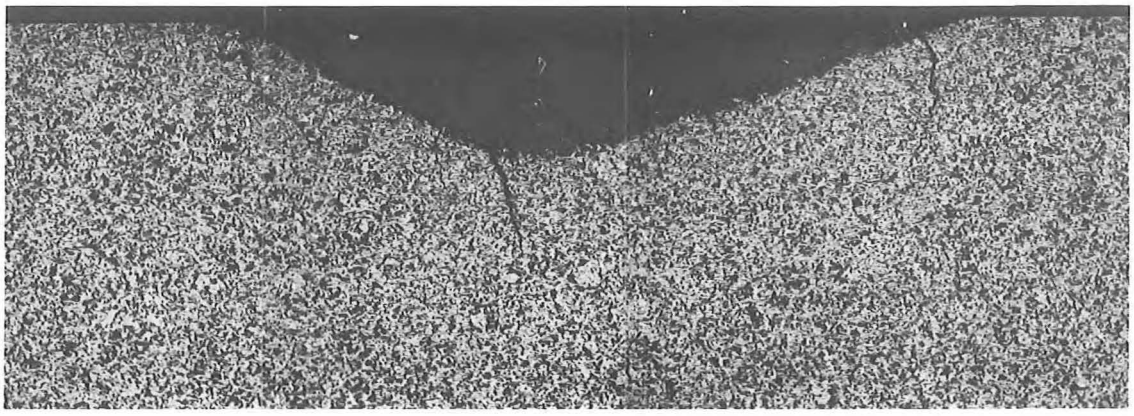

h) FE-289

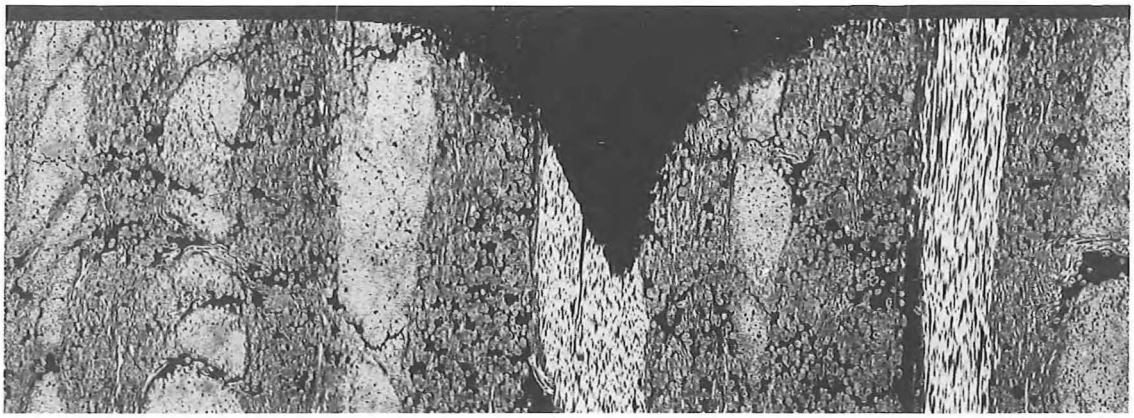

i) E-5923 P (∥)

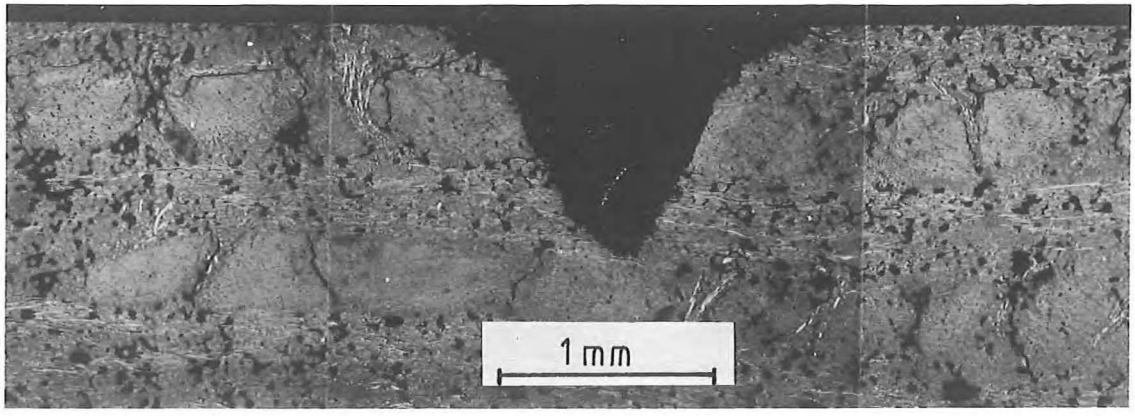

j) E-5923 P (⊥)

Fig. 49:

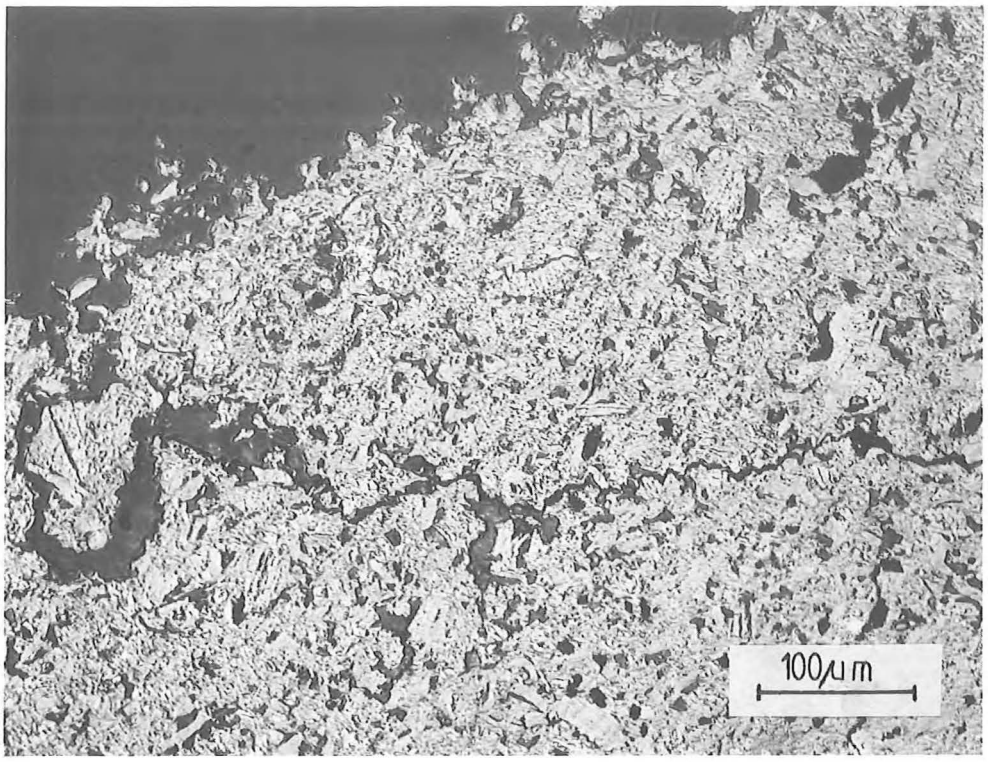

a) FE-289

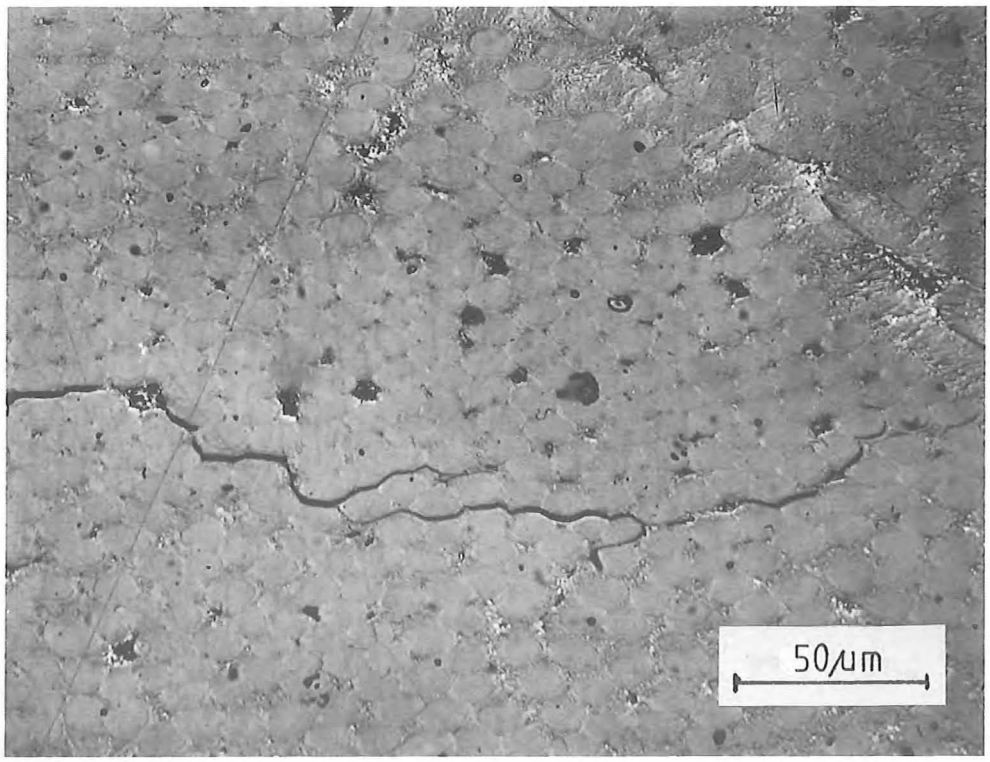

b) E-5923 P (||)

Fig. 50:
Ceramographic sections of graphite samples after a 10 $kWcm^{-2}$ electron beam experiment of 100 ms pulse duration (series 3). High magnification micrographs of cracks.

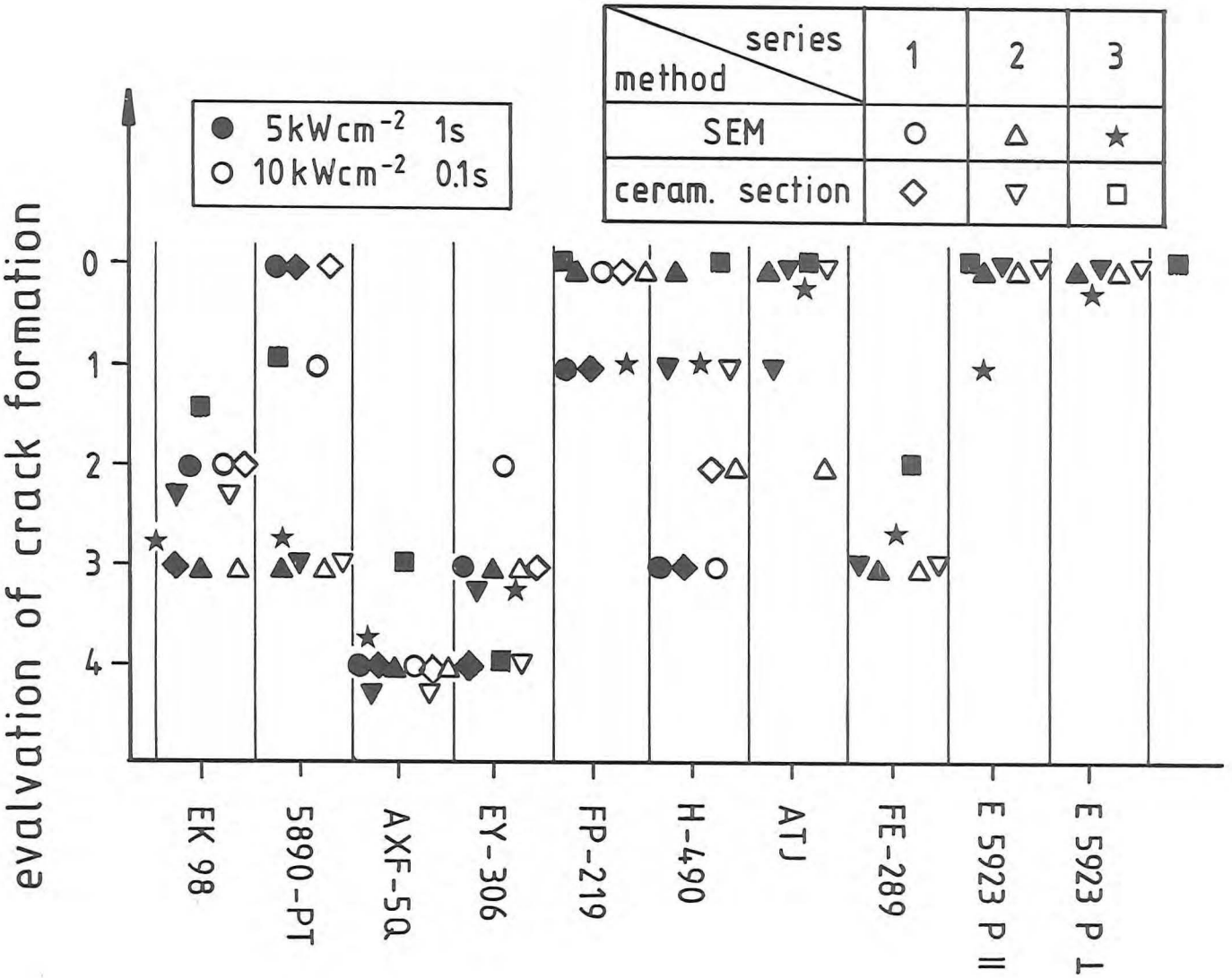

Fig. 51:
Evaluation of the crack formation after 5 $kWcm^{-2}$ - 1 s pulses (filled symbols) and 10 $kWcm^{-2}$ - 100 ms pulses (open symbols) for the experimental series 1, 3 and 4. The effect of crack formation was evaluated separately on SEM-images and ceramographic sections according to the following scale:

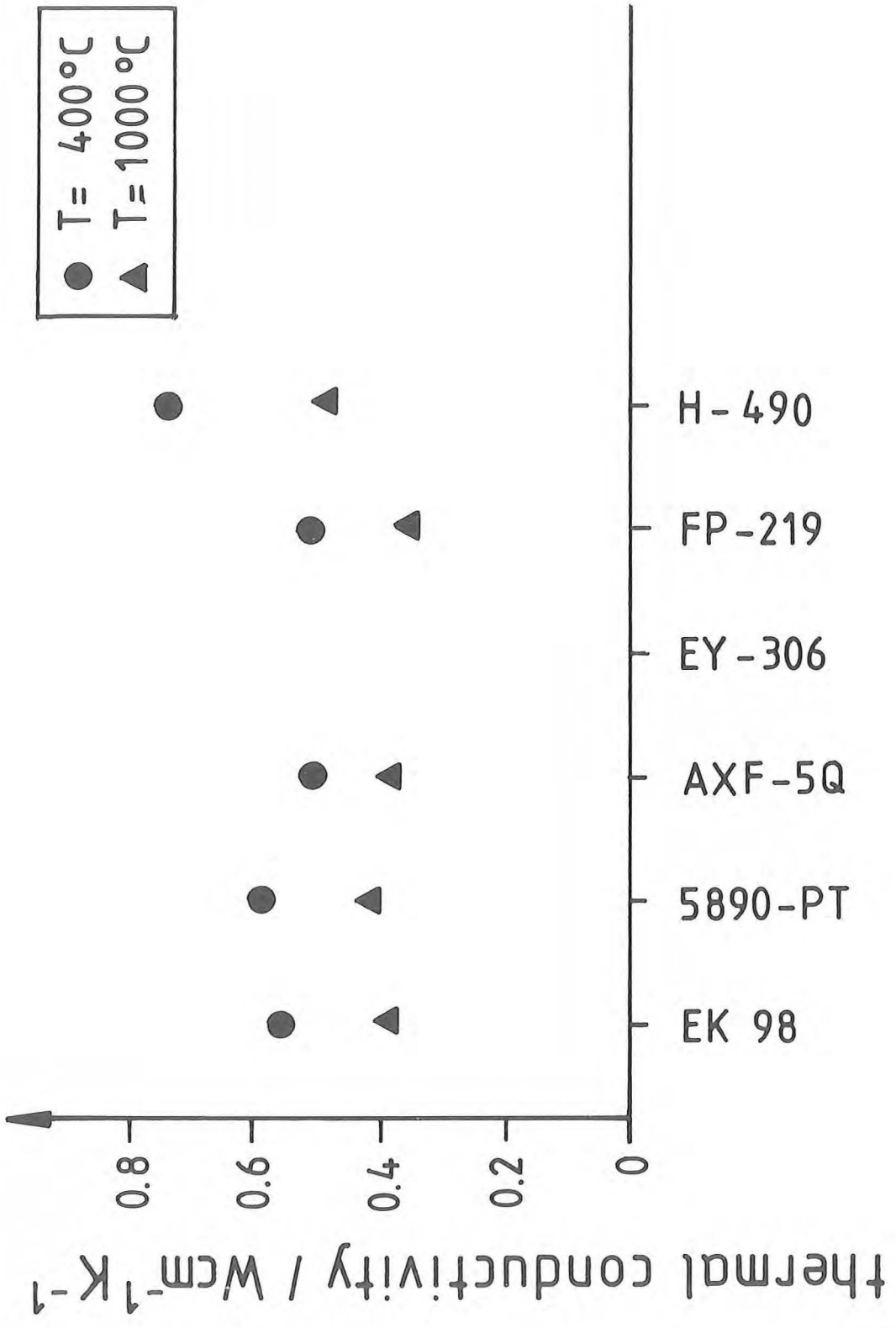

Fig. 52:
Thermal conductivity of various graphites for temperatures T = 400°C and T = 1000°C.

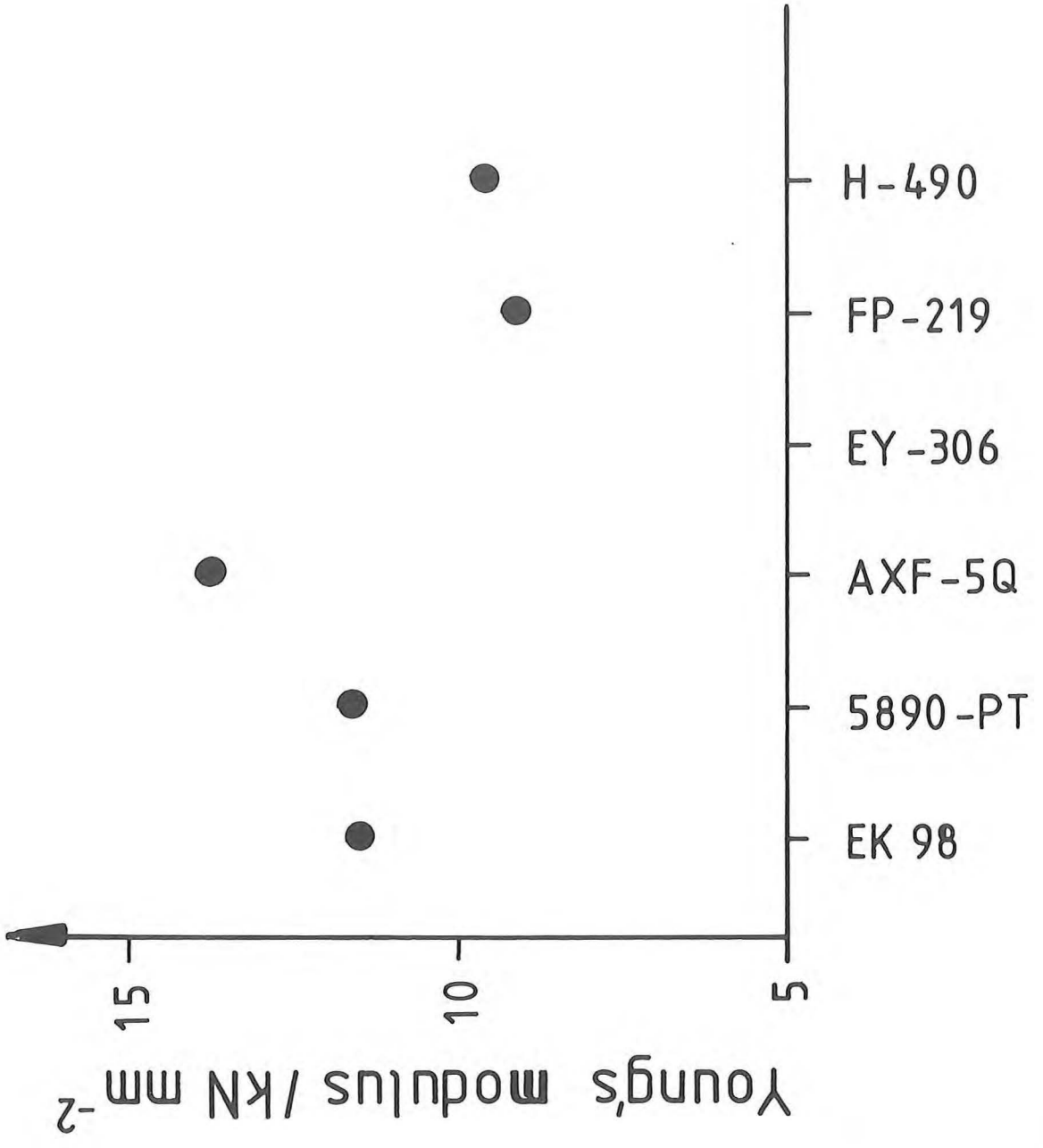

Fig. 53:
Young's modulus of various graphites

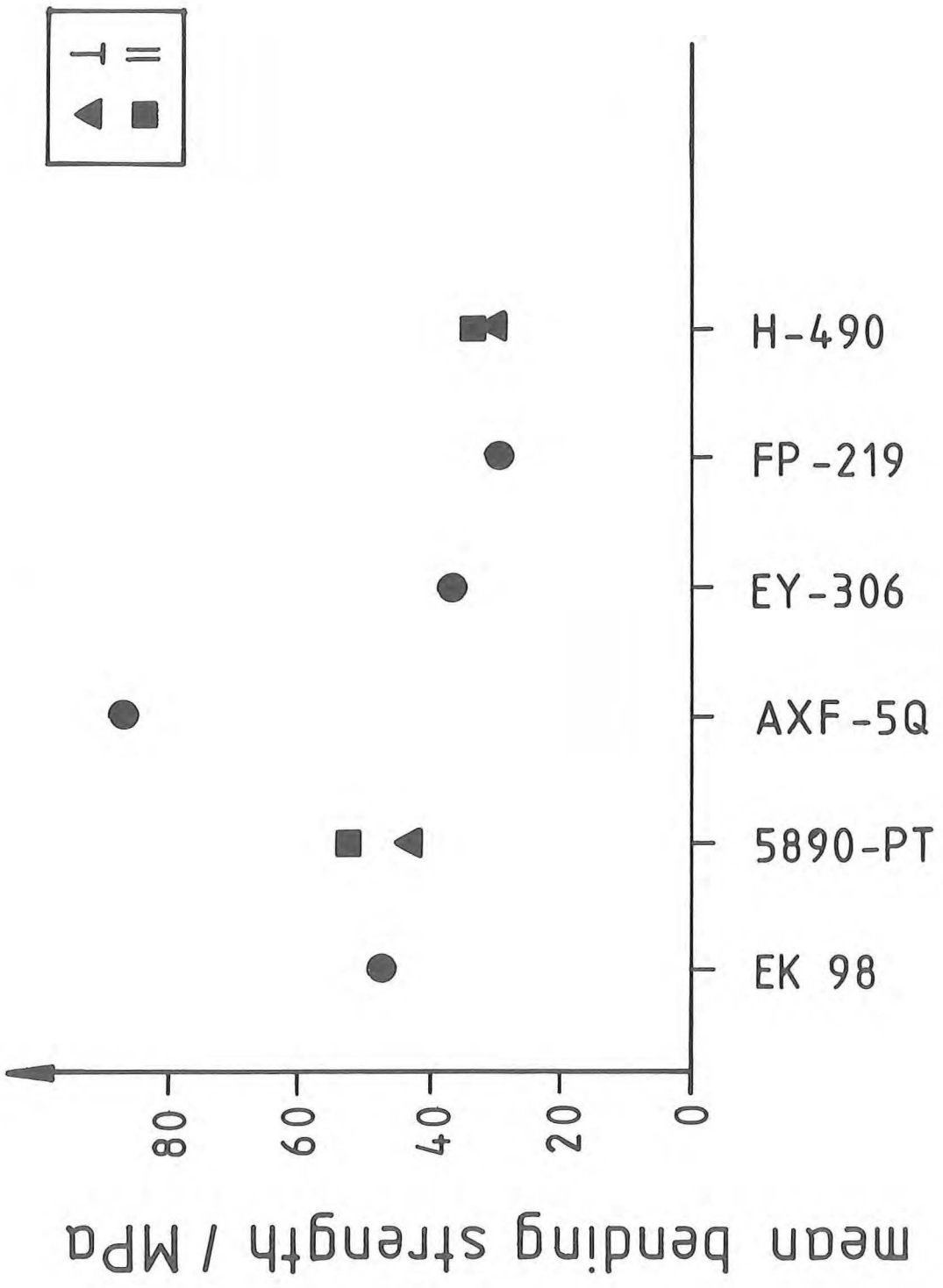

Fig. 54:
Mean bending strength of various graphites

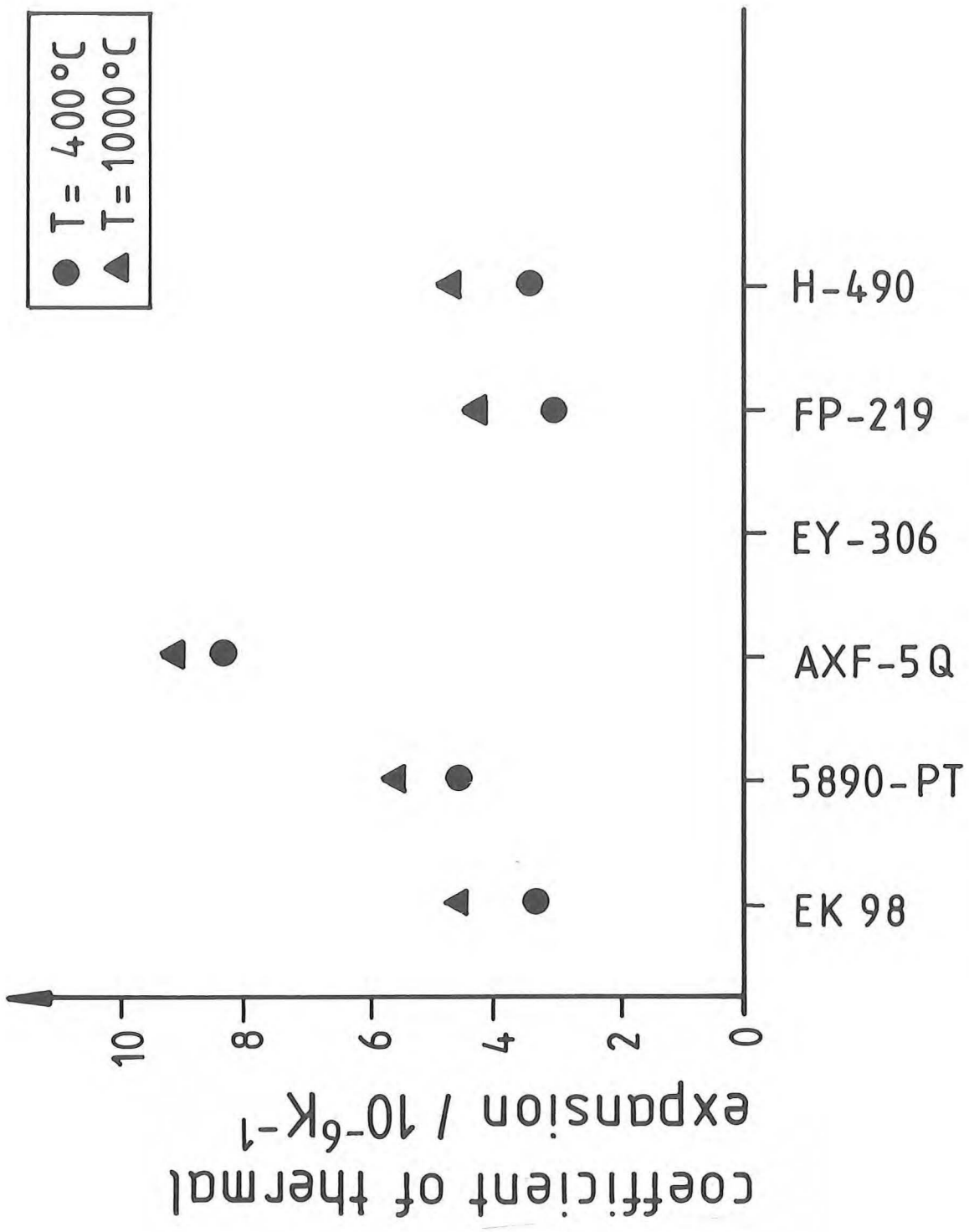

Fig. 55:
Coefficient of thermal expansion of the graphites for two different temperatures.

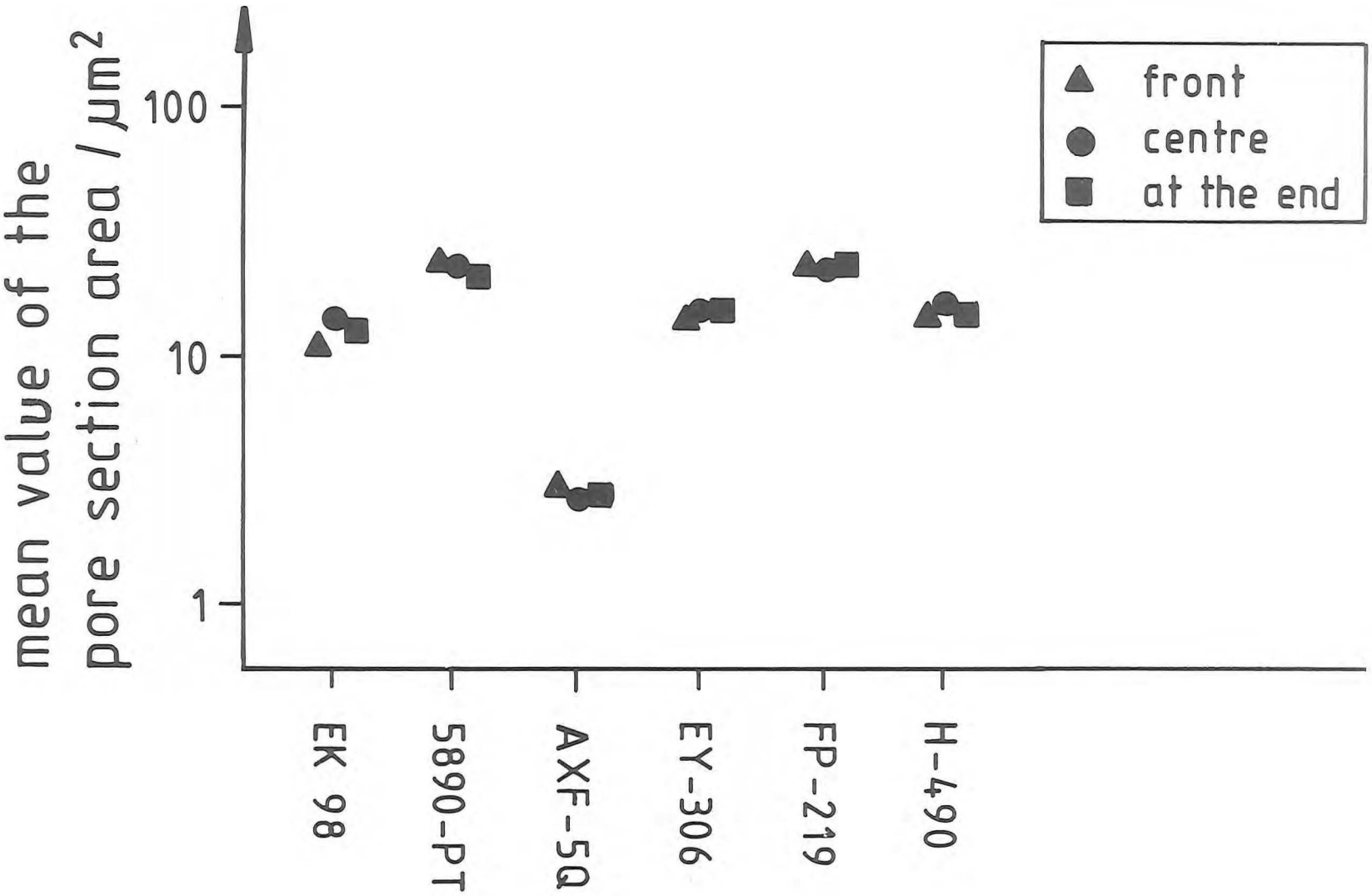

Fig. 56:
Mean value of the pore section area for different graphites determined by quantitative optical microscopy. The symbols indicate the position in the graphite blocks.

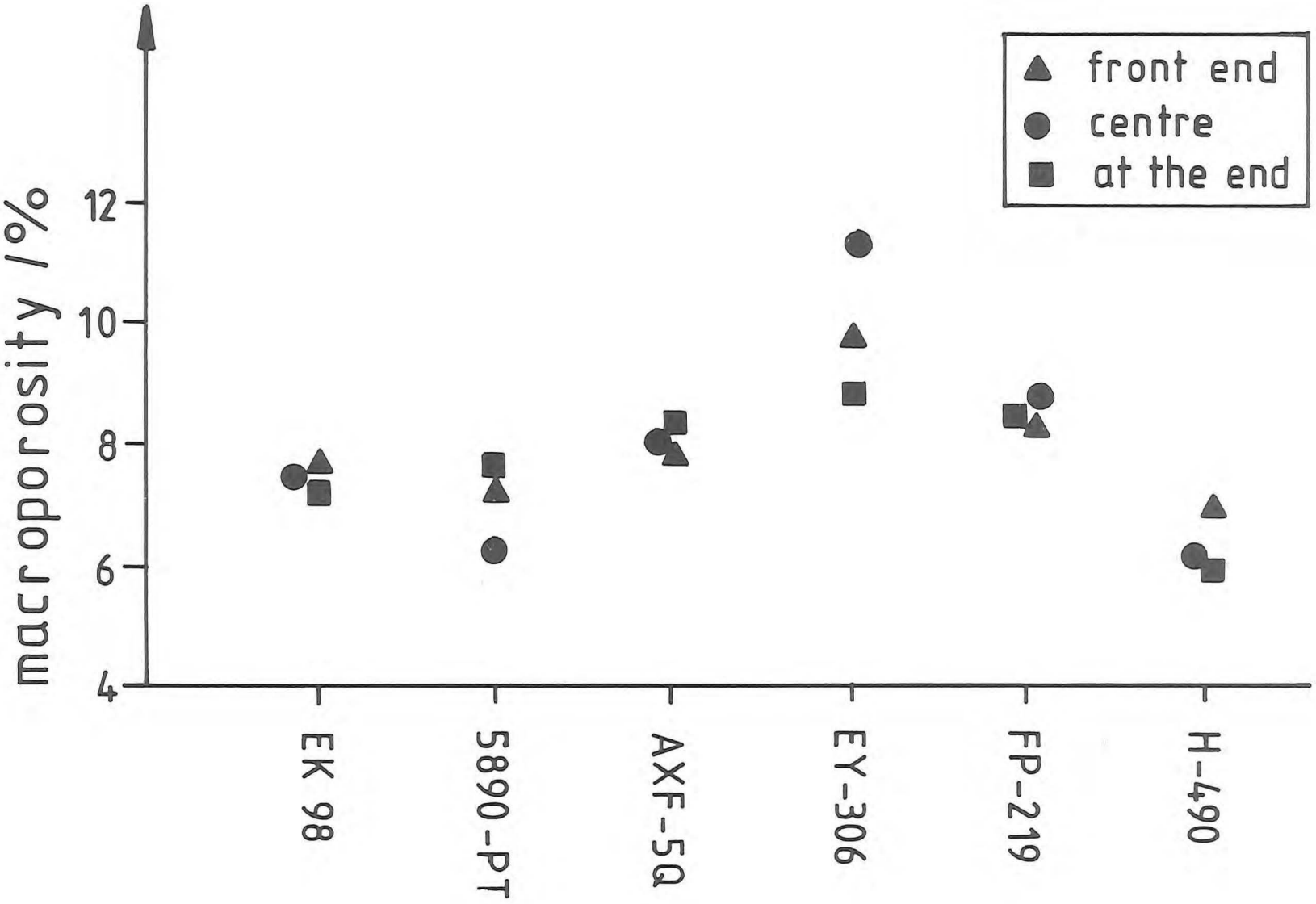

Fig. 57:
Macroporosity of different graphites determined by quantitative optical microscopy.
The symbols indicate the position in the graphite block.

4. References:

1. Binkele, L.: High Temp. - High Press., Vol. 4, 1972

2. Nightingale, R.E.: Nuclear Graphite, Pergamon Press 1962

3. Simmons, J.H.W.: Radiation Damage in Graphite, Pergamon Press, 1965

4. Haering, R.R., Mrozowski, S.: Progress in semiconductors 5, 1960

5. Eichhorn, R., Spies, B., Ritz, P., Depner, K. Panten, M.: A new system for precise beam diagnosis on high power (> 30 kW) electron beam machines, Report II W-Doc IV-378-84, Institut für schweißtechnische Fertigungsverfahren, RWTH Aachen/D, 1984